Adoptable Coastal Remote Sensing Using Wave-field Observations

Instruments, Techniques and Application

Gawehn, M.A.

DOI
10.4233/uuid:9dacf50b-ac87-4ed4-9878-d2f1f415ed83

Publication date
2022

Document Version
Final published version

Citation (APA)
Gawehn, M. A. (2022). *Adoptable Coastal Remote Sensing Using Wave-field Observations: Instruments, Techniques and Application*. [Dissertation (TU Delft), Delft University of Technology].
https://doi.org/10.4233/uuid:9dacf50b-ac87-4ed4-9878-d2f1f415ed83

Adoptable Coastal Remote Sensing Using Wave-field Observations

Instruments, Techniques and Application

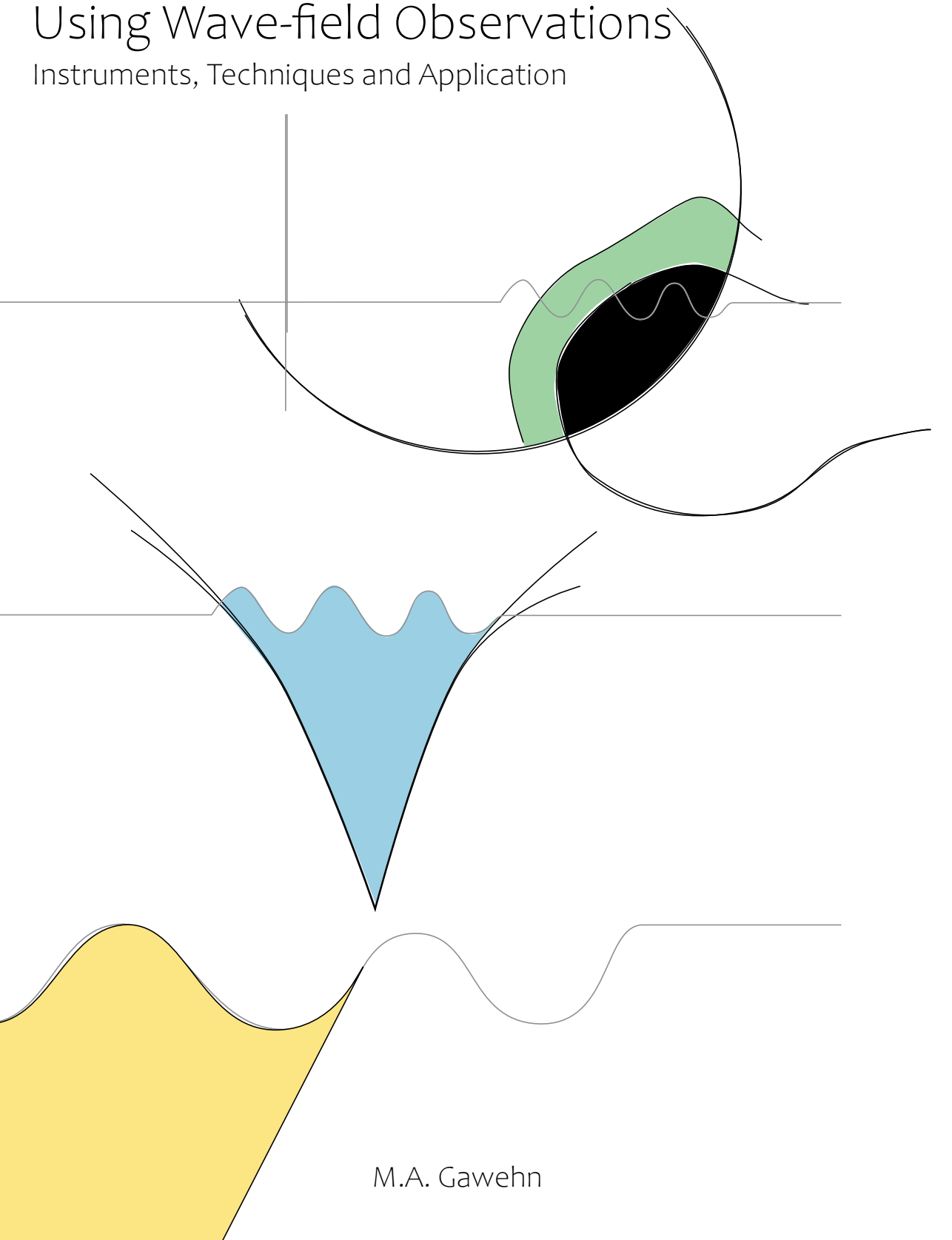

M.A. Gawehn

Adoptable Coastal Remote Sensing Using Wave-field Observations

Instruments, Techniques and Application

Adoptable Coastal Remote Sensing Using Wave-field Observations

Instruments, Techniques and Application

Proefschrift

ter verkrijging van de graad van doctor
aan de Technische Universiteit Delft,
op gezag van de Rector Magnificus Prof. dr. ir. T.H.J.J. van der Hagen,
voorzitter van het College voor Promoties,
in het openbaar te verdedigen op maandag 17 oktober 2022 om 15:00 uur

door

Matthijs Asse GAWEHN

Civiel ingenieur, Technische Universiteit Delft, Nederland,
geboren te Tübingen, Baden-Württemberg, Duitsland.

Dit proefschrift is goedgekeurd door de promotoren.

Samenstelling promotiecommissie:

Rector Magnificus,	voorzitter
Prof. dr. ir. S.G.J. Aarninkhof,	Technische Universiteit Delft, promotor
Dr. ir. S. de Vries,	Technische Universiteit Delft, promotor
Dr. ir. A.R. van Dongeren,	IHE Delft Institute for Water Education, copromotor
Onafhankelijke leden:	
Prof. dr. ir. R.F. Hanssen	Technische Universiteit Delft
Prof. dr. D. van der Wal	Universiteit Twente
Dr. B. Castelle,	CNRS/Université de Bordeaux
Dr. M.L. Palmsten,	United States Geological Survey
Prof. dr. ir. A.J.H.M. Reniers	Technische Universiteit Delft, reservelid

Keywords: coastal remote sensing, mapping, depth inversion, wave field video, operational monitoring, on-the-fly processing, self-adaptive algorithms, XBand-radar, camera, UAV, drone, satellite

Printed by: Ridderprint

Front & Back: Abstract wave-based coastal remote sensing.

ISBN 978-94-6384-377-5

An electronic version of this dissertation is available at
https://repository.tudelft.nl/.

Er zijn diverse dingen
Waarmee men dit kan doen
Dat geldt voor alle kringen
Dat geldt in elk seizoen
Naarmate het blijft groeien
Verhoogt het uw geluk
Begint het meer te boeien
En kan het minder stuk

Verzamelen, Drs. P

Contents

Summary

The aim of this study is to innovate wave-based depth-inversion towards smarter and faster algorithms to be used with various remote sensing instruments for broad community use. Wave-based depth inversion describes a branch of coastal remote sensing, which uses video recordings of a wave-field to derive depths and thereby create digital maps of coastal bathymetries. The technique utilizes the fact that waves react to the underlying bathymetry by changing their length and celerity, respectively getting shorter and slower as the water depth gets shallower. Waves may also change their direction due to refraction. Depth inversion techniques using surface wave patterns can handle clear and turbid waters and thereby a variety of global coastal environments. The idea to use observed wave characteristics as a proxy for the underlying bathymetry already came up during the time of the second world war, when the aim was to acquire bathymetry information for military landing operations. Starting around the 1980's, the idea received more attention among the coastal engineering community, as increased computational power enabled easier analysis of wave-field recordings through spectral decompositions. Since then, different depth inversion algorithms (DIA) have been developed in pursuit of getting increasingly accurate bathymetry maps. Besides estimating depths, some DIAs also incorporate functionalities to map wave propagation directions and wave celerity, and even near-surface currents from wave-field video. While the video recording instruments resemble the hardware, DIAs resemble the software needed for wave-based coastal remote sensing (WCRS).

Yet, WCRS is a specialistic branch within the coastal engineering and -user community. The technique typically requires a certain amount of user-expertise and it has mostly been applied in research settings. While data can be retrieved on kilometre scale with XBand-radars and cameras, it was historically difficult to scale up WCRS to entire coasts, which was a reason to discontinue its application in the Netherlands. Besides land-based instruments (i.e., XBand-radars, fixed camera stations) in the meantime also airborne UAVs, and space-borne satellites can be used to record a wave field, making WCRS more flexible and scalable. These recording instruments have also become more accessible. Moreover, DIAs – the software required to analyse the wave recordings – can be used interchangeably on data of these different instruments. This means that WCRS becomes potentially attractive to a broad user-community of coastal managers, the industry and the coast guard. However, DIAs still restrict broad usage of WCRS: while an important step has been taken in the open accessibility of DIAs, much is still to be gained in their handling and computational speed. This study aims to improve upon that, by building towards operational, self-adaptive and intelligent algorithms, which can provide maps of depth, near-surface currents and wave hydrodynamics on-the-fly. For this pur-

pose, video data from a variety of instruments (fixed camera station, UAV, XBand-radar, satellite) on different spatial scales $O(100\,\mathrm{m}^2, 1\,\mathrm{km}^2, 10\,\mathrm{km}^2, 100\,\mathrm{km}^2)$ and field-sites around the world (Netherlands, UK, USA, Australia, France) are analysed. Combining rapid processing capabilities with a broad applicability this study forms a stepping stone for a potentially broad WCRS user community. The analyses are presented going from land-based to air-borne to space-borne WCRS. This is done in three stages from (1) applying an operational DIA on XBand radar data, to (2) applying an on-the-fly DIA on camera and UAV data, to finally (3) applying a DIA on temporally sparse satellite data.

First, a DIA named XMFit (X-Band Matlab Fitting) is introduced, which is robust, accurate and fast enough for operational use. This is achieved through an iterative procedure that selects the best result among a series of depth and near-surface current estimates. For this study, video data from XBand-radars are analysed. Focusing on depth estimates, XMFit is validated for two case studies in the Netherlands: (1) the "Sand Engine", a beach mega nourishment at a uniform open coast, and (2) the tidal inlet of the Dutch Wadden Sea island Ameland, characterizing a more complex coast. Considering both sites, the algorithm performance is characterized by a spatially averaged depth bias of $-0.9\,\mathrm{m}$ at the Sand Engine (corresponding to an 18 h snapshot of the field site) and a time-varying bias of approximately -2–$0\,\mathrm{m}$ at the Ameland Inlet (corresponding to a one-year time evolution with varying hydrodynamic conditions). When compared to in-situ depth surveys the accuracy is lower, but the time resolution higher. Dutch in-situ surveys typically occur annually, while depth estimates from the Ameland tidal inlet are produced every $50\,\mathrm{min}$ by an operational system using a navigational X-Band radar. It enables to monitor the placement of a $5\,\mathrm{Mm}^3$ ebb-tidal delta nourishment – a pilot measure for coastal management. Volumetric changes in the nourishment area over the year 2018, occurring at $7\,\mathrm{km}$ distance from the radar, are estimated with an error of $7\,\%$. Depth errors statistically correlate with the direction and magnitude of simultaneous near-surface current estimates. Additional experiments on Sand Engine data demonstrate that depth errors may be significantly reduced using an alternative spectral approach and/or by using a Kalman filter.

Having demonstrated the potential of DIAs for operational application, the next step is to design an algorithm that can self-adapt to video from any field-site and can process it on-the-fly. To do so, a DIA is designed whose code architecture for the first time includes the Dynamic Mode Decomposition (DMD) to reduce the data complexity of wavefield video. The DMD is paired with loss-functions to handle spectral noise, and a novel spectral storage system and Kalman filter to achieve fast converging measurements. The algorithm is showcased for videos from ARGUS stations and drones recorded at fieldsites in the USA, UK, Netherlands, and Australia. The performance with respect to mapping bathymetry is validated using ground truth data. It is demonstrated that merely $32\,\mathrm{s}$ of video footage is needed for a first mapping update with average depth errors of 0.9–$2.6\,\mathrm{m}$. These further reduce to 0.5–$1.4\,\mathrm{m}$ as the videos continue and more mapping updates are returned. Simultaneously, coherent maps for wave direction and -celerity are achieved as well as maps of local near-surface currents. The algorithm is capable

of mapping the coastal parameters on-the-fly and thereby offers analysis of video feeds, such as from drones or operational camera installations. Hence, the innovative application of analysis techniques like the DMD enables both accurate and unprecedentedly fast coastal reconnaissance.

With a skilled, intelligent DIA at hand, the question remains whether it can also be used on satellite imagery, as that would further broaden the application range. DIAs commonly analyse video from shore-based camera stations, UAVs or XBand-radars with durations of minutes and at framerates of $1–2\,\mathrm{fps}$ to find relevant wave frequencies. However, these requirements are typically not met by raw, temporally sparse satellite imagery. To overcome this problem a preprocessing step is utilized. Here, a sequence of 12 images of Capbreton, France, collected over a period of $\sim 1.5\,\mathrm{min}$ at a framerate of $1/8\,\mathrm{fps}$ by the Pleiades satellite, is augmented to a pseudo-video with a framerate of $1\,\mathrm{fps}$. For this purpose a recently developed method is used, which considers spatial pathways of propagating waves for temporal video reconstruction. The resulting video is subsequently processed with the self-adaptive DIA. The combination of image augmentation with a frequency-based depth inversion method shows potential for broad application to temporally sparse satellite imagery and thereby aids in the effort towards broad usage of WCRS for mapping coastal bathymetry data around the globe.

By improving DIAs and their application to different instruments, this study has helped to increase the technological readiness of WCRS and its potential to be adopted by end-users. It was shown that WCRS can be performed on wave field records of land-based, airborne and space-born instruments and therewith on scales ranging from $O(100\,\mathrm{m}^2)$(fixed camera) to $O(100\,\mathrm{km}^2)$(X-band radar,satellite). The cost of WCRS is minor, as existing navigational X-band radars can be used, affordable UAVs and cameras, and accessible satellite data. X-band radars can operationally monitor complex coastal environments and recognize morphological trends, UAVs and cameras can be used for fast lean-and-mean mapping of coastal bathymetry, and by estimating depths from satellite imagery valuable data can be collected in otherwise data-poor environments. Yet, further steps should be taken in the accessibility, multifunctionality, quality, robustness and user-friendliness of WCRS. The key takeaway for effective WCRS monitoring is that future developments should strive towards integrated, self-adaptive software, which gives prompt visual response and requires little user-expertise. These measures reduce the difficulty to learn WCRS, increase its compatibility with data from different instruments (Xband-radars, cameras, UAVs, satellites) and thereby enable relatively easy coastal measurements. As a consequence WCRS becomes more adoptable by the coastal remote sensing community. With the exponential growth of data volumes worldwide, future data clouds may facilitate storage and offer future perspectives for online integration of data with numerical models and modern data science techniques like neural networks. This may create new possibilities for understanding system dynamics and thereby further aid decision makers in coastal management, the industry and the coast guard.

Samenvatting

Het doel van deze studie is om golfgebaseerde diepte-inversie te innoveren naar slimmere en snellere algoritmen voor gebruik door een brede gemeenschap. Golfgebaseerde diepte-inversie beschrijft een tak van kust-teledetectie, die gebruik maakt van video-opnamen van een golfveld om dieptes af te leiden en zo kaarten te maken van de bathymetrie van kustgebieden. De techniek maakt gebruik van het feit dat golven reageren op de onderliggende bathymetrie door hun lengte en snelheid te veranderen, respectievelijk korter en langzamer worden naarmate de waterdiepte geringer wordt. Golven kunnen ook van richting veranderen als gevolg van refractie. Diepte-inversietechnieken die gebruik maken van oppervlaktegolfpatronen kunnen zowel heldere als troebele wateren aan en daardoor een verscheidenheid van mondiale kustomgevingen. Het idee om waargenomen golfkarakteristieken te gebruiken als proxy voor de onderliggende bathymetrie ontstond reeds ten tijde van de tweede wereldoorlog, toen het de bedoeling was bathymetrische informatie te verkrijgen voor militaire landingsoperaties. Vanaf de jaren 1980 kreeg het idee meer aandacht in de kustbouwkundige gemeenschap, toen de toegenomen computerkracht de analyse van golfveldopnames door spectrale decompositie gemakkelijker maakte. Sindsdien zijn verschillende diepte-inversie-algoritmen (DIA) ontwikkeld met het oog op steeds nauwkeurigere bathymetriekaarten. Naast het schatten van dieptes bieden sommige DIA's ook de mogelijkheid om golfvoortplantingsrichtingen en golfsnelheden, en zelfs stromingen nabij het oppervlak in kaart te brengen. Samen met de opname-instrumenten vormen DIA's het gebied van wave-based coastal remote sensing (WCRS).

Toch is WCRS een specialistische tak binnen de kustengineering en gebruikersgemeenschap. De techniek vereist doorgaans een zekere mate van deskundigheid van de gebruiker en wordt meestal toegepast in onderzoeksomgevingen. Hoewel met XBand-radars en camera's gegevens op kilometerschaal kunnen worden verkregen, was het historisch moeilijk om WCRS op te schalen naar hele kusten, wat een reden was om de toepassing ervan in Nederland te staken. Naast instrumenten op het land (d.w.z. XBand-radars, vaste camerastations) kunnen inmiddels ook UAV's in de lucht en satellieten in de ruimte worden gebruikt om een golfveld op te nemen, waardoor WCRS flexibeler en schaalbaarder wordt. Deze opname-instrumenten zijn ook toegankelijker geworden. Bovendien kunnen DIA's - de software die nodig is om de golfopnamen te analyseren - op de gegevens van deze verschillende instrumenten door elkaar worden gebruikt. Dit betekent dat WCRS potentieel aantrekkelijk wordt voor een brede gebruikersgemeenschap van kustbeheerders, de industrie en de kustwacht. DIA's beperken echter nog steeds een breed gebruik van WCRS: hoewel er een belangrijke stap is gezet in de open toegankelijkheid van DIA's, valt er nog veel te winnen in de hanteerbaarheid en de rekensnelheid ervan.

Deze studie wil dit verbeteren door te werken aan operationele, zelfaanpassende en intelligente algoritmen, die kaarten kunnen opleveren van diepte, stromingen nabij het oppervlak en golfhydrodynamica on-the-fly. Daartoe worden videogegevens van verschillende instrumenten (vast camerastation, UAV, XBand-radar, satelliet) op verschillende ruimtelijke schalen $O(100\,\mathrm{m}^2, 1\,\mathrm{km}^2, 10\,\mathrm{km}^2, 100\,\mathrm{km}^2)$ en veldlocaties over de hele wereld (Nederland, UK, USA, Australië, Frankrijk) geanalyseerd. Door de combinatie van snelle verwerkingsmogelijkheden en een brede toepasbaarheid vormt deze studie een springplank voor een potentieel brede WCRS-gebruikersgemeenschap. De analyses gaan van WCRS op het land over WCRS in de lucht tot WCRS in de ruimte. Dit gebeurt in drie fasen, van (1) het toepassen van een operationele DIA op XBand radargegevens, naar (2) het toepassen van een on-the-fly DIA op camera- en UAV-gegevens, tot ten slotte (3) het toepassen van een DIA op temporeel schaarse satellietgegevens.

Eerst wordt een DIA met de naam XMFit (X-Band Matlab Fitting) geïntroduceerd, die robuust, nauwkeurig en snel genoeg is voor operationeel gebruik. Dit wordt bereikt door een iteratieve procedure die het beste resultaat selecteert uit een reeks diepte- en stroomschattingen. Voor deze studie worden videogegevens van XBand-radars geanalyseerd. Met de nadruk op diepteschattingen wordt XMFit gevalideerd voor twee case studies in Nederland: (1) de "Zandmotor", een mega-suppletie op het strand bij een uniforme open kust, en (2) het zeegat van het Nederlandse Waddeneiland Ameland, dat een complexere kust karakteriseert. Voor beide veldlocaties wordt de prestatie van het algoritme gekenmerkt door een ruimtelijk gemiddelde dieptefout van $0.9\,\mathrm{m}$ bij de Zandmotor (overeenkomend met een momentopname van 18 uur van de veldlocatie) en een tijdsafhankelijke fout van ongeveer -2–$0\,\mathrm{m}$ bij het Amelander Zeegat (overeenkomend met een tijdsverloop van één jaar met variërende hydrodynamische omstandigheden). In vergelijking met in-situ dieptepeilingen is de nauwkeurigheid lager, maar de tijdsresolutie hoger. Nederlandse in-situ metingen vinden doorgaans jaarlijks plaats, terwijl diepteschattingen van de Ameland getijdeninlaat elke $50\,\mathrm{min}$ worden gemaakt door een operationeel systeem dat gebruik maakt van een X-Band radar voor navigatiedoeleinden. Hiermee kan de plaatsing van een eb-delta suppletie - een proefmaatregel voor kustbeheer - worden gevolgd. Volumetrische veranderingen in het suppletiegebied gedurende het jaar 2018, op een afstand van $7\,\mathrm{km}$ van de radar, worden geschat met een fout van $7\,\%$. Dieptefouten correleren statistisch met de richting en grootte van gelijktijdige schattingen van de stroming nabij het oppervlak. Aanvullende experimenten met Zandmotor data tonen aan dat dieptefouten aanzienlijk kunnen worden verminderd door gebruik te maken van een alternatieve spectrale aanpak en/of een Kalman-filter.

Nadat het potentieel van DIA's voor operationele toepassing is aangetoond, wordt in de opeenvolgende studie een algoritme ontworpen dat zich zelf kan aanpassen aan videobeelden van elke veldlocatie en deze on-the-fly kan verwerken. Daartoe is een DIA ontworpen waarvan de code-architectuur voor het eerst de Dynamic Mode Decomposition (DMD) bevat om de complexiteit van golfveldvideo te verminderen. De DMD wordt gecombineerd met loss-functies om met spectrale ruis om te gaan, en een nieuw spectraal opslagsysteem en een Kalman-filter om snel convergerende

metingen te bereiken. Het algoritme wordt getoond voor video's van ARGUS stations en drones opgenomen op veldlocaties in de VS, VK, Nederland, en Australië. De prestaties met betrekking tot het in kaart brengen van de bathymetrie worden gevalideerd met behulp van in-situ gegevens. Er wordt aangetoond dat slechts $32\,\mathrm{s}$ aan videobeelden nodig zijn voor een eerste karteringsupdate met gemiddelde dieptefouten van 0.9–$2.6\,\mathrm{m}$. Deze fouten nemen verder af tot 0.5–$1.4\,\mathrm{m}$ naarmate de video's vorderen en meer kaartupdates worden gegeven. Gelijktijdig worden coherente kaarten voor golfrichting en -snelheid verkregen, alsmede kaarten van lokale stromingen nabij het oppervlak. Het algoritme is in staat de kustparameters on-the-fly in kaart te brengen en biedt daardoor analyse van video-feeds, zoals van drones of operationele camera-installaties. De innovatieve toepassing van analysetechnieken zoals de DMD maakt dus zowel een nauwkeurige als een ongekend snelle kustverkenning mogelijk.

Met een bekwame, intelligente DIA bij de hand, blijft de vraag of deze ook op satellietbeelden kan worden toegepast. DIA's analyseren gewoonlijk videobeelden van camera's, UAV's of XBand-radars met een duur van minuten en een beeldfrequentie van 1–$2\,\mathrm{fps}$ om relevante golffrequenties te vinden. Aan deze eisen wordt echter meestal niet voldaan door ruwe, in de tijd karige satellietbeelden. Om dit probleem op te lossen wordt gebruik gemaakt van een voorbewerkingsstap. Een reeks van 12 beelden van Capbreton, Frankrijk, verzameld over een periode van $\sim 1.5\,\mathrm{min}$ met een beeldfrequentie van $1/8\,\mathrm{fps}$ door de Pleiades-satelliet, wordt aangevuld tot een pseudo-video met een beeldsnelheid van $1\,\mathrm{fps}$. Daartoe wordt een recent ontwikkelde methode toegepast, die ruimtelijke paden van voortplantende golven gebruikt voor videoreconstructie in de tijd. De resulterende video wordt vervolgens verwerkt met de zelfaanpassende DIA. De combinatie van videoreconstructie met een frequentie-gebaseerde diepte-inversie methode toont potentieel voor brede toepassing op temporeel schaarse satellietbeelden en helpt zo in het streven naar een breed gebruik van WCRS voor het karteren van kust bodems over de hele wereld.

Door de DIA's en de toepassing ervan op verschillende instrumenten te verbeteren, heeft deze studie ertoe bijgedragen de technologische gereedheid van WCRS en diens potentiele toepassing door eindgebruikers te vergroten. Aangetoond is dat WCRS kan worden uitgevoerd op golfveldopnamen van instrumenten op het land, in de lucht en in de ruimte en daarmee op schalen variërend van $O(100\,\mathrm{km}^2)$(vaste camera) tot $O(100\,\mathrm{km}^2)$(X-band radar, satelliet). De kosten van WCRS zijn gering, omdat gebruik kan worden gemaakt van bestaande X-band radars voor navigatie, betaalbare UAVs en camera's, en toegankelijke satellietgegevens. Met X-band radars kunnen complexe kustomgevingen operationeel worden gevolgd en morfologische tendensen worden herkend, UAV's en camera's kunnen worden gebruikt voor snelle lean-and-mean kartering van de bathymetrie van kustgebieden, en door de diepte te schatten aan de hand van satellietbeelden kunnen waardevolle gegevens worden verzameld in omgevingen waar anders weinig gegevens voorhanden zijn. Toch moeten verdere stappen worden gezet in de toegankelijkheid, multifunctionaliteit, kwaliteit, robuustheid en gebruiksvriendelijkheid van WCRS. De belangrijkste conclusie voor effectieve WCRS-monitoring is dat bij toekomstige ontwikkelingen

moet worden gestreefd naar geïntegreerde, zelfaanpassende software, die snel visueel reageert en weinig deskundigheid van de gebruiker vereist. Deze maatregelen verminderen de moeilijkheidsgraad om WCRS te leren, vergroten de compatibiliteit met gegevens van verschillende instrumenten (Xband-radars, camera's, UAV's, satellieten) en maken daardoor relatief eenvoudige kustmetingen mogelijk. Als gevolg daarvan wordt WCRS beter te gebruiken door de kustgemeenschap. Met de exponentiële groei van de datavolumes wereldwijd kunnen toekomstige data clouds de opslag vergemakkelijken en toekomstperspectieven bieden voor online integratie van data met numerieke modellen en moderne data science technieken zoals neurale netwerken. Dit kan nieuwe mogelijkheden creëren om de dynamiek van kustsystemen te begrijpen en zo de besluitvormers bij het kustbeheer, de industrie en de kustwacht te helpen.

1

Introduction

1.1. Motivation

The coastal community needs data for decision making, such as determined by coastal zone management goals, flood safety, ecological and recreational directives [1]. Also swimmer safety, navigational safety and industrial process monitoring determine decision making [2–4]. All these applications need reliable up-to-date coastal data, which involve measurements of hydrodynamics, such as currents and wave characteristics, but also measurements of the underwater topography of the coast, better known as the coastal bathymetry (Figure 1.1).

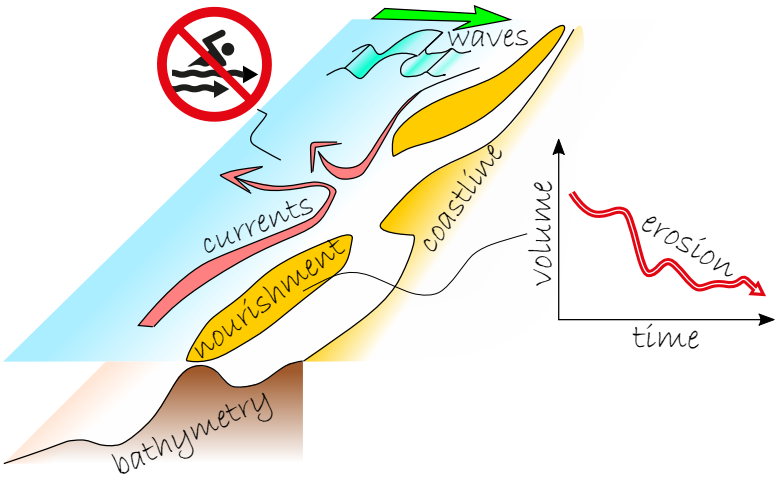

Figure 1.1.: Illustration of coastal data.

Taking the Netherlands as an example, sustainable coastal zone management aims to dynamically preserve the coastline for its flood-safety function, but also for its ecological function and recreation. To assess these coastal functions, up-to-date bathymetry data are crucial for decision makers as to recognize erosion trends. At

the moment, yearly "Jarkus" transects are measured along the entire Dutch coast and in the more complex coastal environments 3-6 yearly "Vaklodingen" measurements aim to capture the coastal state. These measurements are mostly collected in-situ, which means that instruments need to be placed at particular locations in the field, or be carried on foot or on vessels [5]. This practice is labour intensive, expensive and it may take up to a full year to acquire the data [6]. The temporal resolution of these traditional measurements is coarse, whereby the evolution and erosion of for example nourishments can only be monitored roughly [7]. Short-term morphodynamics caused by high-wave events or rip-currents are rarely captured, although they are a prominent cause for (nourishment) erosion [8]. Recognizing short-term dynamics is important as erosion enforces flood hazards, and these flood hazards are predicted to increase future economic and insured losses [9]. Currently, erosion trends must be anticipated year(s) ahead for nourishment programming. Moreover, measured transects typically lay hundred(s) of metres apart, leaving long coastal sections without data. It shows that there is a large data gap to fill in both time and space to improve system understanding and nourishment planning for coastal management ([8], see also Chapter 2,[3]). In the 2000's remote sensing technology was suggested to aid for such coastal management purposes (e.g., [10]). Remote sensing technology collects data from a distance and over an area, for example using cameras or radars. Yet, the adoption of the technology came to a halt, probably due to technical limitations, required expertise and costs involved to scale monitoring up from local areas $O(100\,\mathrm{m}^2)$ to the entire Dutch coastline.

This work is driven by the idea of developing widely applicable and easy-to-use technology to collect and map coastal data, which is available for a broad audience [11]. While it is difficult to make in-situ measurements less labour intensive, it might be possible to innovate coastal remote sensing to be easier to use and scale up.

1.2. Wave-based Coastal Remote Sensing (WCRS)

In particular the field of wave-based coastal remote sensing (WCRS) shows potential for broad application. With WCRS the motions of a wave-field are recorded and these recordings are subsequently analysed. By analysing a wave-field in motion, information can be derived on the waves themselves, such as their celerity and direction, but also information on the underlying bathymetry and currents can be derived. This is possible because waves react to the underlying bathymetry and currents by changing their length, celerity and direction. A benefit of WCRS is that it can be used in clear and turbid coastal waters and thereby in a variety of coastal environments. WCRS includes hardware to record the wave-field and software to analyse the recorded wave-field (Figure 1.2).

1.2.1. Hardware

In the past, mostly land-based instruments, such as Xband-radars or professional camera installations could be used, which were costly and made it difficult to scale

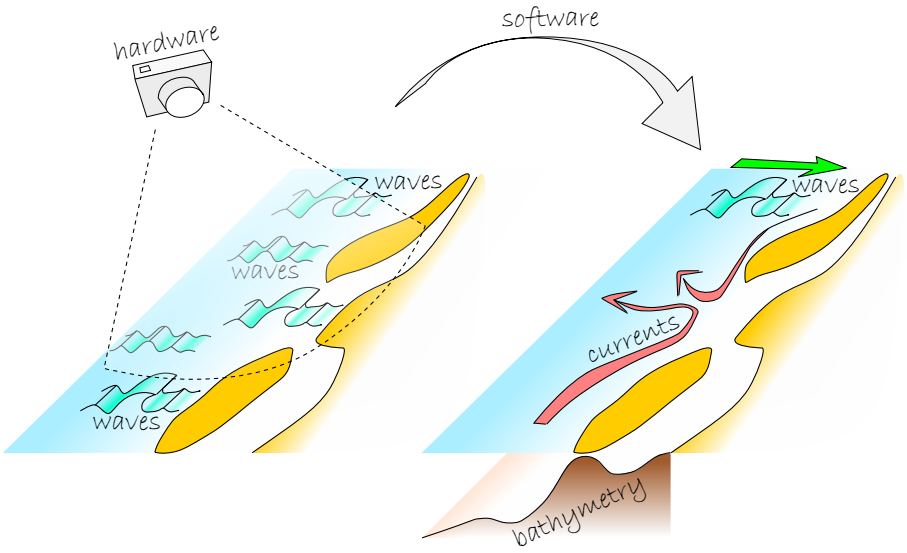

Figure 1.2.: Wave-based coastal remote sensing (WCRS): A wave field in motion is recorded and subsequently analysed to derive wave celerity and direction, currents and bathymetry.

up WCRS (an important reason to discontinue its application in the Netherlands). Yet, nowadays also airborne UAVs, and space-borne satellites can be used, making WCRS more flexible and scalable. Moreover, all recording instruments have become more accessible. WCRS can now be conducted flexibly and economically using affordable UAVs [12]. Global bathymetry data can be collected at times and places where these are not available using satellites [13]. Local, systematic monitoring with fixed cameras now allows to recognize erosion/accretion trends [14] and for some areas bathymetry measurements up to decimetre accuracy are possible [15]. With nowadays hardware, WCRS might be used to address coastal management needs such as to follow the (volumetric) evolution of nourishments. Satellite-based remote sensing could also trace channel migration over Wadden-sea-sized areas [16, 17] and be used to check navigational safety. Besides bathymetry data also hydrodynamic data with high spatio-temporal coverage can be retrieved, for example with Xband-radars [18]. Such data are needed as public safety can be at risk, for example due to the presence of coastal (rip) currents [19]. WCRS could be used to map and identify short-lived, dangerous currents and be a tool to recognize hazardous situations for swimmer safety [2]. Concluding, with nowadays possibilities to use affordable and accessible land-based, airborne and space-borne remote sensing hardware, WCRS has become scalable and it allows to derive data products for decision making, such as coastal erosion/accretion trends for potential nourishment programming and coastal current maps for swimmer safety monitoring. The historic hardware limitations of WCRS have reduced, while software limitations still exist.

1

1.2.2. Software

A limitation of WCRS software lays in the analysis of wave-field recordings, which is done with sophisticated algorithms [20–23]. These algorithms are often referred to as depth-inversion algorithms (DIA), where "depth" directly translates to bathymetry (Figure 1.3). In addition to depth, DIAs can simultaneously estimate currents and wave hydrodynamics and thereby resemble a multifunctional tool to retrieve coastal measurements.

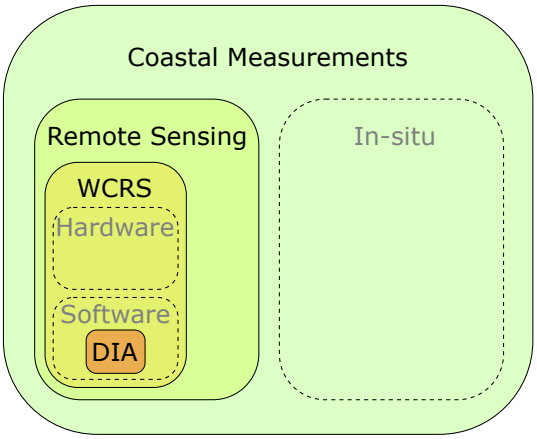

Figure 1.3.: Schematization of depth inversion algorithms (DIA) as an element of wave-based coastal remote sensing (WCRS) and the broader fields of coastal remote sensing and coastal measurements.

However, current DIAs are difficult to use, do to lacking accessibility, required user expertise and no or slow visual response. The issue of accessibility lays in the fact that DIAs are typically non-open source [22], or the programming language in which they are written is non-open source [20]. The required user expertise lays in the knowledge and experience necessary to handle DIAs and tune them to the (site-specific) video data. A lacking visual response is a symptom of the fact that it is usually experts who use DIAs and who are mostly interested in the numbers that are generated.

Hence, although WCRS hardware (the recoding instruments) is affordable and scalable, and the software has multifunctional capability, the technology is seemingly unattractive to be used by a broad community due to the software's lacking accessibility, user friendliness and required expertise.

1.2.3. Technological Readiness and Adoption

WCRS can be placed into a larger framework and be viewed as a technology to be used by potential end-users. In such a framework (i) the maturity of the technology can be assessed, but also (ii) its potential adoption by end-users.

(i) The technological maturity (i.e., the progress in the development) of WCRS

can be assessed by trying to classify it on a scale of technological readiness levels (TRLs) [24]. The metric consists of 9 levels ranging from the initial idea of a technology/product (TRL 1) to its full market release (TRL 9).

TRL 1. basic principles observed

TRL 2. technology concept formulated

TRL 3. experimental proof of concept

TRL 4. technology validated in lab

TRL 5. technology validated in relevant environment

TRL 6. technology demonstrated in relevant environment

TRL 7. system prototype demonstration in operational environment

TRL 8. system complete and qualified

TRL 9. actual system proven in operational environment

WCRS has passed the initial stages of technological readiness with experimental proofs of concept in the 1940's (TRL 3) [25] and more elaborate validations in the 1980's and 1990's (TRL 5) (e.g., [26, 27]). The 2000's can be seen as the start of a demonstration period of WCRS with different instruments and in different environments (TRL 6) (e.g., [23, 28, 29]). This period is also shaped by the systematic development of different DIA's in the 2000's and 2010's (e.g., [20, 21, 30]. This work will demonstrate that WCRS has reached even higher TRLs (7-9), by demonstrating WCRS in an operational environment and employing it for multiple years in government-financed projects. It can be used to answer questions, which have not yet been posed like "can we track a nourishment"? Hence, from a performance point of view, WCRS is already a quite mature technology.

(ii) The theory of diffusion of innovations contains directions on how to assess the likelihood of innovative technology to be adopted. The overarching theory is complex and comprises many aspects concerning the spreading of innovations [11, 31]. This discussion focusses on a subpart of that theory, which is about end-user considerations (EUCs) that promote adoption of a technology:

EUC 1. relative advantage compared to existing tools

EUC 2. compatability with pre-existing systems/hardware

EUC 3. complexity/difficulty to learn

EUC 4. testability

EUC 5. potential for reinvention

EUC 6. observed effects

Viewing these end-user considerations suggests that the adoption of WCRS by the coastal community can be improved. Compared to other existing measurement technology (EUC 1) WCRS has the benefit that data can be collected over entire areas and it has become globally scalable. Moreover it

is multifunctional as both bathymetry and hydrodynamics can be measured simultaneously [32]. Yet, it is cumbersome to use, due to the DIAs' lacking accessibility, user friendliness and required expertise. Regarding the compatability with pre-existing systems (EUC 2), WCRS has large potential as DIAs can work interchangeably on wave-field video of different instruments [33]. A drawback of WCRS is still the complexity and difficulty to learn it (EUC 3). Again, issues arise from the DIAs' lacking accessibility, user friendliness and required expertise. The potential testability of WCRS is high (EUC 4), as it may be applied to wave-field video from various instruments and environments; however, currently video data often need to be requested from their owners for testing. The potential for reinvention of WCRS (EUC 5) is difficult to determine, but it may be possible to use DIAs on imagery that they were not originally designed for, such as temporally sparse imagery from satellites or video feeds. DIAs might also be combined with other remote sensing techniques, such as shoreline tracking algorithms, suggesting that WCRS has a potential for re-combination and added functionality. The observed effects of WCRS (EUC 6) are potentially large, since bathymetric and hydrodynamic data can be mapped for entire areas and this might be done by laymen. This can also have large effect on the presentation of the data to decision makers in coastal management, the industry and the coast guard. Yet, currently DIAs require expert knowledge and provide low or slow visual response, leaving no options to analyse video feeds and/or lean-and-mean mapping of coastal parameters.

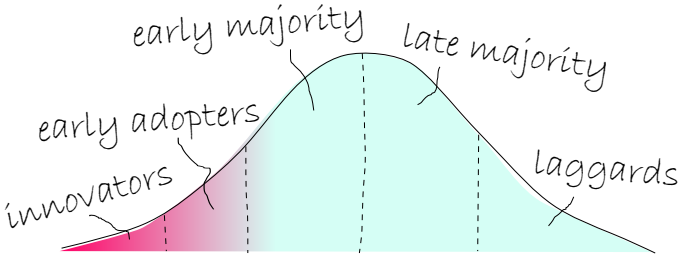

Figure 1.4.: Technology adoption lifecycle

Seeing the potential gain to be achieved in addressing end-user considerations, WCRS technology is at the moment probably still in a phase of early adoption (Figure 1.4). There is a majority of adopters to win over.

Looking at the current status of WCRS suggests that (i) it is a technology with high technological readiness, but also (ii) a technology whose potential to be broadly adopted has not yet been harnessed. This unused potential is what has motivated this work and has lead set of research questions and technological challenges.

1.3. Research Questions

1. To what extent can DIAs be used on wave-field records of different remote sensing instruments (X-band radar, fixed camera, UAV, satellite) to demonstrate scalability and spatiotemporal coverage of WCRS? (TRL 8 and EUCs 1, 2, 4)

2. How can DIAs be used operationally to monitor the placement and evolution of a nourishment for dredging and dumping surveillance and coastal management? (TRLs 7, 9 and EUCs 1, 2)

3. How can DIAs self-adapt to wave-field video from different field-sites to reduce required user-expertise? (EUCs 3, 6)

4. To what extent can DIAs acquire on-the-fly processing capability for analysis of video feeds and lean-and-mean mapping with WCRS? (EUCs 1, 5, 6)

5. How can standard DIAs be used on temporally sparse imagery to achieve an increased application range of WCRS? (EUCs 2, 5)

6. What are the perspectives of WCRS for broad future application? (EUCs 1-6)

1.4. Reader

The overall goal of this thesis is to innovate DIAs towards smarter and faster algorithms that can provide reliable estimates using different instruments and scales, which can be used to identify and derive coastal features and trends. The innovation of DIAs is approached in three steps, which are divided over three chapters (Chapters 2 to 4). Each chapter is published as an individual article [3, 34, 35]. The performance of DIAs is validated by their ability to estimate depth. Results for near-surface current estimates and wave-hydrodynamics are assessed qualitatively.

(Research question 1) As a central thread running through this thesis, different instruments are used to record wave-fields. First an X-band radar (Chapter 2), but successively also stationary cameras, UAVs/drones (Chapter 3) and finally a satellite (Chapter 4).

(Research question 2) The operational application of a DIA to video from a navigational X-band radar is presented in Chapter 2. The DIA leans on traditional methodology (using 3D Fourier based spectral analysis), but is specifically developed to be employed operationally. Using this DIA, it is studied whether coastal management questions can be answered, by monitoring the (volumetric) evolution of a nourishment from a large distance of $7\,\mathrm{km}$.

(Research questions 3, 4) In Chapter 3 an innovative DIA is presented, which is accessible, allows on-the-fly analysis, and is self-adaptive. At the same time it retains the multifunctionality, robustness and accuracy of existing DIAs. This is amongst others achieved by introducing new data analysis techniques, such as the Dynamic Mode Decomposition to reduce video data to essential wave-field components.

(Research question 5) Chapter 4 explores the use of DIAs on temporally sparse satellite imagery. A recently developed method is used to generate a smooth wavefield video from a few satellite snapshots, after which the DIA from Chapter 3 serves to estimate the coastal bathymetry.

(Research question 6) Chapter 5 reflects on the progress made in Chapters 2 to 4 in a synthesis on WCRS and discusses ways for further improvement. This discussion is finalized with a vision for WCRS hardware and software in future global coastal monitoring.

2

Operational bathymetry with Xband-radar

We've got a thing that's called radar love

Radar Love, Golden Earring

This chapter explores the use of an existing navigational XBand radar to monitor coastal bathymetry and volumetric changes of a nourishment over time. By deriving depths from observed wave properties, the bathymetry of the Ameland eb tidal delta and the Sand Engine are mapped and monitored. For this purpose the depth inversion algorithm XMFit is introduced. The study demonstrates that depth inversion of XBand radar video can be used operationally as a monitoring tool for coastal managers.

Lessons learned:

- *The depth inversion algorithm XMFit can be used operationally to estimate bathymetry from XBand radar over long time periods.*
- *The XMFit algorithm uses local 3D Fourier transforms to capture spectral wave contents in time and space. Spectral noise can be robustly discarded by iterating over a series of spectral energy thresholds.*
- *The placement of a* $5\,\mathrm{Mm}^3$ *ebb-tidal delta nourishment – a pilot measure for coastal management – can be followed. Volumetric changes in the nourishment area over the year 2018, occurring at* $7\,\mathrm{km}$ *distance from the radar, were estimated with an error of* $7\,\%$*.*
- *The accuracy of depth estimates varies over time with biases mostly between* -2–$0\,\mathrm{m}$*. Depth errors statistically correlate with the direction and magnitude of simultaneous near-surface current estimates.*

This chapter has been published in Coastal Engineering **159**, 103716 (2020) [3].

2.1. Introduction

With the extensive urbanization of the coastal hinterland, the role of coastal management in the Netherlands has become increasingly important to ensure flood safety and the protection of recreational and ecological values of the coast. Modern coastal maintenance strives towards a "building with nature" approach [1], using soft engineering strategies to mitigate long-term coastal recession. Along uniform coastlines, large $1–2\,\mathrm{Mm}^3$ shoreface nourishments have proved to be an effective strategy [36], and a basic understanding has been established about their behaviour [7, 8]. In pursuit of finding the optimal long-term solution, larger nourishment designs have been explored of which the Sand Engine, a beach mega-nourishment comprising $21\,\mathrm{Mm}^3$ of sand is a famous example [37]. In the meantime even bigger nourishments have been placed with volumes up to $36\,\mathrm{Mm}^3$ [38]. The most recent experiment involved the construction of a $5\,\mathrm{Mm}^3$ nourishment in the outer delta of a complex tidal inlet system at the Wadden Sea island Ameland.

To evaluate the success of these innovative coastal management interventions it is necessary to map them and to monitor their evolution. Due to the large nourishment volumes and long lifetime, monitoring with in-situ techniques is expensive and it may be favorable to use remote sensing techniques instead. Such techniques can capture morphological variability at a large spatial scale in high temporal resolution over long periods of time [14]. To be used in an operational setting, remote sensing techniques need to be robust. We define robust as being able to handle variations in environmental conditions and data quality without the need for manual adjustments and costly person hours. Here, we propose to derive bathymetries with a technique that meets these desired requirements and uses already available X-Band radar data from a lighthouse.

Marine radars operating in the X-Band range are routinely deployed aboard ships and on marine traffic control towers to detect vessels and other floating objects. In coastal areas, such radars may also be used to monitor waves, currents and water depths. Their benefits over in-situ depth surveys are a high spatial and temporal coverage and lower operating and maintenance costs. However, the spatial resolution of X-Band radars can be coarse and, as sampling frequencies are often low, they have a lacking ability to recognize shorter period waves. Moreover, an inherent uncertainty exists in relating radar image intensities to the observed ocean surface properties, bringing challenges to the analysis of X-Band radar data. Moreover, X-Band radars are expensive instruments, which is why it may be attractive to exploit existing navigational radars in areas of interest.

Although considered "noise" for navigational purposes, the wave field leaves a signature on an X-Band radar known as sea clutter. This imprint is produced by radar signal reflection off capillary waves, which are modulated by the underlying surface gravity wave field [39, 40], the so-called Bragg-scattering [41]. Observing the propagation of a wavefield through time offers a possibility to infer information about the waves themselves, but also about currents and depths these waves feel.

In particular for the purpose of depth estimation, several depth inversion algorithms (DIAs) have been developed. Most DIAs use wavefield recordings from either radars or beach cameras, but these methods may be used interchangeably

between instruments [33]. While some DIAs use a sequence of images (i.e., a video of typically $6–12\,\mathrm{min}$) to link wavenumbers to wave frequencies and estimate depths via the linear dispersion relationship [20, 27, 28, 42], other DIAs use the average of a sequence of images (i.e., a time exposure) to estimate depths through spatial patterns of breaking intensity [29, 43]. If the area of interest is large, X-Band radars have an advantage above cameras because of their larger field of view. Other advantages are their operability at night and a smaller sensitvity to rain or sun glare. A large field of view means that depths are estimated far beyond the breaker zone, therefore a dispersion-based DIA is preferred with a sequence of images as input.

The commonly used dispersion-based DIAs to analyse image sequences from XBand-radar, employ three dimensional Fast Fourier Transforms (3D-FFTs) to acquire the necessary wavenumber – frequency relationships. Spatial variations are captured by discretising an image sequence into smaller domains known as computational cubes $(\mathrm{x,y,t})$ [44]. These computational cubes are processed separately. A 3D-FFT then converts each computational cube from the space-time domain $(\mathrm{x,y,t})$ into wave components in the wave number – frequency domain $(\mathrm{k_x,k_y,\omega})$. This information is used to constrain the Doppler-shifted linear dispersion shell

$$\omega = \sqrt{\mathrm{g}|\boldsymbol{k}|\tanh \boldsymbol{k}h} + \boldsymbol{U}\cdot\boldsymbol{k} \tag{2.1}$$

to estimate the water depth, d (m), and the two horizontal current vector components $[u,\ v]$ of $\boldsymbol{U}$ $(\mathrm{m\,s^{-1}})$. The gravitational acceleration is given by g, the wave number vector by $\boldsymbol{k}$ $(\mathrm{rad\,m^{-1}})$ with components $[k_x,\ k_y]$, and ω $(\mathrm{rad\,s^{-1}})$ is the corresponding frequency. The idea to use 3D-FFTs originally came from the estimation of $\boldsymbol{U}$ under known d [26]; however, it could naturally be extended to estimate d as well by keeping d as a free parameter (e.g., [18, 23, 32, 45]). The derivation of the Doppler-shift in the form $+\boldsymbol{U}\cdot\boldsymbol{k}$ in Equation (2.1), assumes a depth uniform current equal to $\boldsymbol{U}$. In practice, the current profile is not uniform over depth and the vector $\boldsymbol{U}$ represents a weighted average of velocities in the upper layer of the water column (e.g., assuming a linearly sheared current profile, waves with periods of $T = 5–8\,\mathrm{s}$ travelling in water depths of $d = 5–15\,\mathrm{m}$ feel velocities that occur at $20–45\,\%$ of the water depth; see eq. 5 in [46]). Therefore, $\boldsymbol{U}$ is commonly also referred to as near-surface current [26, 47].

Several authors have applied the dispersion relation without Doppler-shift ($+\boldsymbol{U}\cdot\boldsymbol{k}$ in Equation (2.1)), neglecting the presence of near-surface currents, to remotely sense d from X-Band radar data [27, 42]. Although conceptually proven, these early developments were applied to limited datasets and lacked quantitative validation. Later, based on two single daily-averaged estimates from Egmond aan Zee (NL) and Teignmouth Pier (UK), Bell [48] demonstrated that error margins could be within $1\,\mathrm{m}$ accuracy for depths up to $12\,\mathrm{m}$, with exception of the breaker zone where errors were approximately $2\,\mathrm{m}$. For the site of Duck (North Carolina, US) with depths up to $6\,\mathrm{m}$, Trizna [44] reported depth errors of $0–4\,\mathrm{m}$ depending on the wave-height and suggested that the inclusion of non-linear wave theory improves estimates. This was then disproven by Flampouris *et al.* [49] who, for a site near the Wadden Sea island Sylt (GE), reported root-mean-square-errors ($RMSE$) of at

least $1.6\,\mathrm{m}$ regardless of the (non-)linear wave theory used.

For airborne optical video, Dugan, Piotrowski and Williams [28] were one of the first to include the Doppler-shift in Equation (2.1), for the joint estimation of d and $\boldsymbol{U}$ using 3D-FFTs. The extension was subsequently also used in the analysis of X-Band radar data from the Dee Estuary (UK) [23]. Although near-surface currents could not be validated, it was noted that their inclusion had improved depth estimates, which is consistent with a recent study showing that currents can influence depth estimates significantly [50]. Based on three high tide estimates, Bell [23] found depth errors to be mostly within a $1\,\mathrm{m}$ range in the spatial domain, however, estimates in the deep channel ($> 20\,\mathrm{m}$) were larger as waves only weakly felt the bottom. More recently, 3D-FFT based DIAs have been applied to complex nearshore situations, for example by Hessner *et al.* [18], who built on work done by Seemann, Ziemer and Senet [51] and Senet, Seemann and Ziemer [47] by solving for d in addition to $\boldsymbol{U}$ for an analysis of two days of radar data from a coastal site in New Zealand with strong tidal currents. Their near-surface current estimates reasonably agreed with model data, yet simultaneous depth estimates lacked validation. Similarly, Hessner, Wallbridge and Dolphin [52] investigated a site at the southeast coast of the UK. Here, accumulated depth estimates were compared to ground truth measurements and agreed qualitatively but error metrics were not quantified. Ludeno *et al.* [32] used an algorithm proposed by Serafino, Lugni and Soldovieri [30] to jointly estimate d and $\boldsymbol{U}$ from $45\,\mathrm{min}$ of radar data from a ferry near the harbour of Salerno (IT) and used a spatial partitioning technique to accelerate computations. The local depth was between 10 and $20\,\mathrm{m}$, which Ludeno *et al.* [32] estimated to have a bias of approximately $1\,\mathrm{m}$. Rutten, De Jong and Ruessink [45] were one of the first to explore the possibility of estimating volume budgets from estimates of d in the nearshore region over a long time period of one year, taking a first step from research to a potential use of radar based DIAs in coastal management. A large depth bias of $2.3\,\mathrm{m}$ for depths smaller than $6\,\mathrm{m}$, however, caused volume estimates to be $3.9\,\mathrm{Mm}^3$ short of what was expected. While near-surface current estimates were not presented, they noted that poor d estimates concurred with poor $\boldsymbol{U}$ estimates.

So far, 3D-FFT based depth inversion from XBand-radar data has focussed on the development and (often conceptual) testing of DIAs [18, 23, 32]. The accuracy of depth estimates is generally in a 1–$2\,\mathrm{m}$ range and depends on the location, radar, and the algorithm used. Moreover, presented error statistics are mostly based on short, experimental data sets. The accuracy is generally lower in deeper areas where waves are hardly affected by the depth [23] and in very shallow water where waves become non-linear (e.g., [44, 53]). Even though the validation of near-surface currents themselves is often lacking, it has been reported that including their effect on waves is important: while it improves depth estimates [23], a poor current estimate can also be an indicator for a poor, joint depth estimate [45]. The effect of higher significant wave heights, $\mathrm{H_s}$, has been shown to increase depth errors in shallower waters [44], while a minimum $H_s > 1\,\mathrm{m}$ is needed for sufficient sea-clutter [23].

3D-FFT based DIAs have mostly been applied in an experimental setting and the

question arises whether they are ready to be used for practical coastal management purposes, such as the quantification of volumetric changes caused by nourishments. To that end, they need to run operationally on long-term radar data and hence be able to handle variations in environmental conditions and data quality. In this paper, we present a 3D-FFT-based DIA named XMFit (**X**-Band **M**atlab **Fit**ting), which manages such variations by selecting the best values from a set of $[d, \boldsymbol{U}]$-solutions, for every location in the radar domain at any point in time. The generation of a set of solutions is done by a set of different energy thresholds to separate spectral wave data from the noise floor. This is different from other currently used DIAs, which may (i) optimize a $[d, \boldsymbol{U}]$-solution by iterating on a first, high energy threshold guess with a lower energy threshold guess including aliases and higher order effects [18, 47] or (ii) by maximizing a normalized scalar product between the image amplitude spectrum and a characteristic function, which omits the use of thresholds [30, 32]. Similar to those algorithms, the present method also includes the Doppler-shift (Equation (2.1)) to allow for the effect of near-surface currents on the depth estimates. XMFit uses different spectral filters, an anti-aliasing step and a least-squares fitting procedure.

We validate the DIA using two different sites in the Netherlands: The Sand Engine, and the ebb-tidal delta of the Ameland Inlet to the Wadden Sea. Detailed ground truth data from 2014 and 2018 are respectively used for validation. With $7.5\,\mathrm{km}$, the XBand-radar range at the Ameland Inlet is double the range previously reported for depth inversion studies and enables us to capture the extensive size of the Inlet. By that, we track a $5\,\mathrm{Mm}^3$ ebb-tidal delta nourishment at $7\,\mathrm{km}$ distance from the radar, creating a one-year time evolution of its volume.

Section 2.2 introduces the XMFit algorithm and its features. In Section 2.3, the field sites and data collection are described. Results on validation and monitoring the placement of the nourishment are presented in Section 2.4. In the Discussion Section 2.5, we elaborate on errors and methods to mitigate them and then conclude our findings in Section 2.6. Radar specifics and details on computational settings are documented in Appendix A.

2.2. Depth-inversion Method

The depth-inversion algorithm XMFit is based on an original idea by Young, Rosenthal and Ziemer [26], where radar image sequences of a wave field are first split into smaller cubes, then processed via 3D-FFT to retrieve spectral wave characteristics, after which the Doppler-shifted dispersion relation can be used to obtain estimates of depth and near-surface currents (Equation (2.1)). In order to process an image sequence, the algorithm requires information about the radar, user settings and optionally a bathymetry and a water level (Figure 2.1, top row). The radar information includes the coordinates of the radar, its radius and the framerate of the image sequence and pixel size. User settings include a grid definition, which consists of the location and size of the computational cubes, and limiters that are used to constrain the analysis.

Before an image sequence is analysed, a high-pass threshold on the significant

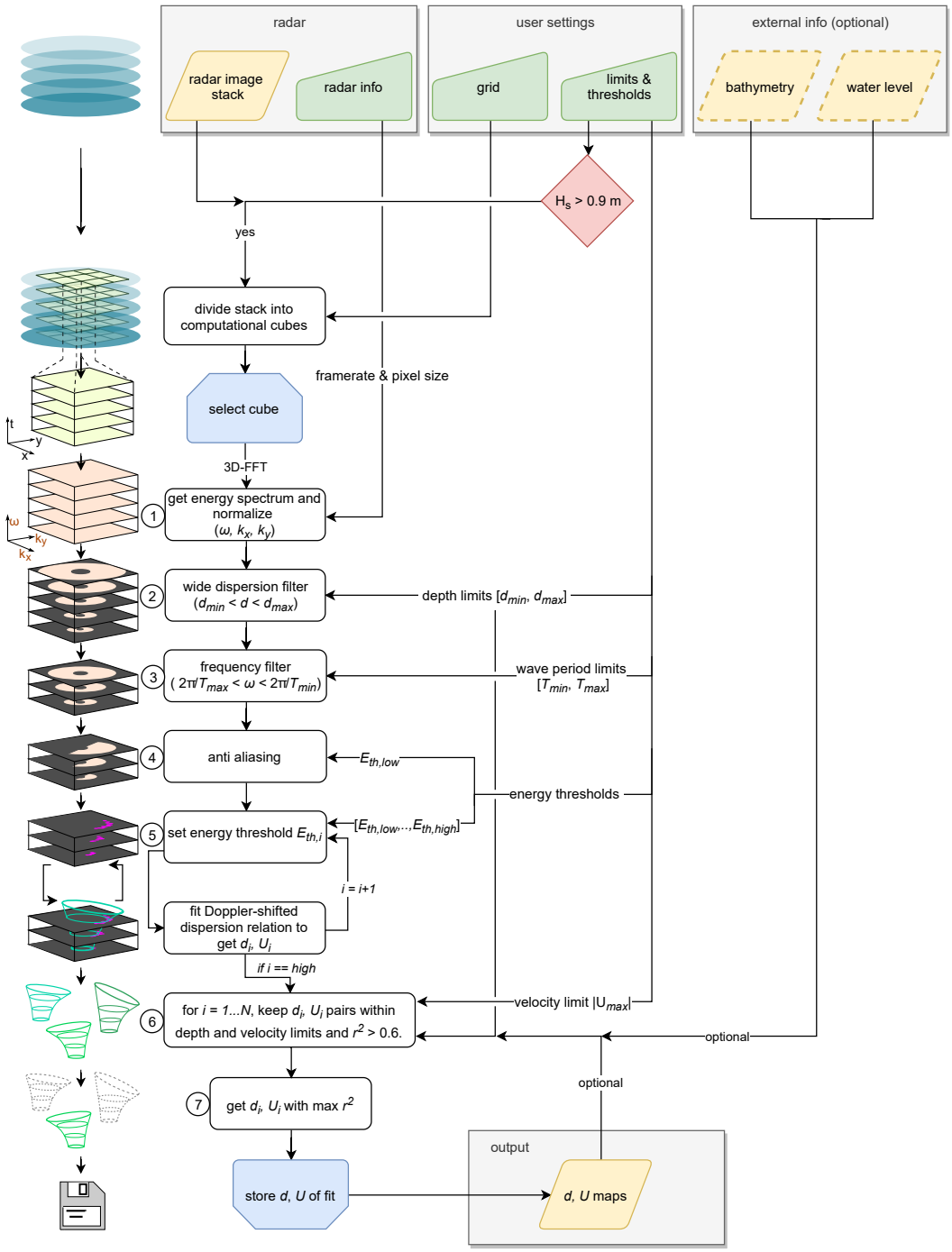

(Caption on next page.)

Figure 2.1.: XMFit workflow for depth and near-surface current inversion from an image sequence. Consecutive processing steps in the flowchart are visualized along their left. The flowchart includes: data (brown), user input (green), decision (red), process loop start (blue; trimmed top corners) and process loop end (blue; trimmed bottom corners), and process (white). Arrows and their annotations signify flow of information. The algorithm requires input on radar specifics, user settings and optionally a bathymetry and water level (grey squares top row). The output contains maps of depth estimates and near-surface current fields (grey square bottom row). Symbols represent: $[k_x, k_y]$ = wavenumber components, ω = wave frequency, $[\mathrm{d_{min}}, \mathrm{d_{max}}]$ = depth limits, $[\mathrm{T_{min}}, \mathrm{T_{max}}]$ = wave period limits, $|\mathrm{U_{max}}|$ = velocity magnitude limit, $[\mathrm{E_{th,low}}, .. \mathrm{E_{th,i}}, .. \mathrm{E_{th,high}}]$ = array of spectral energy thresholds, $[d_i, \boldsymbol{U}_i]$ = depth and near-surface current estimates corresponding to $E_{th,i}$, and $[\mathrm{d}, \mathbf{U}]$ = optimal depth and near-surface current pair.

wave heights of $\mathrm{H_s} = 0.9\,\mathrm{m}$ is made, similar to Bell [23] as a proxy for sufficient sea-clutter (Figure 2.1, red diamond). Note that the wave height information has to be provided as an external input to the DIA.

The processing of an image sequence commences by dividing it into a number of computational cubes ($c = 1 \ldots \mathrm{N}$) according to the user defined grid. Cubes are processed consecutively, each providing an estimate for a depth, d_c, and near-surface current vector, $\boldsymbol{U}_c$, at its location. The inversion of $[d_c, \boldsymbol{U}_c]$ consists of seven steps (Figure 2.1, labels ①...⑦). Since the procedure is identical for all cubes, we drop the subscript c from here onwards and use $[d, \boldsymbol{U}]$ for notational simplicity. The first step is to taper the computational cube with a 3D-Hanning window and to generate a k_x,k_y,ω-energy spectrum via 3D-FFT. If the time-sequence is long enough, the spectrum may also be smoothed through spectral averaging in time, by dividing the cube into smaller time-bins. Using min-max normalization, the spectral energy is then converted to the range $[0,1]$ to prepare it for a fitting procedure later in the process (Figure 2.1, ①). At this stage, the spectrum carries redundant information in non-relevant spectral components, such as noise and aliases, which can be discarded to save computer memory. A wide-dispersion filter removes spectral energy beyond realistic depths (Figure 2.1, ②), by means of limiting dispersion shells corresponding to a minimum depth $\mathrm{d_{min}}$, and a maximum depth $\mathrm{d_{max}}$. These limiting dispersion shells do not include a Doppler-shift, as experience shows that it does not provide additional result accuracy but does increase computation time. A frequency filter removes spectral energy beyond realistic wave periods (Figure 2.1, ③), by means of a minimum wave period $\mathrm{T_{min}}$ and a maximum wave period $\mathrm{T_{max}}$. The limits for realistic water depths and wave periods are supplied by the user and are typically set around $[\mathrm{d_{min}}, \mathrm{d_{max}}] = [0.5, 25]\ (\mathrm{m})$ and $[\mathrm{T_{min}}, \mathrm{T_{max}}] = [4, 15]\ (\mathrm{s})$ respectively; indicating the ranges where we expect waves to be mostly in intermediate or shallow water to get reliable depth estimates. Note that for depths larger than approximately $15\,\mathrm{m}$, shorter period waves ($T < 6\,\mathrm{s}$) are mainly useful in determining near-surface currents.

If the frame rate of the image sequence is low due to a slow turning radar antenna, as is the case in this study with $1/2.85\,\mathrm{s}^{-1}$, the filtered spectrum may show aliasing since the Nyquist frequency is close to the governing wave periods. An anti-aliasing step removes these unwanted by-products, (Figure 2.2; Figure 2.1, ④) and permits the use of data up to two times the Nyquist frequency [51].

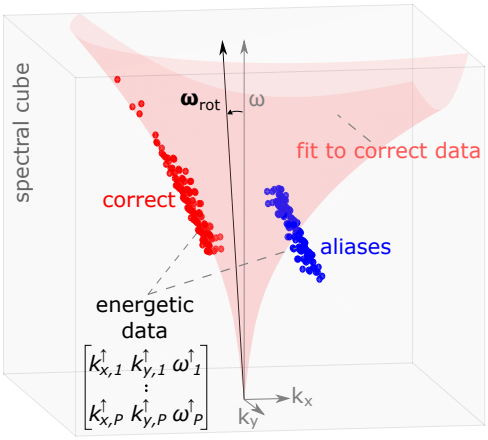

Figure 2.2.: Anti-aliasing on a spectral cube with dimensions $\mathrm{k_x}$, $\mathrm{k_y}$, ω. Energetic spectral data with energies above a threshold $\mathrm{E_{th,low}}$ are given by a set of $p = 1 \ldots \mathrm{P}$ points with coordinates $k^{\uparrow}_{x,p}$, $k^{\uparrow}_{y,p}$, $\omega^{\uparrow}_{p}$. This set contains correct data points (red dots) and aliases (blue dots), below and above the Nyquist frequency (grey plane). Aliases are detected and removed via a singular value decomposition. The ω-axis rotates (ω_{rot}) towards the correct spectral data by which aliases can be separated and a non-linear fit can be done on the correct spectral data (red dispersion shell) according to Equation (2.1). The blue shell indicates the orientation of aliases in the spectrum.

To separate the aliases from correct wave data a singular value decomposition (svd) (Equation (2.2)) is performed on the energetic parts of the spectrum. Energetic parts are defined by all spectral data with energies above a user defined threshold $\mathrm{E_{th,low}}$, which is the lower bound of the set $0 < \{\mathrm{E_{th,low}} \ldots \mathrm{E_{th,high}}\} < 1$ used in the fitting procedure that follows this anti-aliasing step.

$$\boldsymbol{A} = \boldsymbol{U}\boldsymbol{\Sigma}\boldsymbol{V}^{T}$$

where

$$\boldsymbol{A} = [\boldsymbol{k}^{\uparrow}_{x}, \boldsymbol{k}^{\uparrow}_{y}, \boldsymbol{\omega}^{\uparrow}] = \begin{bmatrix} k^{\uparrow}_{x,1} & k^{\uparrow}_{y,1} & \omega^{\uparrow}_{1} \\ k^{\uparrow}_{x,2} & k^{\uparrow}_{y,2} & \omega^{\uparrow}_{2} \\ \vdots & \vdots & \vdots \\ k^{\uparrow}_{x,\mathrm{P}} & k^{\uparrow}_{y,\mathrm{P}} & \omega^{\uparrow}_{\mathrm{P}} \end{bmatrix} \tag{2.2}$$

The matrix $\boldsymbol{A}$ lists the $p = 1 \ldots \mathrm{P}$ energetic points in the spectrum by their spectral coordinates $k^{\uparrow}_{x,p}$, $k^{\uparrow}_{y,p}$, $\omega^{\uparrow}_{p}$ in the columns $[\boldsymbol{k}^{\uparrow}_{x}, \boldsymbol{k}^{\uparrow}_{y}, \boldsymbol{\omega}^{\uparrow}]$, where the upward arrow signifies energy higher than $\mathrm{E_{th,low}}$. The amount of points, P, depends on the

value of $\mathrm{E_{th,low}}$ and the spectral wave signal. The svd factorizes the matrix $\boldsymbol{A}$ into two unitary matrices $\boldsymbol{U}$, $\boldsymbol{V}$ and a diagonal matrix $\boldsymbol{\Sigma}$. The superscript T denotes the transpose. In practice, $\boldsymbol{V}$ represents a rotation of the $\mathrm{k_x}$, $\mathrm{k_y}$, ω-coordinate system: $\boldsymbol{V} = [\boldsymbol{k}_{x,rot}, \boldsymbol{k}_{y,rot}, \boldsymbol{\omega}_{rot}]$, which best follows the spectral data $\boldsymbol{A}$. Due to the position of the aliases in the spectrum, the ω-axis rotates (ω_{rot}) towards the correct spectral data and away from the aliases, which allows for a clear separation: Correct data have higher values on ω_{rot} (found via $\boldsymbol{A}\boldsymbol{\omega}_{rot}$) compared to the original ω-axis and for aliases this is the opposite, which means that they are identified and can be removed.

After pre-processing the spectrum several spectral fits are done. Using a Levenberg-Marquardt minimisation, the Doppler-shifted linear dispersion relationship (Equation (2.1)) is fitted to all spectral data above a certain energy threshold E_{th} to yield an estimate for $[d, \boldsymbol{U}]$. Since the spectrum has been normalized this threshold lies between $0 < E_{th} < 1$. However, the optimal value of E_{th} is not known beforehand. The solution is to iterate an optimal value by making several fits for an array of energy thresholds $\{\mathrm{E_{th,low}}, \ldots, \mathrm{E_{th,high}}\}$, which produces a set of depth and near-surface current pairs $\{[\mathrm{d_{low}}, \mathbf{U}_{\mathrm{low}}], \ldots, [\mathrm{d_{high}}, \mathbf{U}_{\mathrm{high}}]\}$ (Figure 2.1, ⑤). By default, $\{\mathrm{E_{th,low}}, \ldots, \mathrm{E_{th,high}}\}$ covers the range $\{0.4, \ldots, 0.6\}$ in 10 increments, which is a generic setting, but can be adjusted by the user. By using a set of E_{th}, instead of single threshold, we omit the need to tailor the algorithm to each image sequence separately, which makes the algorithm robust to use on long time-series of data.

The goal is now to find the optimal pair of $[\mathrm{d_i}, \mathbf{U_i}]$ among the list of candidates $\{[\mathrm{d_{low}}, \mathbf{U}_{\mathrm{low}}], \ldots, [\mathrm{d_{high}}, \mathbf{U}_{\mathrm{high}}]\}$. Pairs are retained using three criteria: (1) $\mathrm{d_i}$ falls within the pre-set depth range $[\mathrm{d_{min}}, \mathrm{d_{max}}]$, (2) $|\mathbf{U_i}|$ is smaller than a user-defined maximum velocity magnitude $|\mathrm{U_{max}}|$, and (3) the coefficient of determination $r^2 > 0.6$, (Figure 2.1, ⑥). Note that the depth constraint $[\mathrm{d_{min}}, \mathrm{d_{max}}]$ has been used in an earlier step to reduce the spectrum with a wide dispersion filter (Figure 2.1, ②). However, a poor candidate fit on those data may still suggest a solution beyond those limits, therefore criterion (1) is needed here. To improve estimates of an operational system, knowledge about previous depth estimates can be used to (A) tighten criterion (1) or (B) in a Kalman filter. In case of option (A), an average is taken over a certain number of M previous depth estimates, $d_{avg,M}$, and a margin $\Delta\mathrm{d}$ is chosen to tighten criterion (1) by redefining $d_{min} = d_{avg,M} - \frac{1}{2}\Delta\mathrm{d}$ and $d_{max} = d_{avg,M} + \frac{1}{2}\Delta\mathrm{d}$. Option (B) is a postprocessing step and does not affect the depth inversion procedure. In this study we used option (A) for the site of Ameland (Section 2.4) and experimented with option (B) for the Sand Engine (Section 2.5).

The r^2 of criterion (3) is used as the optimization criterion as it indicates how well the non-linear fit represents the spectral data. This value is unity for a perfect match. Hence, the optimal $[\mathrm{d}, \mathbf{U}]$ amongst the remaining candidates is finally found by the fit with maximum r^2, (Figure 2.1, ⑦) and can be stored as the representative estimate for the computational cube. After a computational cube has been processed, the sequence of steps repeats for the next computational cube in the grid (Figure 2.1, steps ①…⑦), eventually producing full maps of depths and near-surface currents (Figure 2.1, output).

2.3. Radar in-situ data collection

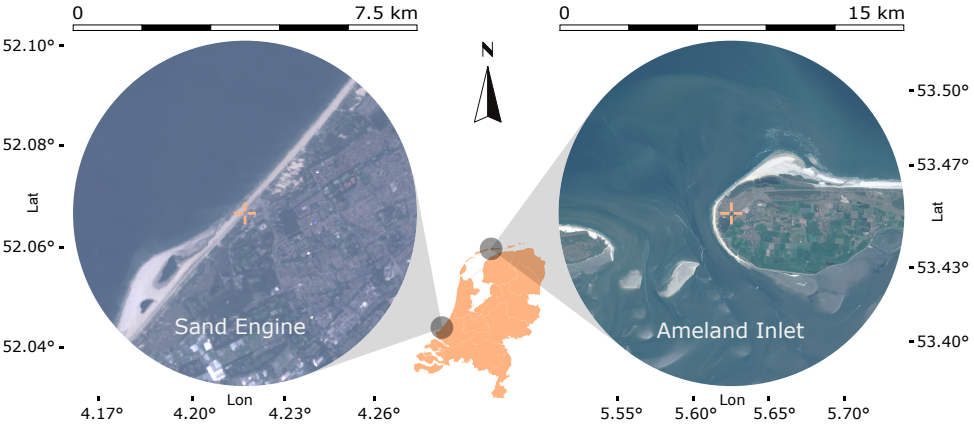

Figure 2.3.: Radar locations (centre crosses) and ranges (see top scales) at the two field sites of Sand Engine (left) and the Ameland inlet (right). A map of the Netherlands (middle) indicates the location of the two sites.

2.3.1. Sand Engine

The first field site is the Sand Engine, a sandy mega-nourishment of approximately $21\,\mathrm{Mm}^3$ constructed on the southwestern Dutch coast in 2011 (Figure 2.3 left). It was designed to combat erosion by diffusing along the coastline over an extended period of $10–20\,\mathrm{yr}$, while minimizing ecological stress and creating space for recreation [37]. To gain insight into the development and impact of the unprecedented scale of the nourishment an extensive monitoring campaign was launched in 2012 [54]. A radar station was installed $3\,\mathrm{km}$ north of the nourishment area, covering approximately $40\,\mathrm{km}^2$. The available radar data covered a short timeframe of $18\,\mathrm{h}$ during 20-21 October 2014 and were used to create a snapshot of the nourishment for that moment. Specific details on the radar properties are summarized in Appendix A.1 Table A.1.

The significant wave height ($\mathrm{H_s}$) ranged from $1.0–1.7\,\mathrm{m}$ and the peak period ($\mathrm{T_p}$) from $6.0–7.0\,\mathrm{s}$, which are average wave conditions for the site [54]. In total, 184 image sequences were available, each consisting of 128 images in intervals of $2.85\,\mathrm{s}$, translating to $6\,\mathrm{min}$ of wave motion at a resolution of $3.75\,\mathrm{m}$. Ground truth data were based on a detailed bathymetrical survey from 6 September 2014 which was merged with Jarkus transect data from 2014 to get greater coverage offshore. A local tide gauge was used to compensate for water level fluctuations in the depth estimates. For consistency, we only use the term depth throughout this chapter, but note that it excludes the influence of water level modulation and is referenced to NAP (Dutch ordnance datum, about Mean Sea Level) for both sites.

2.3.2. Ameland tidal inlet

The second field site is the Ameland Inlet, one of the tidal inlets of the Dutch Wadden Sea (Figure 2.3 right). The inlet is characterized by a wave-dominated ebb-tidal delta and deep tide-dominated inlet channels formed by strong tidal currents with maximum velocities around $1.5\,\mathrm{m\,s^{-1}}$. The semi-diurnal tide has a mean range of approximately $2\,\mathrm{m}$. Over the study period Dec 2017 – Dec 2018, H_s ranged from 0.1–$6.2\,\mathrm{m}$ and T_p from 1.8–$17.0\,\mathrm{s}$. Wave conditions were on average $\mathrm{H_s} = 1.3\,\mathrm{m}$ and $\mathrm{T_p} = 5.6\,\mathrm{s}$ and exceeded $H_s > 3.0\,\mathrm{m}$ and $T_p > 9.0\,\mathrm{s}$ during $5\,\%$ of the time.

The inlet is being extensively monitored within the framework of the Coastal Genesis 2.0 (Dutch: Kustgenese 2.0) research program, which was commissioned by the Dutch Ministry of Infrastructure and Environment in 2017 [55]. As part of the monitoring program, XMFit software runs operationally on X-Band radar data collected at the Ameland lighthouse. The navigational radar monitors the tidal inlet and has a spatial coverage of approximately $180\,\mathrm{km^2}$ (Figure 2.3 right). Specific details on the radar properties can be found in Appendix A.1. The goal of employing the radar is to track the evolution of a pilot nourishment of $5\,\mathrm{Mm^3}$ at the outer rim of an ebb-shield. Commencing 20 March 2018, the gradual placement of the nourishment ended in February 2019.

Radar image sequences at Ameland consist of 256 images spaced at $2.85\,\mathrm{s}$. Image sequences cover a time window of $12\,\mathrm{min}$ and are produced at $20\,\mathrm{min}$ intervals, leaving $8\,\mathrm{min}$ of downtime in between. The pixel size is $7.5\,\mathrm{m}$. Note that the range resolution is $7.5\,\mathrm{m}$, but that the beam widens with distance from the radar. Depending on the alignment of the radar beam and wave crests, we estimate the resolution to be between $7.5\,\mathrm{m}$ and $57\,\mathrm{m}$ at $7\,\mathrm{km}$ distance from the radar (see also Appendix A.1). Due to presently limited storage space (in this case $16\,\mathrm{TB}$), raw image sequences (each $3\,\mathrm{GB}$) are overwritten after 2 months and hence not available for reanalysis. The image sequences are processed locally in the light house such that the much smaller sized result files (each 0.1–$0.5\,\mathrm{MB}$) can be transferred via a $4\,\mathrm{G}$ internet connection. Note that the storage buffer allows for the analysis of up to 72 image sequences a day; the increasing lag can be caught up during times when $H_s < 0.9\,\mathrm{m}$.

Poor depth estimates were suppressed by tightening criterion (1) (section 2) using an averaging window of $\mathrm{M} = 5$ and a depth margin of $\Delta\mathrm{d} = 4\,\mathrm{m}$. Initial bathymetry data was needed to start the process. Tidal depth modulation was accounted for by passing information from a local wave buoy at Terschelling (Figure 2.1: grey square, top right). As initial bathymetry data a combination of surveys from February and September 2017 was used. Their initial influence on the estimates quickly phased out due to the choice of a rather large depth margin $\Delta\mathrm{d}$. To additionally ensure that presented depth estimates were independent from the initial bathymetry the first 1000 estimates were ignored in this study. The choices for the averaging window and the allowable depth margin were made arbitrarily and other values may be chosen, yet the current combination of values underlies the results presented in this study.

Between Dec 2017- Dec 2018, the operational system returned approximately

7500 estimates of morphology. Within this period the Ameland Inlet was surveyed twice using a single beam mounted on a vessel. The first survey was done in the beginning stage of nourishment works 31 May – 5 June 2018 (Survey #1) and the second survey about half way, from 12 – 14 October 2018 (Survey #2). The surveys were done during calm periods that fell below the threshold of $H_s = 0.9\,\mathrm{m}$ used by the operational system to produce depth estimates. For validation, therefore the average was taken over daily median estimates with similar spatial coverage shortly before and after each survey. Specifically for the nourishment location, additional multibeam surveys were available, which were used in this study to compute volumetric changes over the placement period of the nourishment.

The computational grids and user settings underlying the analyses of both the Sand Engine and the Ameland Inlet can be found in Appendix A.2.

2.4. Results

2.4.1. Sand Engine

The application of XMFit to radar images from the Sand Engine produced spatially smooth depth estimates (Figure 2.4a). Comparison of the median depth inversions with depth measurements revealed an overall bias of $-0.9\,\mathrm{m}$, revealing a tendency for depth overestimation by the DIA. The average standard deviation around a depth estimate was $0.85\,\mathrm{m}$ and likely stemmed from tidally induced changes in flow direction relative to the direction of wave incidence, see also Discussion Section 2.5.1. The spatial root mean square error ($RMSE$) was $1.32\,\mathrm{m}$ and was mostly caused by inaccuracies close to shore and at the northern boundary of the radar domain. Near the shoreline, especially around the $5\,\mathrm{m}$ depth contour (Figure 2.4b), waves start to break over the nearshore bars and the used linear wave theory is not representative, which causes errors to be locally larger. This is similar to a previous observation by Bell [48] for Egmond aan Zee, a site about $60\,\mathrm{km}$ to the north of the Sand Engine. Close to the boundary of the radar domain, the radar image quality degrades. Furthermore, at the north-eastern end of the domain the radar beam aligns with wave crests, and depth estimates were poor or not returned. It is interesting to observe that estimates at large depths $d = 10$–$15\,\mathrm{m}$ were generally close to ground truth, although peak wave periods were relatively short $T_p = 6$–$7\,\mathrm{s}$, meaning that an error in wavenumber leads to a large error in depth. There are two reasons why such errors are limited in the current approach: First, wavenumber errors are minimized through spectral averaging with 5 temporal bins (see Appendix A.2). Secondly, many spectral coordinates are used for the non-linear fit (Figure 2.1, (5)). For the Sand Engine at these large depths on average about 75 coordinates spread over several angles and 11 frequencies. An important property of 3D-FFTs in combination with anti-aliasing is that frequencies up to two times the Nyquist frequency can be used for the fit [47, 51]. This supplies extra spectral coordinates for the fit (red points above Nyquist frequency in Figure 2.2), which especially for $T_p = 5$–$6\,\mathrm{s}$ can offer some extra certainty on the depth estimate in this case.

Note that it is possible to improve the results by making changes to the spectral treatment of the radar data or by using a Kalman filter in post-processing, which we address in the Discussion Section 2.5.

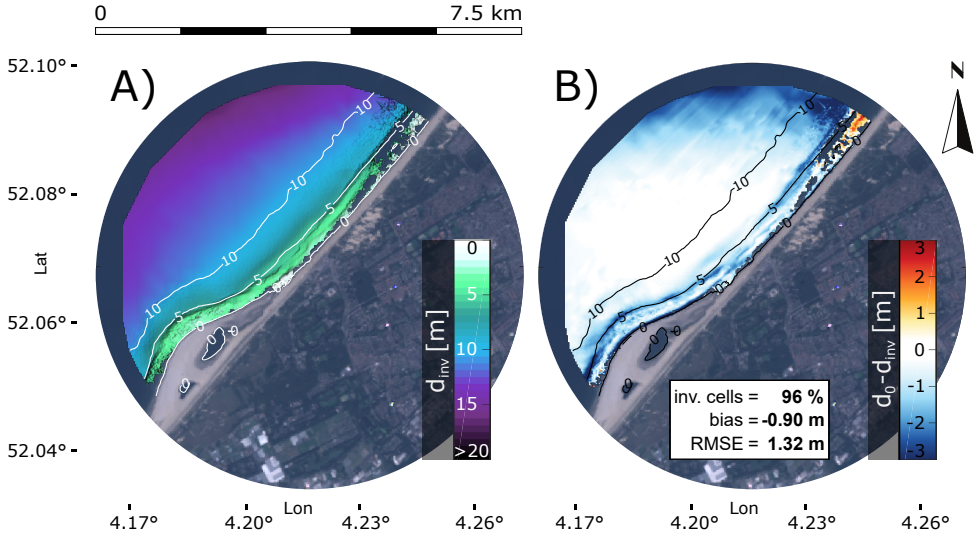

Figure 2.4.: Radar-derived results for the Sand Engine. (a) Inverted depths d_{inv} (m) (colorbar). (b) Comparison of d_{inv} against in-situ measured depths d_0 (m), where red/blue colors indicate under-/overestimation of depth respectively. In both panels, contour lines of measured depths are superimposed for reference. Results represent the median over 184 image sequences spanning $18\,\mathrm{h}$ in total. Values are included for the percentage of grid cells returning a result (inv. cells), the overall bias (bias) and the root mean squared error ($RMSE$).

2.4.2. Ameland tidal inlet

Depth results for the Ameland Inlet distinctly captured the characteristic morphological features of the outer delta (Figure 2.5a,c). The horseshoe-shaped ebb-shield in the west, the central ebb channel, and the large swash platform fronting Ameland were detected by the algorithm. The estimated depths at instances of Survey #1 and Survey #2 compared to ground truth with spatially averaged biases of respectively $0.85\,\mathrm{m}$ and $0.63\,\mathrm{m}$, and $RMSE$s of respectively $1.34\,\mathrm{m}$ and $1.14\,\mathrm{m}$ (Figure 2.5b,d), which were largely determined by inaccuracies between the 5–$10\,\mathrm{m}$ contour lines. We hypothesize these imprecisions to be partly linked to complex local hydrodynamics, which are not accounted for by Equation (2.1), in combination with some radar image related effects. For example, we expect some error due to tide driven shear flows in the channel between the ebb-shield and the swash platform and intense wave breaking and strong wave driven currents along the northern edges of these two features. In the region close to the island of Terschelling, in the western part of the domain (Figure 2.5b), we ascribe some error to

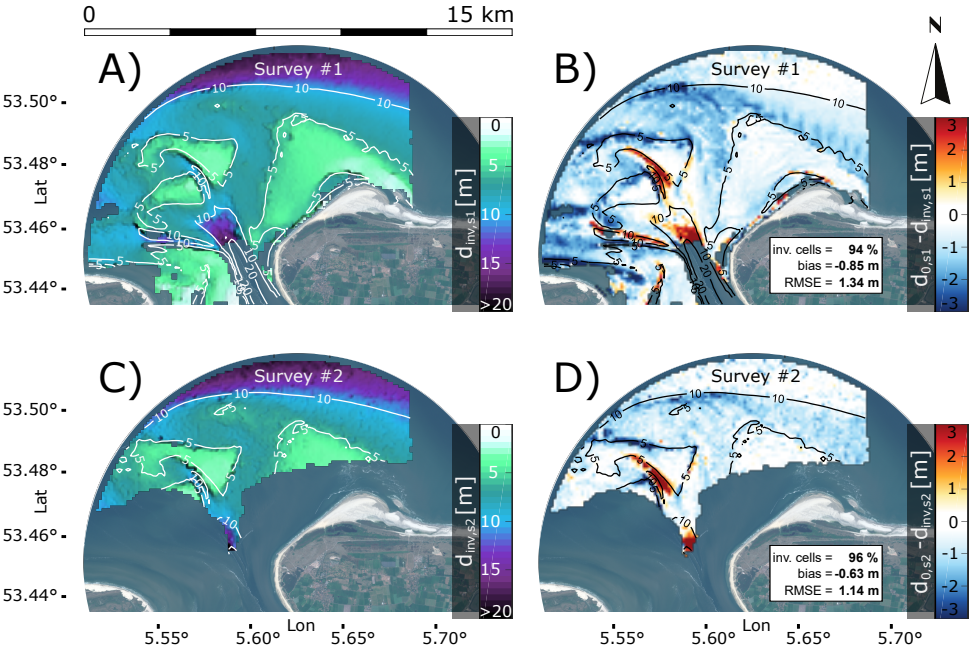

Figure 2.5.: XMFit results from the operational Ameland system as compared to a survey from 31 May to 5 June 2018 (Survey #1) and a survey from 12-14 October 2018 (Survey #2). Panels (a,c): average depth estimates over two days encompassing each survey, as indicated by (a) $d_{inv,S1}$ for Survey #1 and (c) $d_{inv,S2}$ for Survey #2. Single beam observations are outlined by white depth contours. Panels (b,d): difference of inverted depths d_{inv} with the corresponding single beam measurements d_0 (now accentuated by black contours instead of white contours) as indicated by (b) $d_{0,S1}$–$d_{inv,S1}$ for Survey #1 and (d) $d_{0,S2}$–$d_{inv,S2}$ for Survey #2. Similar to the Sand Engine a mostly negative bias (depth overestimation; blue) is observed, being a little higher for Survey #1 (bias = $-0.85\,\mathrm{m}$) than Survey #2 (bias = $-0.63\,\mathrm{m}$).

the unfavourable angle of the radar beam with respect to the incoming wave crests. Yet another source of error was present, as the ebb-shield and the western branch of the ebb channel appeared slightly shifted to the south compared to single beam data. This shift stood out in the comparison with ground truth data (Figure 2.5b,d) through sharp negative biases around feature-edges facing north and corresponding positive biases around feature-edges facing south. Revisiting the raw radar images, revealed that this shift was partly rooted in a localized distortion of the raw radar image data, which was probably caused by a slight misalignment of the radars Northing, but the full origin is unknown and could therefore not be assessed in detail. In contrast, the system performed well for shallow parts such as the large swash platform near Ameland and deep parts to the north of the outer delta. Here, depth estimates were consistently accurate (Figure 2.5b,d: white areas).

The difference between the two time instances of Survey #1 and Survey #2 brought out the signature of the nourishment at the outer rim of the ebb-shield, in the single beam measurements (Figure 2.6b) as well as radar-inverted results (Figure 2.6a). These results were in line with the location of the nourishment site as provided by the dredging contractor. A succession of sedimentation-erosion patterns across north-eastern direction over the ebb-shield furthermore suggested a slight, clockwise turning of the ebb-shield over this four-month period. Although less pronounced than in the single beam measurements (Figure 2.6b), these patterns were also found in the radar-derived results (Figure 2.6a).

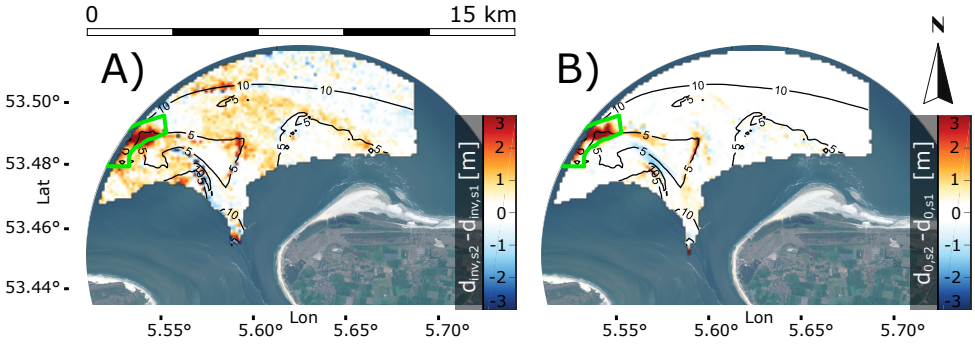

Figure 2.6.: Difference between June (Survey #1) and October (Survey #2) as derived for radar and single beam measurements. (a) radar: inverted depths $d_{inv,S1}$, of Survey #1 are subtracted from $d_{inv,S2}$ of Survey #2. (b) single beam: accordingly, measurements $d_{0,S1}$ of Survey #1 are subtracted from $d_{0,S2}$ of Survey #2. The pilot nourishment fronting the ebb shield is clearly visible in both cases and its position is in line with expectation (green polygon). Note that the surveys do not cover the entire radar domain. For visual clarity, differences between radar results (a) are truncated to the same area as the surveys (b).

Since the nourishment was clearly visible in the time snapshots, the analysis was refined towards a more detailed time evolution to see whether we were able to monitor volume changes in the nourishment area during placement. For this, we used all the results produced between Dec 2017- Dec 2018. Before analysing nourishment volumes, the noise of the radar-derived depth estimates throughout the radar domain was assessed, as this noise could impact volume calculations. A timeseries of the spatially averaged depth bias was computed by the difference between radar-derived estimates and single beam data from Survey #1 (Figure 2.7). It was assumed that the influence of actual morphological change on the bias was negligible compared to the variability in radar depth estimations (cf. Figure 2.6b and Figure 2.5b). Although tidal water level changes were accounted for, the timeseries of depth biases fluctuated roughly between $-2\,\mathrm{m}$ and $0\,\mathrm{m}$. The average standard deviation around a daily depth estimate was $0.71\,\mathrm{m}$. This noise was inherent to the operational system and was likely a product of a combination of factors, such as differences in radar image quality due to external factors (wind, rain, fog), but was also a consequence of applying idealized theory (Equation (2.1)) to a complex and

variable outer delta environment: we found weak linear dependencies of the depth bias on the water level and the wind speed. For low water levels, $\mathrm{NAP}{-}1.5\,\mathrm{m}$, the depth bias was on average $-0.74\,\mathrm{m}$ and decreased linearly to $-1.06\,\mathrm{m}$ for high water levels of $\mathrm{NAP}{+}1.5\,\mathrm{m}$. Yet, with a standard deviation of $0.84\,\mathrm{m}$ the uncertainty in these depth bias values was high and showed that it would be difficult to predict the depth bias from a given water level. A similar linear relation was found between depth bias and wind magnitude: for wind speeds of $3\,\mathrm{m\,s^{-1}}$ the depth bias was on average $\approx -0.5\,\mathrm{m}$, while for wind speeds of $15\,\mathrm{m\,s^{-1}}$ this bias was $\approx -1.2\,\mathrm{m}$. Yet again, the standard deviation was high at $0.81\,\mathrm{m}$, showing that a prediction of the depth bias based on wind speed would be uncertain. Depth estimates also correlated with simultaneous near-surface current estimates, whose directions and magnitudes are indicators for local depth underestimation or overestimation, as we discuss in detail in Section 2.5.1. Since the current fields constantly change in space and time, they likely contribute to the observed fluctuations in the overall depth bias. No correlations of the depth bias with wind direction, wave height or wave period were found.

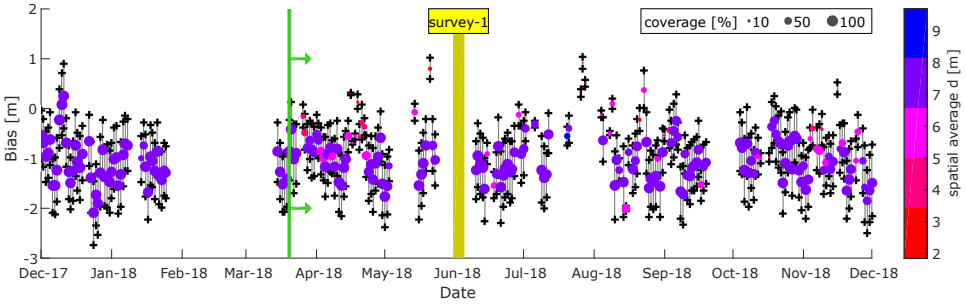

Figure 2.7.: Mean spatial bias over the full radar domain of XMFit estimates with ground truth data surveyed between 31 May to 5 June 2018 (Survey #1, yellow). The start of nourishment works is indicated by a vertical green line. Representative bed elevations are obtained by subtracting local water level measurements from the XMFit depth estimates. Dots represent the daily median result and whiskers the corresponding 25^{th} and 75^{th} percentiles. Colors indicate the average depth over the parts of the radar image that contain results and show that the bias appears lower for moments when only small (small marker size), shallow (magenta, red) areas could be inverted. When coverage is high (large marker size) the bias also accounts for sensitive deeper parts (purple, blue). Note that the lack of data during February is due to a temporary system shutdown.

On the time scale of days, the observed noise would severely impact the calculation of nourishment volumes, therefore a straightforward solution was to ensemble average over a time window: we based volume calculations on median depth estimates in the nourishment area over a sliding time-window of one month. Besides denoising, volume estimates were then continuous in time, bridging over gap periods where the radar system had not been able to produce depth estimates for the

nourishment area (Figure 2.8, gaps between grey bars). A window size of one-month was chosen as most data gaps could be overcome, except for a large gap in February 2018, while noise was largely suppressed. Volume changes were calculated by multiplying the average depth changes by the nourishment area (see Figure 2.6, green polygon). For the comparison, volumes were computed based on inverted depths as well as the depths from the multibeam surveys of the nourishment.

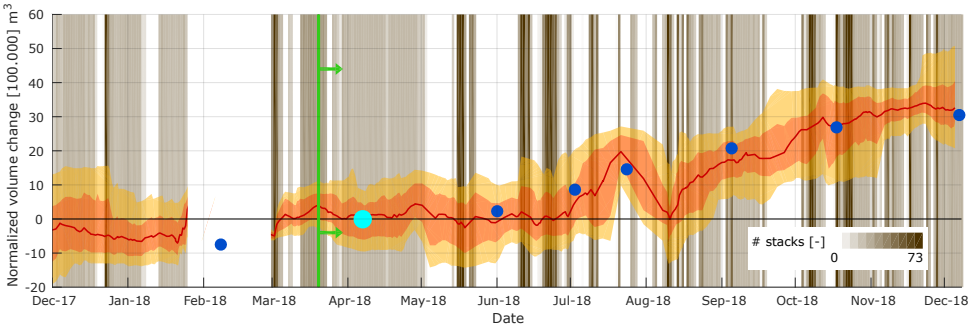

Figure 2.8.: The time-evolution of the sediment volume changes in the nourishment area (Figure 2.6, green polygon) for the period Dec 2017–Dec 2018 according to radar (red line) and multibeam surveys (blue dots). Volume changes are normalized to the 2^{nd} multibeam survey (cyan dot). Per day, the number of available XMFit results that covered the nourishment area – and could hence be used for volume calculations – is indicated by a vertical grey band (see colorbar). The monthly median radar estimate (red line) is presented with corresponding 25^{th}–75^{th} percentile range (shaded red) and 10^{th}–90^{th} percentile range (shaded yellow). The start of nourishment execution, 20 Mar 2018, is indicated by the vertical green line.

To focus the comparison between radar-estimates and multibeam measurements on volume changes, we referenced both the radar estimates and the measurements to the second multibeam measurement. The reason for this is a bias of $2\,\mathrm{Mm}^3$ between the radar estimates and the measurements in the nourishment area at the time of the second multibeam survey (Figure 2.5). We assumed this bias to be constant in time, as fluctuations caused by environmental conditions and data quality should average out using a one-month averaging window over a long period of time. This meant that volume changes could be studied.

Computed volume changes in the nourishment area were relatively stable until they started to increase at the beginning of March 2018 (Figure 2.8). Considering the start of nourishment works (20 March 2018), this increase appeared two weeks premature. This could be explained by the one-month time window to suppress noise, while having no pre-nourishment data in February to counter balance March data. A $RMSE$ of $276\,000\,\mathrm{m}^3$ was calculated based on the 7 instances where radar-derived volumes could be related to the multibeam surveys. It represented an error of $7\,\%$ on the total placement volume of $3.8\,\mathrm{Mm}^3$. It is interesting to

note that the location was at more than $7\,\mathrm{km}$ distance from the radar station, near maximum range.

2.5. Discussion

The depth inversion showed skill for both the Sand Engine as well as the complex Ameland Inlet. Yet, the depth was often overestimated in regions (i) that were close to the boundary of the radar domain (ii) where the radar beam aligned with wave crests (iii) where we expected complex hydrodynamics due to wave breaking, strong currents or shear flows. These errors are related to the backscatter, but also to the limitations of using a simplified physical model (i.e., Equation (2.1), idealized wave-current interaction) for depth inversion. The quality of d estimates by their covariance with $\boldsymbol{U}$ estimates provides insight into the role of the Doppler-shift. This is done from a statistical point of view, based on the extensive dataset from the Ameland Inlet (Section 2.5.1). The d estimates can also be improved. By changing the computation procedure (Section 2.5.2) and/or by post-processing the results (Section 2.5.3), errors in (i) - (iii) are reduced. Experiments to reduce depth errors were conducted for the Sand Engine, since the image sequences could be recomputed at this site. Note that Ameland depth estimates were collected during a time where the DIA did not yet include a measure for error variance, which means that we could not test the Kalman filter on those data.

2.5.1. The role of near-surface current estimates in depth inversion

Near-surface currents are estimated per computational cube via the Doppler-shift ($+\boldsymbol{k}\cdot\boldsymbol{U}$, Equation (2.1)), being the dot product of a wavenumber vector with a near-surface current vector. Only current components in/against the wave direction alter the wave frequency and thereby affect the depth estimate d. To investigate the effect of $\boldsymbol{U}$ on d, near-surface current directions were translated to near-surface current angles ($NSCA$) with respect to wave direction, which was here taken to be the energy-weighted mean wave direction (MWD) over the spectrum.

First a preliminary check was done whether patterns of $\boldsymbol{U}$ and MWD were realistic and thereby suited for further analysis (Figure 2.9). This appeared to be the case: The MWD captured the effect of wave refraction, being stronger during low tide conditions (Figure 2.9b) than during high tide conditions (Figure 2.9a). It also revealed more intricate patterns as for example waves which followed ebb-channels to meet at the bifurcation just below the horseshoe-shaped ebb-shield (Figure 2.9b). Estimated $\boldsymbol{U}$-vectors also appeared realistic, reflecting the characteristic tidal flows expected for the area: The tidal wave travels along the barrier islands (Figure 2.9c,d: vector fields in north-northeast of domain) pushing water into the inlets at upcoming tide (Figure 2.9c: east-south-eastward flow through ebb-channels) and causing outward flow at falling tide (Figure 2.9d: westward flow through western ebb-channel and northward flow through central ebb-channel).

Details such as flow through the small flood channels near Terschelling at rising tide were also captured.

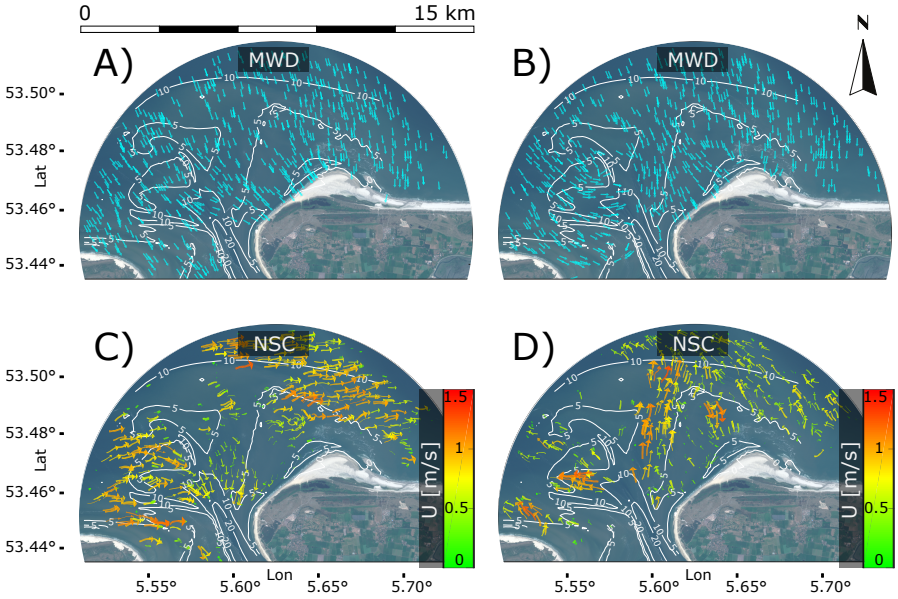

Figure 2.9.: Examples of mean wave directions (MWD) and near-surface currents (NSC) at the Ameland Inlet, as estimated by XMFit. Turquoise arrows indicate MWD-patterns. NSC arrows are scaled and colored according to magnitude (colorbar). Panels (a,c): An example from 25 Oct 2018 at 05:50, rising tide with a water level (WL) = $NAP+1.1\,\mathrm{m}$. Panels (b,d): An example from the preceding falling tide at 01:30, with $WL = NAP-0.9\,\mathrm{m}$.

For the Doppler-shift analysis, we retrieved the required $NSCA$s by expressing near-surface currents relative to the collocated MWDs. The accuracy of depth estimates was measured by the local depth bias $d_{0,S1}-d_{inv}$, which was computed for each cube in the domain and for all available time instances. In this way a comprehensive dataset was constructed, comprising $>20 \times 10^6$ pairs of depth biases and coincident near-surface current vectors. Analogous to Figure 2.7, we used Survey #1 as reference to calculate depth biases.

The analysis revealed that near-surface current estimates in direction of wave propagation ($NSCA \rightarrow 0°$) generally cooccurred with underestimation of depth, while near-surface current estimates against the direction of wave propagation ($NSCA \rightarrow \pm 180°$) coincided with an overestimation of depth (Figure 2.10a: sinusoidal shape). These under- and overestimations increased with increasing near-surface current magnitudes (Figure 2.10a: bright colors at peak $NSCA = 0°$, and trough $NSCA = \pm 180°$). However, weak near-surface current estimates in direction of wave propagation did not guarantee a good depth estimate (Figure 2.10a: dark colors between $NSCA = -60°$ to $63°$). Still, the observations generally show that the Doppler-shift overcompensates for the presence of currents, as without the

Doppler-shift we would expect current-induced depth errors to behave the opposite way ([50]; eq. 10).

In shallow water, $d_{0,S1} = 0.5$–$5.0\,\mathrm{m}$, depth overestimations and depth underestimations nearly balanced each other over the range of $NSCA$s from $-180°$ to $180°$ (Figure 2.10b: median depth bias per $NSCA$, green curve, undulates around zero. Transition from general depth underestimation to overestimation at $NSCA = \pm 73°$, vertical magenta lines). This changed with increasing depth, $d_{0,S1} = 5.0$–$10.0\,\mathrm{m}$, as depth overestimations started to dominate depth underestimations for most NSCAs (Figure 2.10c: green curve only positive for $NSCA$ between $-43°$ to $52°$), with chronical overestimation for $d_{0,S1} = 10.0$–$25.0\,\mathrm{m}$ (Figure 2.10d: green curve stays below zero). However, in direction of wave propagation these overestimations were on average small with values close to zero (Figure 2.10d: green curve within $NSCA < \pm 90°$). Besides the tendency towards depth overestimations, also the sensitivity in the depth estimates increased with increasing depth (cf. Figure 2.10b-d: bandwidth, given by 2.5^{th}–97.5^{th} percentile range, increases from b) $\approx 3\,\mathrm{m}$ to c) $\approx 4\,\mathrm{m}$ to d) $\approx 6\,\mathrm{m}$) especially for situations where near-surface current estimates pointed in direction of wave propagation (cf. Figure 2.10b-d: bandwidth larger for $NSCA < \pm 90°$). It was interesting to observe that for shallow depths estimated maximum near-surface current magnitudes were larger in direction of wave propagation than against it (Figure 2.10b: brightest colors for $NSCA \to 0°$, depth underestimation). For large depths, maximum near-surface current magnitudes were estimated against direction of wave propagation (Figure 2.10c,d: brightest colors for $NSCA \to 180°$, depth overestimation), while near-surface current estimates in direction of wave propagation appeared to be underestimated (Figure 2.10c,d: dark colors for $NSCA < \pm 90°$).

In summary, observed biases in both depth and near-surface current estimates suggest that the non-linear fit of Equation (2.1) to the spectral data is sensitive to the local depth and the wave direction: (1) Generally, depths are underestimated for near-surface currents following the direction of wave propagation and depths are overestimated for opposing near-surface currents. (2) Strong near-surface current estimates correlate with strong depth biases, but a weak near-surface current estimate in direction of wave propagation does not guarantee a small depth bias. (3) For increasing depth, the depth estimate is more uncertain, tends towards overestimation, and especially so for opposing near-surface currents. (4) This is correlated with near-surface currents against direction of wave propagation having larger magnitudes than in direction of wave propagation.

The observations suggest that depth estimates may benefit from stricter constraints on maximum surface current magnitudes (e.g., $|\mathrm{U}_{\mathrm{max}}| < 0.5\,\mathrm{m}$ instead of $|\mathrm{U}_{\mathrm{max}}| < 1.5\,\mathrm{m}$). This entails that it be difficult to find an optimal solution among the list of $[d_i, \boldsymbol{U}_i]$-candidates which satisfies the stricter criterion (Figure 2.1, ⑥). A way to solve this problem could be to penalize the non-linear fit for large $|\boldsymbol{U}|$.

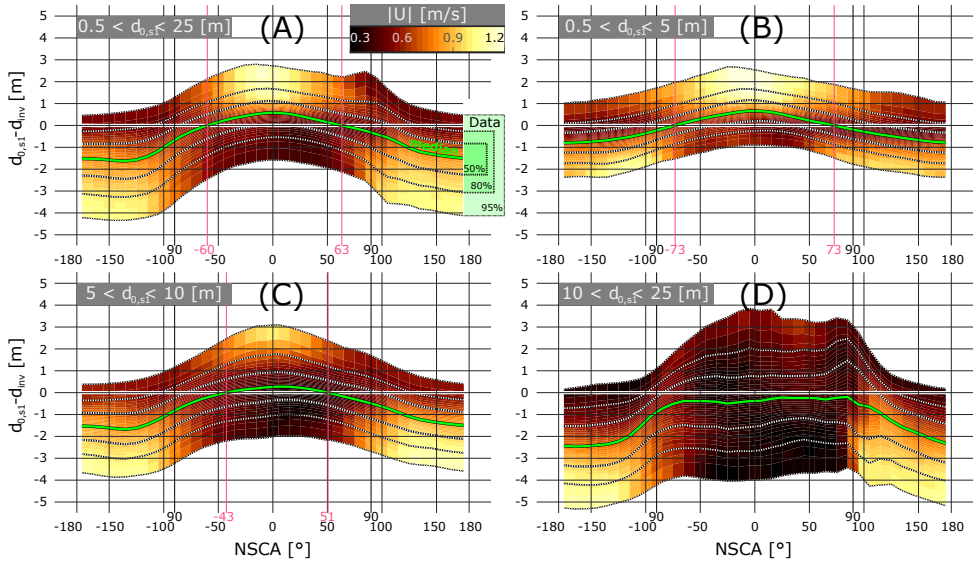

Figure 2.10.: Observed depth bias (vertical axis) as a function of the near-surface current angle (NSCA) with respect to mean wave direction (horizontal axis). At $NSCA = 0\,\mathrm{degree}$, near-surface currents point in direction of wave propagation, whereas for $NSCA = \pm 180°$ they oppose each other. The depth bias is used as proxy for the depth error. Corresponding near-surface current magnitudes ($|\boldsymbol{U}|$) are shown in bronze colors (colorbar). Panels present data within different ranges of depth: a) $0.5 < d_{0,s1} < 25.0\,\mathrm{m}$ (all data); b) $0.5 < d_{0,s1} < 5.0\,\mathrm{m}$; c) $5.0 < d_{0,s1} < 10.0\,\mathrm{m}$; d) $10 < d_{0,s1} < 25.0\,\mathrm{m}$. Depth biases are calculated as the difference between measured depths from Survey #1 and water level corrected inverted depths, $d_{0,s1}$–d_{inv}. Per $NSCA$, the $95\,\%$ range of observed depth biases is presented (bandwidth) along with their median value (green line); the $95\,\%$, $80\,\%$ and $50\,\%$ range contours are indicated with dotted black lines and labelled as shown by the green boxes in panel (a). $NSCA = \pm 90°$ are emphasized by additional vertical grid lines, to indicate where near-surface currents have no effect on waves according to Equation (2.1). The angles that are optimal for depth inversion are given by the zero crossings of the median depth bias and are emphasized by vertical magenta grid lines. The dataset includes the results of all analysed cubes over the entire period from Dec 2017 – Dec 2018, amounting to $>20 \times 10^6$ observations.

2.5.2. Choice of spectrum (amplitude vs. energy)

Depth estimates can also be improved in other ways. Depth inversion results are a product of relating wave characteristics to wave theory. A different representation of the wave characteristics may lead to different results, which is investigated by using amplitude spectra instead of energy spectra. The difference is simply that spectra are not squared after performing the 3D-FFT. It does not alter the wavenumber-frequency relationships, but their weights and hence changes the sets of spectral data that are passed to the non-linear fitter during the thresholding procedure (Figure 2.1, (5)).

The results of this experiment suggest that more favorable sets of spectral data are established if amplitude spectra are used, as the overall depth bias (median over all analyzed image sequences) improved by $0.13\,\mathrm{m}$, from $-0.90\,\mathrm{m}$ to $-0.77\,\mathrm{m}$ (cf. Figure 2.11a,b). The improvements especially occurred around the bars where waves break (Figure 2.11a,b, right column: red line vs. green line between $d0 = 4{-}8\,\mathrm{m}$). This was also emphasized by an improvement of the bias by $0.22\,\mathrm{m}$ for the nearshore area, above the $10\,\mathrm{m}$ depth contour. Similarly, also the $RMSE$ improved by $0.20\,\mathrm{m}$ from $1.32\,\mathrm{m}$ to $1.12\,\mathrm{m}$ with improvements being largest in shallow regions and the bar area. This effect can be explained by the disproportionate spectral weight of breaking waves in the image spectrum who by their asymmetry do not agree with the linear dispersion assumption underlying the analysis. Using an amplitude spectrum keeps the spectral weights closer together and thereby reduces the impact of breakers. Improvements were also noticed for the more difficult area to the north-east of the Sand Engine (Figure 2.11a,b,left column: whitening of north east area), which we ascribe to a relatively weaker impact of bad wave representations; in this case due to radar beam - wave crest alignment and lesser image quality.

2.5.3. Kalman filtering

An alternative way to improve the XMFit results is through post-processing with a Kalman filter. The Kalman filter is used in time on the derived morphological changes, assuming slowly varying morphology in comparison to the radar sampling interval, analogous to Holman, Plant and Holland [20]. The Kalman filter is an instrument for quality control and improvement: It weighs the current depth estimate d_t at time t against a previous estimate $\overline{d}_{t-1}$ at $t-1$ using the Kalman gain, K, by $\overline{d}_t = \overline{d}_{t-1} + K(d_t - \overline{d}_{t-1})$, where overbars denote Kalman adjusted estimates. The Kalman gain requires an indication for the confidence we have in the current d_t estimate (R in eq. 5 of Holman, Plant and Holland [20]). In line with Holman, Plant and Holland [20], we use the error variance σ^2 of the non-linear fit for this purpose. This error variance of d_t is compared against the variance $\overline{\sigma^2}$ of $\overline{d}_{t-1}$ (P in eq. 5-7 of Holman, Plant and Holland [20]), which depends on previous estimates of σ^2, but also on process variance (Q in eq. 6 of Holman, Plant and Holland [20]). The process variance, Q, accounts for morphological change that may occur over the period of observations, but since Sand Engine data only cover a period of $18\,\mathrm{h}$, we neglect it (i.e., $Q = 0$). For further details on the application of a Kalman filter

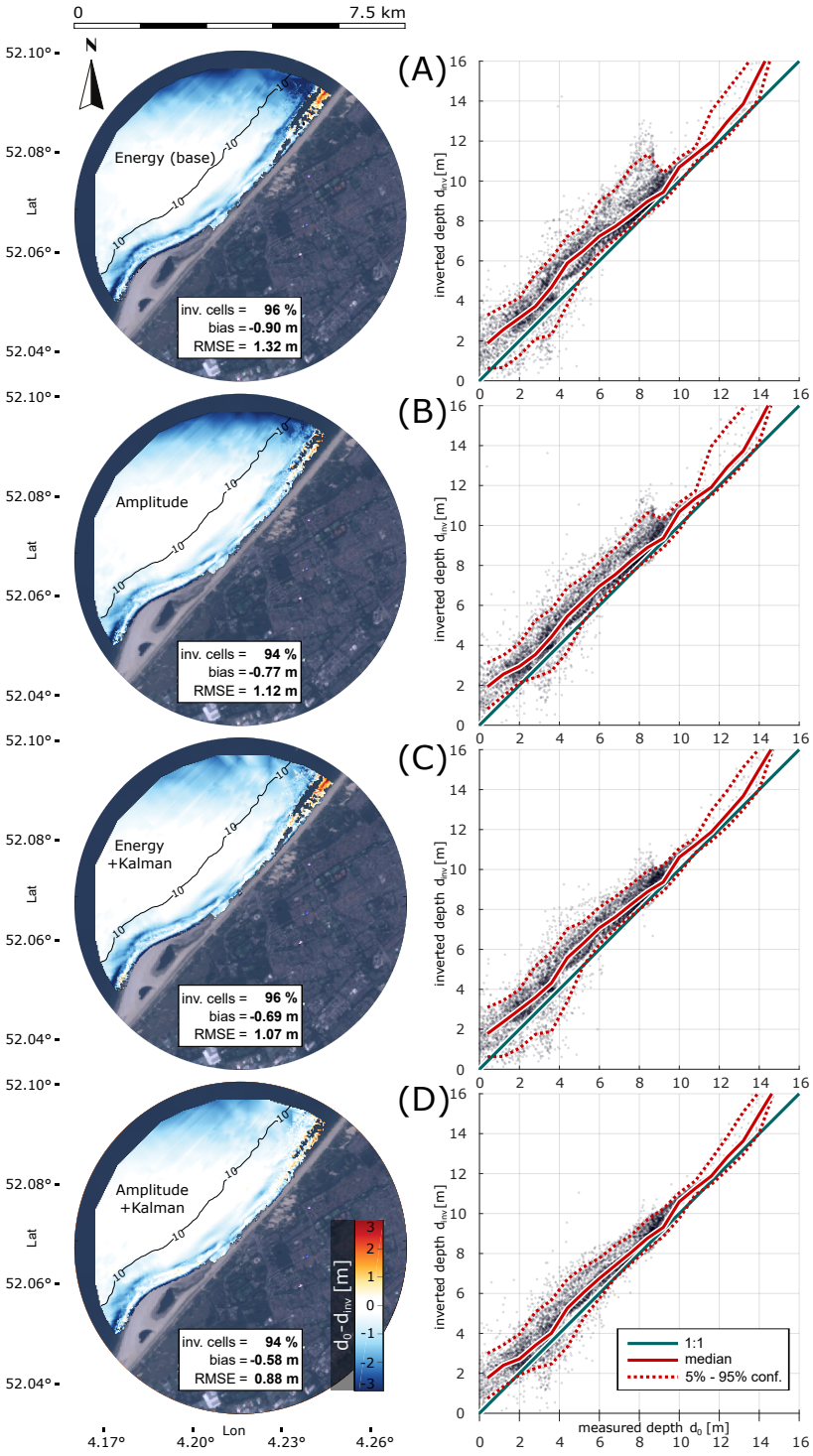

(Caption on next page.)

Figure 2.11.: Methods to improve the XMFit results for the example case of the Sand Engine, shown by comparisons of inverted depths d_{inv} (m) against in-situ measured depths d_0 (m). The left column presents difference maps where red/blue colors indicate under-/overestimation of depth respectively. The right column presents direct comparisons of d_{inv} against d_0, including the $1:1$ reference (green), the median over all d_{inv} at a certain d_0 (red), and the 5–$95\,\%$ confidence interval (dashed red). Panels (a,b): Median depth estimates over all 184 image sequences from 20-21 Oct 2014, for (a) the base case using the energy spectrum and (b) using the amplitude spectrum. Panels (c,d): The final, 184^{th} estimate of the Kalman filter after application to results produced using (c) energy spectra and (d) amplitude spectra.

to bathymetry estimates from a DIA, we refer to Holman, Plant and Holland [20]. This experiment presents the results after the last, 184^{th} Kalman filter iteration.

The Kalman filter reduced the depth bias by $0.21\,\text{m}$, from $-0.90\,\text{m}$ to $-0.69\,\text{m}$, and the $RMSE$ by $0.25\,\text{m}$, from $1.32\,\text{m}$ to $1.07\,\text{m}$ (cf. Figure 2.11a,c). In this case, the improvements were quite evenly distributed across all depths, including deeper areas (Figure 2.11a,c,left column: whitening of northern area; Figure 2.11a,c,right column: narrowing of d_{inv}-confidence interval for $d_0 > 10\,\text{m}$). The combined effect of a Kalman filter and an analysis based on amplitude spectra was a reduction of the overall depth bias to $-0.58\,\text{m}$ and $RMSE$ to $0.88\,\text{m}$ (Figure 2.11d). The broad improvements clearly showed when compared to the base case (cf. Figure 2.11a,d): Depth estimates of the difficult regions in the north and north-east improved (Figure 2.11a,d,left column), but also the breaker region (Figure 2.11a,d,right column), which is known to experience larger errors [23]. Hence, on the short term, the application of a Kalman filter without process variance is superior to using the median estimate. Though we recommend the data to cover at least one tidal cycle as to dampen out temporary tide induced inaccuracies.

Although we could not test the Kalman filter on the Ameland data, due to lacking information on σ^2, it is also not straightforward to apply. While the Kalman filter has proved itself valuable for the Sand Engine and also other uniform coastlines such as Duck [20], more complex coastal systems – like an ebb-tidal delta – may pose a problem when viewed over long periods of time, as morphological change needs to be described by process variance as a function of time and location, $Q(t,x,y)$. Tidal deltas are subject to various drivers and mechanisms that move sediment [56, 57]. Their influence and interactions continuously change in both space and time, which makes it difficult to formulate and quantify $Q(t,x,y)$. A spatiotemporally uniform implementation could be the choice of an upper bound $Q = max(morphological\ change)$, however, remains subject for further study.

By reducing both bias and $RMSE$, the change of spectrum (Section 2.5.2) and the Kalman filter (Section 2.5.3) have demonstrated that results can be improved. Stricter constraints on near-surface current magnitudes may also increase the accuracy of depth estimates (Section 2.5.1). Future work might provide insights that could lead to additional improvement of the results since some bias and $RMSE$ remains. Early thoughts on common sources of error are (i) more radar image pre-

processing to enhance radar image quality with increasing distance from the sensor, for example using FFT-accelerated video reconstruction techniques [58] (ii) the application of multiple radars to cover unfavourable wave-angles and (iii) including breaker intensity as a proxy for depth-induced dissipation to improve estimates in breaker zones [43].

2.6. Conclusions

A depth inversion algorithm (DIA), XMFit (**X**-Band **M**ATLAB **Fit**ting), is a radar-based technique to monitor coastal evolution on large space (10s of kilometers) and time (months) scales. We mapped and analyzed two nourishments in the Netherlands using this technique: (1) an $18\,\mathrm{h}$ snapshot of the beach mega nourishment, the Sand Engine, and (2) a one-year time-series of a $5\,\mathrm{Mm}^3$ pilot nourishment in the ebb-tidal delta of the Wadden Sea island Ameland. Derived morphologies in both cases largely agreed with ground truth data. Depth biases were around $-0.9\,\mathrm{m}$ at the Sand Engine and fluctuated between approximately -2–$0\,\mathrm{m}$ at the Ameland ebb-tidal delta. By averaging and debiasing the radar-derived morphologies, it was possible to accurately quantify the growth of the ebb tidal delta nourishment at Ameland during its placement in 2018 with a volumetric margin error of $7\,\%$. Depth errors in the Ameland delta correlated with near-surface current magnitude and direction relative to the direction of wave propagation. The depth errors were generally smaller for small surface current magnitudes and respectively showed under- and overestimation for near-surface currents, in and against the direction of wave propagation. For the Sand Engine, experiments with the spectral treatment and the conceptual employment of a Kalman filter in post-processing improved the depth bias to $0.6\,\mathrm{m}$. Further improving the results and the algorithm remains a scientific and operational challenge.

This research presents the successful operation of a DIA on data from a navigational X-Band radar to monitor a mega nourishment in a complex tidal inlet system, allowing coastal managers to assess volume changes over time.

3

On-the-fly bathymetry with drones & cameras

alles loopt op klompen en dit is een kokosnoot

Kokosnoot, Drs. P

This chapter explores the possibility to map coastal bathymetry on-the-fly with a depth inversion algorithm (DIA) that self-adapts to given video data. The idea is to create a tool that continuously returns mapping updates, while requiring little user-expertise. The DIA is showcased for video from stationary cameras and drones in the USA, UK, Netherlands, and Australia.

Lessons learned:

- *The proposed DIA can be used for on-the-fly analysis of video (feeds) by continuously giving mapping updates of bathymetry, but also of wave celerity and near-surface currents.*
- *The DIA uses the Dynamic Mode Decomposition (DMD) to reduce the data complexity of wavefield video. The DMD automatically finds dominant wave components by their phase images and corresponding frequencies.*
- *The optimal size of local analysis subdomains is determined automatically per wave component. Subdomains become smaller with increasing frequency, creating pyramid-shaped cells.*
- *Estimates of depth, wave celerity and surface currents quickly converge by temporarily storing and calling up spectral information. Additional fast convergence is achieved using Kalman filtering.*
- *Merely* 32 s *of video footage are needed for a first mapping update with average depth errors of* 0.9–2.6 m. *These further reduce to* 0.5–1.4 m *as the videos continue and more mapping updates are returned.*

This chapter has been published in Remote Sensing **13**, 4742 (2021) [34].

3.1. Introduction

Observations of near-shore hydrodynamics and bathymetry are used for various purposes: to study and manage the coast [3, 55, 59], to update early warning systems [60], to monitor swimmer safety [2, 61, 62], for dredging-and-dumping surveillance [4], and military landing operations [25]. An observation of hydrodynamics or bathymetry with areal coverage, a map, is thereby often beneficial if not a prerequisite to recognize relevant spatial details. A straightforward approach to map coastal hydrodynamics and bathymetry is via video-based remote sensing of a wave-field. In comparison to in-situ measurements, video-based remote sensing is less accurate, however, data acquisition is also less labor-intensive and measurements have high spatial coverage by default.

Different instruments and video processing methods are used to map hydrodynamics and bathymetry. In terms of instruments, videos may be recorded with stationary cameras [63], aircrafts [28], UAVs/drones [12, 64–67], (navigational) X-Band radars [26, 27, 30, 51, 68] or satellites [69, 70]. In terms of video-processing methods, various types exist e.g., [21, 26, 27, 29, 43, 71–74]. Most widely used among the coastal remote sensing community are video processing methods that analyse wave dispersion properties. They prove applicable to different instruments [33, 75] and allow to estimate several coastal parameters. Consecutive frames of a wave-field recording are scanned [26, 76] to extract dominant wave frequencies, ω $(\mathrm{rad\,s^{-1}})$, and associated wave lengths and directions via wavenumber vectors, $\boldsymbol{k}$ with $[k_x, k_y]$ $(\mathrm{rad\,m^{-1}})$ [51, 68, 77–79], but also wave celerity vectors, $\boldsymbol{c}$ with $[c_x, c_y]$ $(\mathrm{m\,s^{-1}})$ [80–82], near-surface current vectors, $\boldsymbol{U}$ with $[u, v]$ $(\mathrm{m\,s^{-1}})$ [18, 26, 28, 47] and the apparent depth, d (m) [20, 25, 27, 28, 42, 83]. While ω, $\boldsymbol{k}$ and $\boldsymbol{c}$ are retrieved directly from wave patterns [84, 85] or their corresponding frequency-wavenumber spectra e.g., [80], (Figure 3.1 left), $\boldsymbol{U}$ and d are retrieved indirectly, albeit simultaneously [3, 21, 23, 32, 50], by matching frequency-wavenumber spectra with a theoretical wave model (Figure 3.1 right). This study focusses on mapping $\boldsymbol{c}$, d and $\boldsymbol{U}$. Vector fields of $\boldsymbol{k}$ are directly coupled to vector fields of $\boldsymbol{c}$ via corresponding ω.

The wave model is typically given by the Doppler-shifted linear dispersion relationship, Equation (3.1):

$$\omega_{model}(d, \boldsymbol{U}) = \sqrt{\mathrm{g}|\boldsymbol{k}| \tanh\left(|\boldsymbol{k}|d\right)} + \boldsymbol{U} \cdot \boldsymbol{k}, \tag{3.1}$$

where ω_{model} $(\mathrm{rad\,s^{-1}})$ is the wave model frequency, which is adjusted with unknown parameters d and $\boldsymbol{U}$ until it optimally matches (and therewith explains) observed ω. The gravitational acceleration is given by g $(\mathrm{rad\,s^{-2}})$. Note that $\boldsymbol{U}$ is derived as the depth-averaged velocity of a depth-uniform current profile; however, in natural settings with depth varying current profiles, $\boldsymbol{U}$ represents the weighted average of velocities in the upper layer and is therefore typically referred to as near-surface current vector [26, 47]. Advanced techniques also allow to resolve the underlying current profile [46, 86]. Yet, the advantage of condensing the profile to a bulk vector $\boldsymbol{U}$ is a comparably simple expression for the Doppler shift ($+\boldsymbol{U} \cdot \boldsymbol{k}$ in Equation (3.1)), by which $\boldsymbol{U}$ can be estimated together with d [23, 32]. Moreover,

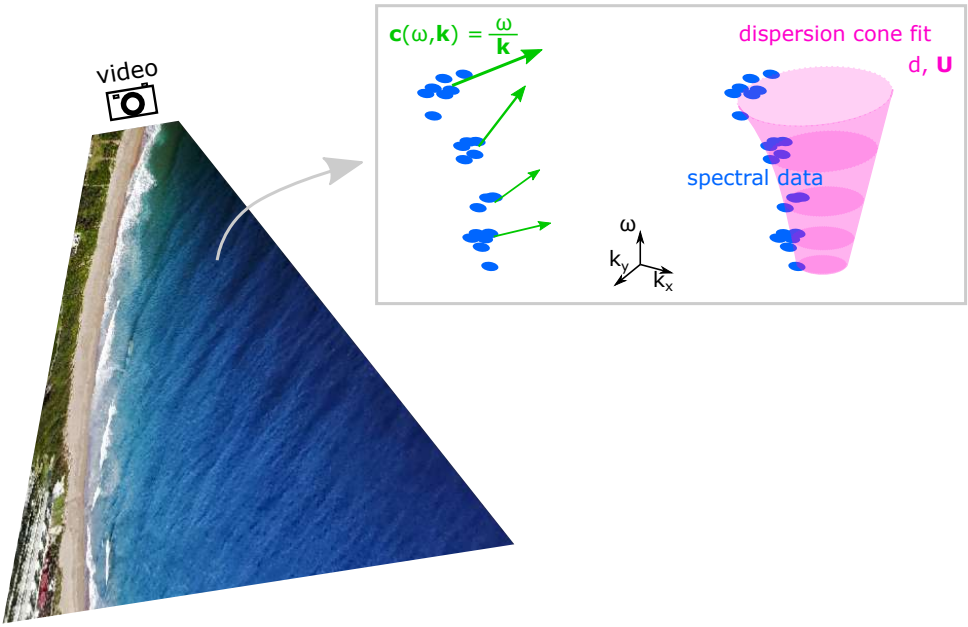

Figure 3.1.: Video of a wave field (**left**) as basis to retrieve wave spectra and coastal parameters ($\boldsymbol{c}$, d, $\boldsymbol{U}$) (**right grey box**). Local gravity wave spectra are given by clouds of frequency-wavenumber (ω,$\boldsymbol{k}$) pairs (blue dots). Local wave celerity vectors $\boldsymbol{c}$ ($\mathrm{m\,s^{-1}}$) (green) are calculated from the frequency ω ($\mathrm{rad\,s^{-1}}$) and wavenumber vector $\boldsymbol{k}$ ($\mathrm{rad\,m^{-1}}$). Fitting the Doppler-shifted linear dispersion relationship as theoretical model (magenta) to the observed spectral data yields local estimates of depth d (m) and near-surface current $\boldsymbol{U}$ ($\mathrm{m\,s^{-1}}$).

near-surface currents can then directly be visualized through maps of vector fields e.g., [18, 52].

Two aspects need to be considered for estimating coastal parameters from video: first, the optimal extraction of wave length and wave frequency characteristics from optical spectra, and second, the optimal estimation of $\boldsymbol{c}$, d, $\boldsymbol{U}$ from the found wave length and -frequency data. Both aspects are successively treated in Section 3.1.1 and Section 3.1.2.

3.1.1. Optimizing wavenumber-frequency extraction from optical spectra

One of the core challenges of wave dispersion-based video processing is to robustly identify the wavenumber-frequency signature of gravity waves ($\boldsymbol{k}^{\uparrow}, \omega^{\uparrow}$, where $\uparrow$ denotes "gravity wave signature"). Different strategies [20, 21, 80, 87] follow different pathways to do this (Figure 3.2). All strategies use grey scale video as basis and inspect local subdomains to capture spatial variation in $\boldsymbol{k}^{\uparrow}$. Searching for an optimal pathway to retrieve $\boldsymbol{k}^{\uparrow}, \omega^{\uparrow}$, the alternatives are briefly presented

(Figure 3.2). Appendix B.1 contains a more detailed review of how successive transformations in different strategies lead to the retrieval of $\boldsymbol{k}^{\uparrow}, \omega^{\uparrow}$ (Figure 3.2, arrows) and summarizes some benefits and drawbacks in (Table B.1).

Local cut-outs from the video form cubes in space time (x,y,t; in short $\mathbf{x}$,t) and can directly be used as analysis subdomains. Decomposing a cube reveals the wave constituents of different frequency, either directly in wavenumber-frequency space (in $\boldsymbol{k}, \omega$) [80] (Figure 3.2, left pathway) or via their complex-valued phase images (in $\boldsymbol{x}, \omega$) [21] (Figure 3.2, center pathway). Separation from the spectral noise floor finally yields $\boldsymbol{k}^{\uparrow}, \omega^{\uparrow}$ (Figure 3.2 bottom). Associated to one frequency component, a phase image is referred to as one-component phase image [21] and shows the distinct wave pattern at a certain wave frequency. The suggested benefit of using one-component phase images is better localization of $\boldsymbol{k}^{\uparrow}$. Instead of deriving Local One-Component Phase Images (LOCPI) from video cut-outs (Figure 3.2, center pathway), also Global One-Component Phase Images (GOCPI) of the full video domain can be derived [87] (Figure 3.2, right pathway). These GOCPI are then further analysed in local subdomains. Independent of using LOCPI [21], GOCPI [87] or both [20], the final phase structure should be spatially coherent to get $\boldsymbol{k}^{\uparrow}$.

Benefits of GOCPI are that they can be generated taking global spatial coherence into account [87], while additionally the dimensionality of the video data can be reduced [87]. Reducing dimensionality is an important asset as it offers a reduction of required computational working memory and thereby an increase in computational speed. For this purpose a singular value decomposition (svd)(Appendix B.1, Equation (B.1)) can be employed, which is a dimensionality reduction technique that is controlled by the variance in the video. The svd splits the video into modes, consisting of spatial and temporal structures. The first $r \sim O(1) - O(10)$ modes typically describe most of the video's variance (see σ_j in Appendix B.1, Equation (B.1)) and thereby capture its essence. The remaining modes confine noise and can be discarded, which reduces the data load. Simarro *et al.* [87] directly use the spatial structures from svd as GOCPI. However, a spatial structure from svd may contain mixed wave patterns of different frequencies (see [88], Fig. 6) such that its corresponding temporal structure is not a pure oscillation. Hence, using spatial structures from svd as GOCPI is suboptimal.

Aiming to map coastal parameters on-the-fly, $\boldsymbol{k}^{\uparrow}, \omega^{\uparrow}$ must be retrieved at minimal computational cost. A strategy similar to Simarro *et al.* [87] is therefore desirable, but with pre-knowledge of oscillating spatial structures when generating GOCPI. This is what the Dynamic Mode Decomposition (DMD) aims to do (Appendix B.1, Table B.1).

The DMD is a mathematical procedure designed to reduce the dimensionality of video data by identifying dominant oscillating spatial structures. Different variants of DMD have been developed e.g., [88–94], employed in various fields of science amongst which electrical engineering [95, 96], system and control applications [91], neuroscience [97], but also physical oceanography [92] and coastal engineering [98].

Here, the spatial structures from DMD represent phase images of waves with

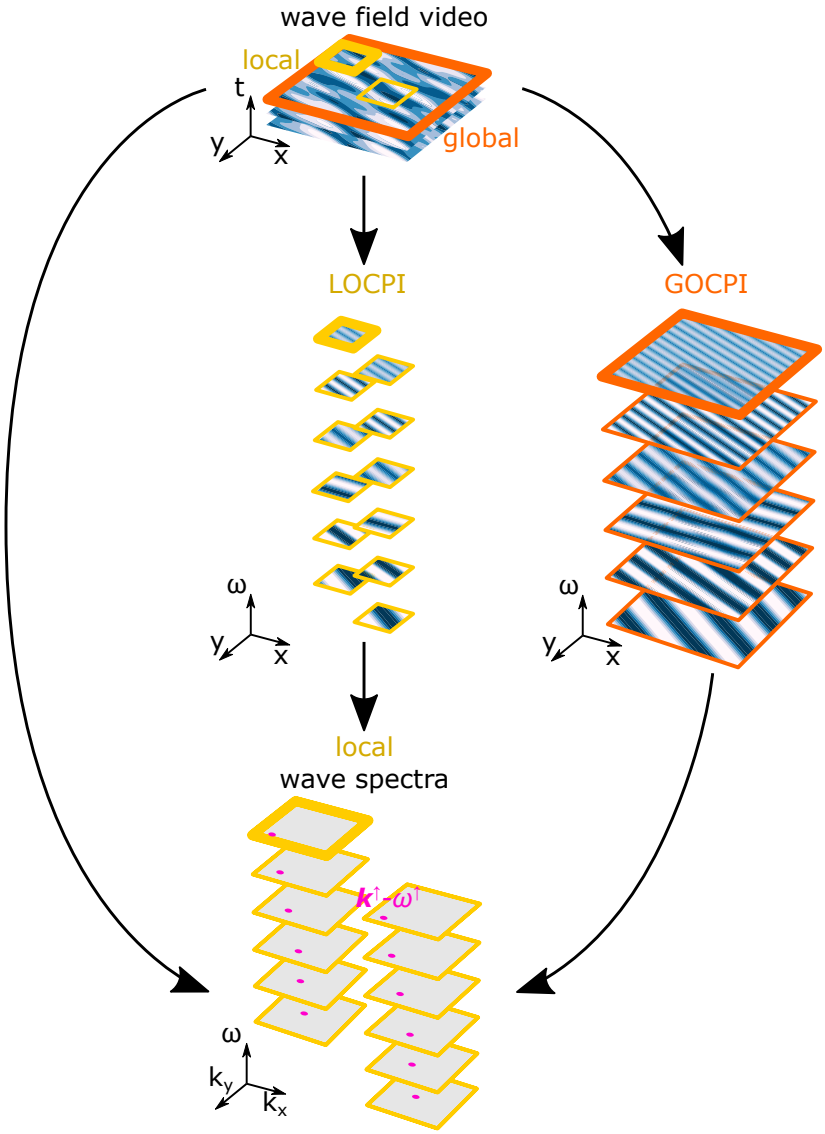

Figure 3.2.: Pathways to identify wavenumber-frequency signatures of gravity waves $(\boldsymbol{k}^{\uparrow}, \omega^{\uparrow})$ (bottom panel, purple dots) in video of a wave field (top panel). The video can be transformed directly from space-time (x,y,t) into the spectral domain (k_x,k_y,ω) (left pathway), or via construction of one-component phase images (x,y,ω), which may be local (LOCPI) (middle pathway) or global (GOCPI)(right pathway). In left and middle pathway all analyses are local (yellow). In the right pathway, the initial construction of GOCPI is global (orange) and then followed by local subdomain analysis to capture spatial variation in $\boldsymbol{k}^{\uparrow}, \omega^{\uparrow}$.

different periods. The DMDs' foundation lies in the assumption that snapshots in a video (sequence of frames) are related to each other through a linear dynamic system of oscillatory components. This means that the benefits of Simarro *et al.* [87], offering GOCPI and the possibility for dimensionality reduction can be complemented with a guarantee that GOCPI oscillate in time. What is more, the oscillation frequencies are inherently found.

To summarize, the DMD can be used to reduce video data to a set of GOCPI (Figure 3.2, right pathway), but with guaranteed oscillatory time behaviour. These GOCPI are the basis to find local $\boldsymbol{k}^{\uparrow}, \omega^{\uparrow}$ signatures (Figure 3.2 left, purple dots): while (global) $\omega^{\uparrow}$ are known from the DMD, $\boldsymbol{k}^{\uparrow}$ still need to be locally deduced. This can be done in various ways, such as via characteristic spatial phase differences in sub-domains [20, 21, 87], or alternatively via (computationally cheap) spatial 2D-FFTs or Particle Image Velocimetry (PIV) [70, 99]. Derived local $\boldsymbol{k}^{\uparrow}, \omega^{\uparrow}$ form the basis to retrieve maps of wave celerity per GOCPI frequency, via $\boldsymbol{c}(\omega^{\uparrow}) = \omega^{\uparrow}/\boldsymbol{k}^{\uparrow}$ [100], but also maps of depths and near surface currents d, $\boldsymbol{U}$ through Equation (3.1).

3.1.2. Optimizing depth and near-surface current estimates

Pursuing the best approximations to d and $\boldsymbol{U}$, optimization problems using Equation (3.1) (with/without Doppler shift $+\boldsymbol{U}\cdot\boldsymbol{k}$) have been stated differently. Some as (non-linear) least-squares (LS) minimization problems [20, 21, 26] and others as maximization problems of a normalized scalar product (NSP) [30, 32]. These schemes have been formulated to handle an abundance of spectral information from Fourier decompositions. However, applying dimensionality reduction techniques to video data concentrates spectral information to its essence offering much less data points for an optimization of d, $\boldsymbol{U}$. As such, inaccuracies and outliers in the spectral data gain negative influence on the solution. Standard LS minimization is not fit to handle this issue and with little data to fit, NSP maximization using a Heaviside step function is a crude approach. Outlier contamination is a common issue in applications such as the training of neural networks [101], because reducing the relatively large residual of an outlier is more attractive in minimizing the cost function than reducing the small residual of an inlier. In standard LS optimization, residuals are squared, whereby the impact of outliers on the solution is disproportionately large. However, LS problem statements have the benefit that many different methods have been developed to solve them [102], among which the Levenberg-Marquardt method is often applied to invert d, $\boldsymbol{U}$ e.g., [3, 20]. It is therefore attractive to adapt LS formulations such that they can handle outliers. This is achieved using various kinds of loss functions [103], among which the Cauchy (also called Lorentzian) loss function is an effective type.

Higher accuracy in d, $\boldsymbol{U}$ can also be achieved by successively producing estimates and converging the results with a Kalman filter [20, 43, 45]. The quality of an estimate is thereby typically judged based on the sensitivity of the fit to the data. If the data are plagued by inaccuracies and outliers, this sensitivity increases, making the Kalman filter a suitable tool to mitigate their influence.

To summarize, while loss-functions can increase the quality of an individual d, $\boldsymbol{U}$ estimate, the application of a Kalman filter increases the quality over several d, $\boldsymbol{U}$ estimates. Both techniques can be used simultaneously.

3.1.3. Outlook

This study is about a self-adaptive, robust method to map $\boldsymbol{c}$, d and $\boldsymbol{U}$ on-the-fly from video of a wave-field. The DMD plays a key role in making the video-processing algorithm self-adaptive to the data and computationally fast: it reduces (video) data complexity, finds the dominant wave-components and allows self-adaptive sampling schemes, which cause the standardly used computational cubes to instead become pyramids for optimal localization. For the optimization of d, $\boldsymbol{U}$ the algorithm implements a loss-function to handle spectral outliers, which seemingly counteracts the error of overestimating $\boldsymbol{U}$ and also reduces depth errors. Two errors commonly interlinked [3, 23, 45, 50]. The algorithm temporarily stores spectral data and employs Kalman filtering for quick convergence of measurements, and comprises a set of rules and filters for autonomous decision making such that the algorithm does not need to be tuned to the field site. In summary, the algorithms main elements include:

- Data reduction and retrieval of wave components through DMD
- Wave component dependent subdomains using pyramid cells
- Counteracting spectral outliers and errors in d,$\boldsymbol{U}$ with loss functions
- Fast convergence of d,$\boldsymbol{U}$ and recognition of current refraction through temporary spectral data storage
- Additional fast convergence of d,$\boldsymbol{U}$ using Kalman filtering

Section 3.2 describes the workflow of the proposed video processing algorithm, which includes explanations of the core principles of the DMD, and the workflow of the algorithm. Section 3.3 describes the field sites and data. In Section 3.4 the algorithm is validated for measuring near-shore bathymetry (i.e., d) based on four field sites in the USA, UK, Netherlands and Australia. A qualitative discussion on the algorithms ability to measure hydrodynamics (i.e., $\boldsymbol{c}$, $\boldsymbol{U}$) follows in Section 3.5, together with a discussion on the algorithms potential for mapping on-the-fly. Findings are concluded in Section 3.6.

3.2. Method

Ahead of presenting the mapping algorithm in Section 3.2.2, first the implemented Dynamic Mode Decomposition (DMD) is explained and demonstrated in Section 3.2.1.

3.2.1. Dynamic Mode Decomposition

The DMD forces oscillatory time dynamics through a set of discrete linear differential equations whose solution consists of complex eigenvalues and eigenvectors. The eigenvalues represent the temporal oscillations, which may include a real part denoting growth or decay. The corresponding eigenvectors are the, so called, Dynamic Modes and represent spatial structures, which after entry-wise normalization to unity represent Global One-Component Phase Images (GOCPI).

Suppose a linear model $\boldsymbol{A}$ can advance a (squeezed) frame $\boldsymbol{x}_n$ at time t_n to the next frame at time t_{n+1}: $\boldsymbol{x}_{n+1} = \boldsymbol{A}\boldsymbol{x}_n$. Extending the model to advance a (time) series of N frames simultaneously, $\boldsymbol{Y} = \boldsymbol{A}\boldsymbol{X}$, where matrices $\boldsymbol{X} = [\boldsymbol{x}_1, \boldsymbol{x}_2, ..., \boldsymbol{x}_{N-1}]$ and $\boldsymbol{Y} = [\boldsymbol{x}_2, \boldsymbol{x}_3, ..., \boldsymbol{x}_N]$ pair each frame $\boldsymbol{x}_{n+1}$ with the previous frame $\boldsymbol{x}_n$. It essentially requires $\boldsymbol{A}$ to propagate a frame through time since $[\boldsymbol{x}_1, \boldsymbol{x}_2, \boldsymbol{x}_3 ...] = [\boldsymbol{x}_1, \boldsymbol{A}\boldsymbol{x}_1, \boldsymbol{A}^2\boldsymbol{x}_1 ...]$, which in mathematical terms is referred to as a Krylov sequence. It indicates that $\boldsymbol{Y} = \boldsymbol{A}\boldsymbol{X}$ is a discrete formulation that is closely tied to a system of continuous differential equations $d\boldsymbol{x}/dt = \boldsymbol{A}\boldsymbol{x}(t)$ and therewith an eigenvalue problem $\lambda\boldsymbol{\varphi}e^{\lambda t} = \boldsymbol{A}\boldsymbol{\varphi}e^{\lambda t}$. Conceptually, $\boldsymbol{A}$ hence describes a dynamical process, whose eigenvectors $\boldsymbol{\varphi}$ present the Dynamic Modes, with the associated frequencies captured in the complex eigenvalues λ. Note that in contrast to the modes retrieved from a svd (Section 3.1.1, [87]), Dynamic Modes do not have to be orthogonal to each other, which implies that they do not have to be fully independent of each other.

The goal of the DMD is to find the eigenvalues and eigenvectors of $\boldsymbol{A}$ at minimal computational cost. Finding the eigenvalues and eigenvectors straightforward by first calculating $\boldsymbol{A} \approx \boldsymbol{Y}\boldsymbol{X}^{\dagger}$ ($\dagger \equiv$ pseudo inverse) poses a problem for computer memory: Say video footage has a frame size of $1000 \times 1000\,\mathrm{px}$, then $\boldsymbol{X}$ and $\boldsymbol{Y}$ have a row size $m = 10^6$ resulting in an $\boldsymbol{A}$ matrix of size $m \times m = 10^6 \times 10^6$. Even in case a computer can handle such data loads, the calculation is slow and the matrix size suggests a large amount of redundancy. The conceptual idea is to convert the eigenvalue problem from m into a lower dimension r. Typically, r is in the range $1 - 100$ such that $r \ll m$, expressing a severe dimensionality reduction. By deflating the eigenvalue problem $m \to r$, eigenvectors and eigenvalues can be quickly calculated. Subsequently, the eigenvectors are inflated again $r \to m$ to yield the Dynamic Modes. Although the details of the conversions differ between DMD algorithms (e.g., standard DMD vs. optimized DMD, respectively [104] and [94]), they share the common principle of using r modes from the svd of $\boldsymbol{X}$ (Appendix B.1, Equation (B.1)) for dimensionality reduction. There exists no general strategy to make a choice for r. It may be based on existing knowledge about the observed system [94], but it can also be based on the amount of singular values needed to capture a certain percentage of the variance in the video, for example $99\,\%$ [88], or on an algorithmic truncation of noise [105].

Note that $\boldsymbol{X}$ (and $\boldsymbol{Y}$) may first be converted to a time-analytic signal [87]. It is not necessary, but has the benefit that the DMD, similar to an FFT, does not produce conjugate Dynamic Mode pairs. Then r frequency components associate to r modes instead of $2r$ modes. Preventing the generation of conjugate modes also prevents the DMD to produce them imperfectly (i.e., with slightly different frequency to their counterpart). Analytic extension comes at computational cost; however, since r

can be halved to achieve the same number of frequency components, successive matrix multiplications within the DMD become computationally cheaper.

An important factor when applying a DMD is whether the recorded data contain standing wave behaviour. Without adjustments a DMD cannot capture standing waves [89]. For a fixed framerate Tu *et al.* [89] offer a straightforward solution through augmentation of the video matrix $\boldsymbol{X}$ with a time-shifted version of itself, by which the DMD acquires the skill to detect standing waves.

From the existing DMD algorithms, the "Optimized DMD based on Variable Projections" [94] is an elaborate variant. Formulated as a least-squares optimization problem, it is more accurate than other DMD algorithms and theoretically allows video frames to be spaced non-equidistantly in time. Instead of splitting the video into two video matrices $\boldsymbol{X}$ and $\boldsymbol{Y}$, it uses a single, transposed video matrix $\boldsymbol{X}^T = [\boldsymbol{x}_1, ...\boldsymbol{x}_N]^T$. A detailed explanation can be found in Appendix B.2. The methods skill for complex harmonic analysis was recently demonstrated in modelling rotating detonation waves [107]. Note that other DMD algorithms could be potent alternatives, for example by allowing elaborate forms of regularization to handle noisy or lower quality images [108].

Wave components in a wave field can be accurately extracted using the DMD [88]. To illustrate this, a wave field consisting of 6 known wave components is considered, recorded over a period of $32\,\mathrm{s}$ at $2\,\mathrm{fps}$. The corresponding video matrix hence comprises 64 frames ($\boldsymbol{X}^T$ has 64 rows, see Appendix B.2, Equation (B.2)). Subsequently, the signal is made time-analytic such that r modes associate to r frequency components. The DMD with $r = 6$ modes, identifies the underlying components precisely (Figure 3.3a, orange stars)(Figure 3.3b). It demonstrates that the DMD is not only powerful in analyzing a short frame sequence, but therein superior compared to a standard timedomain Fast Fourier Transform (FFT) (Figure 3.3a, green squares): the FFT returns (much) more spectral data and with significant redundancy and yet, the pre-set frequency resolution restricts its ability to capture the six intrinsic wave components to a mere rough spectral representation. Half of the components (Figure 3.3a, first, third and fifth component) are poorly captured in frequency and amplitude.

For a real wave field, the amount of wave components is not known a-priori and a choice needs to be made for the amount of modes r returned by the DMD. The question arises what the DMD returns if the choice for r is smaller or larger than the actual number of components in the wave field: if r is smaller, the DMD simply returns fewer components, but those components are still correctly represented (Figure 3.3c, $r = 3$). If r is larger, the DMD still identifies the intrinsic components; however, it also adds spurious modes and these modes may be energetic, which indicates that r being too large is a scenario that should be avoided (Figure 3.3c, $r = 12$). For observations of a real wave-field this scenario is unlikely, as waves have a stochastic nature and typically dense spectra [100]. In fact, for $r \sim O(1) - O(10)$ the number of modes is certainly less than the actual number of wave components (cf. Figure 3.3c, $r = 3$) and the DMDs representation of the wave field simplifies to the governing wave components.

A real wave field may also experience standing wave dynamics as waves reflect

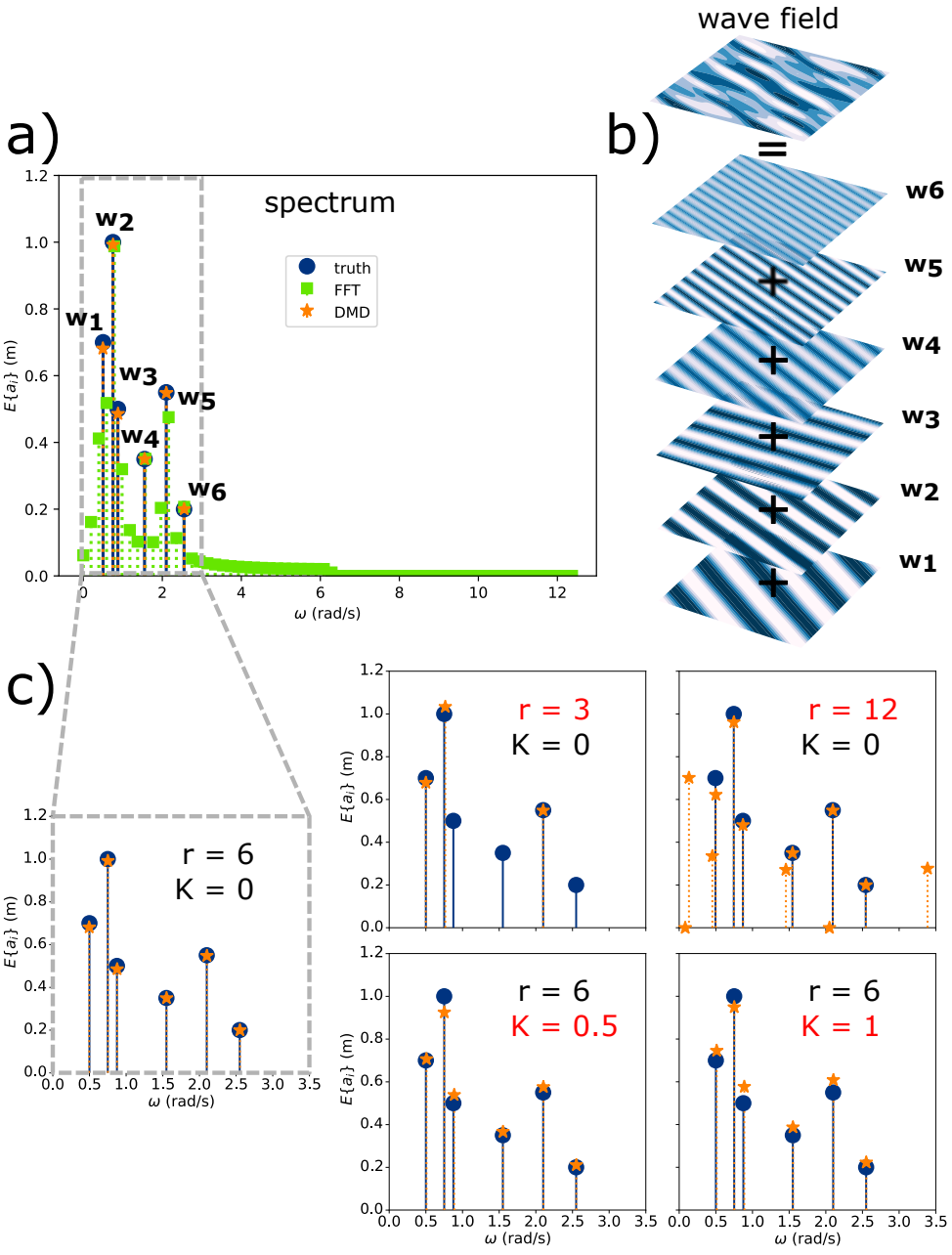

(Caption on next page.)

Figure 3.3.: Dynamic Mode Decomposition (DMD) of an artificial wave field with six wave components (w_1–w_6), recorded over a period of $32\,\mathrm{s}$ at $2\,\mathrm{fps}$, resulting in 64 video frames. (**a**) True amplitude spectrum of the wave field (blue dots), compared against spectra acquired from DMD with $r = 6$ modes (orange stars) and FFT (green squares); $E\{a_i\}\,(\mathrm{m})$ denotes the expected amplitude of the i^{th} wave component and $\omega\ (\mathrm{rad\,s^{-1}})$ the angular frequency. (**b**) Real part of the complex valued Dynamic Modes acquired from DMD, resembling the true wave components. (**c**) The DMD from (a), with $r = 6$ and a progressive wave field with no wave reflection (reflection coefficient $K = 0$) is used as reference (dashed grey outline) in a comparison with DMDs of the same progressive wave field, but where the number of modes is halved ($r = 3$, red) or doubled ($r = 12$, red). If $r > 6$, spurious modes appear. The reference case is also compared against DMDs with the same number of modes ($r = 6$), but of wave fields with mixed progressive standing waves ($K = 0.5$, red) or fully standing waves ($K = 1$, red). To acquire the same expected amplitudes as in the reference case, wave components for the two cases where $K > 0$ are rescaled in amplitude, accounting for their nodal structures in space (see also [106], eq. 11).

back from the shoreline. Although at flat dissipative beaches, sea-swell waves are typically progressive [109], at steeper beaches and longer sea-swell periods, incident wave reflection can be significant with reflection coefficients up to $K = 0.4 - 0.45$ [110–113]. In the presence of hard structures like sea-walls even up to $K \approx 0.9$ [114]. Here, $K = [0, 1]$ denotes [no, full] reflection [106]. High wave reflection signals (partially) standing wave characteristics, prompting adaption of the DMD as of [89]. Doing so enables the DMD to cope with any degree of incident wave reflection (Figure 3.3c, $K = 0$, $K = 0.5$, $K = 1$) and thereby accommodates application to a broad range of wave field scenarios.

3.2.2. Mapping algorithm

The proposed workflow for a self-adaptive and on-the-fly mapping algorithm of coastal hydrodynamics and bathymetry, follows a series of steps (Figure 3.4, labels ①...⑬). The workflow requires video in grey-scale and orthorectified format as basis input. If the video is in color, standard BGR to grey conversions can be used to prepare the video. The orthorectification differs per field site and is briefly treated in Section 3.3. The workflow is set-up in such a way that a video feed could be processed. For that purpose, the algorithm marches forward in time by consecutively analysing short sequences of N video frames (e.g., $N = 64$) and then updating the maps of $\boldsymbol{c}$, d and $\boldsymbol{U}$ after each sequence, which is referred to as mapping updates. Consecutive frame sequences may overlap, as for on-the-fly application is explained in Section 3.5 (see also [115], Fig. 3). Default settings for the algorithm as used in this study are listed in Table B.2 (Appendix B.3).

The workflow commences with the global analysis of a video frame sequence. The first step is to retrieve r Global One-Component Phase Images (GOCPI) through

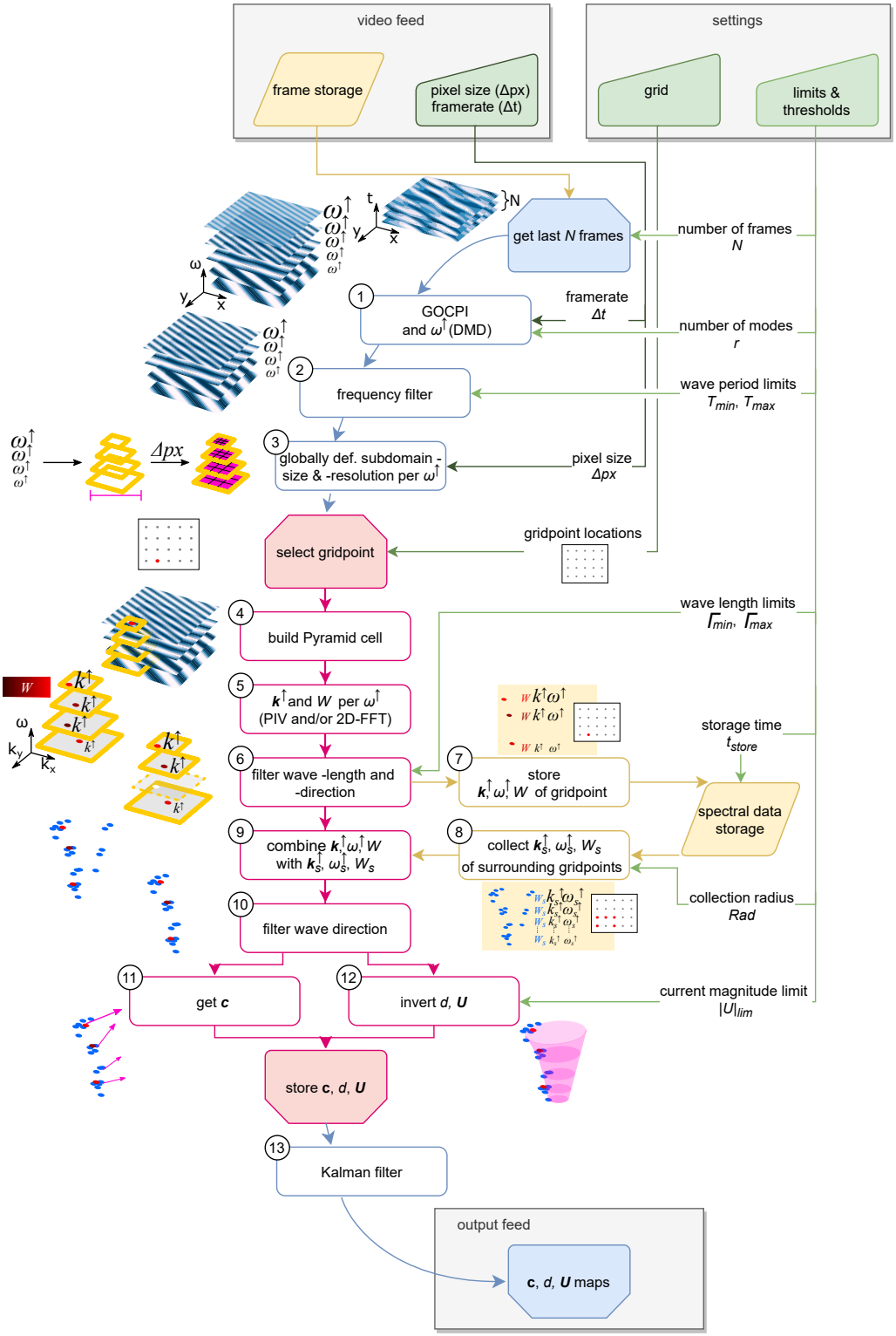

(Caption on next page.)

Figure 3.4.: Workflow for mapping coastal hydrodynamics and bathymetry on-the-fly from video of a wave field. Steps in the flowchart are visualized with icons. Box shapes denote: data (parallelogram), input (right trapezoid), process loop start (trimmed top corners) and process loop end (trimmed bottom corners), and process (rectangle). Box- and arrow colours relate to: storage (gold), input (green), for-loop (blue), parallel-for-loop (magenta). Arrows and their annotations signify flow of information. The input requires video with top-down view, its pixel resolution and framerate. Computational grid and other settings suffice with default values. The output contains maps of wave directions and -celerity, depth, and near-surface currents (grey square bottom row). Symbols represent: $GOCPI$ = Global One-Component Phase Images, $\omega^{\uparrow}$ $(\mathrm{rad\,s^{-1}})$ = wave frequency per $GOCPI$, $\boldsymbol{k}^{\uparrow}$ $(\mathrm{rad\,m^{-1}})$ = wavenumber vector at gridpoint, W (-) = weight per $\boldsymbol{k}^{\uparrow},\omega^{\uparrow}$ pair, $\boldsymbol{c}$ $(\mathrm{m\,s^{-1}})$ = wave celerity vector at gridpoint, d (m) = depth at gridpoint, $\boldsymbol{U}$ $(\mathrm{m\,s^{-1}})$ = near-surface current vector at gridpoint, subscript s = from spectral data storage. Other symbols are labelled with arrow annotations.

DMD (Figure 3.4, ①). GOCPI linked to frequencies outside the ocean wave band (Appendix B.3, Table B.2, $[T_{min}, T_{max}]$), are discarded (Figure 3.4, ②). (Note that in case the video is not extended to a time-analytic signal, also conjugate modes are discarded, see Section 3.2.1). By construction of the DMD, the remaining number p of GOCPI with frequencies $\omega_1^{\uparrow}...\omega_p^{\uparrow}$ describe dominant wave components. These are treated equally important (regardless of their spectral weight b see Appendix B.2).

Knowing $\omega^{\uparrow}$, the maximum wavelengths in each GOCPI are predictable. The size of the subdomains that are used to determine local $\boldsymbol{k}^{\uparrow}$, can thereby be automatically tailored to the individual GOCPI (Figure 3.4, ③). This is done ahead of analysing any location. A conservative rule is to set the subdomain size to one or two offshore wave lengths, $L_{off}(\omega^{\uparrow}) = 2\mathrm{g}\pi/(\omega^{\uparrow})^2$, where g denotes the gravitational acceleration. Here, $2 \times L_{off}(\omega^{\uparrow})$ is used, unless this is too large, for example near a boundary, where the size is reduced up to a minimum of $1 \times L_{off}(\omega^{\uparrow})$. High frequency GOCPI are analysed with smaller subdomains than low frequency GOCPI, such that stacking the subdomains in layers creates a pyramid-shaped cell at a certain location (see Figure 3.4, ③, yellow pyramid). Note that this contrasts with the usual cube-shape, whose size is typically predefined manually e.g., [44, 47].

Since the pixel resolution is constant between cell layers, large layers used for lower frequencies likely encompass plentiful pixels, capturing the underlying waves in unnecessarily high spatial resolution. It is therefore computationally attractive to subsample larger cell layers. The rules for subsampling require a minimum resolution of 8 samples per L_{off}. Instead of skipping pixels for subsampling, the current set-up lowers the resolution through fast bilinear interpolation. It preserves more image information and makes the algorithm robust to videos with different pixel resolutions. For proper analysis a cell layer is set to hold at least 24×24 samples. Note that demanding 8 samples per offshore wave length, may exclude higher frequency GOCPI from being analysed, if the pixel resolution of the video is not high

enough to capture the correspondingly short wave-lengths.

After subdomain sizes and -resolutions have been determined, the *local* analysis of the GOCPI commences. The local analysis occurs around points in a grid. The processing of different grid point locations can be done in parallel, which increases computational speed. Since the algorithm aims to map results on-the-fly, the grid resolution is determined based on computational speed (see also Section 3.5.2). Note that computation speeds are different for different processing machines. A solution to find an optimal number of gridpoints for different processing machines could be to start with a low number of gridpoints and then increase the number of gridpoints for consecutive frame sequences until an optimum is reached.

To analyse a certain grid point, first a pyramid-shaped cell is built around it (Figure 3.4, ④) using GOCPI subdomains as cell layers with formats as determined under step ③. Each cell layer is first autocorrelated in space to accentuate the waveform, and tapered with a two-dimensional Hanning-window, which focusses wave information to the centre point and prepares for analysis with two-dimensional Fast Fourier Transforms (2D-FFTs). For robustness, $\boldsymbol{k}^{\uparrow}$ (Figure 3.4, ⑤) is estimated in two different ways: directly, by analysing spatial properties through 2D-FFT and indirectly, by analysing wave celerity through Particle Image Velocimetry (PIV).

Performing a 2D-FFT on a cell layer yields its spectral content in space. Besides the footprint of a gravity wave component, $\boldsymbol{k}^{\uparrow}$, this also includes spectral noise. Typically, an energy threshold aims to separate the two [47]. To avoid a search for an optimal energy threshold (see Chapter 2,[3]), here simply the spectral point with maximum energy is chosen as $\boldsymbol{k}^{\uparrow}$. Alternatively $\boldsymbol{k}^{\uparrow}$ can be acquired via the wave celerity, $\boldsymbol{k}^{\uparrow} = \omega^{\uparrow}/\boldsymbol{c}^{\uparrow}$. The wave celerity is encoded in the complex values of the cell layer: The difference between the real and imaginary parts denotes a temporal phase shift of $90°$, resembling a quarter wave period. Performing PIV between the real and imaginary image of the cell layer yields the translation of (wave) patterns over a quarter wave period, which directly translates to $\boldsymbol{c}^{\uparrow}$. Note that the temporal phase shift is $90°$ regardless of whether the video matrix $\boldsymbol{X}$ is analytic or whether dealing with standing waves. While the 2D-FFT approach inherently presumes that the observed pattern in a cell layer describes a wave, the PIV approach does not, as it investigates movement of any pattern in the cell layer. Both approaches may have their benefits in case the pattern is noisy and are therefore used synchronically. If one or both estimates are unphysical, they are discarded in following filter steps. Each estimate of $\boldsymbol{k}^{\uparrow}$ gets a weight W assigned, whose value between $[0,\ 1]$ gives an indication of the respectively [low, high] quality of the estimate (Figure 3.4, ⑤ red colourbar). A weight, W, is calculated from the correspondence between two images: the source image and the target image. For the 2D-FFT approach this is the correspondence between the original pattern displayed by the cell-layer and the approximation of this pattern by its most energetic spectral wave component. For PIV it is the correspondence between the translated real image of the cell-layer with the imaginary image of the cell-layer. The correspondence is calculated via $W = 1 - \varepsilon_{im}$, where ε_{im} represents the normalized root-mean-square error between the source image relative to the target image [116].

Together, the estimates of $\boldsymbol{k}^{\uparrow}$ over all $\omega^{\uparrow}$ layers in the pyramid cell, form a sparse

spectral point cloud (SSPC) of $\boldsymbol{k}^{\uparrow}, \omega^{\uparrow}$ pairs with assigned weights W. The SSPC expects to follow a cone-shape as described by the dispersion relationship (Figure 3.1; Equation (3.1)). This pre-knowledge aids in the identification and removal of unphysical $\boldsymbol{k}^{\uparrow}, \omega^{\uparrow}$ points in the SSPC by means of a wavelength and -direction filter (Figure 3.4, (6)). Wave lengths are filtered using their ratio over the offshore wave length $\Gamma = |\boldsymbol{k}_{off}|/|\boldsymbol{k}^{\uparrow}|$, where $|\boldsymbol{k}_{off}| = 2\pi/L_{off}(\omega^{\uparrow})$. SSPC points with $\Gamma < 0.3$, occupy the shallow water regime as they resemble wavelengths larger than twenty times the local depth [117] and are thereby too large to capture morphological detail. Such $\boldsymbol{k}^{\uparrow}$ are deemed unsuited for a localized depth estimate, d. On the other hand, SSPC points with $\Gamma > 1.0$ signalize unphysically short waves if $\boldsymbol{U}$ is small, and are therefore also deemed unsuited. Note that in other algorithms this short period limit is often set lower, to $\Gamma > 0.9$, which presents an approximate elbow value where the uncertainty in estimates of d becomes disproportionately large [82, 87, 118]; however, a higher limit $\Gamma > 1.0$ preserves spectral points that are valuable for the estimation of $\boldsymbol{U}$ and thereby also simultaneous estimates of d. Lastly, the wave direction filter excludes SSPC points which do not align with the general direction by means of the svd filter of Gawehn *et al.* [3] (see Chapter 2 and section 2.2).

The idea behind the next two steps of the workflow (Figure 3.4, (7), (8)) is to augment the SSPC left after (6) with additional spectral points to make it a dense spectral point cloud (DSPC), which captures directional spread in time and space and thereby allows for a solid inversion of d, $\boldsymbol{U}$. As desired and designed, the SSPC as is, holds the essence of the local hydrodynamics. The sparsity, however, brings along statistical uncertainty in time and space. An approach to acquire a DSPC, is to combine several SSPCs into one. The additional SSPCs can be retrieved from preceding updates (i.e., previously analysed frame sequences), but also from surrounding grid locations within a collection radius Rad (Figure 3.4, (8) attached green arrow; Appendix B.3, Table B.2). Such an approach requires memorizing SSPCs in a designated short-term storage. Therein, the just retrieved SSPC is stored (Figure 3.4, (7)) and SSPCs from preceding updates and from surrounding grid locations are called up (Figure 3.4, (8)). The size of the short-term storage for SSPCs is manageable, since by construction, each SSPC holds just a few essential spectral points. Note that accumulating spectral information over successive updates is only a valid approach if their computations occur (near) on-the-fly, because it assumes that the wave signal is stationary across several updates. Hence, SSPC data are discarded after a short stationary time period (e.g., $60\,\mathrm{s}$, see Appendix B.3, Table B.2) and replaced by new SSPCs.

An example illustrates the augmentation of an SSPC to a DSPC by means of stored spectral data: assuming a wave signal is stationary for $1\,\mathrm{min}$, the algorithm stores SSPCs for $1\,\mathrm{min}$. If the processing of a frame sequence takes $15\,\mathrm{s}$, the storage contains *stored* SSPCs of all grid locations from the preceding $60\,\mathrm{s}/15\,\mathrm{s} = 4$ updates. Now, as the algorithm starts to analyse a certain location it retrieves one *new* SSPC for that location. By itself this new SSPC might be sufficient to estimate d, but not $\boldsymbol{U}$. For that, a DSPC is required, which is achieved by augmenting the new SSPC with stored SSPCs from the same grid location and surrounding grid

locations (Figure 3.4, ⑨), be it 10 within some radius Rad. The acquired DSPC then consists of $4_{\text{stored}} \times (1_{\text{gridloc}} + 10_{\text{surr.gridlocs}}) + 1_{\text{new}} \times 1_{\text{gridloc}} = 45$ SSPCs. In this example, the augmentation of the new SSPC of step ⑥ has hence produced a DSCP which is 45 times denser.

Using surrounding grid locations to augment spectral information has benefits and drawbacks. A drawback is that depth estimates d become less localized. A benefit is that wave refraction caused by near surface currents $\boldsymbol{U}$ is captured in space, which is essential for estimating $\boldsymbol{U}$ (and thereby also improves d). To minimize the loss in localization of d, but still have improved $\boldsymbol{U}$ estimates, the SSPCs that make up the DSPC are weighted differently. These SSPC weights are multiplied with the individual quality weights W of the spectral points and subsequently normalized to the range $[0, 1]$. In the current set up, the new SSPC at a certain grid location weighs $50\,\%$. Stored SSPCs of the same grid location weigh together $25\,\%$ and stored SSPCs from surrounding grid locations weigh together $25\,\%$. Hence, $75\,\%$ of the spectral information focusses on the currently analysed grid location and $25\,\%$ focusses on the surrounding area. Thereby aiming to keep d estimates localized, but still construct a DSPC that includes enough current refraction for $\boldsymbol{U}$ estimates.

The DSPC from step ⑨ may include a minority of spectral points from incorrect wave directions. This occurs because some of the SSPCs, which the DSPC consists of, contain too little spectral information to determine wave directions at step ⑥. Therefore, the direction filter repeats for the DSPC (Figure 3.4, ⑩). Now, the DSPC is ready for the algorithm to retrieve wave celerities per frequency, $\boldsymbol{c}^{\uparrow}(\omega^{\uparrow})$ (Figure 3.4, ⑪) and depths and surface currents d, $\boldsymbol{U}$ (Figure 3.4, ⑫). While $\boldsymbol{c}^{\uparrow}$ are directly computed via $\boldsymbol{c}^{\uparrow} = \omega^{\uparrow}/\boldsymbol{k}^{\uparrow}$, the inversion of d, $\boldsymbol{U}$ is done by fitting a wave model, here the Doppler shifted dispersion relationship (Equation (3.1)), to the spectral points of the DSPC. The fit results from of a nonlinear regression that aims to minimize the sum of residuals between the model frequencies $\omega_{j,model}$ (Equation (3.1)) and the observed frequencies $\omega_j^{\uparrow}$ per spectral point j using Equation (3.2). The implicit link of observed $\boldsymbol{k}_j^{\uparrow}$ with $\omega_{j,model}$ and $\omega_j^{\uparrow}$ is assumed trivial.

$$\text{minimize } \mathrm{F}(d,\boldsymbol{U}) = \frac{1}{2}\sum_j W_j \rho\left(f_j(d,\boldsymbol{U})^2\right) \tag{3.2}$$

$$\text{subject to}$$

$$\mathrm{d}_{\min} < d < \mathrm{d}_{\max}$$

$$|\boldsymbol{U}| < |\mathrm{U}|_{\max}$$

$$\text{with}$$

$$\rho\left(f_j(d,\boldsymbol{U})^2\right) = \alpha^2 \ln\left(1 + \frac{f_j(d,\boldsymbol{U})^2}{\alpha^2}\right)$$

$$\text{and}$$

$$f_j(d,\boldsymbol{U}) = \omega_{j,model}(d,\boldsymbol{U}) - \omega_j^{\uparrow},$$

where $\mathrm{F}(d, \boldsymbol{U})$ is the cost function, minimized by adjusting the regression parameters d and $\boldsymbol{U}$. Typically, residuals per spectral point j, are evaluated by the product of their weight W_j with the difference $f_j(..)$ between $\omega_{j,model}$ and $\omega_j^{\uparrow}$. Here, $f_j(..)$ is first modulated by a Cauchy loss function $\rho(..)$ to penalize outliers. A predefined softmargin α tunes $\rho(..)$ to the optimization problem. Setting α such that the Cauchy loss function heavily penalizes residuals larger than $\sim 1/5^{\mathrm{th}}$ of the average DMD frequency resolution produces accurate d, while counteracting overfitting of $\boldsymbol{U}$. Lastly, bounds for depth $[\mathrm{d_{min}}, \mathrm{d_{max}}]$ and surface current magnitude $|\mathrm{U}|_{\mathrm{max}}$ set the range in which a solution for d,$\boldsymbol{U}$ is sought. To improve estimates, first a regression is done without Doppler shift to acquire a close estimate for d that can be used as initializer for the follow up regression including Doppler shift. Adding the first regression has little impact on computation times, since its estimate of d closely approximates the local minimum of the second regression. The minimization of Equation (3.2) occurs using a sequential least squares quadratic programming method (SLSQP) [119], which omits potentially expensive computations of Hessians and allows for straightforward implementation of loss-functions.

The final step of the mapping algorithm is a Kalman filter (Figure 3.4, (13)) that judges the quality of d,$\boldsymbol{U}$ results based on the sensitivity of the fit with regard to earlier updates. It causes d,$\boldsymbol{U}$ estimates to quickly converge over successive updates. The implementation of the Kalman filter is identical to Gawehn *et al.* [3] (Chapter 2 and section 2.5.3). If the observation periods are short, say less than $5\,\mathrm{min}$, morphodynamics but also hydrodynamics can be assumed stationary, such that process variance is negligible. If observation periods are longer, say 10–$20\,\mathrm{min}$, it may become important to capture changes in surface current direction (e.g., due to the formation of a rip current). To allow for such applications, the Kalman filter assumes small process variances $\mathrm{Q_c}$ and $\mathrm{Q_U}$ for respectively phase celerities and near-surface currents (i.e., $\mathrm{Q_c} = 0.0005\,\mathrm{m^2\,s^{-3}}$, $\mathrm{Q_U} = 0.0005\,\mathrm{m^2\,s^{-3}}$, see Appendix B.3, Table B.2).

3.3. Field sites and data

Videos of four different field sites around the world are used to test the algorithms performance (Figure 3.5): Duck (North Carolina, USA) [20], Porthtowan (UK) [120], Scheveningen (NL) [121] and Narrabeen (AU) [122]. Specifics on video collections are listed in Table 3.1. Cameras are positioned at heights of 43–$110\,\mathrm{m}$ to observe waves over a large distance without wave-shadowing effects. The recorded videos are available in orthorectified format. The geometries have been solved using ground control points (GCPs), by matching GCP image coordinates with world coordinates. The accuracy of the geometries differs per site and is quantified by the GCP reprojection error in world coordinates. These reprojection errors are generally in the (sub)meter range, but in case of Scheveningen and Narrabeen they increase to on average $\sim 7\,\mathrm{m}$ at distances of 0.5–$2.0\,\mathrm{km}$ from the camera. At Porthtowan, the reprojection errors are unknown, yet slight errors in the geometry likely exist, particularly further afield [123]. Videos from Duck and Porthtowan (UK) are $\approx 17\,\mathrm{min}$ long and recorded with Argus stations. The videos of Scheveningen and

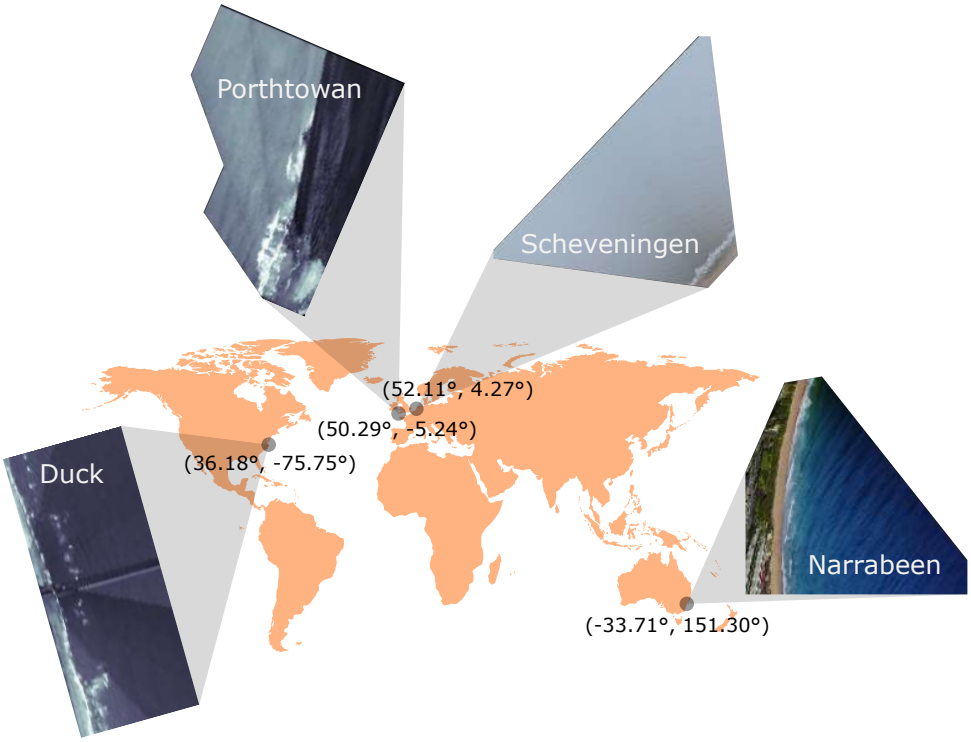

Figure 3.5.: World locations (Lat°, Lon°) of video recordings from Duck (North Carolina, USA), Porthtowan (UK), Scheveningen (NL) and Narrabeen (AU). Videos are recorded with different instruments with different camera properties and therefore have different lighting, format, and orientation.

Narrabeen are $\approx 9\,\mathrm{min}$ long and recorded with UAVs. All videos have a framerate of $\Delta t = 2\,\mathrm{fps}$. Pixel resolutions are $\Delta px = 5\,\mathrm{m}$ for Duck and Porthtowan, and $\Delta px = 2\,\mathrm{m}$ at Scheveningen and Narrabeen. The hydrodynamic conditions vary over the sites between $H_s = 0.80\text{–}1.63\,\mathrm{m}$ and $T_p = 5.0\text{–}10.0\,\mathrm{s}$ (Table 3.2).

Videos of all sites are analysed using sequences of 64 frames equalling $32\,\mathrm{s}$. Marching forward in time, the next frame sequence overlaps $50\,\%$ with the previous sequence (i.e., overlap of 32 frames at $2\,\mathrm{fps}$), resulting in mapping updates every $16\,\mathrm{s}$ of video. This overlap is fixed for reproducibility, since computation times differ per processing machine. For on-the-fly applications, the overlap varies based on processing speed. This is simulated in Section 3.5 using a standard laptop. Each image sequence is decomposed into $\mathrm{r} = 16$ Dynamic Modes. The chosen r represents a balance between significantly reducing dimensionality, while retrieving enough pyramid cell layers to estimate d, $\boldsymbol{U}$. Details on other settings are found in Appendix B.3, Table B.2.

In the next Section 3.4, the results of the mapping algorithm are presented. The

Table 3.1.: Video collection.

Field site	Instr.	Cam. height (m)	Cam. tilt (°)	Video length (min)	Frame rate (fps)	Pixel size (m)	Reprojection error (at dist.)
Duck	Argus	43	$68-82$	17	2	5	$<1\,\mathrm{m}(<500\,\mathrm{m})$
Porthtowan	Argus	44	$75-85$	17	2	5	-
Scheveningen	UAV	110	61	9	2	2	$\sim 1\,\mathrm{m}(<200\,\mathrm{m})$ $\sim 7\,\mathrm{m}(400-600\,\mathrm{m})$
Narrabeen	UAV	89	73	9	2	2	$<1\,\mathrm{m}(<250\,\mathrm{m})$ $\sim 7\,\mathrm{m}(1.5-2\,\mathrm{km})$

Table 3.2.: Hydrodynamic conditions during field-recordings.

Field site	H_s(m)	T_p(s)	WL(m)
Duck	0.79	5.0	0.08
Porthtowan	1.03	10.0	−0.96
Scheveningen	0.75	5.5	0.60
Narrabeen	1.63	8.5	0.67

field-site of Duck, North Carolina, USA, is used as lead case to elucidate the processing steps of the workflow for an arbitrary real case. Final results are presented for all field-sites, Duck (North Carolina, USA), Narrabeen (Australia), Scheveningen (Netherlands), Porthtowan (UK). The quality of the final results for the depth estimates, d, is assessed by comparison with in-situ bathymetry data. Maps for wave direction and -celerity, and near-surface currents are discussed in Section 3.5.

3.4. Results

The site of Duck gives an illustrative example (Figure 3.6) of the processing steps described in Section 3.2.2. After decomposing image sequences of Duck (Figure 3.6a) into 16 Dynamic Modes, the modes are normalized to Global One-Component Phase Images (GOCPI) and filtered for frequency and resolution (as of Figure 3.4). The frequency filter discards 8 GOCPI and another 4 GOCPI fail the criterion of minimum $8\,\mathrm{px}/L_{off}$, leaving 4 GOCPI for further analysis (Figure 3.6b). These remaining GOCPI reveal intricate wave patterns and finely capture wave refraction towards the coast. The associated frequencies $\omega^{\uparrow}(\mathrm{rad\,s^{-1}}) \approx \{0.59, 0.78, 0.97, 1.17\}$ are quite constant across successive image sequences, showing that wave periods $T(\mathrm{s}) = \{10.6, 8.1, 6.5, 5.4\}$ govern the mixed wave field. On the basis of these wave components, the subdomain sizes for local analysis are determined. Stacking them in layers for some grid location, reveals a pyramid-shaped cell and tapering the layers puts focus toward its centre grid point (Figure 3.6c).

Performing PIV and 2D-FFTs to the autocorrelated layers, reveals a sparse spec-

tral point cloud (SSPC) with 8 points, with $\boldsymbol{k}^{\uparrow}$ values increasing for increasing $\omega^{\uparrow}$, sketching a typical wave dispersion curve (Figure 3.6d). In the example, the PIV and 2D-FFT estimates for $\boldsymbol{k}^{\uparrow}$ are almost indistinguishably close in three of the four spectral layers; however, for the upper most layer, they lay further apart. In this case, the point that lays off track corresponds to the 2D-FFT estimate. This is signalled by its quality weight W, which is lower than for the PIV counterpart (Figure 3.6d, blue vs. yellow point). Augmenting the SSPC with stored SSPCs from the past minute (i.e., from 4 previous updates) within a radius of $Rad = 75\,\mathrm{m}$, yields the dense spectral point cloud (DSPC) (Figure 3.6e). The choice of $Rad = 75\,\mathrm{m}$ is arbitrary and represents a balance between extracting information from close by, while capturing sufficient current refraction (especially of shorter period waves). Other choices for Rad may be made, but the algorithm is not too sensitive to this parameter since the surrounding SSPCs within Rad resemble just $25\,\%$ of the total spectral weight. As desired, this lower weighting is apparent from the corresponding spectral points in the DSPC (Figure 3.6e, blue points). Note that in contrast to Duck, points in DSPCs of Porthtowan, Scheveningen and Narrabeen are more dispersed over the frequency domain, because GOCPI frequencies vary more across successive updates (not shown). Finally, the DSPC is fitted with the Doppler-shifted linear dispersion relationship (Equation (3.1)) to produce characteristic cones corresponding to certain d,$\boldsymbol{U}$ estimates (Figure 3.6f, magenta cone). Combining the local estimates from all grid locations yields global maps of d,$\boldsymbol{U}$.

These resulting maps are not only quickly retrieved, but also show that estimates of d are accurate (Figure 3.7). For all four field sites, depth maps compare with ground truth. Recall that the algorithm is not tuned to the individual field sites. While the first depth update – after $32\,\mathrm{s}$ of video – is still rough, it already gives a clear overall picture of the bathymetry with shallower and deeper regions (Figure 3.7, 1^{st} update). Nearshore sandbars at Duck (Figure 3.7a) are readily visible. With the fifth update – after $96\,\mathrm{s}$ of video – (Figure 3.7, 5^{th} update) the depth maps approximate ground truth (cf. Figure 3.7, 5^{th} update and *ground truth*). Estimates quickly improve after the first update, indicating that the temporary spectral storage together with Kalman filtering effectively converge d estimates. Mapping updates continue to improve and become spatially more coherent towards the end of the videos (Figure 3.7, $last$ update).

For all videos, differences with ground truth are minimal over large parts of the observed area (Figure 3.7, *difference*, light areas). Regions with errors $|\Delta d| > 0.5\,\mathrm{m}$ are mostly found in shallow water or the deep water boundary of the observed domain. At Duck and Scheveningen depth overestimation of $\Delta d \approx -0.5$ to $-1.0\,\mathrm{m}$ occurs around the sandbars (Figure 3.7a,c, *difference*, blue areas), while in other shallow parts the errors are smaller. At Porthtowan and Narrabeen the overestimations are larger $\Delta d \approx -0.5$ to $-2.0\,\mathrm{m}$ and generally occur in shallow water (Figure 3.7b,d, difference, blue areas). The reason is probably that wave heights at Porthtowan and Narrabeen are larger $H_s = 1.0$–$1.6\,\mathrm{m}$ (Table 3.2) and more nonlinear close to shore, compared to Duck and Scheveningen where $H_s < 0.8\,\mathrm{m}$ and wave breaking restricts to the sandbars after which most wave nonlinearity is lost.

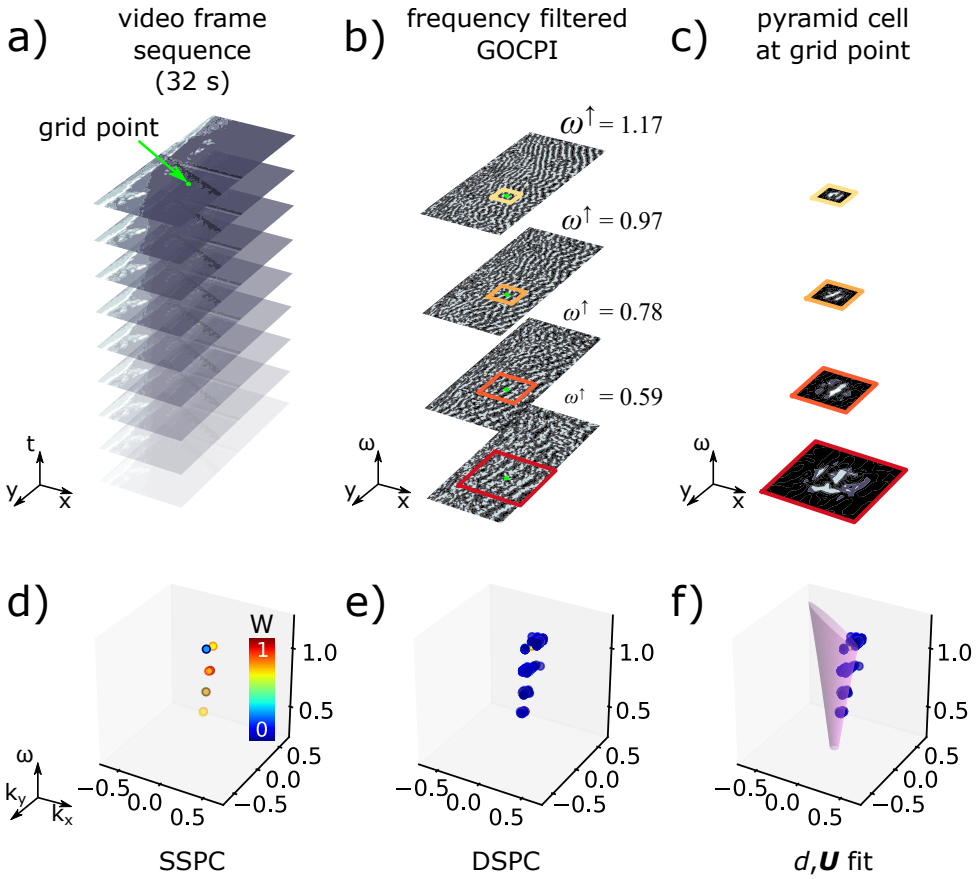

Figure 3.6.: Processing results for a selected grid location at the Duck field site at the 7^{th} update. (**a**) Image sequences (x,y,t space, see Figure 3.2 top) used for successive updates depict $32\,\text{s}$ of wave movement and have $50\,\%$ frame overlap in time. (**b**) Frequency filtered Global One-Component Phase Images (GOCPI) from Dynamic Mode Decomposition (DMD) (x,y,ω space, see Figure 3.2 right pathway) uncovering frequencies $\omega^{\uparrow} = \{0.59, 0.78, 0.97, 1.17\}$ as essential components in the wave field recording. GOCPI outside the gravity wave frequency band are discarded as well as higher frequency GOCPI where $5\,\text{m}$ pixel resolution is insufficient to guarantee at least 8 points per offshore wave length (cf. Figure 3.4, ② and ③). (**c**) The pyramid cell at the grid location, with subdomain layers subsampled for computational speed and tapered with Hanning windows to focus wave information. A colour gradient from red to yellow highlights decreasing subdomain size for increasing frequency. (**d**) Sparse spectral point cloud (SSPC) (k_x,k_y,ω space, see also Figure 3.2 bottom), consisting of pairs of $\boldsymbol{k}^{\uparrow}$ estimates from FFT and PIV per frequency layer $\omega^{\uparrow}$. Colours indicate the weight of each estimate (colour scale)(cf. Figure 3.4, ⑥). (**e**) The SSPC augmented to a dense spectral point cloud (DSPC) using stored spectral data of the grid location and surrounding grid locations within a radius of $75\,\text{m}$ (cf. Figure 3.4, ⑩). Blue colours elucidate the lower weighting of stored spectral data. (**f**) The d,$\boldsymbol{U}$ fit on the DSPC (magenta cone) using Equation (3.1) and Equation (3.2) (cf. Figure 3.4, ⑫).

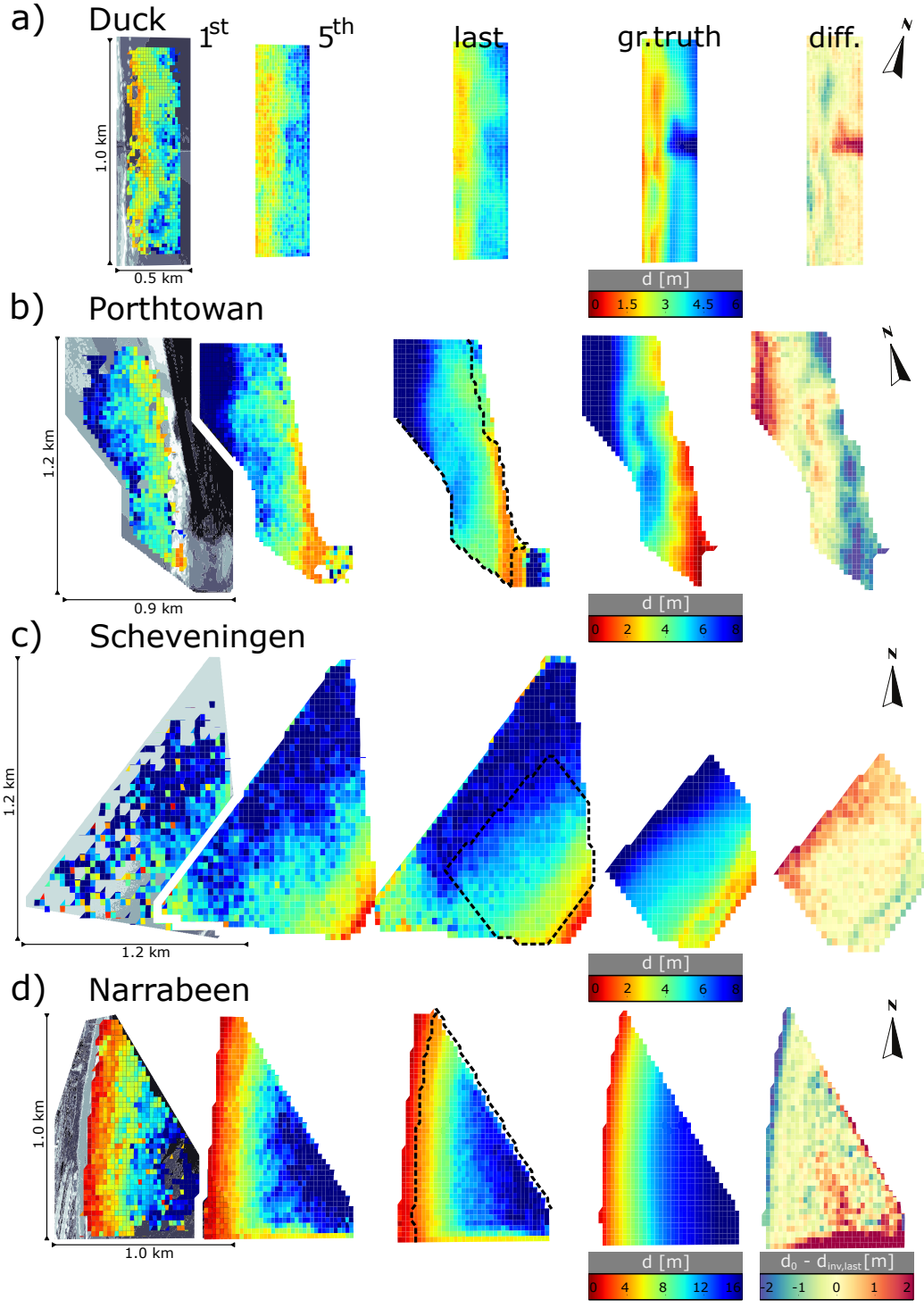

(Caption on next page.)

Figure 3.7.: Depth updates from video of the field sites (**a**) Duck, (**b**) Porthtowan, (**c**) Scheveningen, (**d**) Narrabeen. In (**a,b,c,d**): left most panel depicts an example frame (grey scale) of the video with corresponding dimensions; inverted depths (d_{inv}) of the 1^{st} update are overlaid. Following two panels to the right present inverted depths of the 5^{th} and last update. Ground truth measurements ($gr.\,truth$, d_0) are mapped in the second panel from the right (d_{inv} and d_0 in identical colour scale); the extents are indicated by dashed black lines in panels of last update. Differences between ground truth and last update ($diff.$, $d_0 - d_{inv,last}$) are depicted in right most panel, with red/blue indicating under/overestimation (colour scale).

Another, physical reason for near-shore depth estimates appearing larger is local wave set-up [72], which is not accounted for in the comparison with ground truth. Regions and reasons for depth underestimation differ per site. At Duck, depths are only underestimated around the pier, which blocks the view to the underlying waves (Figure 3.7a, red patch). At Porthtowan and Scheveningen depths are underestimated by $\Delta d \approx 0.5$–$1.5\,\mathrm{m}$ near the offshore boundary (Figure 3.7b,c, red patches). At Porthtowan (Figure 3.7b), the underestimation is mainly caused by the fact that relevant lower frequency cell layers in near-boundary pyramid cells are too large to be used. The underestimated region also lies $>800\,\mathrm{m}$ from the camera, where inaccuracies in geometry influence depth estimates [123]. The size of errors in the video geometries (Table 3.1) suggests a limited effect on depth estimates in general, yet some depth error may be induced in regions further afield (e.g., for $T = 8\,\mathrm{s}$ and $d = 10\,\mathrm{m}$, an error $\Delta L = 7\,\mathrm{m}$ in wave length causes a depth error of $\Delta d \approx 2\,\mathrm{m}$, see also Fig.1 of [82]). At Scheveningen (Figure 3.7b), the underestimated region begins further away from the offshore boundary, where boundary effects should be less pronounced. Here, the underestimation likely stems from the relatively small waves, $H_s = 0.75\,\mathrm{m}$ and $T_p = 5.5\,\mathrm{s}$, who feel little of the underlying bottom. At Narrabeen, underestimation mainly occurs at the boundary farthest from the camera. This underestimation is likely caused by similar boundary effects as at Porthtowan, since also here the underestimated region lies more than $900\,\mathrm{m}$ from the camera. In conclusion, depth maps can show regions that are less accurate, yet all in all, the maps approximate local bathymetries: on average $\sim 80\,\%$ of the mapped area has errors $\Delta d < 1\,\mathrm{m}$.

Direct comparison of estimated depths against ground truth confirms generally accurate depth maps (Figure 3.8). Median depth estimates per given depth are mostly close to ground truth (cf. Figure 3.8, double green curves and black $1:1$ line). For the video of Duck (Figure 3.8a) the similarity is visible for the entire depth range from $d = 1.5$–$5.0\,\mathrm{m}$, except for the scour hole where the pier obscures the underlying waves. At Porthtowan, median depth estimates deviate more from ground truth but remain $\Delta d < 2.0\,\mathrm{m}$ for depths $d < 10\,\mathrm{m}$ (Figure 3.8b). Errors are largest in the breaking region where depths are $d = 2$–$3\,\mathrm{m}$, which is a common observation in depth inversion studies e.g., [48]. This is similar for Narrabeen (Figure 3.8d). Here, however, differences between median depth estimates and ground truth are min-

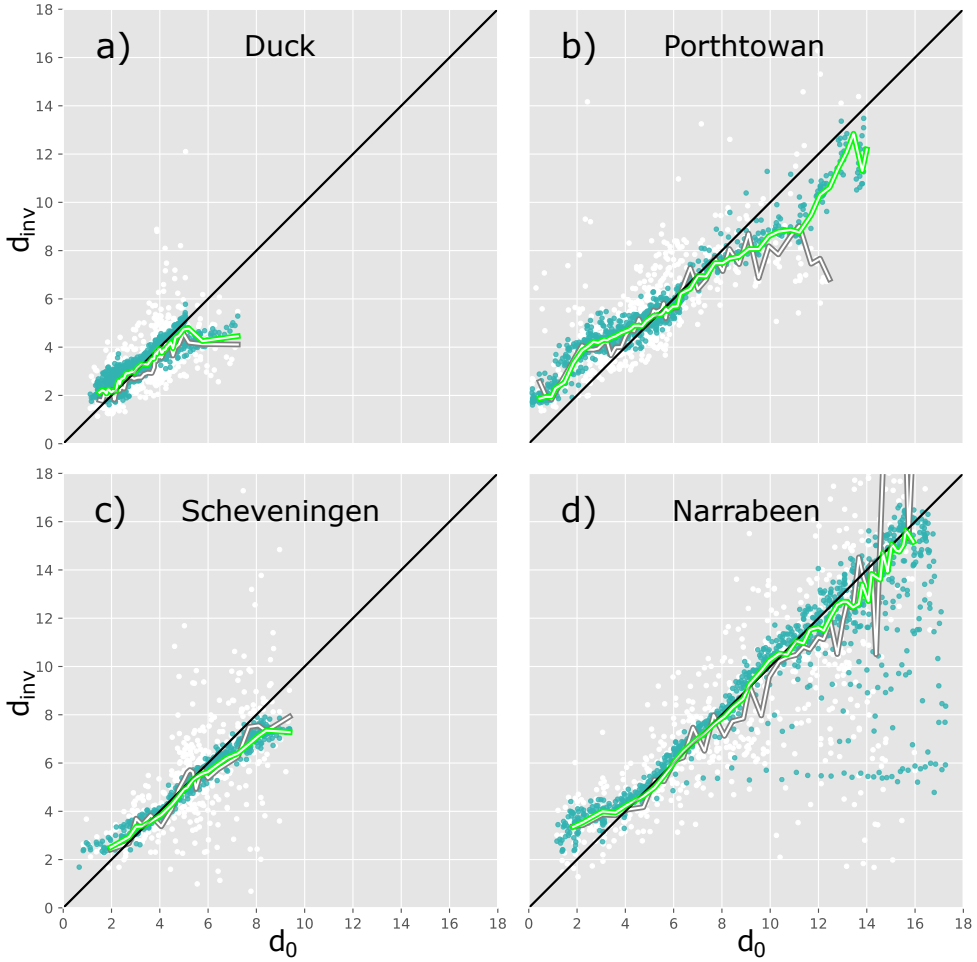

Figure 3.8.: Direct comparison between inverted depths (d_{inv}) and ground truth depths (d_0) for field sites (**a**) Duck, (**b**) Porthtowan, (**c**) Scheveningen, (**d**) Narrabeen. Coloured dots correspond to the last update whose median is shown with a double green line. Analogously, underlying white dots correspond to the first update whose median is shown with a double grey line. Potential water level differences within the observed domains, due to for example near-shore wave set-up, are not accounted for in the comparisons.

imal for the entire depth range beyond that, $d = 3–17\,\mathrm{m}$. In contrast to Porthtowan ($H_s = 1.0\,\mathrm{m}$), the wave heights at Narrabeen are larger ($H_s = 1.6\,\mathrm{m}$), moreover, the few large boundary errors in the statistics are outnumbered by otherwise accurate estimates (Figure 3.8d, relatively few outliers). Median depth estimates at Scheveningen (Figure 3.8c) also confirm earlier spatial observations of slight depth overestimation near the shallow sandbar and underestimation for $d > 7\,\mathrm{m}$.

Although for each field site, the first mapping update after $32\,\mathrm{s}$ of video is considerably more scattered compared to the last update (cf. Figure 3.8, white and blue scattered dots), the median estimate is comparable (cf. Figure 3.8, double grey and double green curves). Hence, the first mapping updates already give a rudimentary impression of the bathymetry, albeit with more local uncertainty. It suggests that waiting for many mapping updates is superfluous and that it may be efficient to stop after a couple of updates, when a certain degree of accuracy in the depth map is reached.

Bulk errors decrease with increasing number of mapping updates (Figure 3.9). Since depth errors are not always constant and linearly distributed over depth (Figure 3.9b) and may contain outliers (Figure 3.9d), the median bias is adopted to quantify structural over- or underestimation, and the interquartile range ($IQR = 75^{\mathrm{th}} - 25^{\mathrm{th}}$ percentile) to measure the scatter. In comparison to other common error measures, note that Duck, with quite linear and normally distributed depth errors (see Figure 3.9a), has a median bias that is almost identical to the commonly used mean bias and its IQR is close to the root mean square error (not shown). Absolute median biases (Figure 3.9, dashed lines) start small $|\Delta d_{bias}| < 0.5\,\mathrm{m}$ with the first update and eventually become $|\Delta d_{bias}| < 0.1\,\mathrm{m}$ at Duck (with update 3), Scheveningen (with update 27) and Narrabeen (with update 10). The median bias at Porthtowan reaches $\Delta d_{bias} \approx -0.25\,\mathrm{m}$. The IQRs (Figure 3.9, solid lines) decrease fast over the first couple of updates, signalling fast improvements in the accuracy of the depth map. After that, the convergence rates start to relax. The total IQR improvements are $0.9\,\mathrm{m} \rightarrow 0.5\,\mathrm{m}$ (Duck), $1.7\,\mathrm{m} \rightarrow 1.4\,\mathrm{m}$ (Porthtowan), $1.6\,\mathrm{m} \rightarrow 0.6\,\mathrm{m}$ (Scheveningen), $2.6\,\mathrm{m} \rightarrow 1.1\,\mathrm{m}$ (Narrabeen). The elbow in the exponentially decreasing curves represents a compromise between size of error and number of updates. It is difficult to pinpoint the exact locations of the elbows, but for Duck and Porthtowan, they appear to be somewhere between the 2^{nd}–6^{th} update, while for Scheveningen and Narrabeen they are more likely located between the 5^{th}–10^{th} update. The reason for the different elbow positions probably roots in the instrumentation: Videos of Duck and Porthtowan are recorded with stationary Argus stations, while the videos of Scheveningen and Narrabeen are recorded with UAVs. In contrast to the Argus stations, UAVs have some freedom to move and are not professionally tuned to the field site, which likely causes depth errors to be initially large; however, these errors decrease rapidly. Concluding the previous findings, a general rule of thumb might be to stop with the 5^{th} update, after $1.5\,\mathrm{min}$ of video. Awaiting more updates may further improve results, but also requires more computation time and larger video length. A single estimate based on $32\,\mathrm{s}$ of video, is enough to get a rough depth map. In the end, the use of the data and therefore required accuracy determine whether to stop the analysis

sooner or later.

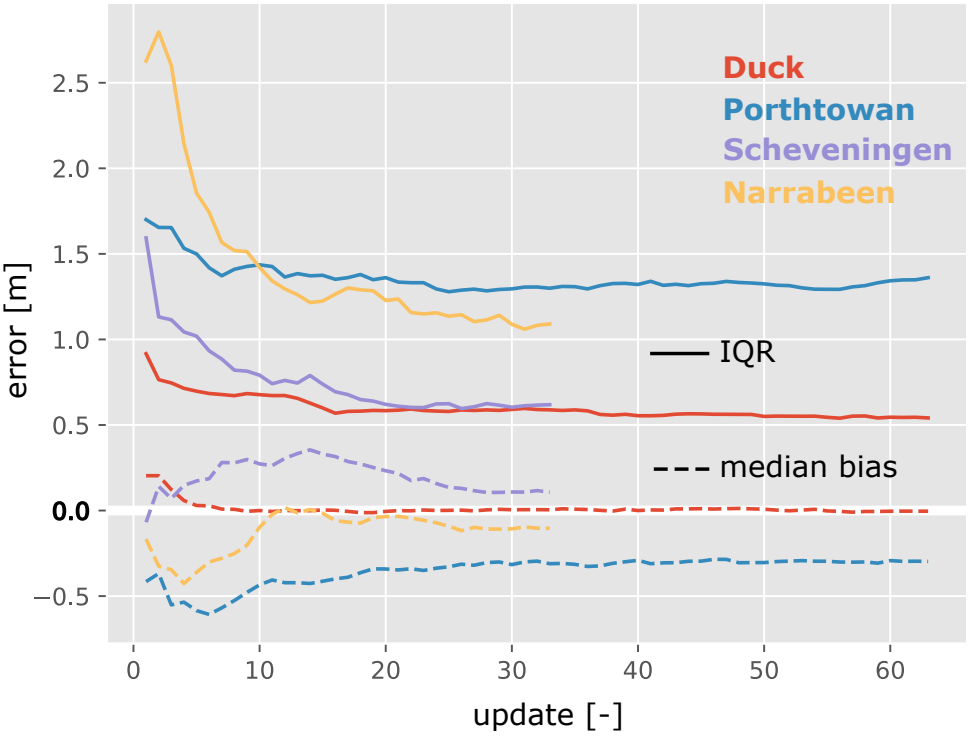

Figure 3.9.: Depth errors at successive updates for field sites Duck (red), Porthtowan (blue), Scheveningen (purple), Narrabeen (orange). Dashed lines present median bias. Solid lines present confidence intervals by the inter quartile range ($IQR = 75^{\text{th}} - 25^{\text{th}}$ percentile).

3.5. Discussion

Alongside the maps of depth, also mapping updates for hydrodynamics, wave celerity, $\boldsymbol{c}$, and local near-surface currents, $\boldsymbol{U}$, are retrieved. Since no ground truth data are available for these parameters, they are discussed qualitatively in Section 3.5.1. The subsequent Section 3.5.2 discusses the algorithms ability to process video on-the-fly.

3.5.1. Maps of $\boldsymbol{c}$ and $\boldsymbol{U}$

While vector fields of $\boldsymbol{c}$ remain quite stable after the first mapping update, vector fields of $\boldsymbol{U}$ require more updates to converge. Here, approximately the 10^{th} update (Figure 3.10) shows convergence of the local current patterns. Also, the current velocities and directions appear realistic. Note that local changes in $\boldsymbol{c}$ and

$\boldsymbol{U}$ still occur after the 10^{th} update, as allowed by the process variance in the Kalman filter (not shown).

Maps of $\boldsymbol{c}$ reflect the general direction of wave propagation for all videos (Figure 3.10, left column). Local vectors are oriented normally to the recorded wave crests and trace characteristic wave refraction towards the coastline. Mean wave directions per wave period are quite similar for all field sites, except for Duck which shows some directional spread between shorter and longer period waves (Figure 3.10a left, red vs. yellow arrows). Wave celerity decreases towards shallower water being most apparent for Porthtowan and Narrabeen. This is expected as cross shore differences in depth are the largest at these locations (Figure 3.10b,d, left). Moreover, the wave celerity of long period waves starts to decrease further offshore than for short period waves (Figure 3.10d left, starting at offshore boundary, green arrows already get shorter while red arrows have constant length until close to shoreline). This is also expected since longer waves feel relatively smaller depths.

Maps of $\boldsymbol{U}$ show intricate patterns that are largely consistent in time and space (Figure 3.10 right). Coastal currents are typically tide or wave driven [117] and have magnitudes of decimetres per second ($\mathrm{dm\,s^{-1}}$) e.g., [124]. They can reach meters per second (e.g., strong rip currents [125] such as the "Backpackers' Express" at Bondi Beach [126]), but such conditions are not likely at the field sites analysed in this study. With mostly $0\text{–}5\,\mathrm{dm\,s^{-1}}$, the maps of $\boldsymbol{U}$ have the correct order of magnitude. At Duck, near-surface currents close to shore often point in offshore directions, while further from shore they also point in southerly directions (Figure 3.10a right). The near-shore offshore-directed flows probably represent the effect of undertow caused by normally incident waves (see Figure 3.10a left). It is interesting to note, that surface current estimates using optical flow on wave averaged images might predict opposite flow directions in shallow water, namely shoreward directed currents, as recent data analyses for a similar wave situation at Duck suggest [127]. The hypothesis is that current estimates from optical flow are more indicative of Stokes Drift, while wave-inverted current estimates capture the undertow. Especially around the thinner part of the sandbar in the south (see also Figure 3.7a, *ground truth*), streamlines from northerly and southerly directions often converge to form a common flow direction offshore, which could be indicative of a local rip current and is not uncommon at this site [128]. Although it is visible throughout many updates (not shown), it is often hard to recognize among enlarged $\boldsymbol{U}$ estimates on the sandbars. Note that $\boldsymbol{U}$ estimates on the sandbars are influenced by distorted wave celerity estimates of breakers, which simultaneously leads to larger depth errors (see Figure 3.7a, *difference*). At Porthtowan, near-surface current estimates generally point in south and south-easterly direction, except for the deeper region where directions are less coherent. Also at shallow parts, currents point away from the coast (Figure 3.10b right). The southerly directed flows may reflect some remaining tidal eb flow consistent with the time of the video recording approaching low water. Similar to Duck, offshore directed flows close to the shoreline are suggestive of a cross-shore directed undertow under almost coast normal wave incidence. Near-surface current estimates at Scheveningen are well

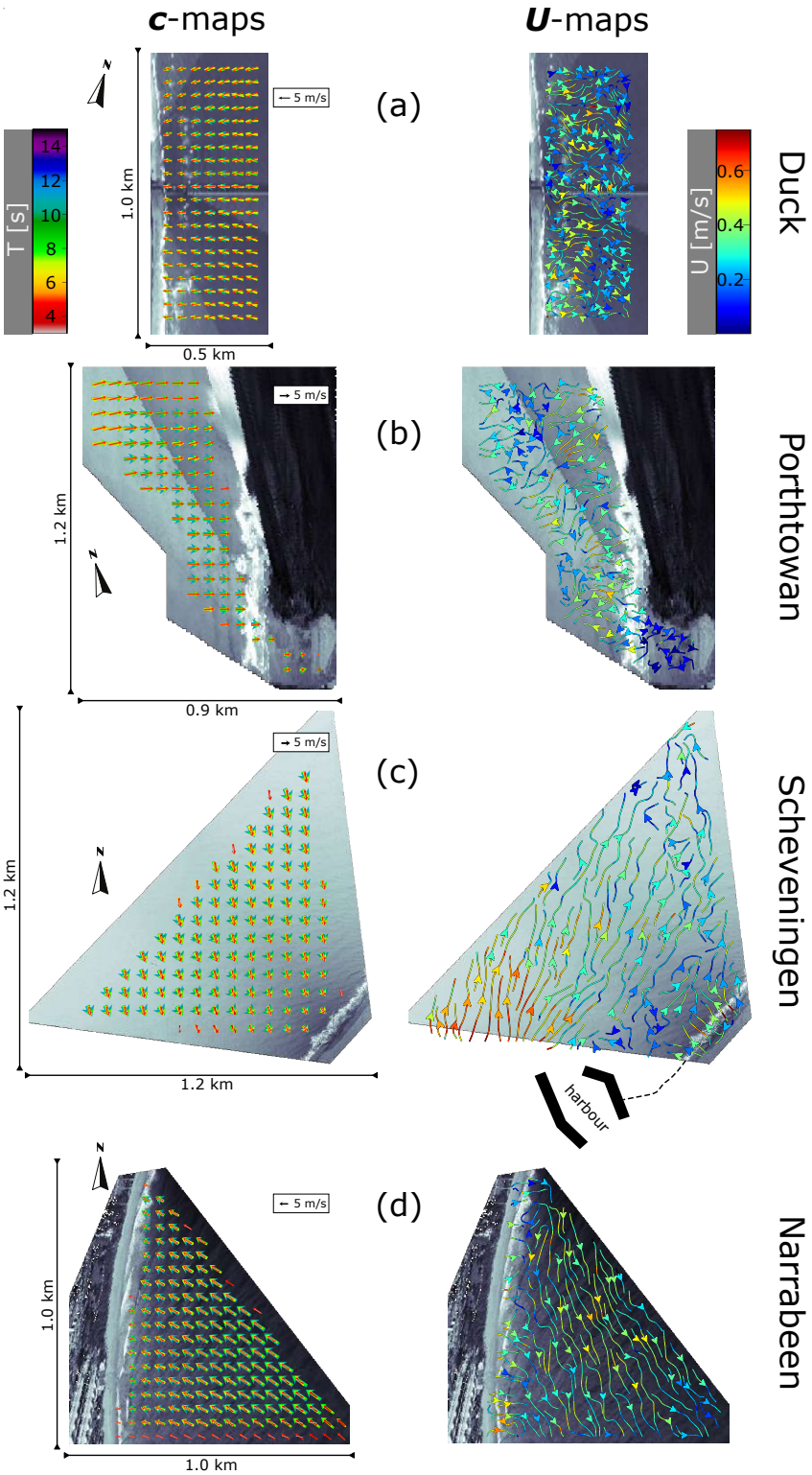

(Caption on next page.)

Figure 3.10.: Maps for wave celerity, $\boldsymbol{c}$, and near surface currents, $\boldsymbol{U}$, for field sites (**a**) Duck, (**b**) Porthtowan, (**c**) Scheveningen, (**d**) Narrabeen. The maps exemplify the 10^{th} update. Wave celerity vectors of different wave periods, T, are superimposed and coloured according to top-left colour scale. Near surface currents are indicated by streamlines whose colours highlight the current magnitudes as of top-right colour scale. In the $\boldsymbol{U}$-map of (c) the Scheveningen harbour is outlined in black.

in line with expectation. The video recording was taken just above a harbour (Figure 3.10c right). During flood, the longshore tidal current accelerates around the harbour jetties forcing larger current velocities and a characteristic region with eddies and opposite directed flows is formed on the lee side of the northern jetty. Both effects are visible and current magnitudes of mostly 0.4–$0.6\,\mathrm{m\,s^{-1}}$ off the coast also agree with typical current magnitudes off the near-by Rotterdam coast. Close to the coastline, $\boldsymbol{U}$ estimates are again offshore oriented, suggesting undertow. Similar to Scheveningen, coastal currents at Narrabeen run mostly alongshore. Here, however, they are likely not driven by tides, but by waves instead. The direction of flow at this location is sensitive to the angle of wave incidence and alongshore differences in wave height and dissipation e.g., [129]. For the recorded situation, the angle of wave incidence suggests northward flow; however, alongshore differences in wave height may still force a southward flow as mapped. The true current direction remains uncertain at this site. Summarizing, near-surface current estimates are coherent and can be explained, but the Scheveningen field-site is most relatable to expected tidal flow patterns (Figure 3.10c, right).

3.5.2. On-the-fly processing

Maps of d, $\boldsymbol{c}$ and $\boldsymbol{U}$ are realistic and ideally returned on-the-fly. To allow for an on-the-fly analysis during this study, specific choices are made to balance calculation time and spatiotemporal resolution of mapping updates. The algorithm marches forward in time by consecutively analysing small sequences of video frames, giving mapping updates after each sequence. The frame sequences partly overlap (see legend Figure 3.11a). For pre-recorded video the overlap could be controlled. It was $50\,\%$, since frame sequences were $32\,\mathrm{s}$ long and the algorithm was set to march forward in $16\,\mathrm{s}$ intervals. For on-the-fly analysis of a video feed, this approach does not work, as processing times start to play a role. A mapping update now needs to reflect the current situation and therefore mostly bases on the latest recorded video frames. Say the processing time of a frame sequence was $20\,\mathrm{s}$, then during the processing, $20\,\mathrm{s}$ of new video frames have been recorded. The next frame sequence to analyse includes these new $20\,\mathrm{s}$ plus $12\,\mathrm{s}$ from the previous frame sequence representing the overlap. The amount of overlap hence depends on the processing time, which may vary per update. Statistically, the shorter a frame sequence, the more it represents a random sample of the wave field, where waves vary in height and direction, currents change etc. [100]. Also the video quality itself may vary due to changes in lighting, the accuracy of the or-

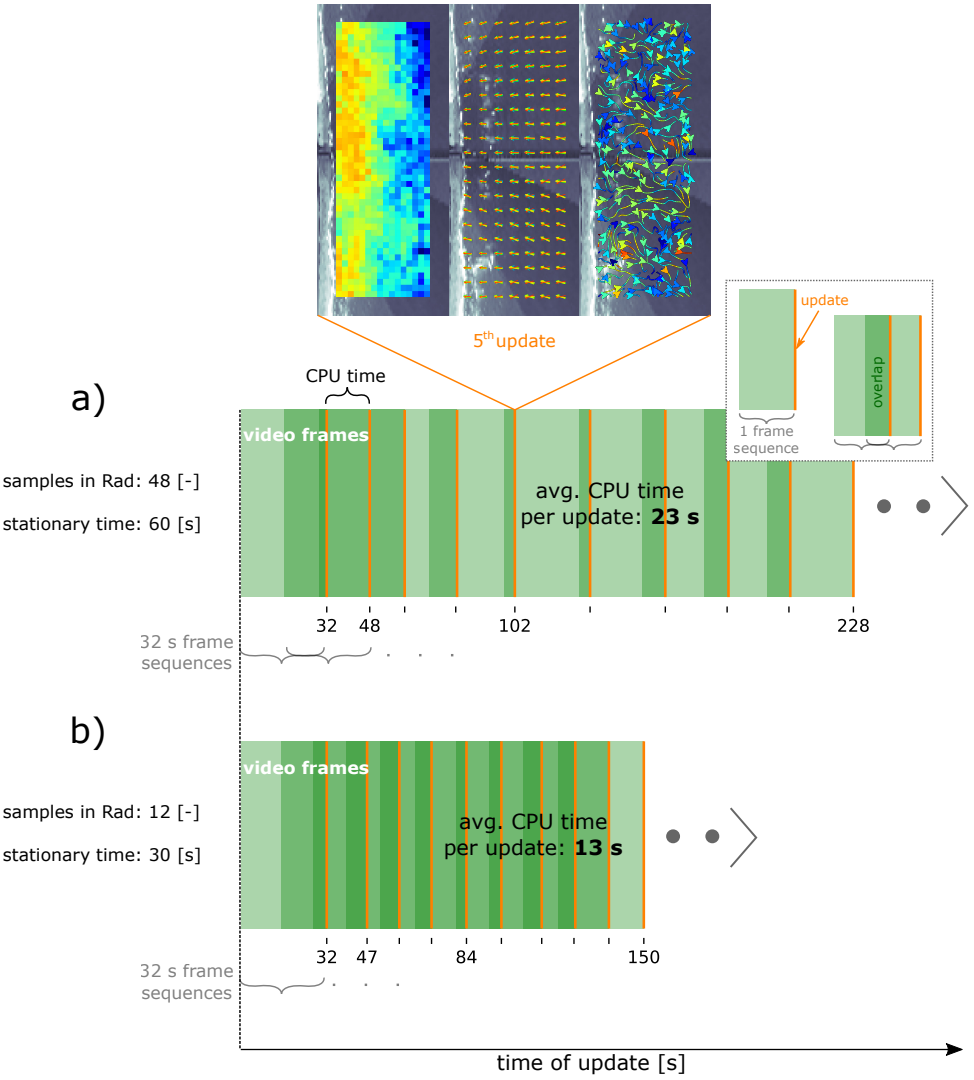

Figure 3.11.: On-the-fly analysis of Duck video. Video frame sequences of $32\,\mathrm{s}$ (green boxes, see legend) are consecutively analysed with mapping updates after each sequence (vertical orange lines). Depending on the computational processing time (CPU time), frame sequences overlap more or less (darker green, see legend). The CPU time mainly depends on the used machine, the grid resolution, and the amount of spectral data. The amount of spectral data is controlled by the number of sample grid points within a radius (Rad, see Section 3.2 and Figure 3.4) from each location and the duration that spectral data are stored and used, which is the duration the wave signal is assumed stationary. Timings of the first ten updates are shown for (**a**) 48 samples in Rad, stationary time $60\,\mathrm{s}$ and (**b**) 12 random samples in Rad, stationary time $30\,\mathrm{s}$. Both grids consist of 720 grid cells. For (a), the 5^{th} mapping update is visualized as example.

thorectification etc. This impacts the processing time, which may hence be slower or faster causing respectively smaller or larger overlap between consecutive frame sequences.

For the results presented up till now, the processing time for an update – using a standard laptop with 4 CPUs and a working memory of $4\,\mathrm{GB}$ – was typically 30–$60\,\mathrm{s}$. If the fixed, $16\,\mathrm{s}$ overlap was changed to instead be variable based on the processing time, this would be too slow. To enter the realm of on-the-fly computation, the processing time hence needs to be further reduced. The three main elements influencing processing time are: (i) the computational power, (ii) the grid resolution, and (iii) the amount of spectral data points stored and used to locally derive $\boldsymbol{c}$, d, $\boldsymbol{U}$. In this study the effect of (ii) and (iii) is considered using the video of Duck as testcase:

(ii) In a first step to increase computational speed, the grid resolution is reduced from 1260 to 720 grid points. As required to simulate on-the-fly analysis, the overlap is set to depend on processing time. The resulting simulation returns mapping updates in variable time intervals with correspondingly variable overlap between analysed frame sequences (Figure 3.11a). Yet, on average every $23\,\mathrm{s}$ a mapping update is given. Although the grid resolution is lower, the bathymetry is still estimated in reasonable detail, as well as wave propagation and near-surface currents. At the 5^{th} update, after $102\,\mathrm{s}$, the results have again converged to a large extent. The analysis could at this point be deemed on-the-fly; however, more frequent updates would further improve the user experience. A detailed view of the first SI≈4 updates reveals that they were returned at a faster pace than consecutive updates (Figure 3.11a, orange lines closer together and more, darker green overlap between frame sequences). During the first updates, the amount of spectral data in storage still increases towards full capacity, which suggests that the rate of updates should increase for a smaller number of spectral data points.

(iii) Reducing the number of spectral data points that are stored and used, reduces the number of spectral points in the dense spectral point clouds (DSPCs). This should be acceptable as long as the true local wave spectra are well represented by the DSPCs. By construction, a DSPC represents an aggregate of (mostly stored) sparse spectral points clouds (SSPCs) (Section 3.2). These SSPCs stem from surrounding grid points within a radius Rad (Appendix B.3, Table B.2, $Rad = 75\,\mathrm{m}$) from the location under analysis and from previous updates within a short period where the wave signal is assumed stationary (see Section 3.2 and Figure 3.4). Now instead of using SSPCs from all grid points within Rad, a random subset can be selected. Here, a random subset of 12 surrounding grid points is selected from the full set of 48 grid points. The amount of SSPCs from this subset of grid points can be reduced even further by simply storing less SSPCs. The storage time, which is the time that the wave signal is assumed stationary (Section 3.2), is here reduced from $60\,\mathrm{s}$ to $30\,\mathrm{s}$. The effect of both measures on processing speed is significant, while mapping results remain similar (not shown). The 5^{th} update now occurs approx. $20\,\mathrm{s}$ earlier and the 10^{th} update even $80\,\mathrm{s}$ earlier compared to the simulation with only a reduced grid resolution (cf. Figure 3.11a and b). Updates are on average returned every $13\,\mathrm{s}$, which may be considered a quite continuous temporal output,

as desired for on-the-fly application (Figure 3.11b). It is noteworthy to mention that convergence rates appear to depend rather on the number of updates than on the timing (not shown), which suggests that it may be favourable to return updates at a faster pace; however, a detailed analysis remains subject for future study.

3.6. Conclusions

This study describes a fast and self-adaptive algorithm to map coastal parameters on-the-fly from aerial wave imagery. Updates of depth, d, wave propagation, $\boldsymbol{c}$, and near-surface currents, $\boldsymbol{U}$, are returned every few seconds, such that a video feed can theoretically be processed on-the-fly and a user does not need to wait end engage in post processing. The input requires orthorectified video with known pixel size (m) and frame rate (fps). Apart from that the algorithm works unsupervised for the presented field sites. The basis for fast computational speed and increased automation lays in the use of the Dynamic Mode Decomposition (DMD), which is a dimensionality reduction technique that disposes redundant video information. It reduces the video to a set of, here 16, intrinsic wave patterns and autonomously finds the corresponding frequencies. Applying a DMD, the search for optimal spatial sampling schemes can also be automated, such that in the end, no manual choices underly the local wave spectra, which are the basis to derive $\boldsymbol{c}$ and invert d, $\boldsymbol{U}$. Consecutive mapping updates are improved by taking specific measures, such as using an innovative system to temporarily store and call up spectral data, but also by penalizing spectral outliers through a loss-function, and Kalman filtering. The algorithms potential for all-round application was demonstrated using video data from stationary camera installations and UAVs, recorded at four different field sites, Duck (USA), Porthtowan (UK), Scheveningen (NL), and Narrabeen (AU), with hydrodynamic conditions ranging between $H_s = 0.75$–$1.63\,\mathrm{m}$ and $T_p = 5$–$10\,\mathrm{s}$. Validating the depth maps, d, showed that they accurately reflected ground truth measurements. The maps quickly improved from the first update to typically the fifth update, at $1.5\,\mathrm{min}$ into the video, after which the rate of improvement relaxed. It suggests that for time-efficient coastal mapping of depths, $1.5\,\mathrm{min}$ of video suffice, such that the next location of interest can be recorded. The inter quartile range (IQR) of depth errors decreased from the first update, with minimum and maximum values of respectively $0.9\,\mathrm{m}$ (Duck) and $2.6\,\mathrm{m}$ (Narrabeen), to the last update, with values of $0.5\,\mathrm{m}$ (Duck) and $1.3\,\mathrm{m}$ (Porthtowan). Absolute depth biases were small throughout all updates, slightly improving from minimum and maximum values of respectively $0.1\,\mathrm{m}$ (Scheveningen) and $0.4\,\mathrm{m}$ (Porthtowan) at the first update to $0.0\,\mathrm{m}$ (Duck) and $0.3\,\mathrm{m}$ (Porthtowan) at the last. Maps of wave celerity, $\boldsymbol{c}$, and near-surface currents, $\boldsymbol{U}$, could not be validated at this stage; however, qualitative assessment showed vector fields of $\boldsymbol{c}$ to match observed wave propagation and vector fields of $\boldsymbol{U}$ to match expected tide- and wave-induced currents. The algorithm finally demonstrated its potential for on-the-fly video feed analysis by taking computational processing times into account. Therewith the groundwork is laid for a fast and easy-to-use tool for coastal reconnaissance. Striving towards universal applicability, more field cases and community

driven development are desired, wherefore the code and data are openly available at https://doi.org/10.4121/c.5704333.

4

Frequency-derived bathymetry with satellite

hey satellite man your time has come your words received by everyone

Satellite, The Hooters

This chapter explores the feasibility to use a frequency-based depth inversion algorithm (DIA) on satellite imagery. Raw satellite imagery is typically deficient in either framerate or record length. Imagery of Capbreton, France, collected by the Pleaides mission, is therefore temporally augmented by considering spatial pathways of propagating waves. The resulting video is subsequently processed with the DIA from Chapter 3.

Lessons learned:

- *Pre-existing techniques for image augmentation and depth inversion can be combined to form a two-step approach for deriving bathymetry from temporally sparse satellite imagery.*
- *A sequence of* 12 *images from Capbreton, France, collected at* 1/8 fps *by the Pleiades satellite, is augmented to a* 1.5 min *(pseudo) video with a framerate of* 1 fps*. The spectral wave-content in the video compares with in-situ buoy measurements.*
- *A depth map is successfully derived using a frequency based DIA. The complex canyon bathymetry is approximated to a large extent as highlighted by an overall depth bias of* −0.5 m*, yet estimates are spatially noisy with an interquartile range of depth errors of* 5.4 m*.*
- *The acquired accuracy is sufficiently high to apply a numerical wave model and predict wave heights over the shoreface.*

This chapter has been published in Remote Sensing **14**, 1847 (2022) [35].

4.1. Introduction

Knowledge of the coastal bathymetry is paramount for evaluating the vulnerability of coastal areas to flooding and erosion [60]. Bathymetric boundary conditions are an important pre-requisite for setting up numerical models that are typically used in such evaluations. With coastal morphology constantly changing, coastal managers need to systematically monitor the shoreface to assess coastal safety [62] and consider possible intervention with protection measures [59]. The need for coastal monitoring increases as climate change expects to impact the coastal zone with accelerated sea level rise, and more frequent and intensive storms [130, 131].

Conventional field measurements are labour-intensive, causing bathymetry data often to be outdated or even absent for large parts of the global coastline. Space-based monitoring offers the opportunity to fill this data gap on a global scale, with satellites having global coverage and potentially allowing bathymetry measurements on large spatial scales [13] at daily to weekly return intervals [132, 133]. Bathymetry can be derived from optical satellite imagery of the water surface by estimating depths from color differences [134, 135] or from wave characteristics [136]. Deriving depths from wave characteristics has the benefit that the technique also works in turbid waters, which often is the case in dynamic coastal zones.

Wave-based depth estimation is commonly performed on a time sequence of wave images. By extracting wave numbers, wave frequencies or a combination through wave celerity, depths are inverted via the theoretical linear dispersion relationship of gravity waves [82]. Ideally, the image record has a minimum length of 32–$90\,\mathrm{s}$ and has a framerate of 1–$2\,\mathrm{fps}$ to capture the relevant gravity wave frequencies [34, 67, 87]. Yet, Earth Observation missions only offer limited temporal information due to the rapid passage of the satellite and required agility to stay focused on a certain area of interest. Two challenging signal-processing cases exist: (1) the record length is short; (2) the framerate is low [137]. An example of case (1) are Sentinel-2 images, which contain an inherent time-shift between colour-bands of $\sim 0.5\,\mathrm{s}$, which consequently can be used to generate an image sequence at $2\,\mathrm{fps}$; due to the limited amount of colour bands the total sequence spans ~ 1–$2\,\mathrm{s}$ [138]. In this case, the retrieval of ocean wave frequencies is challenging by nature of the Gabor-Heisenberg limit [139], which states that a signal cannot be sharply localized in both time and frequency. As an example of case (2), image sequences of satellite missions such as Pleiades or Worldview-2 may span $\sim 100\,\mathrm{s}$ as the satellite can be repointed to the target area during overpass; however, the corresponding framerates are low at 0.08–$0.125\,\mathrm{fps}$ [136, 140], which is in the same order or even lower than the characteristic periods of ocean waves. In this case, the retrieval of the relevant wave frequencies is challenging by nature of the Nyquist limit.

The different satellite missions have each brought forward their own tailor-made algorithms to handle either a short record length or low framerate in pursuit of approximating wave celerity/frequencies and enable depth estimation [69, 70, 138, 141]. These techniques have reported accuracies between $<1\,\mathrm{m}$ to $2.6\,\mathrm{m}$, yet these numbers are based on specific analyses of one or two field cases. When such

techniques are generally applied to more field sites, the accuracy can drop to errors of 6–$9\,\mathrm{m}$ [13].

If the image record length was sufficiently long and the framerate was sufficiently high to naturally extract wave-frequencies (e.g., via Fourier Transformation, Principal Component Analysis or Dynamic Mode Decomposition), many more existing depth inversion algorithms could be used. Such frequency-based depth inversion algorithms are used on imagery of shore-based cameras [20, 87, 142], UAVs [12, 66] and Xband-radars [3, 21, 27, 33] (see also Chapter 2) and have been broadly applied over the past decades. These algorithms have matured with typical accuracies of 0.5–$2\,\mathrm{m}$ [15, 23, 34] and are well-embedded in the coastal remote sensing community. Also, recent efforts have aimed to make these algorithms easy to access and use. Accessibility and use of this algorithms is facilitated by increased robustness, self-adaptation to the data, computational speed, and open availability [15, 34, 143] (see also Chapter 3). Connecting the collection and analysis of satellite imagery to these depth inversion algorithms and their users remains an open challenge. To address this challenge, the satellite data needs to be prepared in a way that wave-frequencies can be naturally extracted. This may be possible for satellite imagery that is deficient in record length and/or in framerate. Recent studies suggest that $\sim 90\,\mathrm{s}$ image sequences of propagating wave fields at framerates of 1–$2\,\mathrm{fps}$ can be created from raw satellite footage of Sentinel-2 (short record length) or Pleiades (low framerate). Almar *et al.* [144] developed a technique to augment temporally sparse wave field observations towards a continuous video: assuming that wave information travels at a certain phase speed through one point in an image to neighbouring points, spatial pathways of wave trains are used to reconstruct local time-series, which spatially combine to a video. Hence, using the physical link between time and space of a wave field in motion, the approach aims to fill gaps in time with relatively high resolute information in space, as was demonstrated for Pleiades satellite imagery at Capbreton, France [144]. The results prompted further in-depth study with synthetic data to create a controlled test environment [137]. Using a numerical model, a wave field over a barred shoreface was generated. The numerical model output was then collected at framerates specific to Sentinel-2 and Pleiades satellite settings (i.e., $2\,\mathrm{fps}$ and $1/8\,\mathrm{fps}$ respectively) to simulate the two image sources. The sparse image data were subsequently augmented to video and validated against the ground truth wave field. In both simulated cases, 8 source images were enough for accurate video reconstruction and using 4 source images was sufficient to capture main wave movement. Note that this was particularly the case for the propagation of wave phases, not their amplitudes; however, amplitudes are of less importance here as they are not needed for depth inversion via linear wave theory. It suggests that video reconstruction is potentially feasible for satellite imagery with either short record length or low framerate, opening a possibility for using established depth inversion algorithms on data from a variety of earth observation missions.

The aim of this study is to explore the feasibility of using a video-based depth inversion algorithm on augmented spaceborne video. As a proof of concept, augmented video from the Pleiades data of Almar *et al.* [144] is used and then processed

with the open-source algorithm of Chapter 3,[34] to invert depths. These depths are subsequently validated against ground truth data to evaluate the feasibility of the methodology for general use.

Section 4.2 describes the Capbreton field site and data. The video augmentation method and the used depth inversion method are summarized in Section 4.3. Results of an application to Pleiades data are presented in Section 4.4. A discussion on the usability of the bathymetry estimates for practical wave-height predictions and a discussion on the detection of sandbars follows in Section 4.5. The findings are concluded in Section 4.6.

4.2. Field site and data

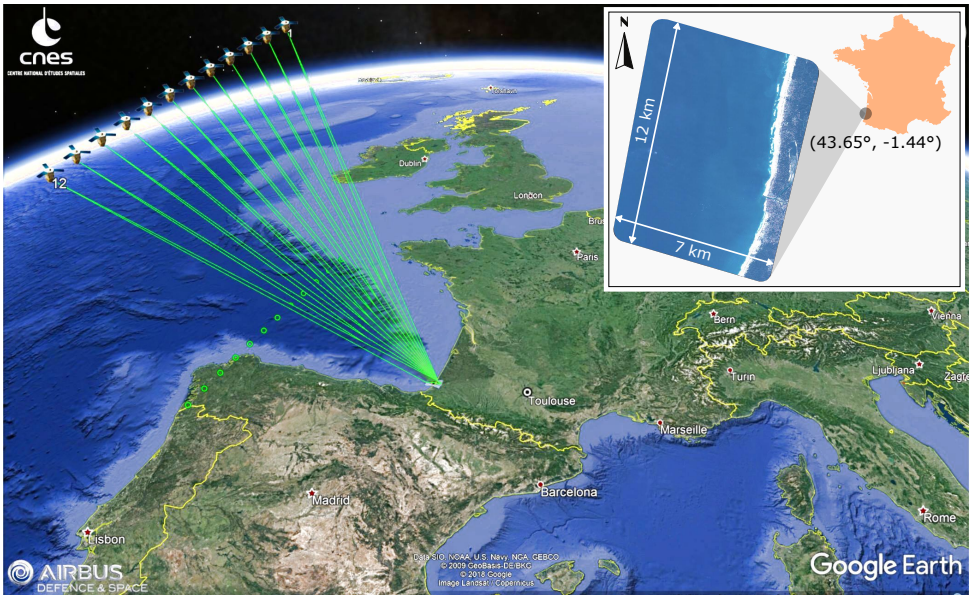

Figure 4.1.: Pleiades satellite collecting 12 images of the field-site Capbreton, France. The observed area and its location (Lat °, Lon °) are depicted in the top right.

The data used in this study were acquired during the COMBI Capbreton 2017 field experiment by the Airbus/CNES Pleiades mission [145]. Capbreton, in South-Western France, was chosen as showcase due to its unique complex bathymetry around a deep underwater canyon [146, 147](Figure 4.1), providing a large range of depths. In a single pass-over, the Pleiades satellite took 12 consecutive images of the target site at $\sim 8\,\mathrm{s}$ intervals and a resolution of $0.7\,\mathrm{m}$. These images were then orthorectified with homologue ground points using SRTM30 DEM and the SIGMA software of CNES. As such, a superimposable image sequence of an area spanning $12\,\mathrm{km}$ alongshore by $7\,\mathrm{km}$ cross-shore was established. A bathymetric survey of this region from 2010 [147] was fused to near-shore surveys from the COMBI

project to generate a ground truth reference map. On the day of recording, 18 November 2017, at 11h35, hydrodynamic conditions were governed by swell waves arriving from north westerly directions at $315°$, with a significant wave height $H_s = 2.0\,\mathrm{m}$ and a peak period of $T_p = 11.6\,\mathrm{s}$.

4.3. Method

To derive bathymetry from temporally sparse satellite imagery with a standard frequency-based depth inversion method, a two-step approach is explored. First, the sparse image sequence ($1/8\,\mathrm{fps}$) is augmented to continuous video ($1\,\mathrm{fps}$) as of Almar *et al.* [144]. Second, this video is processed using the depth inversion algorithm of Chapter 3, [34]. Core elements of both methods are summarized in Section 4.3.1 and Section 4.3.2 respectively.

4.3.1. Temporal image augmentation

For augmenting sparse temporal information with dense spatial information a physical principle related to local wave celerity is used. If travel speed and direction of waves at some point in an image are known, it can be hindcasted where these waves were in the recent past and where they will be in the near future. Hence, by looking at different distances from a certain point stochastic evidence can be found for the time-series in that point. This process is repeated for all pixels in an image. The ensemble of time-series from all these pixels shows the reconstructed video of the moving wave field. The augmentation process represents a stochastic spatio-temporal interpolation, which increases the frequency resolution and extends the Nyquist frequency (as shorter period oscillations can be reconstructed, see [144] Figure 4). It adds frames and counteracts aliasing [137] and thereby specifically aims to prepare for frequency-based analysis with conventional depth inversion algorithms (typically requiring at least ~ 64 frames [34, 87]).

Since the video reconstruction process builds on knowledge of local wave celerity, the accuracy of the celerity determines the quality of the resulting video. Due to the limited temporal images in the raw satellite imagery, the local wave celerity vectors need to be approximated. The wave celerity vectors are determined through spatiotemporal cross-correlation in combination with a Radon transform as of [137, 144]. Note that there exists an ambiguity in the celerity vector orientation of $180°$ (i.e., waves could just as well travel in opposite direction). Here, the wave direction is postulated to be towards the coast, by only considering the signal within 0–$90°$ (Eastward) in Radon polar space. The method could however pick the correct direction by ruling out the unrealistic travel speed of the opposite direction. For this study, images were reconstructed from multiple pass-band filtered images. This was done in the spatial domain using the deep water linear wave dispersion for periods ranging from 5–$20\,\mathrm{s}$.

4.3.2. Frequency-based depth estimation

The algorithm that is used to estimate depths from the augmented satellite video was recently developed and chosen because of its generally accurate performance and open accessibility. The algorithm was built to automatically adapt to given video data and to be computationally fast (see Chapter 3,[34]). Its performance relies on a skill-bed, which largely shows errors in the submeter range. To date, the algorithm has not been tested on augmented spaceborne video, which is a novelty in this study.

One of the key principles of the depth inversion algorithm is to reduce data complexity. For this purpose, a dimensionality reduction technique is employed. It comes in the form of the Dynamic Mode Decomposition (DMD), which allows to automatically extract main wave features and corresponding frequencies from given video of a moving wave field. The wave features are captured by the dynamic modes, which closely relate to so-called "global one-component phase images" (GOCPI) (Chapter 3 and section 3.1.1,[34]). Similar to other depth inversion algorithms [20, 21, 87], such phase images are used to estimate local wavelengths and are therefore a key part of the depth inversion procedure. The GOCPI and their corresponding frequencies can be extracted from relatively short image sequences (64 frames in [34]), which is attractive for the current application. Knowing the dominant frequencies at an early stage, proper sampling schemes can be determined to find local wavenumbers in the GOCPI. Combining frequencies and wavenumbers local wave spectra are formed, which expect to reflect natural wave dispersion properties. Under this assumption, the Doppler-shifted linear dispersion relationship aids as a theoretical model that can be fitted to the observed spectral data to estimate local depths.

The algorithm automatically determines the grid resolution for efficient processing. For large scale bathymetry estimation in the result Section 4.4, this grid resolution is $100\,\mathrm{m}$. In the discussion Section 4.5.2 a local, smaller scale depth inversion analysis is performed with $22\,\mathrm{m}$ grid resolution.

Although the algorithm aims to avoid manual adjustment of settings, the reconstructed satellite video presents a challenging case as the displayed wave hydrodynamics represent an approximation to the real wave-field. In addition, a large portion ($67\,\%$) of the observed area is relatively deep $>15\,\mathrm{m}$, which means that depth induced changes in wave characteristics are limited and thereby harder to detect. We find that slight changes to parameter settings offer improvement for the deeper regions. Changes compared to Gawehn, de Vries and Aarninkhof [34] (see Appendices B and B.3) are listed in Appendix C Table C.1. Most importantly, some leeway is given for maximum wave lengths. In the deeper regions, several wave components are close to their theoretical offshore wave length limit ($L/L_{off} = \Gamma_{max} \approx 1$). To capture this from noisy spectra, detected wavelengths are allowed to marginally exceed this theoretical limit ($\Gamma_{max} = 1.2$, Appendix C Table C.1). It gives leeway for the spectral data cloud to scatter (uniformly) around the deep water dispersion limit and thereby allows for an unbiased fit of the dispersion shell to the data. Further improvement for the deeper regions is gained by slightly increasing the grid cell size. It causes depth estimates to be a little less

localized, but the larger sampling area increases the accuracy of the wavelength estimates offshore.

4.4. Results

The reconstructed video and the following depth inversion are respectively presented in Section 4.4.1 and Section 4.4.2.

4.4.1. Results from the augmentation

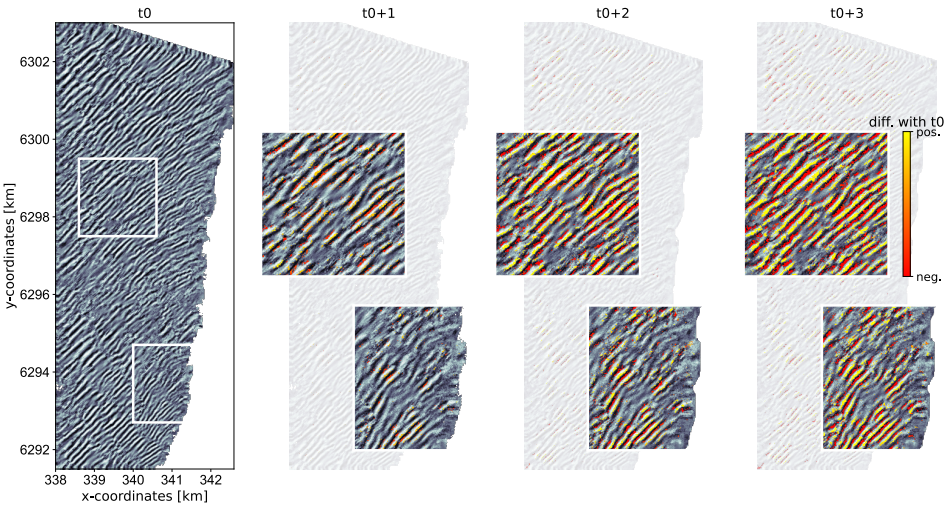

Figure 4.2.: First four frames of the reconstructed video at times $\mathrm{t0} = 0\,\mathrm{s}$ to $\mathrm{t0} + 3 = 3\,\mathrm{s}$. Wave movement is highlighted by zooming in on two example regions (white boxes), and looking at the difference with respect to $\mathrm{t0}$ (colorscale). Yellow, positive differences point out rising water levels due to incoming wave fronts. Red, negative differences point out the associated falling water levels at the back of the wave. For clarity, only differences $>10\,\%$ are depicted.

Augmentation of the 12 Pleiades images to $1\,\mathrm{fps}$ video yields 93 frames. The total length of the video thereby spans just over $1.5\,\mathrm{min}$. Wave patterns are spatially homogenous and show offshore waves to refract and wavelengths to get smaller as they approach the coastline (see Figure 4.2, $\mathrm{t0}$). Wave motion is continuous and appears realistic for large parts of the domain (Figure 4.2, upper boxes). Some small patches exist where the reconstruction quality is lower based on visual assessment (Figure 4.2, lower boxes). Especially near the image or natural boundaries, the augmentation proves more difficult. Fewer spatial points can be used for time-series reconstruction at those locations. Also, depth estimation near the coastline is particularly challenging as the time-series reconstruction becomes less accurate due to complex wave patterns and wave breaking.

To assess whether wave motion in the reconstructed video reflects reality, the optical spectrum of the video is subsampled around and compared against the measured spectrum from a local wave-buoy (Figure 4.3)(see also [148]). The optical spectrum displays the highest variance density at $\sim 315°$ and at frequencies of $0.09–0.13\,\mathrm{Hz}$ which is consistent with the buoy measurements. Angular wave spreading is less pronounced than in the buoy data. This difference may be ascribed to a combination of artefacts from both the buoy data as well as the video reconstruction procedure. Pitch and roll buoys have the tendency to produce broader spectra than reality especially in case of narrow banded spectra [149] (Figure 4.3, top right). The video reconstruction procedure has the opposite tendency, as it determines wave directions uni-directionally from the Radon-transform [144] (Figure 4.3, bottom right). Considering these spectral artefacts, the variance density spectra from the in-situ buoy and the reconstructed video suggest that the reconstructed video captures the present wave field.

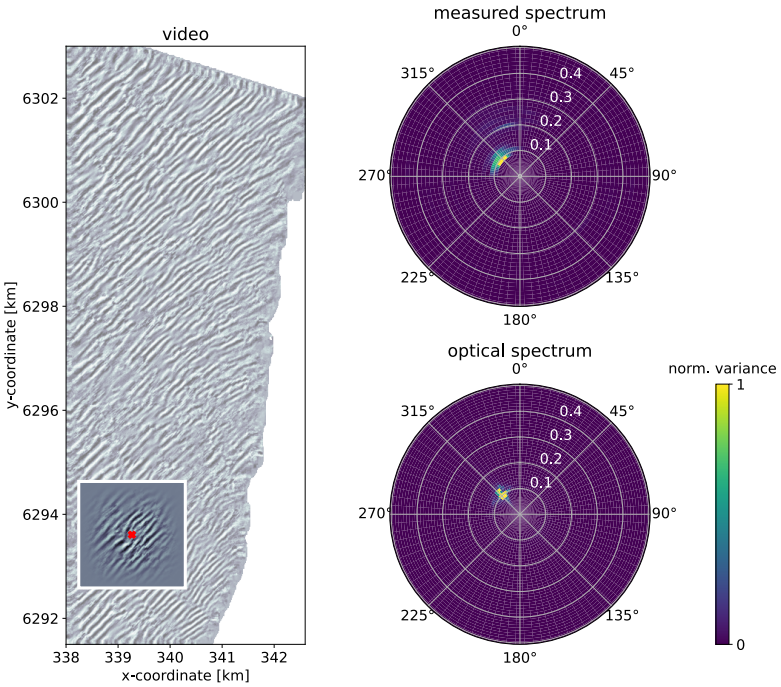

Figure 4.3.: Comparison of an in-situ measured (left, red 'x') variance density spectrum from a local buoy (top right) against a corresponding optical variance density spectrum from reconstructed satellite video (bottom right) of a representative area ($2\,\mathrm{km} \times 2\,\mathrm{km}$) around the buoy location (left, white box). Both spectra are normalized to unit magnitude for comparison.

So far, the quality assessment of the reconstructed video reveals that wave motion is continuous (Figure 4.2) and that local optical spectra compare with measured wave spectra (Figure 4.3). While the presented spectra provide directional informa-

tion about dominant wave periods, they do not couple them to wave lengths. Since this coupling is crucial for estimating depths via the dispersion relationship, the spatial structure of the dominant frequency components is checked. This is done by inspecting the global one-component phase images (GOCPI) per frequency component, gained from the depth inversion algorithm (Chapter 3 and section 3.1.1,[34]) used here (Figure Figure 4.4). For the reconstructed video, the GOCPI depict coherent, long-crested wave patterns in line with a swell wave climate. Moreover, spatial scales and time scales match, as wave lengths decrease for shorter period waves (Figure Figure 4.4, left to right). Overall, the quality assessment of the reconstructed video thereby suggests a solid basis for depth inversion analysis.

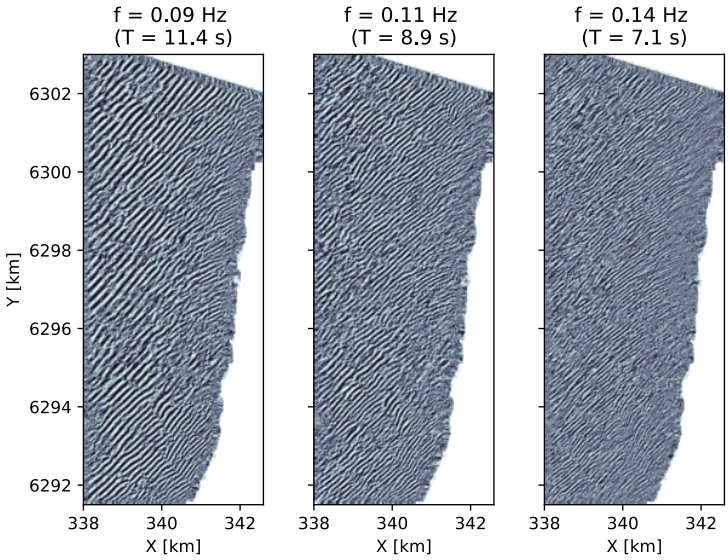

Figure 4.4.: Global one-component phase images (GOCPI) of dominant frequency components $f = 0.09, 0.11, 0.14\,\mathrm{Hz}$ in the reconstructed video. The phase images are naturally retrieved via the Dynamic Mode Decomposition as part of the depth inversion procedure [34]. In total, 9 phase images are used for analysis, of which 3 are presented as example.

4.4.2. Results from depth inversion

Depth results underscore the potential of combining video reconstruction with a standard frequency-based depth inversion technique (Figure 4.5). The estimated depth map correctly represents the overall shoreface from the shoreline down to the deeper offshore at $\sim 35\,\mathrm{m}$ (Figure 4.5 centre). The location of the underwater canyon is also captured, albeit not its depth, which extends to $\sim 200\,\mathrm{m}$ (Figure 4.5 left). At such depths, waves are no longer significantly affected by the bathymetry and therefore the depth comparison should be considered as a weak

proxy. Errors in the depth estimates are largely $< \pm 5\,\mathrm{m}$ (Figure 4.5 right). Mostly around the edge of the canyon and near the shoreline, errors are larger. The edge of the canyon features sharp depth gradients, which are hard to capture because wave patterns are reconstructed [144] and analysed [34] using spatial sampling areas and wave attenuation is not instant. Similar situations occur in areas close to the coastline. Less usable spatial samples to locally reconstruct time-series in combination with wave breaking cause inconsistencies in wave propagation (see also Figure 4.2, lower white box), eventually leading to noisy depth estimates. Yet, for the largest part, the depth estimates approximate ground truth (Figure 4.5 right, light areas).

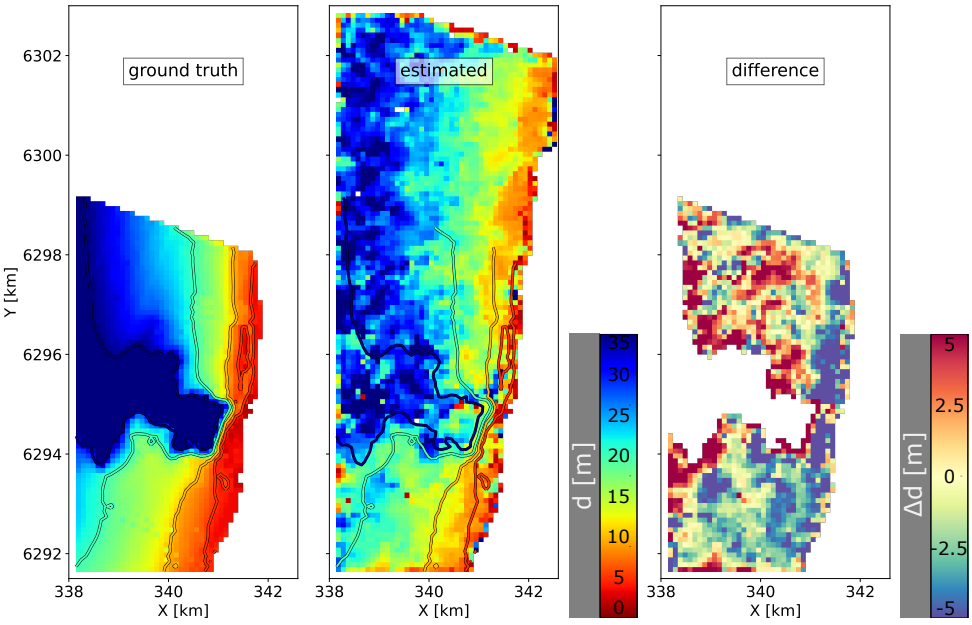

Figure 4.5.: Comparison of depths, d, from ground truth (left) against depths estimated from reconstructed satellite video (centre). Ground truth depth contours are superimposed on estimated depths for reference. Depths are indicated from red (shallow) to blue (deep) as of centre colourbar. The difference, Δd, between estimated depths and ground truth, is presented in right panel, with red/blue respectively denoting under-/overestimation of depth (right colourbar). Parts where $d > 35\,\mathrm{m}$ are masked and indicate the underwater canyon where waves are unaffected by the bathymetry.

The distribution of errors over depth is further studied through a direct comparison between estimated depths and ground truth (Figure 4.6). The median estimate over depth closely follows the ground truth (cf. Figure 4.6, green and black lines) and thereby highlights a small overall depth bias of $-0.9\,\mathrm{m}$. Depth estimates are scattered, which is quantified by the inter quartile range (IQR) (Figure 4.6, red shaded band), which averages to $\mathrm{IQR} = 5.1\,\mathrm{m}$. As indicated by the spatial differ-

ences in depth error (Figure 4.5 right), this scatter in the depth estimates is larger in shallow parts where $d < \sim 7\,\mathrm{m}$ and deeper parts where $d > \sim 23\,\mathrm{m}$. For the depth range in between, the scatter is smaller. In the near-coastal region with depths up to $15\,\mathrm{m}$, the IQR averages to $3.6\,\mathrm{m}$, which is small considering that estimates are extracted from originally just a few temporally sparse satellite snapshots.

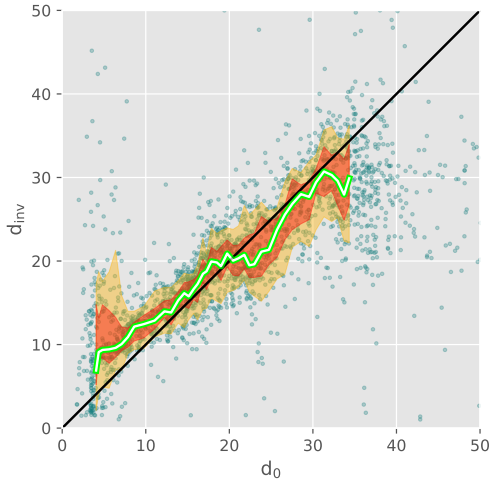

Figure 4.6.: Direct comparison of inverted depths, d_{inv} against ground truth, d_0 (blue dots). The median is indicated in green and aims to approximate the black $1:1$ line. The $25^{th} - 75^{th}$ percentile is shaded red and superimposed on the $10^{th} - 90^{th}$ percentile shaded orange.

Note that some error in the statistics can probably be attributed to morphological changes that occurred between the time of ground truth measurements, mostly dating from 2010, and the time of depth estimates in 2017. Possible depth errors due to surface current effects are expected to be limited as both measured and estimated surface currents were weak. An ADCP recorded current magnitudes of $2\text{–}21\,\mathrm{cm\,s^{-1}}$ ($10^{\mathrm{th}} - 90^{\mathrm{th}}$ percentile), which is representative of typical tidal current magnitudes at Capbreton [150]. Currents impose a Doppler-shift, which the depth inversion algorithm seeks to take into account. Here, this is challenging due to the unidirectionality of waves, but the algorithm estimated near-surface current magnitudes to be mostly $<26\,\mathrm{cm\,s^{-1}}$ ($90\,\%$ of the estimated area), which is in line with ADCP measurements and also suggests a limited effect on inverted depths.

4.5. Discussion

The upcoming Section 4.5.1 discusses the possible use of the large scale bathymetry estimates for predicting and mapping coastal hydrodynamics. Coastal morphodynamics typically occur in the active coastal zone and may produce nearshore features such as sandbars. Section 4.5.2 explores whether such sandbars can be captured.

4.5.1. Using satellite derived depths for coastal wave height predictions

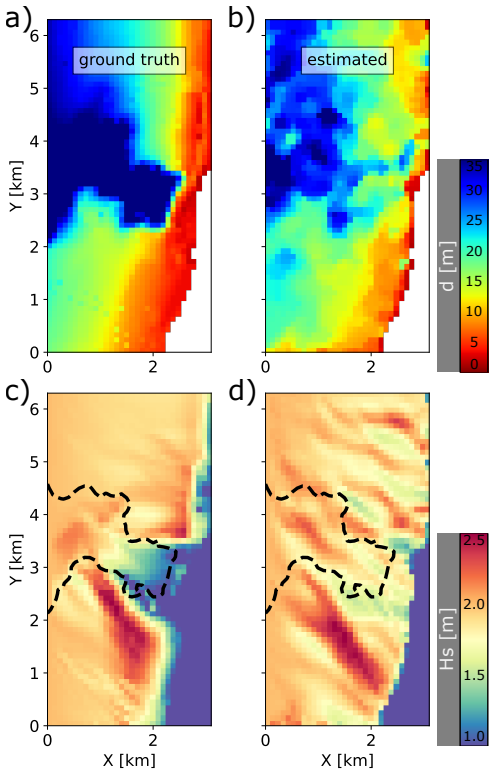

Figure 4.7.: Predicted wave height distributions over ground truth bathymetry and estimated bathymetry of Capbreton using a numerical wave model. **a,b**) ground truth depths and estimated depths, respectively used in the model, where red/blue indicate shallow/deep regions (top colorbar). Salt-and-pepper noise has been removed from (**b**) using a 3×3 median filter. **c,d**) significant wave height distribution associated to (**a,b**), respectively, where red/blue indicate high/low wave heights (bottom colorbar). The $35\,\mathrm{m}$ depth contour is superimposed to outline the location of the canyon. Hydrodynamic field conditions with $H_s = 2\,\mathrm{m}$, $T_p = 11\,\mathrm{s}$ and wave direction $= 315°$ measured by a local buoy (see Figure 4.3) during satellite overpass are used as boundary forcing.

While the estimated bathymetry map of Capbreton approximates reality, the question arises whether it can be used for practical applications, such as for wave height predictions over the coastal shoreface along the coast. Such predictions are typically made with numerical models, in which the local detailed bathymetry is a required boundary condition to propagate wave energy. It is worthwhile exploring whether the large scale, satellite derived bathymetry could substitute for this purpose, as local ground truth data may not always be available.

A straightforward stationary wave model was used to compute wave refraction and the spatial distribution of wave heights at Capbreton [151]. It repeatedly solves the wave action balance and includes dissipation formulations for wave breaking and bottom friction [152, 153]. The model was applied to the estimated bathymetry (Figure 4.7b) as well as the ground truth bathymetry (Figure 4.7a) and the resulting wave height distributions (Figure 4.7c,d) were then qualitatively compared. To mitigate the influence of salt-and-pepper noise, the estimated bathymetry data were first filtered with a small 3×3 median filter. The numerical model was forced using the hydrodynamic conditions observed by the offshore wave buoy during overpass of the satellite ($H_s = 2\,\mathrm{m}$, $T_p = 11\,\mathrm{s}$, wave direction $= 315°$)(see also Figure 4.3).

Figure 4.8.: The beach La Piste at Capbreton, France.

The computed wave heights at Capbreton displayed a characteristic pattern of increased wave heights to the south and north of the canyon and lower wave heights at the canyon head (Figure 4.7c,d). This is consistent with earlier observations for typical winter month conditions at this site [154]. Wave height predictions using the estimated bathymetry (Figure 4.7d) were noisier than for the ground truth bathymetry (Figure 4.7c). Smaller wave heights at the head of the canyon were less pronounced (Figure 4.7d), because the canyon depth was underestimated there (Figure 4.7b). However, the increased wave heights to the north and especially the south of the canyon were captured. Submarine canyons are known to refract waves in complex patterns, leading to a variable distribution of wave heights along the coast [155]. Local focussing of wave energy typically causes hotspots of increased wave height, which may be associated to popular locations for wave surfing [154, 156]. In this case, the southern band of increased wave heights leads up to a beach called La Piste, a renowned wave surfing spot (Figure 4.8). Being able to recognize such wave energy hotspots from satellite derived bathymetries is

valuable, also for safety purposes, as hotspots are a determining factor in coastal hazard assessments [60]. At La Piste wave focussing also contributes to observed shoreline and dune retreat (Figure 4.8).

4.5.2. Satellite derived sandbars

The Capbreton bathymetry is complex, featuring a large underwater canyon, but also fine sandbar structures along the adjacent coastline. Sandbars are an important element for understanding coastal systems [117] and it would therefore be valuable to capture them.

Sandbars are relatively small morphological features and therefore require a more detailed depth inversion analysis. Zooming in on the location of a sandbar at Capbreton, a refined local wave-field video was reconstructed with a framerate of $2\,\mathrm{fps}$ (Figure 4.9a). As these sandbars are located in the near-shore region with characteristic depths of $0{-}15\,\mathrm{m}$ (Figure 4.9b), the depth inversion analysis (Figure 4.9c) was done using the standard algorithm settings of Gawehn, de Vries and Aarninkhof [34] (see Appendices B and B.3).

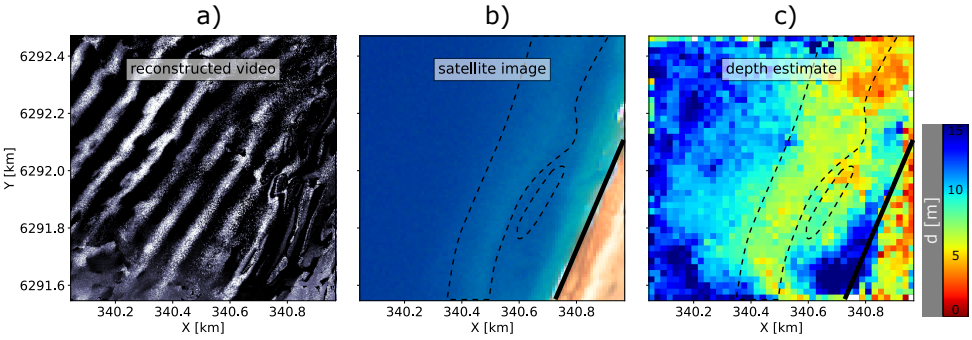

Figure 4.9.: Sandbars from depth inversion of a locally reconstructed video of the near-shore wave-field. **a**) reconstructed video with framerate of $2\,\mathrm{fps}$. **b**) satellite image showing the position of the sandbar. **c**) Depth estimates based on (**a**). For reference, dashed black contours outline the position of the sandbar and the solid black line indicates the position of coastline.

The estimated sandbar morphology (Figure 4.9c) was qualitatively compared to the sandbar position visible through optical imagery (Figure 4.9b). Ground truth bathymetry data were too coarse and outdated in this area. The comparison showed, that the local depth inversion analysis distinctly captured the sandbar morphology. Approaching the sandbar from the offshore, the water depth decreased up to the position of the sandbar at an estimated depth of $\sim 5\,\mathrm{m}$, which is in line with expectation for this site [147]. This was then followed by a trough shoreward of the sandbar and eventually the coastline. The analysis demonstrates that the proposed depth inversion methodology can expose small-scale features from satellite imagery, and may thereby add morphological detail in regions with absent or coarse knowledge of the present bathymetry. Sandbar estimates could potentially be im-

proved using wave breaking and -dissipation as additional proxy for depth [29, 43] or be combined with depth estimates from satellite SAR imagery on cloudy days [157, 158].

4.6. Conclusions

This study explored the estimation of coastal bathymetry from satellite imagery with a frequency-based depth inversion method. Wave-based depth inversion methods in the frequency domain share a large user community and are widely applied to derive bathymetry from video of camera stations, UAVs and Xband-radars. It would therefore be appealing if these standard methods could also be used on satellite imagery. However, as is, the temporal resolution of satellite imagery remains sparse. To enable frequency-based depth inversion to work, satellite imagery was temporally augmented in this study, which was achieved using pre-existing techniques. As such, depth inversion becomes a two-step process, with the first step being the augmentation of sparse satellite imagery to video, and the second step being the analysis of this video with a frequency-based depth inversion method. As a proof of concept, Pleiades images of the study site Capbreton in France were temporally augmented from originally $1/8\,\mathrm{fps}$ to $1\,\mathrm{fps}$ video lasting just over $1.5\,\mathrm{min}$. The resulting augmented video showed smooth propagation of wave crests and its spectral content accurately represented in-situ buoy measurements. The video was subsequently analysed using a frequency-based depth inversion algorithm, which works largely unsupervised and is openly accessible. The resulting depth estimates approximated the ground truth with an overall depth bias of $-0.9\,\mathrm{m}$, yet estimates were spatially noisy with an interquartile range of depth errors of $5.1\,\mathrm{m}$. Still, the acquired accuracy was sufficiently high to correctly predict wave heights over the shoreface with a numerical wave model and to find hotspots where wave refraction leads to focussing of wave energy that has potential implications for coastal hazard assessments. Furthermore, detailed depth inversion analysis of the near-shore region demonstrated the potential to capture small-scale morphological features such as sandbars. This study demonstrates that pre-existing techniques can be combined to estimate bathymetry from satellite imagery and that these estimated bathymetries may serve coastal management purposes.

5

Synthesis of wave-based coastal remote sensing

All we need is one worldwide vision

One Vision, Queen

5.1. Introduction

The success of wave-based coastal remote sensing techniques (WCRS) depends on the ability of end-users to solve problems using these techniques [10, 11, 31]. Identifying coastal problems, answering managements questions and execute policy requires data, and these data can be provided by WCRS. Such data include up-to-date bathymetry to assess the state of the shoreface and identify erosional/accretional trends, but may also include information about hazardous hydrodynamics.

Chapter 1 placed WCRS within the broader context of a technology to be used by potential end-users. One can thereby think of the maturity of a technology in terms of technological readiness, but also of a technology's potential to be adopted. This thesis was motivated by the observation that WCRS showed high technological readiness, but that existing WCRS software prevented a broad adoption by the coastal community. This Chapter 5 reflects on the technological readiness and adoptability of WCRS based on the work conducted in this thesis (Section 5.2) and discusses some properties of WCRS, which can be further improved upon in the future (Section 5.3). The discussion is followed by a brief summary (Section 5.4) and context with neighbouring remote sensing techniques (Section 5.5). Finally a vision is given for the future of WCRS (Section 5.6). With the exponential growth of data volumes worldwide [159], future software will have to process raw (video) data on-board, such that smaller data volumes can be transferred for storage (see Chapter 2; [3]). Data clouds will be able to facilitate storage and offer future perspectives for online integration of data with numerical models and modern data

science techniques like neural networks. This will create new possibilities for understanding system dynamics, through allowing on-the-fly hindcasting and forecasting and thereby provide valuable tools for decision makers in coastal management, the industry and the coast guard.

5.2. Technological readiness and adoption

In Chapter 2, [3] the technological readiness of WCRS was tested. It was demonstrated that WCRS works in an operational environment, which corresponds to a technological readiness level (TRL) 7 (see Chapter 1). That study subsequently initiated the multi-year employment of WCRS in a government-financed project, showing that WCRS technology is fully ready for market use (see Chapter 1, TRL 9) [160], at least for this XBand-radar application. Still, it is questionable whether WCRS is complete and qualified (TRL 8). WCRS is complete and qualified in terms of scalability, as this study demonstrated that fixed land-based and flexible airborne (Chapters 2 and 3) instruments can provide data on local scales of $O(100\,\mathrm{m}^2)$-$O(100\,\mathrm{km}^2)$, and this can now be extended to global scales with space-borne (Chapter 4) instruments (Figure 5.1). Moreover, such large scale data can be achieved at high temporal resolution and more affordably compared to in-situ measurements: after setting up an Xband-radar it can provide several bathymetry maps a day, as was demonstrated in Chapter 2, which is not feasible with in-situ transector multibeam surveys.

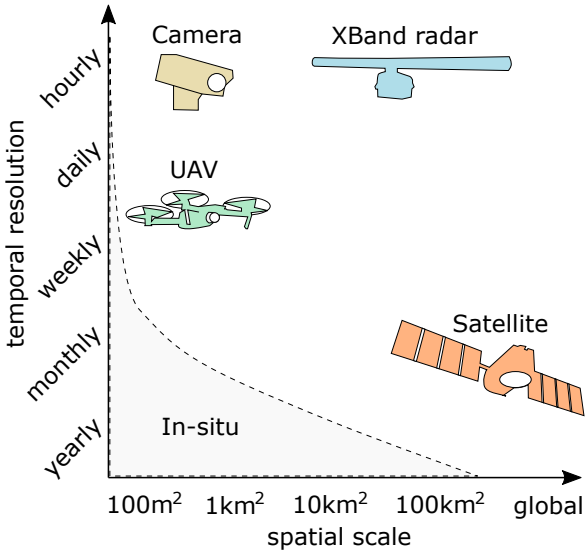

Figure 5.1.: Idealized illustration of characteristic spatial scales and temporal resolutions of the remote sensing instruments used in this study. In-situ data collection is indicated in grey for comparison.

Yet, to date, there exists no all-round software package to be used on different

remote sensing hardware for operational use. Depth inversion algorithms (DIA) form a crucial part of the required software and by developing self-adaptive software (Chapter 3, [34]) and applying it to multiple instruments (Chapters 2 to 4, [3, 34, 35]), this work contributed to reach TRL 8. Yet, further steps are necessary for standalone, fully-integrated software. Concluding, this work has helped to bring WCRS further towards TRL 8 and 9, but there is still a need for further automation and technological completeness.

To assess the status in the adoptability of WCRS, the end-user considerations (EUCs) of Chapter 1 are revisited:

- ☑ (EUC 1) relative advantage compared to existing tools
- ☑ (EUC 2) compatibility with pre-existing systems/hardware
- ☑ (EUC 3) complexity/difficulty to learn
- ☑ (EUC 4) testability
- ☑ (EUC 5) potential for reinvention
- ☑ (EUC 6) observed effects

Viewing these EUCs as a check-list, confirms that this studies' aim to innovate wave-based depth inversion towards accessible, smarter and faster algorithms does (indeed) promote broad community use: Relative advantages compared to existing tools/algorithms (EUC 1) are possibilities to operationally monitor complex systems over large areas and monitor nourishments from large distances. Other advantages are improved accessibility and user-friendliness of DIAs and possibilities to acquire depth estimates on-the-fly enabling the analysis of video feeds and lean-and-mean mapping (Chapter 3, [34]). Also the compatibility of WCRS with pre-existing systems (EUC 2) was proven by application to data from four different remote sensing instruments (Chapters 2 to 4, [3, 34, 35]). The complexity/difficulty to learn WCRS (EUC 3) was directly addressed by designing self-adaptive algorithms (Chapter 3, [34]). The testability of WCRS (EUC 4) has also been improved, by establishing a skill-bed and making software openly accessible (Chapter 3, [34]). It was also possible to reinvent WCRS (EUC 5) by showing potential application of DIAs to video feeds (Chapter 3, [34]), but also to sparse video-footage, which it was initially not designed for (Chapter 4, [35]).

Finally, by striving towards fast, visually responsive, yet robust, multifunctional and accurate DIAs, potential end-users can easily collect, map and present coastal data, which has observed effects (EUC 6). This was first shown by relatively inexperienced people (students who just entered their masters). During a field experiment at the Sand Engine (Figure 5.2a) it was aimed to derive bathymetry using a UAV (Figure 5.2b) and validate those data against ground truth bathymetry data. Aside from setting out GCPs and the orthorectification of the drone movie, the laymen required little help in the process. The application of the self-adaptive DIA was straightforward. Without any tuning of the DIA, within $10\,\mathrm{min}$ an accurate map of bathymetry was obtained (Figure 5.2c) with errors of mostly $0{-}1\,\mathrm{m}$ within

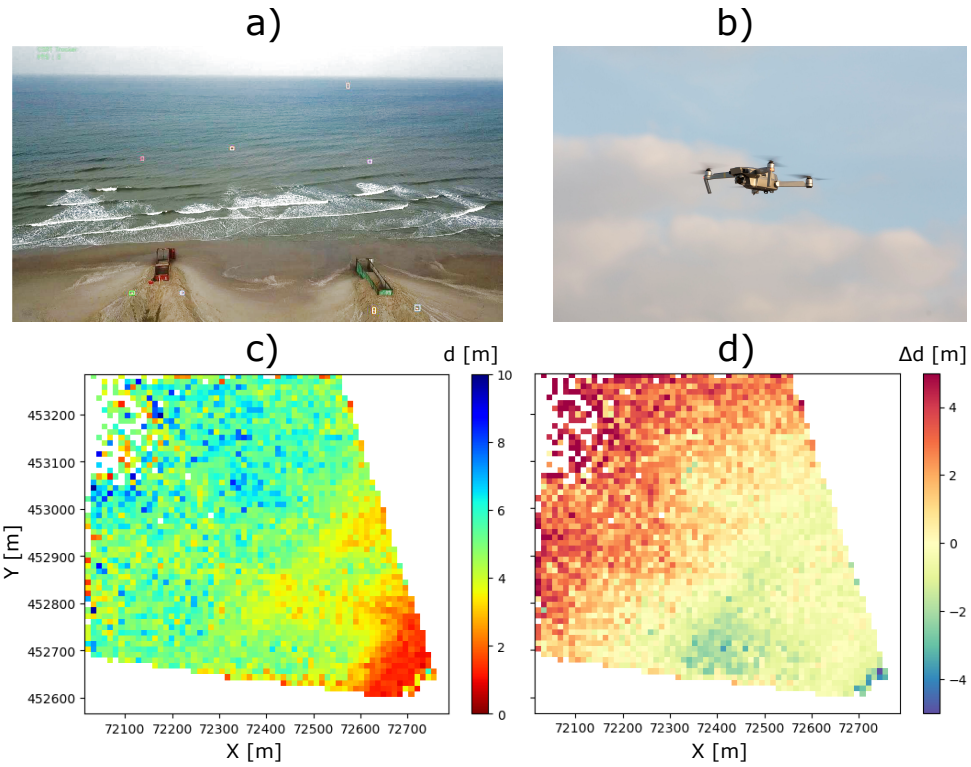

Figure 5.2.: Laymen application of a self-adaptive depth inversion algorithm (DIA). a) View of the field site at the Sand Engine and b) the used drone, a DJI Mavic. c) Depth, d, obtained with novel DIA, based on a drone field survey in October 2020 with significant wave heights of $0.7\,\mathrm{m}$. d) Difference, Δd, with ground truth.

$500\,\mathrm{m}$ from the coast (Figure 5.2d). This user case gives a first indication that self-adaptive DIAs may be suited for a large user community with little to no experience in remote sensing. Yet, this is still to be shown in practice, as more people start to use such DIAs.

From the viewpoint of end-user adoption, the concept and development of fast and self-adaptive software in this study stimulates a broader community use of WCRS, making way for an early majority of adopters (see Figure 1.4, Chapter 1).

5.3. Five properties of WCRS: Current status and future developments

The improvement of WCRS for effective coastal monitoring is a process to be continued. The ability of end-users to acquire data with WCRS increases with more affordable hardware and easy-to-use, yet powerful software. The success

will be reflected by a broad coastal user community ranging from researchers to managers, to the coast guard and the industry. The more people are able to use WCRS the more effective it is. To steer future developments, a set of five WCRS properties is suggested, which can be improved upon:

- accessibility
- multifunctionality
- quality
- robustness
- user friendliness

These five properties regard both the instruments to record the wave-field and the software to analyse the recorded wave-field. This work has contributed to improving the software-side and more specifically, the DIAs used to make estimates of depth, near-surface currents and wave celerity (Chapters 2 to 4, [3, 34, 35])

If the complexity of WCRS decreases the end-user community increases as it becomes easier to collect information to address a coastal problem. This Section 5.3 elaborates on that using the five highlighted properties of WCRS as guideline. The state of each property is discussed in detail and possible future developments are suggested.

Accessibility

WCRS is in the process of becoming more accessible, both the necessary hardware as well as the software. This process of becoming more accessible is an important change starting in the early 2010's.

WCRS hardware (camera, UAV, Xband-radar, satellite) has gone through different phases of accessibility from the past until now. For several decades, hardware was expensive (e.g., [161, 162]). Professional stationary camera installations were costly, UAV's were not as far developed and also costly. Satellite data were also either costly and/or not open-source, such as data from Landsat. Some satellite data were not yet available such as Sentinel-2 data. XBand-radar is still an expensive instrument. In recent years technical innovations have brought forth affordable high resolution cameras and affordable UAV's with autonomous stabilization and equipped with high quality gimbles and cameras. Although, currently the use of UAV's experiences a set back, as regulations to fly drones become stricter and licensed pilots are required [163]. Satellite data are becoming more open source and Chapter 2 has demonstrated that existing navigational XBand radars can be utilized.

In terms of software, also large steps have been made in their accessibility. Cameras, for example of UAV's, can be automatically calibrated with built-in software or with tools from openly accessible platforms such as OpenCV [164]. Such platforms provide an inventory of sophisticated software tools,

which can be used to reduce the complexity of WCRS, for example by enabling autonomous optical tracking of Ground Control Points (GCP) needed for orthorectification. Satellite data can be accessed and processed via platforms such as the Google Earth Engine and occur in the cloud [165]. From own experience, XBand-radars still require specialist, third-party software tools, which are not easily accessible. Until recently, post-processing software to estimate depths, wave directions or surface currents were not open-source. Not being able to utilize the capabilities of such software, WCRS was difficult without involvement of third-parties. This is changing due to a growing open-science mindset, which shows to accelerate research [166], increases public attention and brings new opportunities for collaboration [143], jobs and funding [167]. Software like cBathy [20] has become open-source and accessible via platforms such as GitHub [143], yet it is currently only available in commercial Matlab programming language. The software developed during this study is openly available [34] and also programmed in open source Python language.

However, the use of WCRS typically necessitates a three-step process, (1) the collection of the video data, (2) a pre-processing step to convert video to orthorectified format and (3) the post-processing step with a DIA. For orthorectification an additional challenge lays in the use of GCPs, which are typically manually put into the field and individually located with GPS. All these steps might be combined into a single, integrated, multifunctional WCRS software.

Future developments: To reach a broad user-community, improvements can still be made. In terms of hardware, WCRS is an accessible alternative to in-situ techniques (e.g., a UAV is more affordable than a jet-ski). In terms of software, many algorithms are only available in the form of computer code like Matlab or Python. If organisations such as the coast guard or the industry are meant to use WCRS, software will have to be provided in the form of stand-alone, freely downloadable applications in order to be accessible. One of the desired goals of this study was to develop such an application for analysis of drone video feeds Figure 5.3. To achieve this goal, methodological innovation of DIAs was still required, which resulted in a prototype algorithm that could be used in an application [168]. It is now the task of (software) developers to transform bare Python and Matlab codes of DIAs and implement them in stand-alone applications (e.g., for Android or iOS). This task might be achieved through collaboration with university students from software engineering departments. Stand-alone applications will increase accessibility and thereby benefit a broad WCRS user community. These applications should be integrated, seamlessly combining video recording with pre-processing and post-processing. Concretely, it is desirable if the process of orthorectifying video and the process of analysing the video could be combined and performed on-the-fly to a video-feed. This is technologically feasible.

Specifically the process of orthorectification should be simplified, as it can form a labor-intensive pre-processing step. Orthorectification might be sim-

Figure 5.3.: Field visit to the Sand Engine. Members of the ZABAWAS foundation without technical background are flying a UAV. A tablet displays the drone video feed. It would be ideal if an application could be opened to show maps of the local bathymetry and surface currents on-the-fly.

plified for hardware with RTK-GPS, as it may circumvent the necessity for GCPs [169]; however, RTK-GPS functionality (e.g., for UAVs) is currently expensive and hence does not score on accessibility. A different approach could be to combine optical imagery of a certain instrument (e.g., UAV) with geo-located satellite imagery. By automatically detecting overlapping features between satellite imagery and imagery from a different recording instrument (e.g., UAV), the satellite GPS coordinates of those features could be used to orthorectify the imagery of the other recording instrument [12]. This requires automatic feature detection to find natural GCPs. In the past this was not a viable option as potent feature detectors were patented, but in the meantime open source alternatives like ORB exist [170]. Note that Convolutional neural networks (CNN) could also orthorectify drone imagery an do so on-the-fly, even in GPS-denied environments [171]. Seamlessly integrating the orthorectification process with the video collection and on-the-fly DIA post-processing in a stand-alone application would present a major step forward: reducing the complexity of WCRS and thereby increasing its accessibility.

Multifunctionality

An intrinsic strength of WCRS is that it can be multifunctional. It is possible to estimate several hydrodynamic parameters and morphology simultaneously from video and/or time exposures, regardless of the used instrument e.g., [33, 75]. During this study, algorithms were developed, which offered to map wave-hydrodynamics, near-surface currents and depths, all simultaneously,

see Chapters 2 and 3. WCRS also allows to map current profiles [46] and wave heights e.g., [172, 173], albeit such methods are typically not integrated in depth inversion algorithms (DIAs).

The multifunctional capability means a multifunctional range of application. This range of application is determined by coastal zone management goals, flood safety, ecological and recreational directives, swimmer safety, but possibly also navigational safety and industrial process monitoring [1–4]. These applications need reliable up-to-date coastal data from which relevant products can be derived like erosion trends, volumetric changes, nourishment behaviour, system behaviour, but also hotspots for endangered swimmer safety or wave-surfing hotspots.

In the intoduction Chapter 1 an example was given for coastal management needs in the Netherlands, such as the need to know coastal erosion in order to plan for intervention measures. This work has demonstrated that WCRS can answer questions like ”what is the evolution of a nourishment?”, by deriving trends in nourishment volumes and recognizing (the movement of) morphological features (Chapters 2 and 4). Even complex morphological system behaviour can be monitored [160], such as ebb-channel migration and switching, which can be valuable for navigational safety. On-the-fly WCRS estimates could also allow to identify temporary hotspots of strong currents (Chapter 3) in the field. Chapter 4 has also shown that large-scale, spaceborne bathymetry estimates can be combined with fast numerical models to reveal hotspots of increased wave energy having implications for recreational coastal functions like wave-surfing, but also public safety. The current study has made WCRS easier to use, faster and gave insight into measurement reliability and demonstrated that it is ready for implementation in monitoring projects.

Future developments: There are two main challenges for multifunctional WCRS. The first challenge concerns (1) multifunctional software, and the second challenge concerns the (2) multifunctional application of WCRS.

(1) The multifunctionality of the software could be further extended by adding functionality to estimate current profiles and wave heights. Stand-alone applications could be programmed towards such all-purpose software for use by a broad coastal community. Methodologically, the necessary tools exist and could be combined. Note that both for process integration as well as the estimation of various coastal parameters neural networks are a potent future alternative. Convolutional neural networks (CNN) have not only made their entry in DIAs [71, 73]. Fast advancements in computer vision have recently brought forth neural networks capable of unprecedented instant three dimensional real-world reconstruction from a few snapshots[174]. Such methods can enable on-the-fly three dimensional wave-field analysis instead of two dimensional analysis, offering extraction of wave-energy spectra instead of optical intensity spectra and direct derivation of local wave heights. These estimates could directly be used to identify hotspots for endangered public

safety, but also hotspots for coastal recreation (e.g., wave-surfing). Hence, machine learning offers new perspectives for multifunctional and instantaneous WCRS.

(2) The second challenge lays in the multifunctional application of WCRS. The Dutch Ministry of Infrastructure and Water Management shows renewed interest in the application of WCRS for real-time coastal bathymetry monitoring [3, 160]. Other organizations should follow this lead, as it aids in refining user-needs [10]. The technological readiness of WCRS is at a stage where it is able to provide necessary up-to-date coastal information with little effort compared to traditional spatio-temporally coarse (in-situ) measurements. This implies that efforts should be channelled towards reaching out to researchers through presentations and regular workshops such as via the Coastal Imaging Research Network [143]. Similarly, WCRS can be pitched to coastal managers, the industry and the coast guard. Yet, for convincing arguments, specifically to the industry and coast guard, the WCRS software should first be more integrated as to demonstrate easy implementation and adoption (see *accessibility* and Section 5.2).

Quality

The quality of WCRS is determined by estimate accuracy and spatial coverage, which can be influenced by the instrument to record video (see Chapters 3 and 4), the software to analyse video [169], but also hydrodynamic [44] and weather conditions ([3, 15]). Typically, an image resolution of $5–10\,\mathrm{m}$ suffices, which can be achieved with most instruments. A clear sky is favourable and can be a necessity for passive sensor instruments, like optical cameras of fixed stations, UAVs or satellites. But clear skies can also cause sun-glare, especially in records from fixed camera stations or UAVs, which can decrease spatial data coverage [15]. Instruments with active sensors, like Xband-radars are known to produce qualitatively sufficient wave-imagery also under poor weather conditions like rain and fog [175].

In terms of software, most wave-based DIAs are based on linear wave theory, which seemingly works for most field applications, but also has its limitations for example under breaking waves or storm weather conditions. Typically, estimates of depth have errors $<2\,\mathrm{m}$ and data coverage is $90–100\,\%$, as was found for a wide range of hydrodynamic conditions with both a Fourier-based DIA (Chapter 2), but also a DMD-based DIA (Chapter 3) and which is in line with other reported DIA accuracies (e.g.,[20, 23, 44]). Different measures can be taken to improve estimates, such as Kalman filters [20]. This work showed that improvement can also be achieved with loss-functions in optimization and temporary spectral data storage (see Chapter 3, [34]). Depth errors $<2\,\mathrm{m}$ are larger than for in-situ measurements, for example from jet-ski surveys (errors $\sim 10\,\mathrm{cm}$, [176]), but they allow to derive relevant products such as volumetric changes of a nourishment to significant accuracy ($7\,\%$)(Chapter 2). An important factor influencing result accuracy is the record length, which may

be restricted. Openly available satellite imagery contains little temporal information, which leads to increased uncertainty in the determination of wave celerity and wave frequency - the basis to derive depths and near-surface currents (see Chapter 4, [35]). This work demonstrated that spatial pathways of wave trains can be used to increase the temporal confidence in wave frequencies as to estimate coastal parameters with standard, frequency-based DIAs. Estimates of depths remain less accurate with errors $<5\,\mathrm{m}$ if temporal information is sparse. Still, even if estimate accuracies are seemingly rough, bathymetry maps with large spatial coverage (e.g., from satellites, see Chapter 4) have quality for end-users, as they can be used in hydrodynamic models to identify hotspots of increased wave height along a coastline and thereby allow for first-order assessments on coastal recreational- and safety functions (see Chapter 4, [35]). Thereby WCRS can readily help as an operational or lean-and-mean assessment tool in making coastal management decisions, without necessitating high depth estimate accuracy.

The quality of near-surface currents was not validated for accuracy, because ground-truth data were not available. However, the estimated near-surface current maps often compared qualitatively to expected local currents, for example by correctly indicating zones where currents were stronger (e.g., currents through ebb-channel Ameland inlet in Figure 2.9, Section 2.5.1 or convergence around Scheveningen harbour in Figure 3.10, Section 3.5.1), which can be valuable to monitor swimmer safety.

Future developments: Software to map coastal indicators such as depths and near-surface currents may be further improved. Depths estimates might be improved by combining estimates from linear-wave theory with wave-dissipation based estimates [29, 43] and color-based depth estimates [134, 135]. Near-surface current estimates might be improved by accounting for their variability over depth [86], but also by combining wave-derived estimates with optical-flow of the undisturbed, wave-averaged, water surface [127]. Yet, the quality of WCRS does not lay in its accuracy, but in its ability to provide spatial and presentable information with little effort. The accuracy is fundamentally restricted by the physical model (e.g., linear wave theory), the size of the waves (e.g., the spatial resolution) and weather conditions. For many years developers have invested in improving accuracy, which appears to have come to a halt at errors of several decimeters [15]. Future developments should now focus on other aspects, like smart, visually attractive and responsive stand-alone applications to reach a broad coastal community.

Robustness

WCRS should be robust, which is defined as the ability to generate continuous, reliable and usable products. In terms of hardware the user has a choice. XBand-radars can continuously and robustly produce wave-field video, because they are less susceptible to poor weather conditions and work during

the dark [175]. Optical instruments provide less continuous and robust wave-field video as they are largely restricted to day-light conditions (apart from specialistic infrared cameras, which work during the dark [177]) and do not provide usable wave-imagery during poor weather conditions, like thick fog or heavy rain (or cloud cover in case of satellites). Yet, the different instruments can be robust enough to assess a certain coastal problem, depending on the required spatiotemporal scale. For example, five cloud-free and wave-rich satellite image records per year may be enough to follow long-term changes in bathymetry at a certain fieldsite, such that it is not required to use the high temporal resolution of an XBand radar.

WCRS estimates are ideally robust to different fieldsites and hydrodynamic conditions. In the past, WCRS software has often been applied experimentally on short data sets (e.g.,[23]) and/or single field sites (e.g., [15, 20]). Such an approach does not provide confidence in using the software operationally. This study tried to change this experimental and/or single field-site practice by validating and presenting DIA performances for long time periods and several field sites. It was demonstrated that traditional 3D-FFT based algorithms can be used operationally to robustly extract spectral wave characteristics over long time periods (Chapter 2, [3]). This was demonstrated for continuous video data from an XBand radar. Depth estimates, near-surface current estimates and wave directions were returned operationally. In a second step, the robustness of an algorithm was tested by application to a set of video data from different instruments, field sites, lighting conditions and hydrodynamic conditions (Chapter 3, [34]). This approach was inspired by the use of skill-beds for validating the robustness of numerical models [178].

Future developments: The robustness of algorithms should be tested for different instruments, field sites and hydrodynamic conditions. For this purpose it would be favourable to adopt the common practice of skill-beds for validating the robustness of WCRS algorithms. A general and openly accessible skill-bed containing videos of different field-sites (Duck, Porthtowan, Narrabeen, Scheveningen) with corresponding ground truth data could thereby be a big step forward. This work has initiated the generation of such a skill-bed, which is hosted on an openly accessible platform [179].

User-friendliness

In the past, WCRS has not been user-friendly. The cost of applying WCRS came in the form of required user-knowledge on photogrammetry, DIAs and general software skills. These costs had to compete with the benefits of spatial measurements, multifunctionality and the fact that WCRS relies on straightforward optical analysis. In fact, optical analysis is an extensively researched field of science (e.g., used in robotics, the car industry etc. [164, 180, 181]), which suggests that tools exist to make WCRS more user-friendly. Yet, large improvements can still be achieved.

In terms of instruments, cameras and UAVs have become more user friendly

and also satellite data have become easier to use with tools like the Google Earth Engine [165]. XBand radars can be user friendly if the internal processing produces workable video. The possibilities for improvement mainly lay in the software. Until recently, the focus in improving depth and current inversion software has mainly been on the accuracy of the estimates. Little attention has been put on features that would make such algorithms more user-friendly. This study has started to address user-friendliness by striving for fast, intelligent, and visually responsive algorithms (Chapter 3,[34]). A goal was to develop algorithms that could return maps of estimated coastal parameters on-the-fly. Potential end-users would thereby receive immediate and continuous visual response. Another aim was to create algorithms that would not have to be tailored to hydrodynamic conditions (Chapter 3,[3]) and field-sites (Chapter 3,[34]) through manual adjustments of settings. Instead, the algorithms should self-adapt to the data, moving the expertise from the user to an intelligent algorithm.

Future developments: Making WCRS algorithms user-friendly makes it more attractive to use them. In this study, important steps have been made towards this goal, but further improvements are still required. WCRS algorithms should become visually attractive. Again, integrated, standalone-applications are a way to improve, but also the response that WCRS algorithms provide. It is key to move away from the three-step process of video collection, pre-processing and post-processing, and instead move towards integrated software that provides direct response to the user during data collection. Such algorithms are ideally self-adaptive and computationally fast. Standalone applications could additionally include tools to directly derive products like erosion trends, track nourishments or other morphological features and alert the end-user if bathymetry trends or (rip) currents indicate that human action/intervention is required.

5.4. Summary

Since the beginnings of WCRS, the algorithms to derive depths, near-surface currents and wave celerity have become more accessible [143], multifunctional [32], robust [18] and the quality improved [33]. This work put additional attention to the user-friendliness of such algorithms, by making them smarter and faster [3, 34]. By reaching broader user communities, WCRS becomes an increasingly effective coastal monitoring tool. Still much improvement can be gained and efforts should now be channelled towards integrated and fast standalone applications.

WCRS is already a useful tool to derive products for coastal assessments even if it has not yet reached its full potential, for example in terms of multifunctionality or accuracy. To illustrate, monitoring volume changes of a large nourishment may not necessitate highly accurate depth measurements in the moment. It is rather important to detect and monitor changes over longer time periods to be able to plan for possible new intervention measures [36]. For such a purpose, the hardware and software may also not have to be multifunctional, as long as they work robustly for

measuring depths over longer time periods (Chapter 2,[3]).

So how to currently utilize WCRS as an end-user? That depends on the available instrumentation, the budget, and the coastal problem at hand. In this work, different instruments were used to derive depths: Xband-radar (Chapter 2), stationary cameras (Chapter 3), UAV's (Chapter 3) and a satellite (Chapter 4). The choice between instruments can be made based on what is already available, for example a UAV, or be based on what is the most effective instrument for the scale and purpose at hand (Figure 5.1). For example, if changes in bathymetry due to dredging and dumping operations have to be monitored, it might be easiest to use a UAV that sits in the shelf. Yet, if the monitoring program is meant to continue over long periods of time for a large area, it could be more effective to invest in an XBand radar. It might also be an option to combine data of different instruments, for example, the UAV monitoring program could be extended with openly accessible satellite data. Hence, different options exist to choose from as an end-user.

The algorithm that is used to make estimates from video, mostly depends on the coastal parameter which is to be monitored, but also accessibility and user-friendliness may play role. For example, different options exist to estimate depths. Some of the algorithms are openly accessible, like cBathy [20] or the on-the-fly algorithm developed during this study [168]. Yet, not every algorithm is also multifunctional. For example, if besides depths it is desired to map surface current patterns, one might resort to algorithms like XMFit.

5.5. Neighbouring remote sensing techniques

Besides WCRS other remote sensing techniques exist that can be of interest. For example, much effort has been put into the tracking of shoreline positions [182–184]. This can locally be done via projects like CoastSnap [183], which involve the public to take images of beaches. Global tracking of shoreline positions can be done using openly available satellite imagery [182, 184]. Such data can give first order impressions of coastal erosion or accretion and are often already openly available. A benefit of shoreline detection is that shorelines observed during different tidal levels can also be used as isolines of the intertidal bathymetry [185]. In contrast to WCRS, no physical model underlies the intertidal bathymetry estimate, making it ideal to capture the morphology around the coastline where WCRS accuracy suffers from errors due to non-linear wave dynamics (e.g., [48]). Intertidal bathymetries can also be joined with near-shore WCRS bathymetry estimates to extend coverage and converge accuracy [43].

Similar to estimating bathymetry from WCRS, it is also possible to derive bathymetry from multispectral optical imagery [135]. Such bathymetry estimates can reach high accuracies of a few decimetres, but depend on light penetration through the water body. Multispectral bathymetry estimates are therefore sensitive to water turbidity and depth estimates typically do not extend to depths of $15–30\,\mathrm{m}$ [17], as is the case for WCRS (see Chapters 2 to 4).

Besides optical tracking of the shoreline, many more coastal remote sensing techniques and instruments exist (e.g., lidar [186], HF radars [187, 188], structure from

motion [189] etc.). WCRS has its separate position in coastal remote sensing and is generally attractive because different instruments can be used to record video from which a variety of coastal parameters can be estimated, such as bathymetry, but also currents and wave characteristics.

5.6. Vision for the future

So how will future coastal remote sensing look like? It will be simple and mostly space-borne, as it becomes easier to launch satellites and their revisiting periods become shorter (Figure 5.1: satellite moves up towards position XBand radar). As more of these satellite data become openly accessible, this data source will likely start to dominate, which is underscored by the exponentially increasing number of publications concerning "satellite coastal remote sensing" (Figure 5.4, red). Yet, the other remote sensing techniques remain a workable alternative.

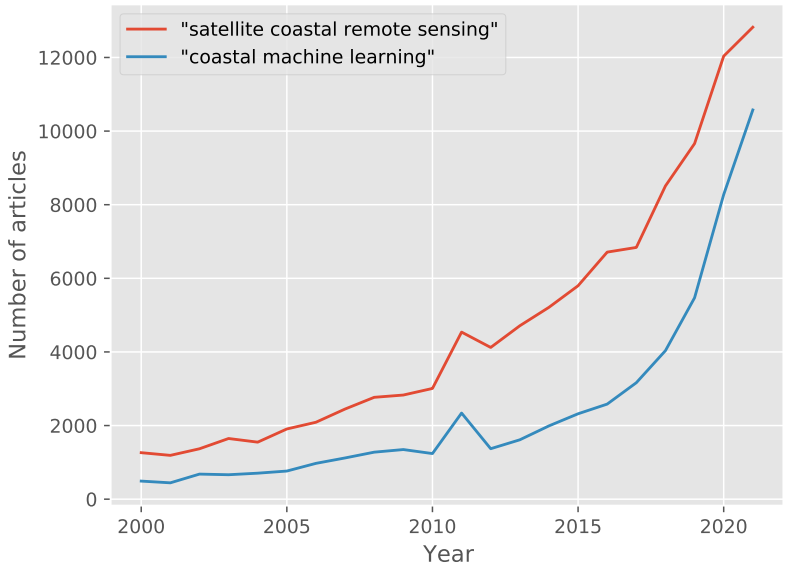

Figure 5.4.: Number of articles published per year containing the key words "satellite coastal remote sensing" (red) and "coastal machine learning" (blue). Source: https://app.dimensions.ai

In efforts to integrate software and map as many coastal parameters as possible, WCRS will become part of a larger framework. Together with wave dissipation based algorithms [29, 43], optical flow algorithms [127], shoreline tracking algorithms [182] and color-based algorithms [135], coastal parameters will be mapped accurately and robustly at high time resolution. The different techniques will be coupled

and computations will occur on-board of the instrument (Chapter 2,[3]), which sends the resulting data to a data cloud, similar to a Google Earth Engine [165]. One can also think of a back and forth coupling with advanced process based numerical models to further improve accuracy in depth and current estimates via data assimilation and Kalman filter based approaches [43, 75]. This would also improve the hydrodynamic and morphodynamic model predictions (e.g., with Delft3D flexible Mesh [190]), such that they could bridge over observation-free periods.

At some point neural networks will start to replace all the existing techniques to deliver ever more accurate and plentiful coastal information. The developments in the field of (coastal) machine learning are rapidly increasing, as indicated by the exponential increase in the number of published articles in this field (Figure 5.4, blue). This number of articles has more than tripled over the past five years 2016-2021. In the future, neural networks will achieve on-the-fly orthorectification [171], spatially three-dimensional wave-field analysis [174] and all-purpose parameter inversion [71, 73]. Such networks will also utilize observations from non-optical satellites, like Synthetic Aperture Radar (SAR) satellites (e.g., Sentinel-1, [191]) and laser-altimetry satellites (e.g., ICESat-2, [192]). The collection of space-borne instruments will be able to collect the desired data during every weather condition.

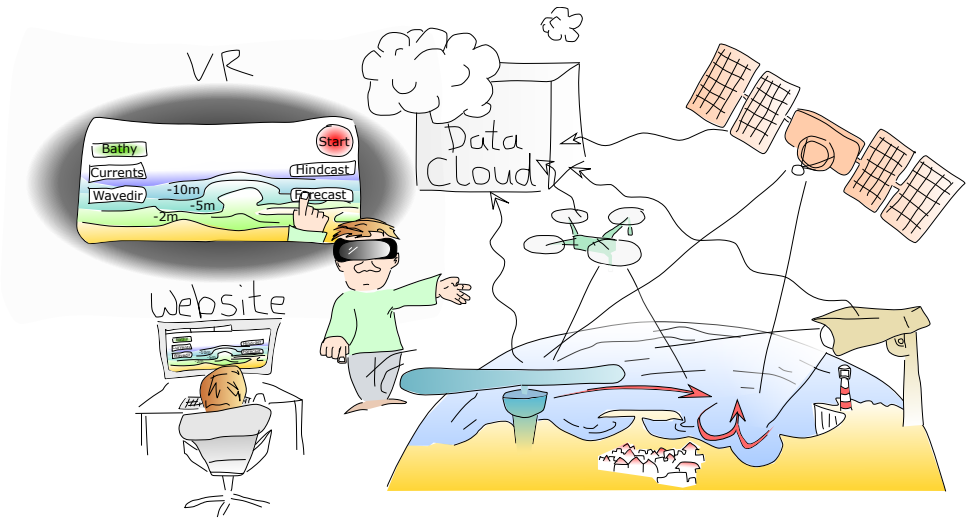

Figure 5.5.: Future of remote sensing. Imagery will be processed on the fly and transferred to the cloud. End-users can access the data online or in virtual reality. Remote sensing data and numerical models will be integrated and hindcasts and forecasts can be made online and on-the-fly.

The only thing left to do as an end-user, will be to access a website (Figure 5.5). This website will show the coastal data for the entire globe (e.g., as [165, 184]). The same platform will also include future predictions, based on neural networks combining observed data with on-the-fly predictions of numerical models running in the cloud. The user will also be able to visit a coastal site in virtual reality,

look under the waves to see the bathymetry and currents and see how they have changed in the past and how they will change in the future. The user will be able to experience different scenarios in virtual reality and will be able to understand if and what interventions need to be undertaken. The user will also be able to give feedback on the performance of the tools and will thereby help to optimize them to their needs, such that developers and users together create a dynamic WCRS environment.

6

Conclusions

The previous chapters demonstrate that a broad coastal community can effectively collect coastal information at different scales from wave-based coastal remote sensing (WCRS). Monitoring coastal bathymetry, near-surface currents and wave hydrodynamics is not only valuable to researchers, but also for decision making in coastal management. Also the industry and coast guard may benefit from the lean-and-mean mapping possibilities of WCRS.

With different instruments to chose from, such as XBand-radars, stationary camera installations, UAVs/drones or satellites, WCRS has become accessible, scalable and more attractive to use. Previous financial barriers are disappearing, as instruments like UAVs have become affordable and as pre-existing instruments, like navigational XBand radars can be employed. Besides that, the application of these remote sensing instruments is less labor-intensive compared to traditional in-situ measurement techniques.

WCRS instruments typically have large spatial coverage and can be used to generate an image sequence, or video, of the coastal waters at some location of interest. Specifically, the wave field and its motions are thereby valuable to record as they contain information about both hydrodynamics and bathymetry. By studying the observed wave characteristics, it is possible to determine the main wave components in the wave field and their wave-direction and phase celerity. Studying wave characteristics moreover allows to invert depths and apparent near-surface currents. This is due to the fact, that waves feel the underlying bathymetry and currents, and react by changing their appearance. Hence, a variety of both hydrodynamic and morphological coastal parameters can be estimated and mapped, from simply observing a wave-field in motion. From these data erosion/accretion trends can be derived, the evolution of nourishments, but also hotspots of concentrated coastal currents or wave-energy.

Over the past four decades, different methods and algorithms have been developed to process image sequences of a wave field and derive the desired hydrodynamics and morphology. Specifically in the context of estimating coastal depths (as proxy for bathymetry), such algorithms are referred to as ”depth inversion algorithm” (DIA). Although they are an appealing alternative to labor-intensive in-situ

measurements along transects, DIAs have often only been applied experimentally. Practical applications, for example for coastal management purposes, have been limited. The group of WCRS users has remained small within the broader coastal community. Plausible reasons are plentiful and found in both hardware and software.

Some problems belong to the past, such as the accessibility of remote sensing instruments, which were previously expensive to purchase (e.g., high resolute camera systems) or not accessible at all (satellites, UAVs). Other problems are in the process of being resolved, such as the open availability of DIAs. With nowadays possibilities to straightforwardly use various remote sensing instruments and share software on openly accessible platforms, the aim of this work was to innovate DIAs towards operational, smarter and faster algorithms. Hopes are that this will stimulate a broader use of WCRS by the coastal community. This work required methodological innovation and gave answer to a set of research questions, which will be addressed point-by-point in the following:

To what extent can DIAs be used on wave-field records of different remote sensing instruments (X-band radar, fixed camera, UAV, satellite) to demonstrate scalability and spatiotemporal coverage of WCRS? (Chapters 2 to 4,[3, 34, 35])

- DIAs can be applied to wave-field records of XBand-radars, fixed cameras, UAVs and satellites. Operational use of a DIA on XBand-radar video enables monitoring on scales of $\mathcal{O}(10\text{–}100\,\mathrm{km}^2)$ at a temporal resolution of $\frac{1}{50}\mathrm{map/min}$ (Chapter 2,[3]). Video from fixed cameras and drones can be analyzed on scales of $\mathcal{O}(0.1\text{–}1\,\mathrm{km}^2)$ at a temporal resolution of $\frac{1}{12}\mathrm{map/s}$ (i.e., on-the-fly) (Chapter 2,[3]). Satellite imagery can be monitored at scales of $\mathcal{O}(100\,\mathrm{km}^2)$, where the temporal resolution mostly depends on the revisiting time of the satellite (days-weeks).

How can DIAs be used operationally to monitor the placement and evolution of a nourishment for dredging and dumping surveillance and coastal management? (Chapter 2,[3])

- a DIA can be configured for operational monitoring. A robust, continuous analysis is achievable by using an iterative approach to handle spectral noise. A 3D-FFT-based spectral decomposition was chosen as basis for the DIA, which is a frequently used approach. It suggests that such ”standard” DIAs are suited for operational application over long time periods.
- errors in depth estimates of $\pm 2\,\mathrm{m}$ do not prevent coastal managers to gain valuable insights. Complex tidal inlet bathymetries of more than $200\,\mathrm{km}^2$ can be monitored over periods of years at a time resolution of hours. What is more, volumetric changes in a nourishment area can be accurately followed, and that can be done from a distance of $7\,\mathrm{km}$. For that purpose an XBand-radar can serve as remote sensing instrument.

- an existing XBand radar, originally set up for navigational purposes, can be used as remote sensing instrument. It stresses the fact that seemingly expensive instruments can be accessible.

How can DIAs self-adapt to wave-field video from different field-sites to reduce required user-expertise (Chapter 3,[34])

- a DIA can be designed to self-adapt to given video data, such that little expertise is needed to apply the DIA. This was demonstrated by analysing video of stationary camera installations and UAVs recorded at four different fieldsites around the world - without manually adjusting algorithm settings.
- to test and validate a DIA, it is favourable to create a skill-bed consisting of several videos and ground truth data. In line with what is common practice for validating numerical models.
- to acquire a self-adaptive and fast DIA, several innovative techniques can be combined. The Dynamic Mode Decomposition (DMD) reduces the data complexity of wavefield video and automatically finds dominant wave components by their phase images and corresponding frequencies. This technique can be combined with loss-functions to counteract spectral outliers and overestimation of near-surface currents, which also has positive effect on the accuracy of depth estimates. Lastly, estimates of depth, wave celerity and surface currents can be quickly converged by temporarily storing and calling up spectral information. Additional fast convergence is achieved using Kalman filtering.

To what extent can DIAs acquire on-the-fly processing capability for analysis of video feeds and lean-and-mean mapping with WCRS? (Chapter 3,[34])

- the processing of video data can occur on-the-fly, with frequent visual response (every few seconds). It suggests the potential application to video feeds of for example UAVs, where continuously mapping updates are given of the bathymetry, but also of wave celerity and near-surface currents. This provides perspective for mapping hydrodynamic and morphological parameters in the field.
- merely $32\,\mathrm{s}$ of video footage were needed for a first mapping update with average depth errors of 0.9–$2.6\,\mathrm{m}$. These further reduced to 0.5–$1.4\,\mathrm{m}$ as the videos continued and more mapping updates were returned.

How can standard DIAs be used on temporally sparse imagery to achieve an increased application range of WCRS? (Chapter 4,[35])

- using pre-existing techniques, satellite data can be augmented to (pseudo) video, which accurately resembles the present wave-field. A sequence of 12

images from Capbreton, France, collected at $1/8\,\mathrm{fps}$ by the Pleiades satellite, was augmented to a $1.5\,\mathrm{min}$ (pseudo) video with a framerate of $1\,\mathrm{fps}$. The spectral wave-content in the video compared with in-situ buoy measurements.

- augmented satellite imagery can successfully be analysed with a frequency-based DIA to map bathymetry. A complex canyon bathymetry was approximated to a large extent as highlighted by an overall depth bias of $-0.9\,\mathrm{m}$, yet estimates were spatially noisy with an interquartile range of depth errors of $5.1\,\mathrm{m}$.

- in line with findings of Chapter 2 the acquired accuracy of depth estimates, although inferior to in-situ surveys, can be sufficient for practical use. The remotely sensed bathymetry could be applied within a numerical wave model to predict wave heights over the shoreface. Hotspots where wave refraction leads to focussing of wave energy were correctly identified, which has potential implications for coastal hazard assessments.

- Small scale morphological features, such as sandbars could be captured.

What are the perspectives of WCRS for broad future application? (Chapter 5)

This work has demonstrated that WCRS with DIAs provides a flexible set of instruments and tools, to be used by and be useful to the coastal community. The presented possibilities and capabilities of WCRS sketch new perspectives for future application. Coastal management can benefit as complex morphodynamic systems and nourishments can be operationally monitored, for example using existing navigational XBand radars. But also the dredging industry and the coast guard may benefit from lean-and-mean mapping of depths and currents in the field, for example using UAVs and on-the-fly mapping algorithms.

By establishing self-adaptive and on-the-fly software, this study has taken important steps to open WCRS up to a broader end-user community. Laymen can now map the coastal bathymetry. Moreover, by proving WCRS in an operational environment this work has brought the technology to higher readiness levels. Still further improvements are necessary to make WCRS more effective. These improvements can be achieved on five properties of WCRS: accessibility, multifunctionality, quality, robustness and user-friendliness. The key takeaway for effective, adoptable WCRS is that developments should strive towards integrated, self-adaptive software, which gives prompt visual response and requires little user-expertise. These measures reduce the difficulty to learn WCRS, increase its compatibility with data from different instruments (cameras, UAVs, Xband-radars, satellites) and thereby enable relatively easy coastal measurements.

As satellite data become more available to the general public, an important new image source with global coverage can be exploited for potential hydrodynamic and morphological analysis. In the future, spaceborne remote sensing will play a crucial role in the acquisition of coastal data. These data may be combined with numerical

models to establish integrated software for hindcasting and forecasting and could be powered by machine learning techniques and cloud computing.

Acknowledgements

Four years of research has been four years of fun and a number of people are responsible for that.

To my family

Christa and Joachim, the best way to relax once in a while is to be at hotel mom. Plentiful food and drinks always make for a smooth ride with reading and writing papers. You are always confident that things turn out the right way and with that mindset I cruise through life. Erik and Bas, I enjoy the brotherly vibe, which is just always there vibrating through spacetime. Definitely the best family there is.

Britt, mijn dagelijks entertainment. Working from home has got a whole new dimension with you. I'm not sure whether you knew what I was doing aside from looking nerdy at a black screen with code. Sometimes I didn't know myself. I enjoy your company every day and nothing is better than to start with a nice Brittmade coffee in the morning. To be continued.

Géza, you can't read this, but as long as you wiggle your tail everything and everybody is happy. All the time.

To my dear PhD fellows

Anne, Anna and Christa, although I've spent only two of the four years in the office, it has always been great to be there. Most impressive was your ability to listen to stuff coming out of my mouth, which was often timed to moments when you were deeply focused and needed a distraction. Our trip to Florida was memorable: drinks, airboat trips, SUP, crocodiles, crocodile burgers, manatees (no manatee burgers) and not to forget the big finale of a solid sunburn after sailing with Nathaniel. We had fun at work (always a crate of beer in the closet, is it still there?), but also outside of work. Every one of you is a great and inspiring researcher and I have no doubt that we will keep crossing paths, whether at work or at a sailing championship Anna?, a picknick on the Marker Wadden Anne?, or another visit to the US Christa?

The saturday night gang, Ermano, Irene, Jessica, Robert, Chris, Matt, Orson, Erik and Stefan, it has been fun hanging around with you. Whether at PS or during wedding drinks in the Hague. Once a while my head popped up at your office doors and it was always time for a cup of delicious, freshly ground coffee from the machine. See you around.

It was also always worth to stretch the legs and go for a trip to the fluid lab. Deep down in those lairs, often awaited me the positivity of Lodewijk, Stuart, Yorick, Ana,

Jill and Matt and, yes, coffee. Or in the case of Lodewijk, a coup of tea. Once in while, Stuart had yet again organized a BBQ or a Bavarian Fluid Mechanics Workshop and I was always honoured to be invited. In summary, all the fluids flow in the lab.

To my dear supervisors

Stefan and Sierd: you were the best supervisors I could have wished for.

Sierd, you had the amazing ability to give me tremendous amounts of freedom and still channel that towards written products. That has made my PhD. I did not experience the infamous dip during the past four years, on the contrary it was a delight: I always woke up happy in the morning, knowing I could do another day of research. You are an inspiring, unbiased person and you've triggered me with your way of thought. You and Marion are the nicest people, inviting me to your home for absolutely delicious French food, but also going for Pizza or popping by a small Thai restaurant. One thing is for sure, we both love food. And a fitting beverage. If anything stands out, it is your love for Currywurst, which you will never miss out on during a classic motorbike trip to Germany.

Stefan, you are open, friendly and spontaneous. On the fourth day of my PhD we already sat in the train to Germany with Tjerk and we immediately had a good time. Half a year later we crossed paths in the hallway: "Hey Matthijs, do you want to come with me to Germany to visit the King" and yes I did, and so we toured to the eastern neighbours again, this time in your car. In the meantime you know this, but by taking me on this trip you have become the reason for me meeting my better half. It clearly shows what you do best: you bring people together. Any PhD will be happy under your supervision as their well-being comes first, a "how are you" will always precede the order of the day.

Sierd and Stefan you make for a great supervising team, you are connected by open-mindedness, but probably more importantly your common love for our eastern neighbours.

To my friends in France

i.e., Rafael and Erwin. Thank you for the great time in Toulouse. I was humbled that you immediately involved me in your research after we met for the first time. If I remember correctly, that was back in 2018 during the CIRN meeting. In the meantime, we've supervised a master student together, and we have published two papers. As always, the best part though was that we dined at French and Lebanese (plus de falafel s'il vous plait) restaurants in Toulouse and bouldered together. Can't wait for the next activity.

To my AMO collegues

Once at AMO you are sold. I am proud to be part of the family. It was great to stay involved over the past four years and hear about all the amazing models that were being developed and projects that were going on. I can't wait to fully return again. Starting with a Latte macchiato in morning, right Björn?

To the members of ZABAWAS

Thank you for giving me the opportunity to do this research. I feel privileged that I could spend four years on research, meet other researchers in the field and build a network. It was a pleasure meeting you several times at the Sand-Engine to go for a walk, discuss all the beautiful things coastal research has to offer and top it off with a nice dinner. I hope that there are more opportunities like that to come.

Bibliography

[1] H. de Vriend and M. van Koningsveld. *Building with Nature: Thinking, acting and interacting differently.* Tech. rep. 2012. doi: 10.1080/02513625.2014.925714. arXiv: arXiv:1011.1669v3.

[2] M. Radermacher, M. Wengrove, J. Van Thiel De Vries and R. Holman. 'Applicability of video-derived bathymetry estimates to nearshore current model predictions'. In: *Journal of Coastal Research* 70.70 (2014), pp. 290–295. issn: 15515036. doi: 10.2112/SI70-049.1.

[3] M. Gawehn, A. van Dongeren, S. de Vries, C. Swinkels, R. Hoekstra, S. Aarninkhof and J. Friedman. 'The application of a radar-based depth inversion method to monitor near-shore nourishments on an open sandy coast and an ebb-tidal delta'. In: *Coastal Engineering* 159.April (2020), p. 103716. issn: 03783839. doi: 10.1016/j.coastaleng.2020.103716.

[4] A. Netzband and C. Adnitt. 'Dredging Management Practices for the Environment : a Structured Selection Approach'. In: *Terra Et Aqua* 114 (2009), pp. 3–8.

[5] A. Ton, M. Lee, S. Vos, M. Gawehn, K. den Heijer and S. Aarninkhof. 'Beach and nearshore monitoring techniques'. In: *Sandy Beach Morphodynamics*. Ed. by D. Jackson and A. Short. Elsevier, 2020. Chap. 27, pp. 659–687. isbn: 9780081029275. doi: 10.1016/B978-0-08-102927-5.00027-8. url: http://dx.doi.org/10.1016/B978-0-08-102927-5/00027-8%20https://linkinghub.elsevier.com/retrieve/pii/B9780081029275000278.

[6] S. De Vries. 'Physics of Blown Sand and Coastal Dunes'. PhD thesis. Delft Technical University, 2013, p. 289. isbn: 9789055841745.

[7] Q. Lodder and P. Sørensen. 'Comparing the morphological behaviour of Dutch-Danish shoreface nourishments'. In: *Coastal Management: Changing coast, changing climate, changing minds* (2015).

[8] B. Huisman, D.-J. Walstra, M. Radermacher, M. de Schipper and G. Ruessink. 'Observations and Modelling of Shoreface Nourishment Behaviour'. In: *Journal of Marine Science and Engineering* 7.3 (2019), p. 59. doi: 10.3390/jmse7030059.

[9] W. J. Botzen and J. C. Van Den Bergh. 'Insurance against climate change and flooding in the Netherlands: Present, future, and comparison with other countries'. In: *Risk Analysis* 28.2 (2008), pp. 413–426. issn: 02724332. doi: 10.1111/j.1539-6924.2008.01035.x.

[10] M. Van Koningsveld, M. A. Davidson and D. A. Huntley. 'Matching science with coastal management needs: The search for appropriate coastal state indicators'. In: *Journal of Coastal Research* 21.3 (2005), pp. 399–411. issn: 07490208. doi: 10.2112/03-0076.1.

[11] E. M. Rogers. *Diffusion of innovations*. 3rd. New York : Free Press ; London : Collier Macmillan, 1983, pp. 1–453. isbn: 0-02-926650-5 AACR2.

[12] E. W. Bergsma, R. Almar, L. P. Melo de Almeida and M. Sall. 'On the operational use of UAVs for video-derived bathymetry'. In: *Coastal Engineering* 152.July (2019), p. 103527. issn: 03783839. doi: 10.1016/j.coastaleng.2019.103527.

[13] R. Almar, E. W. Bergsma, G. Thoumyre, M. W. Baba, G. Cesbron, C. Daly, T. Garlan and A. Lifermann. 'Global satellite-based coastal bathymetry from waves'. In: *Remote Sensing* 13.22 (2021), pp. 1–13. issn: 20724292. doi: 10.3390/rs13224628.

[14] E. W. Bergsma, D. C. Conley, M. A. Davidson, T. J. O'Hare and R. Almar. 'Storm event to seasonal evolution of nearshore bathymetry derived from shore-based video imagery'. In: *Remote Sensing* 11.5 (2019), pp. 1–23. issn: 20724292. doi: 10.3390/rs11050519.

[15] R. Holman and E. W. Bergsma. 'Updates to and performance of the cbathy algorithm for estimating nearshore bathymetry from remote sensing imagery'. In: *Remote Sensing* 13.19 (2021), pp. 1–25. issn: 20724292. doi: 10.3390/rs13193996.

[16] G. Donchyts, G. Santinelli, A. P. Luijendijk, F. Baart and M. Verlaan. 'Automated extraction and fusion of the intertidal and subtidal bathymetry from the Landsat and Sentinel satellite data'. In: *NCK*. Enkhuizen, Netherlands: NCK, 2019, p. 1. url: https://www.nck-web.org/boa-2019/154-automated-extraction-and-fusion-of-the-intertidal-and-subtidal-bathymetry-from-the-landsat-and-sentinel-satellite-data.

[17] I. Caballero and R. P. Stumpf. 'On the use of Sentinel-2 satellites and lidar surveys for the change detection of shallow bathymetry: The case study of North Carolina inlets'. In: *Coastal Engineering* 169 (2021), p. 103936. issn: 03783839. doi: 10.1016/j.coastaleng.2021.103936.

[18] K. Hessner, K. Reichert, J. Carlos, N. Borge, C. L. Stevens and M. J. Smith. 'High-resolution X-Band radar measurements of currents , bathymetry and sea state in highly inhomogeneous coastal areas'. In: *Ocean Dynamics* (2014), pp. 989–998. doi: 10.1007/s10236-014-0724-7.

[19] R. A. Dalrymple, J. H. MacMahan, A. J. Reniers and V. Nelko. 'Rip currents'. In: *Annual Review of Fluid Mechanics* 43 (2011), pp. 551–581. issn: 00664189. doi: 10.1146/annurev-fluid-122109-160733.

[20] R. Holman, N. Plant and T. Holland. 'CBathy: A robust algorithm for estimating nearshore bathymetry'. In: *Journal of Geophysical Research: Oceans* 118.5 (2013), pp. 2595–2609. issn: 21699291. doi: 10.1002/jgrc.20199.

[21] C. M. Senet, J. Seemann, S. Flampouris and F. Ziemer. 'Determination of bathymetric and current maps by the method DiSC based on the analysis of nautical X-band radar image sequences of the sea surface (November 2007)'. In: *IEEE Transactions on Geoscience and Remote Sensing* 46.8 (2008), pp. 2267–2279. issn: 01962892. doi: 10.1109/TGRS.2008.916474.

[22] K. Reichert, K. Hessner, J. C. Nieto Borge and J. Dittmer. 'WaMoS II: A radar based wave and current monitoring system'. In: *Proceedings of the 1999 Ninth International Offshore and Polar Engineering Conference (Volume 3), Brest, France, 30 May - 4 June 1999* (1999), pp. 139–143.

[23] P. Bell. 'Mapping Shallow Water Coastal Areas Using a Standard Marine X-Band Radar'. In: *Hydro8, Liverpool, 4th-6th November 2008* (2008), pp. 1–9.

[24] European Commission. *Technology Readiness Levels (TRL)*. Tech. rep. 2014. 2014, p. 1. url: http://ec.europa.eu/research/participants/data/ref/h2020/wp/2014_2015/annexes/h2020-wp1415-annex-g-trl_en.pdf.

[25] W. Williams. 'The Determination of Gradients on Enemy-Held Beaches'. In: *The Geographical Journal* 109.1/3 (1947), pp. 76–90. url: http://www.jstor.org/stable/1789903.

[26] I. R. Young, W. Rosenthal and F. Ziemer. 'A three-dimensional analysis of marine radar images for the determination of ocean wave directionality and surface currents.' In: *Journal of Geophysical Research* 90.C1 (1985), pp. 1049–1059. issn: 01480227. doi: 10.1029/JC090iC01p01049.

[27] P. Bell. 'Shallow water bathymetry derived from an analysis of X-band marine radar images of waves'. In: *Coastal Engineering* 37.3-4 (1999), pp. 513–527. issn: 03783839. doi: 10.1016/S0378-3839(99)00041-1.

[28] J. P. Dugan, C. C. Piotrowski and J. Z. Williams. 'Water depth and surface current retrievals from airborne optical measurements of surface gravity wave dispersion'. In: *Journal of Geophysical Research: Oceans* 106.C8 (2001), pp. 16903–16915. issn: 21699291. doi: 10.1029/2000jc000369.

[29] S. G. J. Aarninkhof, B. G. Ruessink and J. A. Roelvink. 'Nearshore subtidal bathymetry from time-exposure video images'. In: *Journal of Geophysical Research: Oceans* 110.6 (2005), pp. 1–13. issn: 21699291. doi: 10.1029/2004JC002791.

[30] F. Serafino, C. Lugni and F. Soldovieri. 'A novel strategy for the surface current determination from marine X-Band radar data'. In: *IEEE Geoscience and Remote Sensing Letters* 7.2 (2010), pp. 231–235. issn: 1545598X. doi: 10.1109/LGRS.2009.2031878.

[31] M. Dobbins, R. Cockerill and J. Barnsley. 'Factors affecting the utilization of systematic reviews: A study of public health decision makers'. In: *International Journal of Technology Assessment in Health Care* 17.2 (2001), pp. 203–214. issn: 02664623. doi: 10.1017/S0266462300105069.

[32] G. Ludeno, F. Reale, F. Dentale, E. P. Carratelli, A. Natale, F. Soldovieri and F. Serafino. 'An X-band radar system for bathymetry and wave field analysis in a harbour area'. In: *Sensors (Switzerland)* 15.1 (2015), pp. 1691–1707. issn: 14248220. doi: 10.3390/s150101691.

[33] D. A. Honegger, M. C. Haller and R. A. Holman. 'High-resolution bathymetry estimates via X-band marine radar: 1. beaches'. In: *Coastal Engineering* 149.March (2019), pp. 39–48. issn: 03783839. doi: 10.1016/j.coastaleng.2019.03.003.

[34] M. Gawehn, S. de Vries and S. Aarninkhof. 'A Self-Adaptive Method for Mapping Coastal Bathymetry On-The-Fly from Wave Field Video'. In: *Remote Sensing* 13.23 (2021), p. 4742. issn: 20724292. doi: 10.3390/rs13234742.

[35] M. Gawehn, R. Almar, E. W. J. Bergsma, S. de Vries and S. Aarninkhof. 'Depth Inversion from Wave Frequencies in Temporally Augmented Satellite Video'. In: *Remote Sensing* 14.8 (Apr. 2022), p. 1847. issn: 2072-4292. doi: 10.3390/rs14081847.

[36] L. Hamm, M. Capobianco, H. H. Dette, A. Lechuga, R. Spanhoff and M. J. Stive. 'A summary of European experience with shore nourishment'. In: *Coastal Engineering* (2002). issn: 03783839. doi: 10.1016/S0378-3839(02)00127-8.

[37] M. J. Stive, M. A. de Schipper, A. P. Luijendijk, S. G. Aarninkhof, C. van Gelder-Maas, J. S. van Thiel de Vries, S. de Vries, M. Henriquez, S. Marx and R. Ranasinghe. 'A New Alternative to Saving Our Beaches from Sea-Level Rise: The Sand Engine'. In: *Journal of Coastal Research* 290 (2013), pp. 1001–1008. issn: 0749-0208. doi: 10.2112/jcoastres-d-13-00070.1.

[38] A. Kroon, B. van Leeuwen, D.-J. Walstra and L. Gerard. 'Dealing with uncertainties in long-term predictions of a coastal nourishment'. In: *Coastal Management* (2016), pp. 9–18. doi: doi:10.1680/cm.61149.009.

[39] J. Borge, R. Rodríguez, K. Hessner and P. González. 'Inversion of marine radar images for surface wave analysis'. In: *Journal of Atmospheric and Oceanic Technology* 21.8 (2004), pp. 1291–1300. issn: 07390572. doi: 10.1175/1520-0426(2004)021<1291:IOMRIF>2.0.CO;2.

[40] G. R. Valenzuela. 'Theories for the interaction of electromagnetic and oceanic waves - A review'. In: *Boundary-Layer Meteorology* 13.1-4 (1978), pp. 61–85. issn: 00068314. doi: 10.1007/BF00913863.

[41] W. J. Plant. 'Bragg Scattering of Electromagnetic Waves from the Air/Sea Interface'. In: *Surface Waves and Fluxes*. Dordrecht: Springer, 1990, pp. 41–108. doi: 10.1007/978-94-009-0627-3_2.

[42] K. Hessner, K. Reichert and W. Rosenthal. 'Mapping of Sea Bottom Topography in Shallow Seas by Using a Nautical Radar'. In: *2nd International Symposium on Operationalization of Remote Sensing, Enschede, The Netherlands*. 1999, pp. 1–5.

[43] A. van Dongeren, N. Plant, A. Cohen, D. Roelvink, M. C. Haller and P. Catalán. 'Beach Wizard: Nearshore bathymetry estimation through assimilation of model computations and remote observations'. In: *Coastal Engineering* 55.12 (2008), pp. 1016–1027. issn: 03783839. doi: 10.1016/j.coastaleng.2008.04.011.

[44] D. Trizna. 'Errors in bathymetric retrievals using linear dispersion in 3-D FFT analysis of marine radar ocean wave imagery'. In: *IEEE Transactions on Geoscience and Remote Sensing* 39.11 (2001), pp. 2465–2469. issn: 01962892. doi: 10.1109/36.964983.

[45] J. Rutten, S. M. De Jong and G. Ruessink. 'Accuracy of Nearshore Bathymetry Inverted from X-Band Radar and Optical Video Data'. In: *IEEE Transactions on Geoscience and Remote Sensing* 55.2 (2017), pp. 1106–1116. issn: 01962892. doi: 10.1109/TGRS.2016.2619481.

[46] J. Campana, E. J. Terrill and T. de Paolo. 'The development of an inversion technique to extract vertical current profiles from X-band radar observations'. In: *Journal of Atmospheric and Oceanic Technology* 33.9 (2016), pp. 2015–2028. issn: 15200426. doi: 10.1175/JTECH-D-15-0145.1.

[47] C. M. Senet, J. Seemann and F. Ziemer. 'The near-surface current velocity determined from image sequences of the sea surface'. In: *IEEE Transactions on Geoscience and Remote Sensing* 39.3 (2001), pp. 492–505. issn: 01962892. doi: 10.1109/36.911108.

[48] P. Bell. 'Determination of bathymetry using marine radar images of waves'. In: *Ocean Wave Measurement and Analysis* (2001), pp. 251–257. doi: 10.1061/40604(273)26. url: http://nora.nerc.ac.uk/2601/.

[49] S. Flampouris, J. Seemann, C. Senet and F. Ziemer. 'The influence of the inverted sea wave theories on the derivation of coastal bathymetry'. In: *IEEE Geoscience and Remote Sensing Letters* 8.3 (2011), pp. 436–440. issn: 1545598X. doi: 10.1109/LGRS.2010.2082491.

[50] D. A. Honegger, M. C. Haller and R. A. Holman. 'High-resolution bathymetry estimates via X-band marine radar: 2. Effects of currents at tidal inlets'. In: *Coastal Engineering* 156.December 2019 (2020), p. 103626. issn: 03783839. doi: 10.1016/j.coastaleng.2019.103626.

[51] J. Seemann, F. Ziemer and C. Senet. 'A method for computing calibrated ocean wave spectra from measurements with a nautical X-band radar'. In: *Oceans '97. MTS/IEEE Conference Proceedings*. Vol. 2. IEEE, 1997, pp. 1148–1154. isbn: 0-7803-4108-2. doi: 10.1109/OCEANS.1997.624154. url: http://ieeexplore.ieee.org/document/624154/.

[52] K. Hessner, S. Wallbridge and T. Dolphin. 'Validation of areal wave and current measurements based on X-band radar'. In: *2015 IEEE/OES 11th Current, Waves and Turbulence Measurement, CWTM 2015* (2015), pp. 1–10. doi: 10.1109/CWTM.2015.7098102.

[53] T. K. Holland. 'Application of the linear dispersion relation with respect to depth inversion and remotely sensed imagery'. In: *IEEE Transactions on Geoscience and Remote Sensing* 39.9 (2001), pp. 2060–2072. issn: 01962892. doi: 10.1109/36.951097.

[54] M. A. de Schipper, S. de Vries, G. Ruessink, R. C. de Zeeuw, J. Rutten, C. van Gelder-Maas and M. J. Stive. 'Initial spreading of a mega feeder nourishment: Observations of the Sand Engine pilot project'. In: *Coastal Engineering* 111 (2016), pp. 23–38. issn: 03783839. doi: 10.1016/j.coastaleng.2015.10.011.

[55] B. C. Van Prooijen, M. F. Tissier, F. P. De Wit, S. G. Pearson, L. B. Brakenhoff, M. C. Van Maarseveen, M. Van Der Vegt, J. W. Mol, F. Kok, H. Holzhauer, J. J. Van Der Werf, T. Vermaas, M. Gawehn, B. Grasmeijer, E. P. Elias, P. K. Tonnon, G. Santinelli, J. A. Antolínez, P. L. M. De Vet, A. J. Reniers, Z. B. Wang, C. Den Heijer, C. Van Gelder-Maas, R. J. Wilmink, C. A. Schipper and H. De Looff. 'Measurements of hydrodynamics, sediment, morphology and benthos on Ameland ebb-tidal delta and lower shoreface'. In: *Earth System Science Data* 12.4 (2020), pp. 2775–2786. issn: 18663516. doi: 10.5194/essd-12-2775-2020.

[56] E. P. Elias, A. J. Van der Spek, S. G. Pearson and J. Cleveringa. 'Understanding sediment bypassing processes through analysis of high-frequency observations of Ameland Inlet, the Netherlands'. In: *Marine Geology* 415.May (2019), pp. 1–27. issn: 00253227. doi: 10.1016/j.margeo.2019.06.001.

[57] K. J. Lenstra, S. R. Pluis, W. Ridderinkhof, G. Ruessink and M. van der Vegt. 'Cyclic channel-shoal dynamics at the Ameland inlet: the impact on waves, tides, and sediment transport'. In: *Ocean Dynamics* 69.4 (2019), pp. 409–425. issn: 16167228. doi: 10.1007/s10236-019-01249-3.

[58] S. H. Chan, R. Khoshabeh, K. B. Gibson, P. E. Gill and T. Q. Nguyen. 'An augmented Lagrangian method for total variation video restoration'. In: *IEEE Transactions on Image Processing* 20.11 (2011), pp. 3097–3111. issn: 10577149. doi: 10.1109/TIP.2011.2158229.

[59] M. A. de Schipper, B. C. Ludka, B. Raubenheimer, A. P. Luijendijk and T. A. Schlacher. 'Beach nourishment has complex implications for the future of sandy shores'. In: *Nature Reviews Earth and Environment* 2.1 (2021), pp. 70–84. issn: 2662138X. doi: 10.1038/s43017-020-00109-9.

[60] A. van Dongeren, P. Ciavola, G. Martinez, C. Viavattene, T. Bogaard, O. Ferreira, R. Higgins and R. McCall. 'Introduction to RISC-KIT: Resilience-increasing strategies for coasts'. In: *Coastal Engineering* 134.October 2017

(2018), pp. 2–9. issn: 03783839. doi: 10.1016/j.coastaleng.2017.10.007.

[61] M. J. Austin, T. M. Scott, P. E. Russell and G. Masselink. 'Rip current prediction: Development, validation, and evaluation of an operational tool'. In: *Journal of Coastal Research* 29.2 (2013), pp. 283–300. issn: 07490208. doi: 10.2112/JCOASTRES-D-12-00093.1.

[62] M. Davidson, S. Aarninkhof, M. Van Koningsveld and R. Holman. 'Developing coastal video monitoring systems in support of coastal zone management'. In: *Journal of Coastal research* 2004.39 (2006), pp. 49–56. issn: 0749-0208.

[63] R. A. Holman and J. Stanley. 'The history and technical capabilities of Argus'. In: *Coastal Engineering* 54.6-7 (2007), pp. 477–491. issn: 03783839. doi: 10.1016/j.coastaleng.2007.01.003.

[64] K. L. Brodie, B. L. Bruder, R. K. Slocum and N. J. Spore. 'Simultaneous Mapping of Coastal Topography and Bathymetry from a Lightweight Multicamera UAS'. In: *IEEE Transactions on Geoscience and Remote Sensing* 57.9 (2019), pp. 6844–6864. issn: 15580644. doi: 10.1109/TGRS.2019.2909026.

[65] K. T. Holland, D. M. Lalejini, S. D. Spansel and R. A. Holman. 'Littoral environmental reconnaissance using tactical imagery from unmanned aircraft systems'. In: *Ocean Sensing and Monitoring II* 7678 (2010), p. 767806. issn: 0277786X. doi: 10.1117/12.852952.

[66] R. A. Holman, K. T. Holland, D. M. Lalejini and S. D. Spansel. 'Surf zone characterization from Unmanned Aerial Vehicle imagery'. In: *Ocean Dynamics* 61.11 (2011), pp. 1927–1935. issn: 16167341. doi: 10.1007/s10236-011-0447-y.

[67] R. A. Holman, K. L. Brodie and N. J. Spore. 'Surf Zone Characterization Using a Small Quadcopter: Technical Issues and Procedures'. In: *IEEE Transactions on Geoscience and Remote Sensing* 55.4 (2017), pp. 2017–2027. issn: 01962892. doi: 10.1109/TGRS.2016.2635120.

[68] F. Ziemer. 'Directional spectra from shipboard navigation radar during LEWEX'. In: *Directional Ocean Wave Spectra: Measuring, Modeling, Predicting, and Applying*. Ed. by R. C. Beal. Vol. 1. Baltimore: THE JOHNS HOPKINS UNIVERSITY PRESS, 1991, pp. 125–127. isbn: 0801842611.

[69] R. Abileah. 'Mapping near shore bathymetry using wave kinematics in a time series of WorldView-2 satellite images'. In: *International Geoscience and Remote Sensing Symposium (IGARSS)* 2 (2013), pp. 2274–2277. doi: 10.1109/IGARSS.2013.6723271.

[70] R. Almar, E. W. Bergsma, P. Maisongrande and L. P. M. de Almeida. 'Wave-derived coastal bathymetry from satellite video imagery: A showcase with Pleiades persistent mode'. In: *Remote Sensing of Environment* 231.July (2019), p. 111263. issn: 00344257. doi: 10.1016/j.rse.2019.111263.

[71] R. Benshila, G. Thoumyre, M. A. Najar, G. Abessolo, R. Almar, E. Bergsma, G. Hugonnard, L. Labracherie, B. Lavie, T. Ragonneau, E. Simon, B. Vieuble and D. Wilson. 'A Deep Learning Approach for Estimation of the Nearshore Bathymetry'. In: *Journal of Coastal Research* 95.sp1 (2020), pp. 1011–1015. issn: 15515036. doi: 10.2112/SI95-197.1.

[72] P. Chernyshov, T. Vrecica, M. Streßer, R. Carrasco and Y. Toledo. 'Rapid wavelet-based bathymetry inversion method for nearshore X-band radars'. In: *Remote Sensing of Environment* 240.January (2020), p. 111688. issn: 00344257. doi: 10.1016/j.rse.2020.111688.

[73] A. M. Collins, K. L. Brodie, B. A. Spicer, T. J. Hesser, M. W. Farthing, J. Lee and J. W. Long. 'Bathymetric inversion and uncertainty estimation from synthetic surf-zone imagery with machine learning'. In: *Remote Sensing* 12.20 (2020), pp. 1–28. issn: 20724292. doi: 10.3390/rs12203364.

[74] H. Ghorbanidehno, J. Lee, M. Farthing, T. Hesser, P. K. Kitanidis and E. F. Darve. 'Novel data assimilation algorithm for nearshore bathymetry'. In: *Journal of Atmospheric and Oceanic Technology* 36.4 (2019), pp. 699–715. issn: 15200426. doi: 10.1175/JTECH-D-18-0067.1.

[75] G. W. Wilson, H. T. Özkan-Haller, R. A. Holman, M. C. Haller, D. A. Honegger and C. C. Chickadel. 'Surf zone bathymetry and circulation predictions via data assimilation of remote sensing observations'. In: *Journal of Geophysical Research: Oceans* 119.3 (Mar. 2014), pp. 1993–2016. issn: 21699275. doi: 10.1002/2013JC009213.

[76] V. Atanassov, W. Rosenthal and F. Ziemer. 'Removal of ambiguity of two-dimensional power spectra obtained by processing ship radar images of ocean waves'. In: *Journal of Geophysical Research* 90.C1 (1985), p. 1061. issn: 0148-0227. doi: 10.1029/JC090iC01p01061.

[77] J. C. N. Borge, K. Reichert and J. Dittmer. 'Use of nautical radar as a wave monitoring instrument'. In: *Coastal Engineering* 37.3-4 (1999), pp. 331–342. issn: 03783839. doi: 10.1016/S0378-3839(99)00032-0.

[78] P. Izquierdo and C. Guedes Soares. 'Analysis of sea waves and wind from X-band radar'. In: *Ocean Engineering* 32.11-12 (2005), pp. 1404–1419. issn: 00298018. doi: 10.1016/j.oceaneng.2004.11.005.

[79] J. Wolf and P. S. Bell. 'Waves at Holderness from X-band radar'. In: *Coastal Engineering* 43.3-4 (2001), pp. 247–263. issn: 03783839. doi: 10.1016/S0378-3839(01)00016-3.

[80] G. B. Irani, B. L. Gotwols and A. W. Bjerkaas. 'THE 1978 OCEAN WAVE DYNAMICS EXPERIMENT, Optical and in Situ Measurement of the Phase Velocity of Wind Waves'. In: *Wave Dynamics and Radio Probing of the Ocean Surface*. Ed. by O. Phillips and K. Hasselmann. 1st ed. New York and London: Plenum Press, 1986. Chap. 10, pp. 165–179. isbn: 9781468489828.

[81] B. Jähne, J. Klinke, P. Geißler and F. Hering. 'Image Sequence Analysis of Ocean Wind Waves'. In: *Proceedings of the International Seminar on Imaging in Transport Processes*. Athens, Greece, 1992, pp. 1–12.

[82] H. F. Stockdon and R. A. Holman. 'Estimation of wave phase speed and nearshore bathymetry from video imagery'. In: *Journal of Geophysical Research: Oceans* 105.C9 (2000), pp. 22015–22033. issn: 21699291. doi: 10.1029/1999jc000124.

[83] S. Zuckerman and S. Anderson. 'Bathymetry and water-level estimation using x-band radar at a tidal inlet'. In: *Journal of Coastal Research* 34.5 (2018), pp. 1227–1235. issn: 15515036. doi: 10.2112/JCOASTRES-D-17-00182.1.

[84] A. D. Heathershaw, M. W. Blackley and P. J. Hardcastle. 'Wave direction estimates in coastal waters using radar'. In: *Coastal Engineering* 3.C (1979), pp. 249–267. issn: 03783839. doi: 10.1016/0378-3839(79)90027-9.

[85] M. G. Mattie and D. Lee Harris. 'The Use of Imaging Radar in Studying Ocean Waves'. In: *Coastal Engineering* (1978), pp. 174–189.

[86] B. K. Smeltzer, E. Æsøy, A. Ådnøy and S. Ellingsen. 'An Improved Method for Determining Near-Surface Currents From Wave Dispersion Measurements'. In: *Journal of Geophysical Research: Oceans* 124.12 (2019), pp. 8832–8851. issn: 21699291. doi: 10.1029/2019JC015202. arXiv: 1904.11575.

[87] G. Simarro, D. Calvete, P. Luque, A. Orfila and F. Ribas. 'UBathy: A new approach for bathymetric inversion from video imagery'. In: *Remote Sensing* 11.23 (2019), pp. 1–24. issn: 20724292. doi: 10.3390/rs11232722.

[88] S. L. Brunton, J. L. Proctor, J. H. Tu and J. N. Kutz. 'Compressed sensing and dynamic mode decomposition'. In: *Journal of Computational Dynamics* 2.2 (2015), pp. 165–191. issn: 21582505. doi: 10.3934/jcd.2015002.

[89] J. H. Tu, C. W. Rowley, D. M. Luchtenburg, S. L. Brunton and J. N. Kutz. 'On dynamic mode decomposition: Theory and applications'. In: *Journal of Computational Dynamics* 1.2 (2014), pp. 391–421. issn: 21582505. doi: 10.3934/jcd.2014.1.391. arXiv: 1312.0041.

[90] M. R. Jovanović, P. J. Schmid and J. W. Nichols. 'Sparsity-promoting dynamic mode decomposition'. In: *Physics of Fluids* 26.2 (2014). issn: 10897666. doi: 10.1063/1.4863670. arXiv: 1309.4165.

[91] J. L. Proctor, S. L. Brunton and J. N. Kutz. 'Dynamic mode decomposition with control'. In: *SIAM Journal on Applied Dynamical Systems* 15.1 (2016), pp. 142–161. issn: 15360040. doi: 10.1137/15M1013857. arXiv: 1409.6358.

[92] J. N. Kutz, X. Fu and S. L. Brunton. 'Multiresolution dynamic mode decomposition'. In: *SIAM Journal on Applied Dynamical Systems* 15.2 (2016), pp. 713–735. issn: 15360040. doi: 10.1137/15M1023543. arXiv: 1506.00564.

[93] S. Klus, P. Gelß, S. Peitz and C. Schütte. 'Tensor-based dynamic mode decomposition'. In: *Nonlinearity* 31.7 (2018), pp. 3359–3380. issn: 13616544. doi: 10.1088/1361-6544/aabc8f. arXiv: 1606.06625.

[94] T. Askham and J. N. Kutz. 'Variable projection methods for an optimized dynamic mode decomposition'. In: *SIAM Journal on Applied Dynamical Systems* 17.1 (2018), pp. 380–416. issn: 15360040. doi: 10.1137/M1124176. arXiv: 1704.02343.

[95] E. Barocio, B. C. Pal, N. F. Thornhill and A. R. Messina. 'A Dynamic Mode Decomposition Framework for Global Power System Oscillation Analysis'. In: *IEEE Transactions on Power Systems* 30.6 (2015), pp. 2902–2912. issn: 08858950. doi: 10.1109/TPWRS.2014.2368078.

[96] N. Mohan, K. P. Soman and S. Sachin Kumar. 'A data-driven strategy for short-term electric load forecasting using dynamic mode decomposition model'. In: *Applied Energy* 232.October (2018), pp. 229–244. issn: 03062619. doi: 10.1016/j.apenergy.2018.09.190.

[97] B. W. Brunton, L. A. Johnson, J. G. Ojemann and J. N. Kutz. 'Extracting spatial-temporal coherent patterns in large-scale neural recordings using dynamic mode decomposition'. In: *Journal of Neuroscience Methods* 258 (2016), pp. 1–15. issn: 1872678X. doi: 10.1016/j.jneumeth.2015.10.010. arXiv: 1409.5496.

[98] R.-q. Wang, L. M. Herdman, L. Erikson, P. Barnard, M. Hummel and M. T. Stacey. 'Interactions of Estuarine Shoreline Infrastructure With Multiscale Sea Level Variability'. In: *Journal of Geophysical Research: Oceans* 122.12 (Dec. 2017), pp. 9962–9979. issn: 2169-9275. doi: 10.1002/2017JC012730. url: https://onlinelibrary.wiley.com/doi/10.1002/2017JC012730.

[99] Z. J. Taylor, R. Gurka, G. A. Kopp and A. Liberzon. 'Long-duration time-resolved PIV to study unsteady aerodynamics'. In: *IEEE Transactions on Instrumentation and Measurement* 59.12 (2010), pp. 3262–3269. issn: 00189456. doi: 10.1109/TIM.2010.2047149.

[100] L. H. Holthuijsen. *Waves in Oceanic and Coastal Waters*. Cambridge: Cambridge University Press, 2007. isbn: ISBN-13: 978-0-521-86028. url: www.cambridge.org.

[101] J. T. Barron. 'A general and adaptive robust loss function'. In: *Proceedings of the IEEE Computer Society Conference on Computer Vision and Pattern Recognition* 2019-June (2019), pp. 4326–4334. issn: 10636919. doi: 10.1109/CVPR.2019.00446. arXiv: 1701.03077.

[102] K. Madsen, H. B. Nielsen and O. Tingleff. *Methods for Non-Linear Least Squares Problems (2nd ed.)* 2nd ed. 2004, pp. 1–58. url: https://orbit.dtu.dk/en/publications/methods-for-non-linear-least-squares-problems-2nd-ed.

[103] M. J. Black and A. Rangarajan. 'On the unification of line processes, outlier rejection, and robust statistics with applications in early vision'. In: *International Journal of Computer Vision* 19.1 (1996), pp. 57–91. issn: 09205691. doi: 10.1007/BF00131148.

[104] P. J. Schmid. 'Dynamic mode decomposition of numerical and experimental data'. In: *Journal of Fluid Mechanics* 656 (2010), pp. 5–28. issn: 14697645. doi: 10.1017/S0022112010001217.

[105] M. Gavish and D. L. Donoho. 'The optimal hard threshold for singular values is $4/\sqrt{3}$'. In: *IEEE Transactions on Information Theory* 60.8 (2014), pp. 5040–5053. issn: 00189448. doi: 10.1109/TIT.2014.2323359. arXiv: 1305.5870.

[106] Y. Goda and Y. Suzuki. 'Estimation of incident and reflected waves in random wave experiments'. In: *Proceedings of the 15th International Conference on Coastal Engineering*. 1976, pp. 828–845.

[107] A. Mendible, J. Koch, H. Lange, S. L. Brunton and J. N. Kutz. 'Data-driven modeling of rotating detonation waves'. In: *Physical Review Fluids* 6.5 (2021), pp. 1–20. issn: 2469990X. doi: 10.1103/PhysRevFluids.6.050507. arXiv: 2008.05586.

[108] T. Askham, P. Zheng, A. Aravkin and J. N. Kutz. 'Robust and scalable methods for the dynamic mode decomposition'. In: *arXiv preprint* 1 (2017), pp. 1–21. arXiv: 1712.01883. url: http://arxiv.org/abs/1712.01883.

[109] S. Elgar, T. H. C. Herbers and R. T. Guza. 'Reflection of Ocean Surface Gravity Waves from a Natural Beach'. In: *Journal of Physical Oceanography* 24.7 (1994), pp. 1503–1511.

[110] K. L. Brodie, B. Raubenheimer, S. Elgar, R. K. Slocum and J. E. McNinch. 'Lidar and pressure measurements of inner-surfzone waves and setup'. In: *Journal of Atmospheric and Oceanic Technology* 32.10 (2015), pp. 1945–1959. issn: 15200426. doi: 10.1175/JTECH-D-14-00222.1.

[111] D. A. Huntley, D. Simmonds and R. Tatavarti. 'Use of Collocated Sensors to Measure Coastal Wave Reflection'. In: *Journal of Waterway, Port, Coastal, and Ocean Engineering* 125.1 (1999), pp. 46–52. issn: 0733-950X. doi: 10.1061/(asce)0733-950x(1999)125:1(46).

[112] J. A. Battjes. 'Surf similarity'. In: *Proceedings 14 th International Conference on Coastal Engineering*. Vol. 1. 1974, pp. 466–480.

[113] B. Raubenheimer and R. T. Guza. 'Observations and predictions of run-up'. In: *Journal of Geophysical Research C: Oceans* 101.C11 (1996), pp. 25575–25587. issn: 01480227. doi: 10.1029/96JC02432.

[114] J. R. Miles, P. E. Russell and D. A. Huntley. 'Sediment transport and wave reflection near a seawall'. In: *Proceedings of the Coastal Engineering Conference* 3.Silvester 1977 (1997), pp. 2612–2624. issn: 08938717. doi: 10.1061/9780784402429.202.

[115] M. Gawehn, S. de Vries and S. Aarninkhof. 'Depth and Surface Current Inversion on the Fly: a New Video Based Approach Using the Dynamic Mode Decomposition'. In: *Coastal Sediments 2019 - Proceedings Of The 9th International Conference*. Tampa/St. Pete, 2019, pp. 2511–2520. doi: 10.1142/9789811204487_0216.

[116] J. R. Fienup. 'Invariant error metrics for image reconstruction'. In: *Applied Optics* 36.32 (1997), p. 8352. issn: 0003-6935. doi: 10.1364/ao.36.008352.

[117] J. Bosboom and M. J. F. Stive. *Coastal Dynamics*. TU Delft Open, 2021, p. 595. isbn: 9789463663700. doi: 10.5074/T.2021.001. url: https://textbooks.open.tudelft.nl/textbooks/catalog/book/37.

[118] P. S. Bell and J. C. Osler. 'Mapping bathymetry using X-band marine radar data recorded from a moving vessel'. In: *Ocean Dynamics* 61.12 (2011), pp. 2141–2156. issn: 16167341. doi: 10.1007/s10236-011-0478-4.

[119] D. Kraft. *A Software Package for Sequential Quadratic Programming*. Tech. rep. Köln, Germany: DLR German Aerospace Center - Institute for Flight Mechanics, 1988.

[120] E. W. Bergsma, D. C. Conley, M. A. Davidson and T. J. O'Hare. 'Video-based nearshore bathymetry estimation in macro-tidal environments'. In: *Marine Geology* 374 (2016), pp. 31–41. issn: 00253227. doi: 10.1016/j.margeo.2016.02.001. url: http://dx.doi.org/10.1016/j.margeo.2016.02.001.

[121] J. L. Aarnink. 'Bathymetry Mapping Using Drone Imagery'. MSc Thesis. TU Delft, 2017, p. 89. url: https://repository.tudelft.nl/islandora/object/uuid%3Ad607109b-5891-46bc-8670-fc9b99a2b409.

[122] K. Vos. 'Remote sensing of the nearshore zone using a rotary-wing UAV'. MSc Thesis. University of New South Wales and Ecole Polytechnique Federale De Lausanne, Switzerland, 2017, p. 84.

[123] E. W. J. Bergsma. 'Application of an improved video-based depth inversion technique to a macrotidal sandy beach'. PhD thesis. University of Plymouth, 2017, p. 228. url: http://hdl.handle.net/10026.1/8736.

[124] A. J. Reniers, E. B. Thornton, T. P. Stanton and J. A. Roelvink. 'Vertical flow structure during Sandy Duck: Observations and modeling'. In: *Coastal Engineering* 51.3 (2004), pp. 237–260. issn: 03783839. doi: 10.1016/j.coastaleng.2004.02.001.

[125] C. J. Sonu. 'Field observation of nearshore circulation and meandering currents'. In: *Journal of Geophysical Research* 77.18 (June 1972), pp. 3232–3247. issn: 01480227. doi: 10.1029/JC077i018p03232.

[126] A. D. Short. 'Australian rip systems - Friend or foe?' In: *Journal of Coastal Research* 2007.SPEC. ISSUE 50 (2007), pp. 7–11. issn: 07490208. url: https://www.jstor.org/stable/26481546.

[127] D. Anderson, A. Spicer Bak, K. L. Brodie, N. Cohn, R. A. Holman and J. Stanley. 'Quantifying optically derived two-dimensional wave-averaged currents in the surf zone'. In: *Remote Sensing* 13.4 (2021), pp. 1–20. issn: 20724292. doi: 10.3390/rs13040690.

[128] M. C. Haller, D. Honegger and P. A. Catalan. 'Rip Current Observations via Marine Radar'. In: *Journal of Waterway, Port, Coastal, and Ocean Engineering* 140.2 (2014), pp. 115–124. issn: 0733-950X. doi: 10.1061/(asce)ww.1943-5460.0000229.

[129] T. R. Mortlock, I. D. Goodwin, J. K. McAneney and K. Roche. 'The June 2016 Australian East Coast Low: Importance of wave direction for coastal erosion assessment'. In: *Water (Switzerland)* 9.2 (2017), pp. 1–22. issn: 20734441. doi: 10.3390/w9020121.

[130] R. Almar, R. Ranasinghe, E. W. Bergsma, H. Diaz, A. Melet, F. Papa, M. Vousdoukas, P. Athanasiou, O. Dada, L. P. Almeida and E. Kestenare. 'A global analysis of extreme coastal water levels with implications for potential coastal overtopping'. In: *Nature Communications* 12.1 (2021), pp. 1–9. issn: 20411723. doi: 10.1038/s41467-021-24008-9. url: http://dx.doi.org/10.1038/s41467-021-24008-9.

[131] S. Vitousek, P. L. Barnard, C. H. Fletcher, N. Frazer, L. Erikson and C. D. Storlazzi. 'Doubling of coastal flooding frequency within decades due to sea-level rise'. In: *Scientific Reports* 7.1 (2017), pp. 1–9. issn: 20452322. doi: 10.1038/s41598-017-01362-7.

[132] E. W. Bergsma and R. Almar. 'Coastal coverage of ESA' Sentinel 2 mission'. In: *Advances in Space Research* 65.11 (2020), pp. 2636–2644. issn: 18791948. doi: 10.1016/j.asr.2020.03.001.

[133] J. Li and D. P. Roy. 'A global analysis of Sentinel-2a, Sentinel-2b and Landsat-8 data revisit intervals and implications for terrestrial monitoring'. In: *Remote Sensing* 9.9 (2017). issn: 20724292. doi: 10.3390/rs9090902.

[134] D. R. Lyzenga. 'Remote sensing of bottom reflectance and water attenuation parameters in shallow water using aircraft and landsat data'. In: *International Journal of Remote Sensing* 2.1 (1981), pp. 71–82. issn: 13665901. doi: 10.1080/01431168108948342.

[135] R. P. Stumpf, K. Holderied and M. Sinclair. 'Determination of water depth with high-resolution satellite imagery over variable bottom types'. In: *Limnology and Oceanography* 48.1 II (2003), pp. 547–556. issn: 00243590. doi: 10.4319/lo.2003.48.1_part_2.0547.

[136] R. Abileah. 'Mapping shallow water depth from satellite'. In: *American Society for Photogrammetry and Remote Sensing - Annual Conference of the American Society for Photogrammetry and Remote Sensing 2006: Prospecting for Geospatial Information Integration* 1 (2006), pp. 1–7.

[137] R. Almar, E. W. Bergsma, M. A. Gawehn, S. G. Aarninkhof and R. Benshila. 'High-frequency Temporal Wave-pattern Reconstruction from a Few Satellite Images: A New Method towards Estimating Regional Bathymetry'. In: *Journal of Coastal Research* 95.sp1 (2020), pp. 996–1000. issn: 15515036. doi: 10.2112/SI95-194.1.

[138] E. W. Bergsma, R. Almar and P. Maisongrande. 'Radon-augmented Sentinel-2 satellite imagery to derive wave-patterns and regional bathymetry'. In: *Remote Sensing* 11.16 (2019), pp. 1–16. issn: 20724292. doi: 10.3390/rs11161918.

[139] D. Gabor. 'A Theory of Communication'. In: *Journal of the Institution of Electrical Engineers-Part III: Radio and Communication Engineering* 93.26 (1946), pp. 429–441.

[140] L. P. Almeida, R. Almar, E. W. Bergsma, E. Berthier, P. Baptista, E. Garel, O. A. Dada and B. Alves. 'Deriving high spatial-resolution coastal topography from sub-meter satellite stereo imagery'. In: *Remote Sensing* 11.5 (2019). issn: 20724292. doi: 10.3390/rs11050590.

[141] M. de Michele, D. Raucoules, D. Idier, F. Smai and M. Foumelis. 'Shallow bathymetry from multiple sentinel 2 images via the joint estimation of wave celerity and wavelength'. In: *Remote Sensing* 13.11 (2021), pp. 1–12. issn: 20724292. doi: 10.3390/rs13112149.

[142] G. Abessolo Ondoa, R. Almar, B. Castelle, L. Testut, F. Léger, Z. Sohou, F. Bonou, E. W. Bergsma, B. Meyssignac and M. Larson. 'Sea level at the coast from video-sensed waves: Comparison to tidal gauges and satellite altimetry'. In: *Journal of Atmospheric and Oceanic Technology* 36.8 (2019), pp. 1591–1603. issn: 15200426. doi: 10.1175/JTECH-D-18-0203.1.

[143] M. L. Palmsten and K. L. Brodie. 'The Coastal Imaging Research Network (CIRN)'. In: *Remote Sensing* 14.3 (2022), pp. 1–18. issn: 20724292. doi: 10.3390/rs14030453.

[144] R. Almar, E. W. Bergsma, P. Maisongrande, A. Giros and L. P. Almeida. 'On the application of a two-dimension spatio-temporal cross-correlation method to inverse coastal bathymetry from waves using a satellite-based video sequence'. In: *International Geoscience and Remote Sensing Symposium (IGARSS)* (2019), pp. 8205–8208. doi: 10.1109/IGARSS.2019.8899819.

[145] L. Coeurdevey and C. Gabriel-Robez. *Pléiades Imagery - User Guide*. Tech. rep. October. 2012, pp. 1–118.

[146] J. M. Jouanneau and C. Latouche. 'Continental fluxes to the Bay of Biscay: Processes and behaviour'. In: *Ocean and Shoreline Management* 12.5-6 (1989), pp. 477–485. issn: 09518312. doi: 10.1016/0951-8312(89)90025-8.

[147] A. Mazières, H. Gillet, B. Castelle, T. Mulder, C. Guyot, T. Garlan and C. Mallet. 'High-resolution morphobathymetric analysis and evolution of Capbreton submarine canyon head (Southeast Bay of Biscay-French Atlantic Coast) over the last decade using descriptive and numerical modeling'. In: *Marine Geology* 351 (2014), pp. 1–12. issn: 00253227. doi: 10.1016/j.margeo.2014.03.001. url: http://dx.doi.org/10.1016/j.margeo.2014.03.001.

[148] R. Almar, E. W. J. Bergsma, P. A. Catalan, R. Cienfuegos, L. Suarez, F. Lucero, A. Nicolae Lerma, F. Desmazes, E. Perugini, M. L. Palmsten and C. Chickadel. 'Sea State from Single Optical Images: A Methodology to Derive Wind-Generated Ocean Waves from Cameras, Drones and Satellites'. In: *Remote Sensing* 13.4 (Feb. 2021), p. 679. issn: 2072-4292. doi: 10.3390/rs13040679. url: https://www.mdpi.com/2072-4292/13/4/679.

[149] A. J. Kuik, G. P. van Vledder and L. H. Holthuijsen. 'A Method for the Routine Analysis of Pitch-and-Roll Buoy Wave Data'. In: *Journal of Physical Oceanography* 18.7 (July 1988), pp. 1020–1034. issn: 0022-3670. doi: 10.1175/1520-0485(1988)018<1020:AMFTRA>2.0.CO;2. url: http://journals.ametsoc.org/doi/10.1175/1520-0485(1988)018%3C1020:AMFTRA%3E2.0.CO;2.

[150] R. Campbell, A. Martinez, C. Letetrel and A. Rio. 'Methodology for estimating the French tidal current energy resource'. In: *International Journal of Marine Energy* 19.2017 (2017), pp. 256–271. issn: 22141669. doi: 10.1016/j.ijome.2017.07.011. url: https://doi.org/10.1016/j.ijome.2017.07.011.

[151] N. Booij, R. C. Ris and L. H. Holthuijsen. 'A third-generation wave model for coastal regions 1. Model description and validation'. In: *Journal of Geophysical Research: Oceans* 104.C4 (1999), pp. 7649–7666. issn: 21699291. doi: 10.1029/98JC02622.

[152] T. E. Baldock, P. Holmes, S. Bunker and P. Van Weert. 'Cross-shore hydrodynamics within an unsaturated surf zone'. In: *Coastal Engineering* 34.3-4 (1998), pp. 173–196. issn: 03783839. doi: 10.1016/S0378-3839(98)00017-9.

[153] I. G. Jonsson. 'Wave Boundary Layers and Friction Factors'. In: *Coastal Engineering 1966*. M. New York, NY: American Society of Civil Engineers, Nov. 1967, pp. 127–148. isbn: 9780872620087. doi: 10.1061/9780872620087.010. url: http://ascelibrary.org/doi/10.1061/9780872620087.010.

[154] X. Lastiri, S. Abadie, P. Maron, M. Delpey, P. Liria, J. Mader and V. Roeber. 'Wave energy assessment in the south aquitaine nearshore zone from a 44-year hindcast'. In: *Journal of Marine Science and Engineering* 8.3 (2020). issn: 20771312. doi: 10.3390/jmse8030199.

[155] D. Manian, J. M. Kaihatu and E. M. Zechman. 'Using genetic algorithms to optimize bathymetric sampling for predictive model input'. In: *Journal of Atmospheric and Oceanic Technology* 29.3 (2012), pp. 464–477. issn: 07390572. doi: 10.1175/JTECH-D-11-00051.1.

[156] J. M. Kaihatu, K. L. Edwards and W. C. O'Reilly. 'Model predictions of nearshore processes near complex bathymetry'. In: *Oceans Conference Record (IEEE)* 2 (2002), pp. 685–691. issn: 01977385. doi: 10.1109/oceans.2002.1192052.

[157] S. D. Jawak, S. S. Vadlamani and A. J. Luis. 'A Synoptic Review on Deriving Bathymetry Information Using Remote Sensing Technologies: Models, Methods and Comparisons'. In: *Advances in Remote Sensing* 04.02 (2015), pp. 147–162. issn: 2169-267X. doi: 10.4236/ars.2015.42013.

[158] W. G. Huang, B. Fu, C. B. Zhou, J. S. Yang, A. Q. Shi and D. L. Li. 'Shallow water bathymetric surveys by spaceborne synthetic aperture radar'. In: *International Geoscience and Remote Sensing Symposium (IGARSS)* 6.February 2001 (2001), pp. 2810–2812. doi: 10.1109/igarss.2001.978171.

[159] D. Reinsel, J. Gantz and J. Rydning. 'Data Age 2025 : Don 't Focus on Big Data; Focus on the Data That's Big'. In: *IDC White Paper* April (2017), pp. 1–25. url: https://www.seagate.com/files/www-content/our-story/trends/files/Seagate-WP-DataAge2025-March-2017.pdf.

[160] M. Gawehn. *Verdere ontwikkeling X-Band radar voor morfologische analyses Amelander Zeegat 2020-21*. Tech. rep. Delft: Deltares, 2022, pp. 1–27.

[161] Pingdom. *What would they cost today? 10 classic pieces of tech history at today's prices*. 2011. url: https://www.pingdom.com/blog/what-would-they-cost-today-10-classic-pieces-of-tech-history-at-todays-prices/ (visited on 24/02/2022).

[162] M. Williams. *Are Cameras Actually More Expensive Now Than Ever Before?* 2021. url: https://petapixel.com/2021/07/09/are-cameras-actually-more-expensive-now-than-ever-before/ (visited on 24/02/2022).

[163] E. eRules. *Easy Access Rules for Unmanned Aircraft Systems (Revision from September 2021)*. Tech. rep. EASA European Union Aviation Safety Agency, 2021, p. 308. url: http://eur-lex.europa.eu/,.

[164] G. Bradski. 'The OpenCV Library'. In: *Dr. Dobb's Journal of Software Tools* 3 (2000), pp. 1–81.

[165] N. Gorelick, M. Hancher, M. Dixon, S. Ilyushchenko, D. Thau and R. Moore. 'Google Earth Engine: Planetary-scale geospatial analysis for everyone'. In: *Remote Sensing of Environment* 202 (2017), pp. 18–27. issn: 00344257. doi: 10.1016/j.rse.2017.06.031. url: https://doi.org/10.1016/j.rse.2017.06.031.

[166] M. Woelfle, P. Olliaro and M. H. Todd. 'Open science is a research accelerator'. In: *Nature Chemistry* 3.10 (2011), pp. 745–748. issn: 17554330. doi: 10.1038/nchem.1149.

[167] E. C. McKiernan, P. E. Bourne, C. T. Brown, S. Buck, A. Kenall, J. Lin, D. McDougall, B. A. Nosek, K. Ram, C. K. Soderberg, J. R. Spies, K. Thaney, A. Updegrove, K. H. Woo and T. Yarkoni. 'How open science helps researchers succeed'. In: *eLife* 5.JULY (2016), pp. 1–19. issn: 2050084X. doi: 10.7554/eLife.16800.

[168] M. Gawehn. *Software for self-adaptive and on-the-fly mapping of coastal parameters from video of a wave field*. Delft, 2021. doi: doi.org/10.4121/17000107.v1.

[169] E. W. Bergsma and R. Almar. 'Video-based depth inversion techniques, a method comparison with synthetic cases'. In: *Coastal Engineering* 138.August 2017 (2018), pp. 199–209. issn: 03783839. doi: 10.1016/j.coastaleng.2018.04.025. url: https://doi.org/10.1016/j.coastaleng.2018.04.025.

[170] E. Rublee, V. Rabaud, K. Konolige and G. Bradski. 'ORB: An efficient alternative to SIFT or SURF'. In: *Proceedings of the IEEE International Conference on Computer Vision* (2011), pp. 2564–2571. doi: 10.1109/ICCV.2011.6126544.

[171] Y. Pi, N. D. Nath and A. H. Bezhadan. 'Deep Neural Networks for Drone View Localization and Mapping in GPS-Denied Environments'. In: *Proc. 37th CIB W78 Information Technology for Construction Conference*. 2020, pp. 1–16. doi: 10.46421/2706-6568.37.2020.paper001.

[172] R. Gangeskar. 'An algorithm for estimation of wave height from shadowing in X-band radar sea surface images'. In: *IEEE Transactions on Geoscience and Remote Sensing* 52.6 (2014), pp. 3373–3381. issn: 01962892. doi: 10.1109/TGRS.2013.2272701.

[173] Y. Gal, M. Browne and C. Lane. 'Long-term automated monitoring of nearshore wave height from digital video'. In: *IEEE Transactions on Geoscience and Remote Sensing* 52.6 (2014), pp. 3412–3420. issn: 01962892. doi: 10.1109/TGRS.2013.2272790.

[174] T. Müller, A. Evans, C. Schied and A. Keller. 'Instant Neural Graphics Primitives with a Multiresolution Hash Encoding'. In: (2022). arXiv: 2201.05989. url: http://arxiv.org/abs/2201.05989.

[175] J. E. McNinch. 'Bar and Swash Imaging Radar (BASIR): A mobile x-band radar designed for mapping nearshore sand bars and swash-defined shorelines over large distances'. In: *Journal of Coastal Research* 23.1 (2007), pp. 59–74. issn: 07490208. doi: 10.2112/05-0452.1.

[176] S. T. J. Van Son, R. C. Lindenbergh, M. A. De Schipper, S. De Vries and K. Duijnmayer. 'Application Monitoring bathymetric changes at storm scale technical'. In: *PositionIT* January (2010), pp. 59–65.

[177] R. Holman and M. C. Haller. 'Remote sensing of the nearshore'. In: *Annual Review of Marine Science* 5 (2013), pp. 95–113. issn: 19411405. doi: 10.1146/annurev-marine-121211-172408.

[178] Deltares. *XBEach skillbed report, revision 5765*. Tech. rep. October. Delft, 2020, pp. 1–105.

[179] M. Gawehn. *Video and ground truth bathymetry data from Porthtowan, Scheveningen, Narrabeen.* 2021. doi: 10.4121/17000161.v1.

[180] T. Zhou, M. Brown, N. Snavely and D. G. Lowe. 'Unsupervised Learning of Depth and Ego-Motion from Video'. In: *Proceedings of the IEEE conference on computer vision and pattern recognition* (Apr. 2017), pp. 1851–1858. arXiv: 1704.07813. url: https://onlinelibrary.wiley.com/doi/10.1002/cber.19941271219%20http://arxiv.org/abs/1704.07813.

[181] A. Geiger, P. Lenz, C. Stiller and R. Urtasun. 'Vision meets robotics: The KITTI dataset'. In: *International Journal of Robotics Research* 32.11 (2013), pp. 1231–1237. issn: 02783649. doi: 10.1177/0278364913491297.

[182] K. Vos, K. D. Splinter, M. D. Harley, J. A. Simmons and I. L. Turner. 'CoastSat: A Google Earth Engine-enabled Python toolkit to extract shorelines from publicly available satellite imagery'. In: *Environmental Modelling and Software* 122 (2019), p. 104528. issn: 13648152. doi: 10.1016/j.envsoft.2019.104528. url: https://doi.org/10.1016/j.envsoft.2019.104528.

[183] M. D. Harley, M. A. Kinsela, E. Sánchez-García and K. Vos. 'Shoreline change mapping using crowd-sourced smartphone images'. In: *Coastal Engineering* 150.September 2018 (2019), pp. 175–189. issn: 03783839. doi: 10.1016/j.coastaleng.2019.04.003. url: https://doi.org/10.1016/j.coastaleng.2019.04.003.

[184] A. Luijendijk, G. Hagenaars, R. Ranasinghe, F. Baart, G. Donchyts and S. Aarninkhof. 'The State of the World's Beaches'. In: *Scientific Reports* 8.1 (2018), pp. 1–11. issn: 20452322. doi: 10.1038/s41598-018-24630-6.

[185] S. G. Aarninkhof, I. L. Turner, T. D. Dronkers, M. Caljouw and L. Nipius. 'A video-based technique for mapping intertidal beach bathymetry'. In: *Coastal Engineering* 49.4 (2003), pp. 275–289. issn: 03783839. doi: 10.1016/S0378-3839(03)00064-4.

[186] J. C. Brock and S. J. Purkis. 'The emerging role of lidar remote sensing in coastal research and resource management'. In: *Journal of Coastal Research* SPECIAL ISSUE 53 (2009), pp. 1–5. issn: 07490208. doi: 10.2112/SI53-001.1.

[187] L. R. Wyatt. 'Measuring the ocean wave directional spectrum 'First Five' with HF radar'. In: *Ocean Dynamics* 69.1 (Jan. 2019), pp. 123–144. issn: 1616-7341. doi: 10.1007/s10236-018-1235-8. url: http://link.springer.com/10.1007/s10236-018-1235-8.

[188] H. C. Graber, B. K. Haus, R. D. Chapman and L. K. Shay. 'HF radar comparisons with moored estimates of current speed and direction: Expected differences and implications'. In: *Journal of Geophysical Research: Oceans* 102.C8 (1997), pp. 18749–18766. issn: 21699291. doi: 10.1029/97JC01190.

[189] A. Ritchie, J. Warrick and G. Hatcher. 'New Applications of Structure-from-Motion Photogrammetry for Coastal Process Studies'. In: *Proceedings of the AGU Fall Meeting Abstracts, Washington, DC, USA, 10–14 December 2018*. Washington, 2018, p. EP54B–30.

[190] Deltares. *Delft3D dM Suite 2D3D 2022 (User Manual)*. Tech. rep. Delft: Deltares, 2022, p. 423.

[191] R. Torres, P. Snoeij, D. Geudtner, D. Bibby, M. Davidson, E. Attema, P. Potin, B. Ö. Rommen, N. Floury, M. Brown, I. N. Traver, P. Deghaye, B. Duesmann, B. Rosich, N. Miranda, C. Bruno, M. L'Abbate, R. Croci, A. Pietropaolo, M. Huchler and F. Rostan. 'GMES Sentinel-1 mission'. In: *Remote Sensing of Environment* 120 (2012), pp. 9–24. issn: 00344257. doi: 10.1016/j.rse.2011.05.028. url: http://dx.doi.org/10.1016/j.rse.2011.05.028.

[192] W. Abdalati, H. J. Zwally, R. Bindschadler, B. Csatho, S. L. Farrell, H. A. Fricker, D. Harding, R. Kwok, M. Lefsky, T. Markus, A. Marshak, T. Neumann, S. Palm, B. Schutz, B. Smith, J. Spinhirne and C. Webb. 'The ICESat-2 laser altimetry mission'. In: *Proceedings of the IEEE* 98.5 (2010), pp. 735–751. issn: 00189219. doi: 10.1109/JPROC.2009.2034765.

[193] N. G. Plant, K. T. Holland and M. C. Haller. 'Ocean wavenumber estimation from wave-resolving time series imagery'. In: *IEEE Transactions on Geoscience and Remote Sensing* 46.9 (2008), pp. 2644–2658. issn: 01962892. doi: 10.1109/TGRS.2008.919821.

[194] W. E. Boyce and R. C. DiPrima. *Elementary Differential Equations and Boundary Value Problems*. 9th ed. Hoboken: John Wiley and Sons, Inc., 2010. isbn: 978-0-470-39873-9.

[195] M. Gawehn, A. van Dongeren, A. van Rooijen, C. D. Storlazzi, O. M. Cheriton and A. Reniers. 'Identification and classification of very low frequency waves on a coral reef flat'. In: *Journal of Geophysical Research: Oceans* 121.10 (Oct. 2016), pp. 7560–7574. issn: 21699275. doi: 10.1002/2016JC011834. url: http://doi.wiley.com/10.1002/2016JC011834.

[196] A. Vött, H. J. Bruins, M. Gawehn, B. N. Goodman-Tchernov, P. M. De Martini, D. Kelletat, G. Mastronuzzi, K. Reicherter, B. R. Röbke, A. Scheffers, T. Willershäuser, P. Avramidis, P. Bellanova, P. J. Costa, C. Finkler, H. Hadler, B. Koster, J. Lario, E. Reinhardt, M. Mathes-Schmidt, K. Ntageretzis, D. Pantosti, I. Papanikolaou, P. Sansò, G. Scicchitano, A. Smedile and W. Szczuciński. 'Publicity waves based on manipulated geoscientific data suggesting climatic trigger for majority of tsunami findings in the mediterranean – response to 'tsunamis in the geological record: Making waves with a cautionary tale from the mediterranean' by marr'. In: *Zeitschrift fur Geomorphologie* 62.May (2019), pp. 7–45. issn: 18641687. doi: 10.1127/zfg_suppl/2018/0547.

[197] F. Grossmann, M. Gawehn, S. de Vries, F. P. de Wit and S. G. J. Aarninkhof. 'Comparison of Currents Derived from X-band Radar and Collected In-situ Data in Ameland Inlet Comparison of Currents Derived from X-band Radar and Collected In-situ Data in Ameland Inlet'. In: *Coastal Structures*. Karlsruhe, Germany: HENRY, 2019, pp. 416–425. isbn: 9783939230649. doi: 10.18451/978-3-939230-64-9.

A

Appendix A

A.1. Radar properties

Table A.1.: Radar properties at the Sand Engine and Ameland Inlet

Properties	Sand Engine	Ameland Inlet
Antenna Height (m, NAP)	15	60
System Type (-)	Terma Scanter 2000	Terma Scanter 2001
Antenna Width (ft)	14	21
Range (km)	3.75	7.5
Pulse Length (ns)	50	60
Horizontal Beam Width (°)	0.5	0.43
Vertical Beam Width (°)	23	23
PRF (kHz)	4.0	2.2
Rotation Speed (rpm)	25	21
Output Power (kW)	25	25
Polarization (-)	VV	VV

A.2. Computational settings

A.2.1. Sand Engine

For computational efficiency of XMFit, a variable grid spacing of $25\,\mathrm{m}$ near the shoreline and $250\,\mathrm{m}$ further offshore was used, resulting in 9380 grid points. The computational cubes were time-averaged by subdividing them into 32 image bins with 8 images overlap. The spatial extents were $64\,\mathrm{px}$ ($240\,\mathrm{m}$) within $300\,\mathrm{m}$

Parts of this appendix have been published in Coastal Engineering **159**, 103716 (2020) [3].

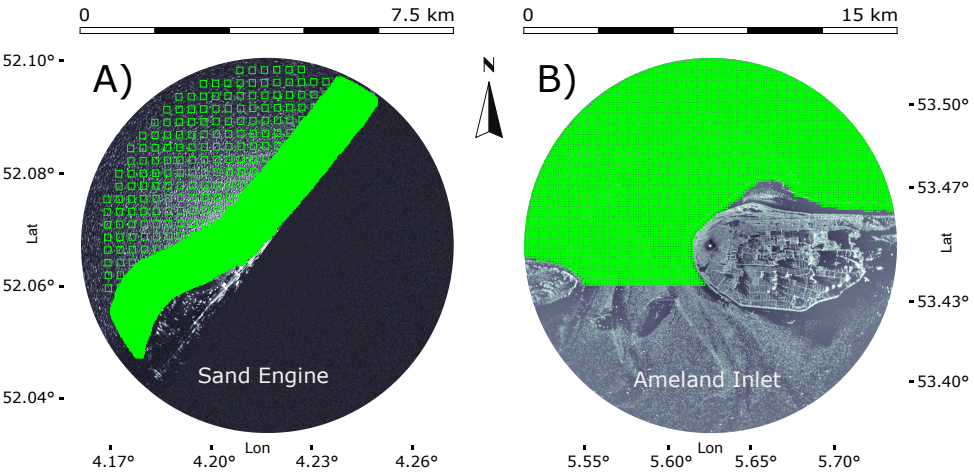

Figure A.1.: Computational grids (green) used for (a) the Sand Engine (b) and the Ameland Inlet. The grids are overlaid on typical radar images of both sites.

from the shoreline and $128\,\mathrm{px}$ $(480\,\mathrm{m})$ further offshore. The reduced cube size in the nearshore region was chosen in order to capture more morphological detail.

For consistency, XMFit settings were chosen to be similar to the application at Ameland. The spectral frequency filter was set to include shorter wave periods, $[\mathrm{T_{min}}, \mathrm{T_{max}}] = [3.5, 15]$ (s) (Figure 2.1, ②). Depth limits were set to $[\mathrm{d_{min}}, \mathrm{d_{max}}] = [0.5, 25]$ (m) (Figure 2.1, ③), and the near-surface current velocity limit was set to $|\mathrm{U_{max}}| = 1.25(\mathrm{m\,s^{-1}})$ (Figure 2.1, ⑥).

A.2.2. Ameland tidal inlet

In case of the Ameland Inlet, a constant grid spacing of $100\,\mathrm{m}$ was used amounting to 8328 grid points in total. Computational cubes were time-averaged using 32 image bins without overlap and had a spatial extent of $128\,\mathrm{px}$ $(960\,\mathrm{m})$.

The inversion process was constrained by the wave period limits$[\mathrm{T_{min}}, \mathrm{T_{max}}] = [5, 15]$ (s) (Figure 2.1, ②), depth limits $[\mathrm{d_{min}}, \mathrm{d_{max}}] = [0.2, 25]$ (m) (Figure 2.1, ③), and $|\mathrm{U_{max}}| = 1.5$ $(\mathrm{m\,s^{-1}})$ (Figure 2.1, ⑥).

B

Appendix B

B.1. Review of strategies to extract spectral gravity wave signatures

- *e.g.,Young, Rosenthal and Ziemer [26], Dugan, Piotrowski and Williams [28], Ziemer [68] and Irani, Gotwols and Bjerkaas [80]*

  The most straightforward strategy is to transform local video cut-outs from 3D $\mathbf{x}, t$ into 3D $\mathbf{k}, \omega$ spectra via 3D Fast Fourier Transforms (3D-FFTs). An energy threshold can then be used to separate the spectral footprint of gravity waves $\boldsymbol{k}^{\uparrow}, \omega^{\uparrow}$ from the noise floor. A benefit of this approach is the possibility to retrieve spectral data up to 2 times the Nyquist frequency [51], which can be important if frame rates are low (e.g., slow radar rotation speeds).

- *Senet* et al. *[21]*

  The strategy starts as [26, 28, 68, 80], but with reduced size of the video cut-out, which requires a follow up step: After producing 3D $\mathbf{k}, \omega$ spectra, they are sliced into separate 2D wavenumber layers $\boldsymbol{k}_j, \omega_j$ per constant frequency ω_j. These spectral layers are then filtered to separate the wavenumber signature of gravity waves from the noise floor. Subsequently, using inverse 2D Fast Fourier Transforms (2D-FFT^{-1}), each filtered 2D $\boldsymbol{k}_j, \omega_j$ layer is transformed back to the spatial domain to produce a corresponding complex valued image ($\boldsymbol{x}_j, \omega_j$), which depicts the local wave pattern associated to ω_j. Being associated to one frequency component and neglecting spatial differences in amplitude (which can be achieved through entry wise normalization), the complex valued images represent LOCPI. Finally, assuming the wave field is homogenous, spatial gradients in each LOCPI yield a local representative

Parts of this appendix have been published in Remote Sensing **13**, 4742 (2021) [34].

Table B.1.: Pros and cons of different strategies used to retrieve local gravity wave $\boldsymbol{k}^{\uparrow}, \omega^{\uparrow}$ signatures from video of a moving wave-field.

Strategy	Pros	Cons
e.g.,[80]	• simple approach • spectral data: $2\times$ Nyquist limit	• comp. load: full dimensional video
[21]	• LOCPI: sugg. higher localisation • spectral data: $2\times$ Nyquist limit	• comp. load: full dimensional video
[20]	• LOCPI: sugg. higher localisation • freedom local pixel sampling	• comp. load: full dimensional video • approximate $\omega^{\uparrow}$
[87]	• G$\widetilde{OC}$PI: sugg. higher localisation • freedom global pixel sampling • globally coherent wave patterns • predict subdomain sizes from $\omega^{\uparrow}$ • comp. load: reduce dimensionality	• Sensitive to mixing Fourier modes
proposed	• GOCPI: sugg. higher localisation • freedom global pixel sampling • globally coherent wave patterns • predict subdomain sizes from $\omega^{\uparrow}$ • comp. load: reduce dimensionality	

vector $\boldsymbol{k}_j^{\uparrow}$ associated to that frequency component $\omega_j = \omega_j^{\uparrow}$. The suggested benefit of extracting $\boldsymbol{k}_j^{\uparrow}$ from LOCPI, instead of straight from 3D $\mathbf{k}, \omega$ spectra, is that the reduced size of the video cut-out leads to better localisation of $\boldsymbol{k}^{\uparrow}, \omega^{\uparrow}$.

- *Holman, Plant and Holland [20], Stockdon and Holman [82] and Plant, Holland and Haller [193]*

  Similar to [21], this strategy constructs one-component phase images. First, the video is transformed from 3D $\mathbf{x}, \mathrm{t}$ to 3D $\mathbf{x}, \omega$ via FFTs in time. This process finds GOCPI per Fourier frequency, but without taking spatial coherence into account. A subsequent local analysis aims to find this spatial coherency. Cross-spectral matrices are computed for predefined frequency bands with central frequencies ω_c. The idea is that the strongest eigenvector of each cross-spectral matrix, after entry-wise normalization to unit magnitude, resembles a spatially coherent LOCPI $(\boldsymbol{x}_c, \omega_c)$ corresponding to ω_c. Analogous to [21], $\boldsymbol{k}^{\uparrow}$ is finally deduced from phase gradients and $\omega_c = \omega_c^{\uparrow}$. A benefit of this strategy is that the video can be sampled in any fashion (e.g., non-

regularly) in preparation of local cross-spectral matrices. A drawback of this strategy is the uncertainty around the frequency associated to $\boldsymbol{k}^{\uparrow}$ as it lies within a frequency band and needs to be approximated by the bands' central frequency $\omega_c^{\uparrow}$.

- *Simarro* et al. *[87]*

  The most recently developed strategy suggests that globally coherent GOCPI can be found through a singular value decomposition of the time-analytic signal of the video. First, the video is reshaped into a matrix $\boldsymbol{X}$, whose columns represent the video frames squeezed into arrays and whose rows hence contain the timeseries of a pixel. Each timeseries is converted into its analytic signal using the Hilbert transform, which makes the timeseries complex valued (with a single-sided frequency spectrum) and prepares for a natural retrieval of phases. A singular value decomposition (svd) of the video matrix $\boldsymbol{X}$, Equation (B.1), then describes the video as a sum of modes, given by pairs of spatial structures and their associated temporal evolution:

$$\boldsymbol{X} = \boldsymbol{U}\boldsymbol{\Sigma}\boldsymbol{V}^{*} = \sum_{j}^{j^{th}\text{ mode}} \widetilde{\sigma_j \boldsymbol{u}_j \boldsymbol{v}_j^{*}} \ , \tag{B.1}$$

  where the orthonormal columns $\boldsymbol{u}_j$ of $\boldsymbol{U}$ represent the (squeezed) spatial structures ($\neq \boldsymbol{U}$ of Equation (3.1)), the columns $\boldsymbol{v}_j$ of $\boldsymbol{V}$ the associated temporal evolution, and the diagonal matrix contains the singular values σ_j, which sorted in decreasing order denote the contribution of each mode to the total variance in $\boldsymbol{X}$. The asterisk denotes the complex conjugate transpose.

  Unfolding $\boldsymbol{u}_j$ into the two spatial video dimensions, now provides GOCPI. Simarro *et al.* [87] argue that the associated time evolution $\boldsymbol{v}_j$ closely corresponds to a fixed-frequency oscillation ω_j and can therefore be estimated by the averaged temporal phase gradient. This moreover implies that $\boldsymbol{u}_j$ *approximately* resemble Global *One-Component* Phase Images $(\boldsymbol{x}_j, \omega_j)$, that is GOCPI. In practice, the final deduction of local $\boldsymbol{k}^{\uparrow}$ is done from phase gradients in local subdomains of the GOCPI.

  However, the GOCPI being only *approximately* one-component (i.e., G$\widetilde{O\mathcal{C}}$PI, where $\sim$ denotes approximate) flags a deeply rooted issue: using the svd on a wave signal, whether analytic or not, is prone to the mixing of Fourier modes, meaning that wave patterns of different frequencies mix together in $\boldsymbol{u}_j$ (Equation (B.1)) (see [88], Fig. 6). The problem can be understood from the fact that the svd result for $\boldsymbol{u}_j$ is invariant to the ordering of the video frames [88]. As such, these G$\widetilde{O\mathcal{C}}$PIs do not reflect the distinctly sinusoidal time dynamics of ocean waves.

B.2. Optimized DMD based on Variable Projections

B.2.1. Synopsis

The optimized DMD by Askham and Kutz [94] finds a solution to Equation (B.2) via non-linear least-squares minimization (Equation (B.3)).

$$\boldsymbol{X}^T \approx \boldsymbol{\Psi}(\boldsymbol{\omega}, t)\boldsymbol{B} \tag{B.2}$$

or

$$\overbrace{\begin{bmatrix} - & \boldsymbol{x}_1 & - \\ \vdots & \vdots & \vdots \\ - & \boldsymbol{x}_m & - \end{bmatrix}}^{m\times n} \approx \overbrace{\begin{bmatrix} e^{\omega_1 t_1} & \dots & e^{\omega_r t_1} \\ \vdots & \ddots & \vdots \\ e^{\omega_1 t_m} & \dots & e^{\omega_r t_m} \end{bmatrix}}^{m\times r} \overbrace{\begin{bmatrix} - & \boldsymbol{\beta}_1 & - \\ \vdots & \vdots & \vdots \\ - & \boldsymbol{\beta}_r & - \end{bmatrix}}^{r\times n}$$

solved via

$$\text{minimize} \frac{1}{2}\|\boldsymbol{X}^T - \boldsymbol{\Psi}(\boldsymbol{\omega}, t)\boldsymbol{B}\|^2 \tag{B.3}$$

Tailored to the case of processing grey-scaled video frames, the rows $\boldsymbol{x}_1 \dots \boldsymbol{x}_m$ of $\boldsymbol{X}^T \in \mathbb{R}^{m\times n}$ denote the m frames of the video, each squeezed into an array of n pixels (e.g., 10×10 frame becomes $n = 100$ array). Typically, the number of pixels is larger than the number of video frames, $n > m$. The superscript T signifies that the video matrix $\boldsymbol{X}$ is transposed in this DMD formulation. The complex valued matrix $\boldsymbol{\Psi}(\boldsymbol{\omega}, t) \in \mathbb{C}^{m\times r}$ holds in its columns the timeseries of r sinusoids with frequencies $\boldsymbol{\omega} = \{\omega_1 \dots \omega_r\}$ over time $\mathrm{t}_1 \dots \mathrm{t}_\mathrm{m}$ such that $\Psi(\omega, t)_{i,j} = e^{\omega_j t_i}$. The dependency on t_i is implicit (i.e., t_i are known). The rank r is a choice, typically $r \sim O(1) - O(10)$, such that $r < m < n$. The rows $\beta_1 \dots \beta_r$ of $\boldsymbol{B} \in \mathbb{C}^{r\times n}$ resemble weighted Dynamic Modes coupled to the frequencies $\omega_1 \dots \omega_r$. The key to "variable projections" [94] is that Equation (B.2) can be solved purely by optimizing $\boldsymbol{\omega}$: Say $\boldsymbol{\omega}$ was known, then $\boldsymbol{B} \approx \Psi(\omega, t)^\dagger \boldsymbol{X}$ and Equation (B.3) becomes $\text{minimize}\frac{1}{2}\|\boldsymbol{X} - \boldsymbol{\Psi}(\boldsymbol{\omega}, t)\boldsymbol{\Psi}(\boldsymbol{\omega}, t)^\dagger \boldsymbol{X}\|^2$, which can be iteratively solved using a Levenberg-Marquardt algorithm. For computational details see [94].

Finding a local minimizer for $\boldsymbol{\omega}$ automatically finds corresponding $\boldsymbol{B}$, whose weighted Dynamic Modes $\boldsymbol{\beta}_j$ reflect pre-products of one-component phase-images. The frequencies and corresponding phase-images are hence found together as the optimal building blocks to form the video matrix $\boldsymbol{X}^T$. Note that conform the introduction of the DMD in Section 3.2.1, the weighted Dynamic Modes $\boldsymbol{\beta}_j$ resemble (scaled) eigenvectors of the linear model $\boldsymbol{A}$ in the system of differential equations $d\boldsymbol{x}/dt = \boldsymbol{A}\boldsymbol{x}(t)$. This is shown in Appendix B.2.2. Weighted Dynamic Modes $\boldsymbol{\beta}_j$ are split into a Dynamic Mode with unit norm, $\boldsymbol{\varphi}_j = \boldsymbol{\beta}_j / b_j$ with associated spectral weight $b_j = \|\boldsymbol{\beta}_j\|$. The complex valued entries of $\boldsymbol{\varphi}_j$ differ in magnitude, accounting for spatial differences in the importance of the Dynamic Mode. To retrieve a phase-image, all entries of $\boldsymbol{\varphi}_j$ need to be normalized to unit magnitude, upon which the array can be reshaped back into a plane of the original video-frame dimensions.

To boost computational speed, the dimensionality of the video matrix $\boldsymbol{X}^T$ can first be strongly reduced $m \times n \rightarrow m \times r$ by projecting $\boldsymbol{X}$ onto the first r columns $\boldsymbol{U}_r = \{\boldsymbol{u}_1, ...\boldsymbol{u}_r\}$ in $\boldsymbol{U}$ of its svd (Equation (B.1)), $\tilde{\boldsymbol{X}} = \boldsymbol{U}_r^T \boldsymbol{X}$. Substituting $\tilde{\boldsymbol{X}}^T$ for $\boldsymbol{X}^T$ in Equations (B.2) and (B.3), yields a set of deflated Dynamic Modes $\tilde{\boldsymbol{B}}$, which are straightforwardly inflated back to the original video frame dimensions, via $\boldsymbol{B}^T = \boldsymbol{U}\tilde{\boldsymbol{B}}^T$ (see [94], Alg. 3). The weights and frequencies stay the same.

The optimized DMD needs proper initialization [94]. The implicit trapezoidal rule (i.e., 2^{nd} order Adams Moulton formula) in the exact DMD-like algorithm 4 of Askham and Kutz [94] may fail a proper initialization of the optimized DMD. This especially occurs if $r > 1.5 - 2$ times the actual number of components in the data. It is therefore advisable to use a 3^{rd} or 4^{th} order Adams-Moulton formula instead ([194], p.466). For regular, equispaced video frames, alternatively also a standard or exact DMD algorithm ([89], Alg. 1 or Alg. 2) can be used as initializer; however, the computation requires more working memory.

B.2.2. Eigenvectors $\boldsymbol{B}$ of linear model $\boldsymbol{A}$

Askham and Kutz [94] and Boyce and DiPrima [194], p.414-419

A system of differential equations $d\boldsymbol{x}/dt = \boldsymbol{A}\boldsymbol{x}(t)$ has a (fundamental) set of vector functions $\boldsymbol{x}_j(t) = \boldsymbol{\varphi}_j e^{\omega_j t}$ as solutions (Equation (B.4), LHS), where each $\boldsymbol{x}_j(t)$ combines an eigenvector $\boldsymbol{\varphi}_j$ of $\boldsymbol{A}$ with an exponential function of the corresponding eigenvalue ω_j of $\boldsymbol{A}$ (Equation (B.4), RHS).

$$\begin{bmatrix} | & | & \dots \\ \boldsymbol{x}_1(t) & \boldsymbol{x}_2(t) & \dots \\ | & | & \dots \end{bmatrix} = \begin{bmatrix} | & | & \dots \\ \boldsymbol{\varphi}_1 & \boldsymbol{\varphi}_2 & \dots \\ | & | & \dots \end{bmatrix} \begin{bmatrix} e^{\omega_1 t} & & \\ & e^{\omega_2 t} & \\ & & \ddots \end{bmatrix} \tag{B.4}$$

or

$$\boldsymbol{X}(t) = \boldsymbol{\Phi}\boldsymbol{Q}(\boldsymbol{\omega}, t)$$

A superposition of these vector functions yields the general solution to the system of differential equations: $\boldsymbol{x}(t) = \boldsymbol{X}(t)\boldsymbol{c}$, where $\boldsymbol{X}(t)$ is referred to as the fundamental matrix and $\boldsymbol{c}$ is a vector of coefficients.

Given some initial conditions $\boldsymbol{x}(0) = \boldsymbol{x_0}$ and noticing that $\boldsymbol{X}(0) = \boldsymbol{\Phi}$ (since $\boldsymbol{Q}(\boldsymbol{\omega}, 0) = \boldsymbol{I}$) the coefficients $\boldsymbol{c}$ are determined straightforward (from the general solution) $\boldsymbol{x_0} = \boldsymbol{\Phi c} \rightarrow \boldsymbol{c} = \boldsymbol{\Phi}^\dagger \boldsymbol{x_0}$. Substituting the expression for $\mathbf{c}$ back into the general solution and using $\boldsymbol{X}(t) = \boldsymbol{\Phi}\boldsymbol{Q}(\boldsymbol{\omega}, t)$ (Equation (B.4)) finds Equation (B.5):

$$\boldsymbol{x}(t) = \boldsymbol{\Phi}\boldsymbol{Q}(\boldsymbol{\omega}, t)\boldsymbol{\Phi}^\dagger \boldsymbol{x_0} \tag{B.5}$$

Now note the similarity between Equation (B.2) and Equation (B.5): If a frame $\boldsymbol{x}_i$ (Equation (B.2)) $= \boldsymbol{x}(t_i)$ (Equation (B.5)), and recognizing that $\Psi(\omega, t)_{i,j} = Q(\omega, t_i)_{j,j} = e^{\omega_j t_i}$, then $\boldsymbol{\beta}_j = s\boldsymbol{\varphi}_j$. Where the scalar value $s = \Phi^\dagger_{j,:}\boldsymbol{x_0}$. It proves that the weighted Dynamic Modes $\boldsymbol{\beta}_j$ resemble scaled eigenvectors $s\boldsymbol{\varphi}_j$ of the linear model $\boldsymbol{A}$ in the system of differential equations $d\boldsymbol{x}/dt = \boldsymbol{A}\boldsymbol{x}(t)$. Moreover, it

shows that Equation (B.2) is inherently linked to the differential equation problem Equation (B.5), and that given $\boldsymbol{x}(t_i)$ at sample times t_i, Equation (B.5) can hence be used to solve this system of differential equations for $\boldsymbol{A}$.

B.3. Default algorithm settings

Table B.2.: Default parameter values of the mapping algorithm .

Parameter	Value
N	64 frames
overlap	16 s (results, Section 3.4) variable (on-the-fly, Section 3.5)
analytic extension of $\boldsymbol{X}$	True
mode frequencies (= r if $\boldsymbol{X}$ is *analytic*)	16
$[T_{min}, T_{max}]$	[3,15] s
subdomain size per $\omega^{\uparrow}$	$2 \times L_{off}(\omega^{\uparrow})$ (maximum) $1 \times L_{off}(\omega^{\uparrow})$ (minimum)
$[\Gamma_{min}, \Gamma_{max}]$	[0.3,1.0]
Rad	75 m
stationary time (temp. spectral storage)	60 s
α	0.012
$\lvert\boldsymbol{U}\rvert_{max}$	$0.75\,\mathrm{m\,s^{-1}}$
$[d_{min}, d_{max}]$	[0.1,50] m
Q_c	$0.0005\,\mathrm{m^2\,s^{-3}}$
Q_U	$0.0005\,\mathrm{m^2\,s^{-3}}$

C

Appendix C

C.1. Depth inversion paramter settings

Table C.1.: Default parameter values of the depth inversion algorithm

Parameter	Value
overlap	56 s (in [34]: 16 s)
time analytic extension	False (in [34]: True)
maximum subdomain size per frequency	$2.5 \times L_{off}(\omega^{\uparrow})$ (in [34]: $2.0 \times L_{off}(\omega^{\uparrow})$)
Γ_{max}	1.2 (in [34]: 1.0)
α	0.0075 (conform 1 fps video)

Parts of this appendix have been published in Remote Sensing **14**, 1847 (2022) [35].

List of Publications

Peer-reviewed Journal Articles

First Author

4. M. Gawehn, R. Almar, E. W. J. Bergsma, S. de Vries and S. Aarninkhof. 'Depth Inversion from Wave Frequencies in Temporally Augmented Satellite Video'. In: *Remote Sensing* 14.8 (Apr. 2022), p. 1847. issn: 2072-4292. doi: 10.3390/rs14081847

3. M. Gawehn, S. de Vries and S. Aarninkhof. 'A Self-Adaptive Method for Mapping Coastal Bathymetry On-The-Fly from Wave Field Video'. In: *Remote Sensing* 13.23 (2021), p. 4742. issn: 20724292. doi: 10.3390/rs13234742

2. M. Gawehn, A. van Dongeren, S. de Vries, C. Swinkels, R. Hoekstra, S. Aarninkhof and J. Friedman. 'The application of a radar-based depth inversion method to monitor near-shore nourishments on an open sandy coast and an ebb-tidal delta'. In: *Coastal Engineering* 159.April (2020), p. 103716. issn: 03783839. doi: 10.1016/j.coastaleng.2020.103716

1. M. Gawehn, A. van Dongeren, A. van Rooijen, C. D. Storlazzi, O. M. Cheriton and A. Reniers. 'Identification and classification of very low frequency waves on a coral reef flat'. In: *Journal of Geophysical Research: Oceans* 121.10 (Oct. 2016), pp. 7560–7574. issn: 21699275. doi: 10.1002/2016JC011834. url: http://doi.wiley.com/10.1002/2016JC011834

Co-Author

3. B. C. Van Prooijen, M. F. Tissier, F. P. De Wit, S. G. Pearson, L. B. Brakenhoff, M. C. Van Maarseveen, M. Van Der Vegt, J. W. Mol, F. Kok, H. Holzhauer, J. J. Van Der Werf, T. Vermaas, M. Gawehn, B. Grasmeijer, E. P. Elias, P. K. Tonnon, G. Santinelli, J. A. Antolínez, P. L. M. De Vet, A. J. Reniers, Z. B. Wang, C. Den Heijer, C. Van Gelder-Maas, R. J. Wilmink, C. A. Schipper and H. De Looff. 'Measurements of hydrodynamics, sediment, morphology and benthos on Ameland ebb-tidal delta and lower shoreface'. In: *Earth System Science Data* 12.4 (2020), pp. 2775–2786. issn: 18663516. doi: 10.5194/essd-12-2775-2020

2. R. Almar, E. W. Bergsma, M. A. Gawehn, S. G. Aarninkhof and R. Benshila. 'High-frequency Temporal Wave-pattern Reconstruction from a Few Satellite Images: A New Method towards Estimating Regional Bathymetry'. In: *Journal of Coastal Research* 95.sp1 (2020), pp. 996–1000. issn: 15515036. doi: 10.2112/SI95-194.1

1. A. Vött, H. J. Bruins, M. Gawehn, B. N. Goodman-Tchernov, P. M. De Martini, D. Kelletat, G. Mastronuzzi, K. Reicherter, B. R. Röbke, A. Scheffers, T. Willershäuser, P. Avramidis, P. Bellanova, P. J. Costa, C. Finkler, H. Hadler, B. Koster, J. Lario, E. Reinhardt, M. Mathes-Schmidt, K. Ntageretzis, D. Pantosti, I. Papanikolaou, P. Sansò, G. Scicchitano, A. Smedile and W. Szczuciński. 'Publicity waves based on manipulated geoscientific data suggesting climatic trigger for majority of tsunami findings in the mediterranean – response to 'tsunamis in the geological record: Making waves with a cautionary tale from the mediterranean' by marr'. In: *Zeitschrift fur Geomorphologie* 62.May (2019), pp. 7–45. issn: 18641687. doi: 10.1127/zfg_suppl/2018/0547

Peer-reviewed Conference Papers

First Author

1. M. Gawehn, S. de Vries and S. Aarninkhof. 'Depth and Surface Current Inversion on the Fly: a New Video Based Approach Using the Dynamic Mode Decomposition'. In: *Coastal Sediments 2019 - Proceedings Of The 9th International Conference*. Tampa/St. Pete, 2019, pp. 2511–2520. doi: 10.1142/9789811204487_0216

Co-Author

1. F. Grossmann, M. Gawehn, S. de Vries, F. P. de Wit and S. G. J. Aarninkhof. 'Comparison of Currents Derived from X-band Radar and Collected In-situ Data in Ameland Inlet Comparison of Currents Derived from X-band Radar and Collected In-situ Data in Ameland Inlet'. In: *Coastal Structures*. Karlsruhe, Germany: HENRY, 2019, pp. 416–425. isbn: 9783939230649. doi: 10.18451/978-3-939230-64-9

Book Chapters

Co-Author

1. A. Ton, M. Lee, S. Vos, M. Gawehn, K. den Heijer and S. Aarninkhof. 'Beach and nearshore monitoring techniques'. In: *Sandy Beach Morphodynamics*. Ed. by D. Jackson and A. Short. Elsevier, 2020. Chap. 27, pp. 659–687. isbn: 9780081029275. doi: 10.1016/B978-0-08-102927-5.00027-8. url: http://dx.doi.org/10.1016/B978-0-08-102927-5/00027-8%20https://linkinghub.elsevier.com/retrieve/pii/B9780081029275000278

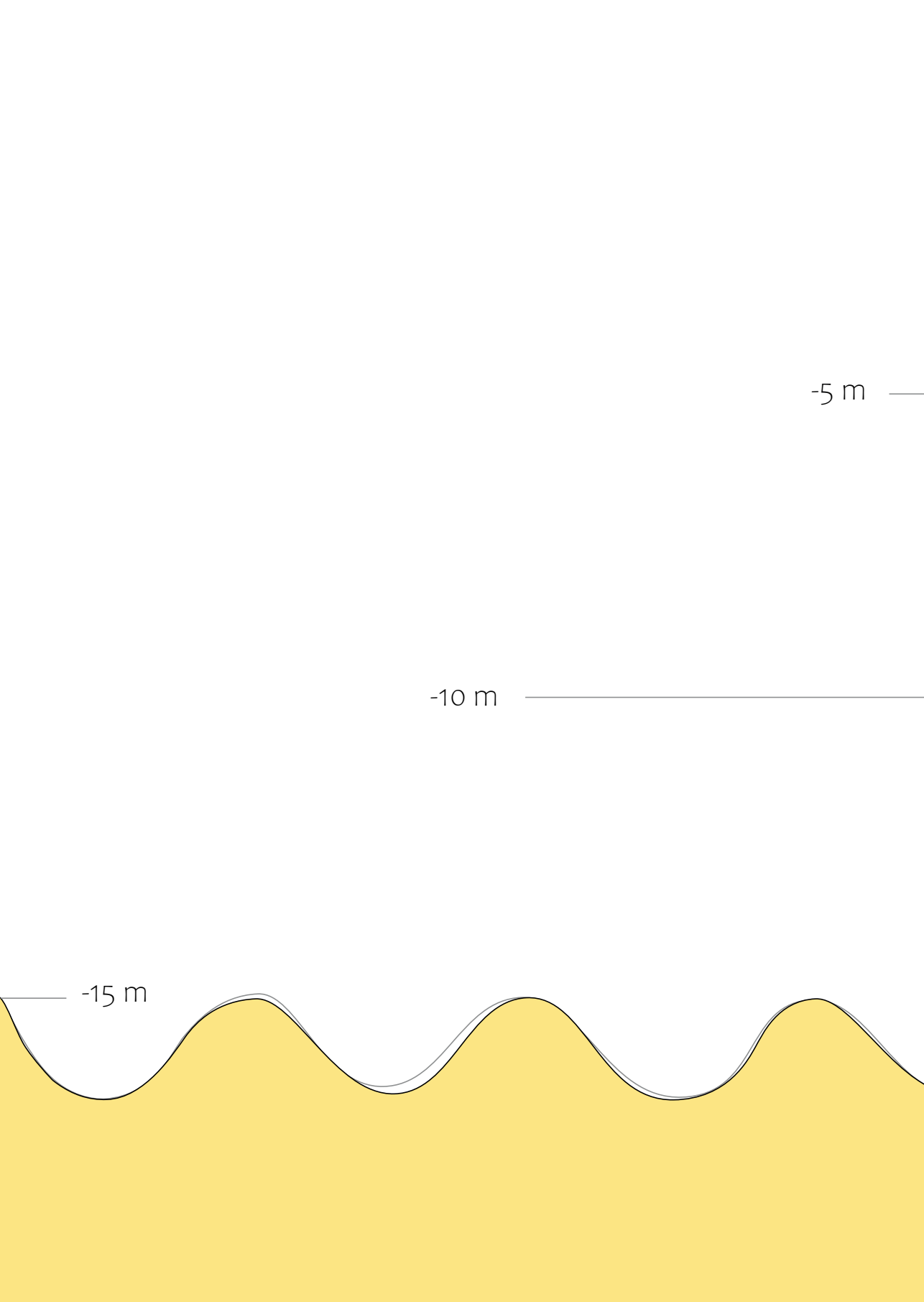
-5 m
-10 m
-15 m